frontiers | Research Topics

# Common and distinct mechanisms of migraine and stroke

**Edited by**
Rashid Giniatullin, Arn M. J. M. Van Den Maagdenberg, Rustem Khazipov and Jukka Jolkkonen

**Published in**
Frontiers in Cellular Neuroscience
Frontiers in Neuroscience
Frontiers in Pharmacology

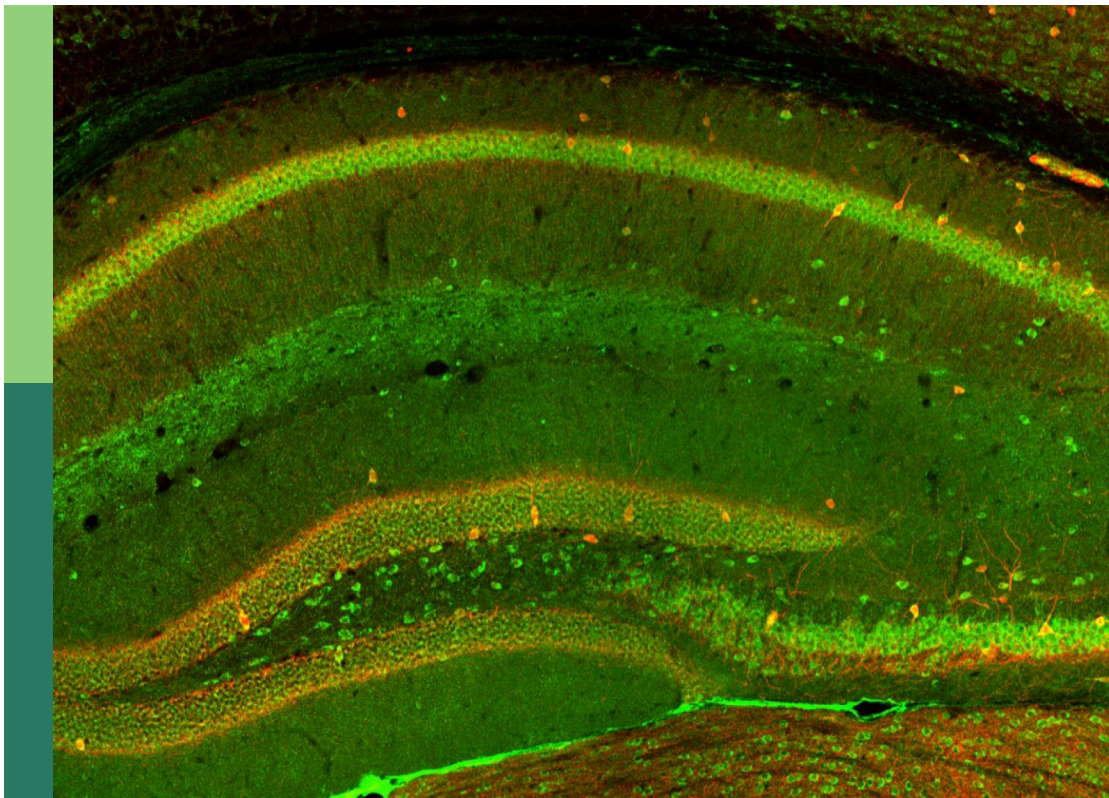

ISSN 1664-8714
ISBN 978-2-83252-019-2
DOI 10.3389/978-2-83252-019-2

## About Frontiers

Frontiers is more than just an open access publisher of scholarly articles: it is a pioneering approach to the world of academia, radically improving the way scholarly research is managed. The grand vision of Frontiers is a world where all people have an equal opportunity to seek, share and generate knowledge. Frontiers provides immediate and permanent online open access to all its publications, but this alone is not enough to realize our grand goals.

## Frontiers journal series

The Frontiers journal series is a multi-tier and interdisciplinary set of open-access, online journals, promising a paradigm shift from the current review, selection and dissemination processes in academic publishing. All Frontiers journals are driven by researchers for researchers; therefore, they constitute a service to the scholarly community. At the same time, the *Frontiers journal series* operates on a revolutionary invention, the tiered publishing system, initially addressing specific communities of scholars, and gradually climbing up to broader public understanding, thus serving the interests of the lay society, too.

## Dedication to quality

Each Frontiers article is a landmark of the highest quality, thanks to genuinely collaborative interactions between authors and review editors, who include some of the world's best academicians. Research must be certified by peers before entering a stream of knowledge that may eventually reach the public - and shape society; therefore, Frontiers only applies the most rigorous and unbiased reviews. Frontiers revolutionizes research publishing by freely delivering the most outstanding research, evaluated with no bias from both the academic and social point of view. By applying the most advanced information technologies, Frontiers is catapulting scholarly publishing into a new generation.

## What are Frontiers Research Topics?

Frontiers Research Topics are very popular trademarks of the *Frontiers journals series*: they are collections of at least ten articles, all centered on a particular subject. With their unique mix of varied contributions from Original Research to Review Articles, Frontiers Research Topics unify the most influential researchers, the latest key findings and historical advances in a hot research area.

Find out more on how to host your own Frontiers Research Topic or contribute to one as an author by contacting the Frontiers editorial office: frontiersin.org/about/contact

# Common and distinct mechanisms of migraine and stroke

**Topic editors**

Rashid Giniatullin — University of Eastern Finland, Finland

Arn M. J. M. Van Den Maagdenberg — Leiden University Medical Center (LUMC), Netherlands

Rustem Khazipov — Institut National de la Santé et de la Recherche Médicale (INSERM), France

Jukka Jolkkonen — University of Eastern Finland, Finland

**Citation**

Giniatullin, R., Van Den Maagdenberg, A. M. J. M., Khazipov, R., Jolkkonen, J., eds. (2023). *Common and distinct mechanisms of migraine and stroke*. Lausanne: Frontiers Media SA. doi: 10.3389/978-2-83252-019-2

# Table of contents

frontiers | Frontiers in Cellular Neuroscience

TYPE Editorial
PUBLISHED 13 March 2023
DOI 10.3389/fncel.2023.1171836



OPEN ACCESS

EDITED AND REVIEWED BY
Dirk M. Hermann,
University of Duisburg-Essen, Germany

*CORRESPONDENCE
Roustem Khazipov
✉ roustem.khazipov@inserm.fr

SPECIALTY SECTION
This article was submitted to Cellular Neuropathology, a section of the journal Frontiers in Cellular Neuroscience

RECEIVED 22 February 2023
ACCEPTED 24 February 2023
PUBLISHED 13 March 2023

CITATION
Giniatullin R, Khazipov R, van den Maagdenberg AMJM and Jolkkonen J (2023) Editorial: Common and distinct mechanisms of migraine and stroke.
*Front. Cell. Neurosci.* 17:1171836.
doi: 10.3389/fncel.2023.1171836



# Editorial: Common and distinct mechanisms of migraine and stroke

Rashid Giniatullin [1], Roustem Khazipov [2,3]*, Arn M. J. M. van den Maagdenberg [4,5] and Jukka Jolkkonen [1]

[1]A.I.Virtanen Institute for Molecular Sciences, University of Eastern Finland, Kuopio, Finland, [2]INMED, INSERM UMR1249, Aix-Marseille University, Marseille, France, [3]Laboratory of Neurobiology, Kazan University, Kazan, Russia, [4]Department of Human Genetics, Leiden University Medical Center, Leiden, Netherlands, [5]Department of Neurology, Leiden University Medical Center, Leiden, Netherlands

KEYWORDS

**brain ischemia, migraine, spreading depolarization (SD), peri-infarct depolarizations, stroke**

Editorial on the Research Topic
Common and distinct mechanisms of migraine and stroke

The Research Topic "*Common and distinct mechanisms of migraine and stroke*" is focused on the underlying mechanisms of both disorders. Both migraine and stroke are common and costly disorders that pose a great burden on the patient, their family, and society. Epidemiological studies have demonstrated a bidirectional comorbidity, which poses the question to what extent similar molecular mechanisms lead to the disorders and the co-occurrence in a patient. Evidence for a mechanistic link between stroke and migraine is strongest for migraine with aura and suggests that spreading depolarization (SD) in the brain is a key shared mechanism. Still, other mechanisms, e.g., neuroinflammation and oxidative stress, likely contribute to both pathologies, and a hypercoagulable state may also play a role in both migraine and stroke (Figure 1). Whereas, current evidence suggests a "stroke-migraine SD continuum," we lack detailed knowledge on the full spectrum of underlying neurobiological mechanisms in migraine and stroke, hence the focus of the Research Topic.

The presented research aims at elucidating disease mechanisms that play a role in stroke and, to a certain extent, shed light on the relationship between stroke and migraine (Figure 1). The collection of contributions on SD is crowned by a comprehensive review by Lemale et al. on the SD continuum in various clinical conditions, ranging from migraine to ischemic stroke and traumatic brain injury. A claim was made that SD represents a prime, most neglected, pathophysiological process in acute neurology. The authors review the basal mechanisms underlying SD and associated changes in cortical activity and provide evidence that associations between SD and spreading depression of activity are by no means trivial, but rather pose unsolved mechanistic puzzles. Lu and Scharfman presented a methodological advance to study SD using hippocampal slices in a submerged chamber with a flow of low-magnesium/high-potassium solution above and below the slice that reliably evokes recurrent SDs and seizure-like events. Their model provides new opportunities to explore SDs and interactions between SDs and paroxysmal activities. Gainetdinov et al. presented a quite unique developmentally immature SD phenotype with small depolarizations, transient recovery, and maintained excitability in neonatal cortical neurons during SD evoked by oxygen-glucose deprivation.

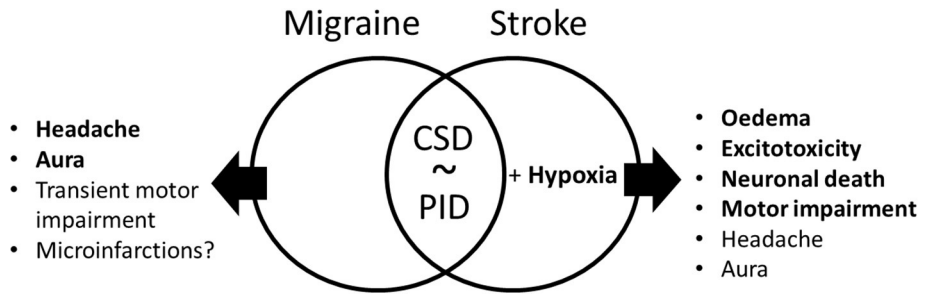


FIGURE 1
Common and distinct symptoms and mechanisms in migraine and stroke. Both migraine and stroke might have common symptoms, such as headache and aura, as well as sustained in stroke and transient in familial hemiplegic migraine motor impairment. The central mechanism in stroke is neuronal death, while there is some evidence of the presence of microinfarctions in migraine. The best obvious common mechanism of the two disorders is cortical spreading depolarization (CSD) in migraine with aura that is similar to peri-infarct depolarization in ischemic stroke. The PID in stroke is also associated with local hypoxia, which exaggerates the outcome of this pathology via edema, excitotoxicity, and finally leads to neuronal death.

In search for a treatment, Wei et al. explored for beneficial effects of oxymatrine, a quinolizidine alkaloid used in traditional Chinese herb medicine, against neonatal hypoxic–ischemic brain damage. Oxymatrine exerted neuroprotective effects both *in vivo* and *in vitro* in models of hypoxia-ischemia that involve the PI3K/Akt/mTOR pathway and attenuation of excessive autophagy.

Suleimanova et al. investigated through computational modeling, nociceptive signaling in familial hemiplegic migraine type 3 (FHM3) caused by gain-of-function mutations in the *SCN1A* gene. The gene encodes the $\alpha_1$ subunit of voltage-gated $Na_V1.1$ sodium channels with mutations linked to epilepsy and stroke, which are comorbid with migraine. The combined activation by ATP and serotonin of purinergic P2X3 and serotonergic 5-HT3 receptors, expressed on trigeminal afferents, resulted in high-frequency spiking activity in the disease condition. Of several FHM3 mutations, missense mutation L263V has the longer activation state and induced the most profound spiking activity in the meninges, predicting more severe headache symptoms in patients with this mutation.

Linstra et al. investigated the connection between migraine and stroke, and especially sex differences in the risk of stroke in patients with migraine, among 2,492 patients with ischemic stroke, of which 425 also had migraine. A history of migraine appears not to be associated with changes in the prevalence of conventional cardiovascular risk factors. However, young women with migraine had a higher risk for stroke whereas men with migraine had a poorer outcome compared to those without migraine.

van der Weerd et al. performed a systematic review of 24 studies with data on sex differences in hemostatic factors in ischemic stroke. Data from 25 factors were investigated in a total of 7,247 patients. Although lack of data, foremost of replication of findings in independent studies that calls for follow-up studies, current data suggested higher levels of procoagulant factors (FVII-C, FXI, D-dimer, tPA, and PAI-1) in women and higher coagulant inhibitors (protein-S and P-selectin) in men.

In a mechanistic study, Liu Y. et al. explored the DNA methylation status in blood samples of stroke patients. Compared to controls, almost 300 genes showed different methylation levels, of which seven were validated in larger patient groups, with *CAMTA1* being significantly altered. The authors also generated a *CAMTA1* knockout in SH-SY5Y neuroblastoma cells, revealing an enrichment of gene sets that are involved in cellular proliferation and cell cycle. When knockout cells were subjected to oxygen-glucose deprivation and reperfusion, which induces neuronal injury related to brain ischemia, it was shown that cyclin D1, an essential regulator of cell cycle progression, was upregulated, suggesting that *CAMTA1* plays a role in stroke.

The last contribution to the Research Topic came from Liu C. et al. who used a bioinformatics approach to identify possible therapeutic targets related to ferroptosis, a type of programmed cell death characterized by iron-dependent accumulation of lipid peroxides. By combing ischemic stroke microarray data with publically available data on ferroptosis regulators and disease associations, they identified 33 differentially expressed genes relevant to ferroptosis. Four of which, *HMOX1*, *STAT3*, *CYBB,* and *TLR4*, were enriched in the HIF-1 signaling pathway. Subsequent analyses revealed an upregulation of these genes in mouse brain tissue after ischemic stroke by middle cerebral artery occlusion (MCAO)/reperfusion. Dexmedetomidine, a selective α2-receptor agonist, reduced MCAO-induced cell death and improved neurobehavioral deficits. Also, it reversed the abovementioned expression changes as well as levels of inflammatory factors TNFα and IL-6, thereby providing evidence that the compound inhibits ferroptosis mechanisms in ischemic stroke.

In summary, this Research Topic highlights common mechanisms and complex, often intertwined, relationships between migraine and stroke. Newly discovered mechanisms revealed potential therapeutic targets that need confirmation in clinically predictive animal models. Large patient cohort studies revealed clinical risk factors and sex differences in migraine and stroke. Together, the collected articles are an important reference to guide the field in finding fundamental answers to the overlapping pathology in migraine and stroke, which eventually is expected to lead to safe, effective, and personalized treatments.

## Author contributions

All authors listed have made a substantial, direct, and intellectual contribution to the work and approved it for publication.

## Conflict of interest

The authors declare that the research was conducted in the absence of any commercial or financial relationships that could be construed as a potential conflict of interest.

## Publisher's note

frontiers in Pharmacology

ORIGINAL RESEARCH
published: 13 April 2021
doi: 10.3389/fphar.2021.642415

# Neuroprotective Effects of Oxymatrine on PI3K/Akt/mTOR Pathway After Hypoxic-Ischemic Brain Damage in Neonatal Rats

*Wei Wei*[1†], *Min Lu*[1†], *Xiao-bing Lan*[2], *Ning Liu*[2], *Wei-ke Su*[1*], *Alexandr V. Dushkin*[4*] and *Jian-qiang Yu*[2,3*]

[1]Collaborative Innovation Center of Yangtze River Delta Region Green Pharmaceuticals, Zhejiang University of Technology, Hangzhou, China, [2]Department of Pharmacology, Ningxia Medical University, Yinchuan, China, [3]Ningxia Hui Medicine Modern Engineering Research Center and Collaborative Innovation Center, Ningxia Medical University, Yinchuan, China, [4]Institute of Solid State Chemistry and Mechanochemistry, Novosibirsk, Russia

OPEN ACCESS

**Edited by:**
Rustem Khazipov,
Institut National de la Santé et de la Recherche Médicale (INSERM), France

**Reviewed by:**
Ewa Krystyna Szczepanska-Sadowska,
Medical University of Warsaw, Poland
Chuansheng Zhao,
The First Affiliated Hospital of China Medical University, China

***Correspondence:**
Wei-ke Su
pharmlab@zjut.edu.cn
Alexandr V. Dushkin
drivergood@mail.ru
Jian-qiang Yu
yujq910315@163.com

[†]These authors contributed equally to this work.

**Specialty section:**
This article was submitted to Neuropharmacology, a section of the journal Frontiers in Pharmacology

**Received:** 16 December 2020
**Accepted:** 25 February 2021
**Published:** 13 April 2021

**Citation:**
Wei W, Lu M, Lan X, Liu N, Su W, Dushkin AV and Yu J (2021) Neuroprotective Effects of Oxymatrine on PI3K/Akt/mTOR Pathway After Hypoxic-Ischemic Brain Damage in Neonatal Rats. Front. Pharmacol. 12:642415. doi: 10.3389/fphar.2021.642415

Oxymatrine (OMT), a quinolizidine alkaloid extracted from traditional Chinese herb *Sophora flavescens* Ait, has drawn attention because of its beneficial bioactivities against hypoxic–ischemic brain damage (HIBD). However, the underlying molecular mechanism remains unclear. In this study, we determined the *in vivo* and *in vitro* effects of OMT on seven-day old Sprague–Dawley rats with HIBD and in a rat model of primary hippocampal neuron oxygen glucose deprivation reoxygenation (OGD/R). This study was aimed to evaluate whether OMT exerted neuroprotective effects mediated by the (phosphatidylinositol 3-kinase/protein kinase B/mammalian target of rapamycin) PI3K/Akt/mTOR pathway after HIBD. Experimental results showed that the alkaloid significantly improved the early neurofunctional development, brain water content, abnormal pathological changes, and necrosis of neurons after HIBD. Moreover, OMT enhanced the cell viability and stabilized the mitochondrial permeability transition pore in the primary hippocampal neurons after OGD/R. OMT significantly decreased the autophagosome generation, elevated the expression of PI3K, Akt, and mTOR, and simultaneously reversed the mRNA expression of microtubule-associated protein 1-light chain 3 (LC3), Beclin-1, and sequestosomel (P62) induced by hypoxia and ischemia. However, these protective effects against HIBD could be suppressed when rapamycin, a specific inhibitor of mTOR, was included. Hence, the OMT exerted neuroprotective effects against HIBD by attenuating excessive autophagy by mediating the PI3K/Akt/mTOR pathway.

**Keywords: hypoxic-ischemic brain damage, oxymatrine, neuroprotective, autophagy, PI3K/AKT/mTOR**

## INTRODUCTION

Neonatal perinatal asphyxia usually results in hypoxic–ischemic brain damage (HIBD), which is characterized by cerebral hypoxia and decreased or suspended cerebral blood flows. This HIBD condition, is closely related to acute death and subsequent life-long neurological deficits in neonates and accounts for approximately 23% of the annual neonatal deaths (Lawn et al., 2005; Martin et al., 2019). Although antenatal and neonatal cares have been advanced in the past several decades, the incidence of HIBD is approximately 26 cases per 1,000 live births in developing countries (Yıldız

et al., 2017; Li et al., 2019). Hypothermia is currently the only established treatment option that decreases the risk of death and neurodevelopmental impairment in infants with HIBD (Jacobs et al., 2013), such as cerebral palsy, hearing loss and other neuromotor disorders, from 60 to 45% (Martin et al., 2019). However, approximately 50% of infants are still at risk of neurological sequelae and even death with hypothermia treatment (Edwards et al., 2010; Wu and Gonzalez, 2015).

Potential injurious factors of neonatal HIBD are complex and involve mitochondrial damage, excitotoxicity, oxidative stress, inflammation, apoptosis and autophagy (Douglas-Escobar and Weiss, 2015). Autophagy is a programmed cell death pattern of self-degradation in aging, damaged organelles and long-lifespan proteins. Neuronal autophagy plays an important role in hypoxia–ischemia (HI)-induced neuronal loss. This process is also a double-edged sword, that is moderate autophagy can maintain the homeostasis and function of neurons. By contrast, excessive autophagy may destroy organelles and cytosol, leading to the destruction of cellular structures and functions. Reducing excessive autophagy and increasing neuronal survival can be effective therapeutic targets for neonatal HI brain injury. The kinase cascade including phosphoinositide 3 kinase (PI3K), protein kinase B (Akt), and the mammalian target of rapamycin (mTOR) (PI3K/Akt/mTOR) signaling pathway, is the central cascade involved in cell transcription, translation, migration, metabolism, proliferation, and survival (Koh and Lo, 2015). As the only protective pathway of autophagy, this cascade is closely related to the regulation of autophagy. Several studies have demonstrated that the PI3K/Akt/mTOR signaling pathway could attenuate autophagy when it is activated (Liu et al., 2019). The neuroprotective effect of the PI3K/Akt/mTOR pathway has been widely studied in cerebral ischemia. Previous studies have also shown that the inhibition of autophagy exert neuroprotective effects by regulating the PI3K/Akt/mTOR signaling pathway (Koh and Lo, 2015; Huang et al., 2018).

Chinese medicinal herbs have been widely used in clinical treatment because of their multiple targeting capacity and protective benefits in traditional Chinese medicine. Oxymatrine (OMT), a quinolizidine alkaloid extracted from traditional Chinese herb *Sophora flavescens* Ait (Funaya and Haginaka, 2012; Panthati et al., 2012) (Chinese name "Kushen"), has been proved to vast pharmacological actions, such as anti-inflammation, antioxidant, antiviral, immunomodulation, and neuroprotection activities (Cui et al., 2011; Dong et al., 2013; Wang and Jia, 2014; Zhao et al., 2015). We also showed in our previous study that this alkaloid could ameliorate brain injury in hypoxic-ischemic neonatal rats (Huang et al., 2018). However, the molecular mechanism of neuroprotection by OMT remains unclear. Based on a study that reported the involvement of PI3K/Akt/mTOR in the autophagy processes in HIBD, we hypothesized that PI3K/Akt/mTOR pathways could be a part of the therapeutic effects of OMT. Therefore, we performed *in vivo* and *in vitro* experiments to explore deeply the protective effect of OMT after HIBD and determine its relationship with the PI3K/Akt/mTOR signaling pathway in regulating autophagy.

# MATERIALS AND METHODS

## Animals and Establishment of the HIBD Model

Seven-day old Sprague–Dawley rats, 12–17 g weight (The ratio of male to female is 1:1) were provided by the Experimental Animal Center of Ningxia Medical University (animal license number: SCXK Ningxia 2015-0001). All surgeries and sample collection were carried out under diethyl ether anesthesia to minimize suffering and the number of animals used. The protocols were performed in accordance with the current guidance for the care of laboratory animals in Ningxia Medical University. All the researchers who performed testing were blinded.

A modified Rice-Vannucci model was established as previously described (Vannucci and Vannucci, 2005). Seven-day-old Postnatal 7 days (P7) neonatal Sprague–Dawley rats were narcotized by ether inhalation, the left common carotid artery was ligated with 6-0 silk and cut off within 5 min. After the surgery, the rats were allowed to return to their dam and recover for 1.5 h. Then, the pups were placed in a low-oxygen container (8% oxygen in nitrogen) maintained at 37°C and hypoxia for 2.5 h. All surviving pups were returned to their dam after 2.5 h of hypoxia. In the sham group, the left common carotid artery was only exposed. Our previous experiments showed that brain tissue suffers moderate damage at 48 h time point (Huang et al., 2018), we selected this time point for the following experiments.

## Drug Administration

OMT (Beijing Zhongke quality inspection Biotechnology Co., Ltd., China, purity = 98.26%, Batch NO: Y-013-161216) was dissolved in normal saline (NS; 0.9% NaCl) before the experiment. Drugs were administered intraperitoneally at 0.1 ml/10 g body weight. To determine the neuroprotective effects on HIBD, unsexed pups were assigned randomly into 3 groups ($n = 6$ for each group) as follows: Group 1, control (sham surgery) with an equal volume by body weight of NS; Group 2, subjected to cerebral hypoxia-ischemia (HI) with an equal volume by body weight of NS; Group 3, HI with OMT (120 mg/kg). OMT was intraperitoneally (ip) injected at 12 h intervals for 2 days. To further assess between the neuroprotective of OMT and the PI3K/Akt/mTOR pathway, the mTOR inhibitor rapamycin (MCE, America) were dissolved in 2% carboxymethylcellulose sodium (CMC-Na) and administered via intraperitoneal (ip) injection 1 h before HI (Bodine et al., 2001).

## Measurement of Neurobehavioral Development

According to previous published literature (Wu et al., 2017), the neurological reflexes including righting reflex, negative geotaxis reflex and cliff avoidance reflex was elicited at 48 h after HI. An outside environment was maintained at 37°C, each reflex assessed subsequently, and the pups were given 5 min of rest.

## Determination of Infarct Volume

After 48 hours of HI, the brain infarct volume was measured according to the previously described (Wei et al., 2019). The infarct volumes were measured through image analysis software (Image-Pro Plus, United States). The brain infarction volume was calculated accurately as follows to exclude the influence of cerebral edema (Lin et al., 1993): The percentage of brain infarction (%) = (normal hemisphere volume − non-infarct volume of the infarct side)/normal hemisphere volume × 100.

## Measurement of the Brain Water Content

The cerebral water content according to the wet-dry method as previously described (Wang et al., 2018). Briefly, brains were removed quickly and acquired the wet weight using an electronic analytic balance. Then, the samples were dried in a 100°C oven for 24 h and weighed again to obtain the dry weight. The following formula was used to determine the degree of brain water content: water content (%) = (wet weight − dry weight)/wet weight × 100% (Zhu et al., 2018).

## Hematoxylin and Eosin (HE) Staining

After 48 h of HI, rats were anesthetized and perfused with ice NS followed by 4% cold paraformaldehyde. Then, the brains removed immediately and submerged in 4% paraformaldehyde for overnight. Every tissue specimen was dehydrated and embedded in paraffin, and then successive brain coronal sections (5 μm) made with a microtome (Leica, Germany). The sections were dried at 80°C for 30 min, deparaffinized, rehydrated and stained with hematoxylin and eosin. The histopathological changes in cerebral hippocampus CA1, hippocampus CA3 and cortex were observed with light microscopy (Olympus BX-51, Japan) at a magnification of 200× and 400×.

## Terminal Deoxynucleotidyl Transferase-Mediated dUTP Nick-End Labeling (TUNEL) Staining

The slices were deparaffinized, rehydrated and then permeated with proteinase K to increase cell membrane permeability. The DNA fragmentation of apoptotic or necrotic cells bound to the terminal deoxynucleotidyl transferase (TdT) enzyme in a reaction buffer. After rinsing with PBS thoroughly, slides were mounted with 4′, 6-diamidino-2-phenylindole (DAPI) for at room temperature for nuclear staining. Ultimately, the TUNEL-positive neurons in 6 cortical fields of each group were photographed randomly with an Olympus fluorescence microscope (Olympus FV1000, Japan) at a magnification of 400×. The following formula was used to calculate the rate of apoptosis: apoptotic neurons amount/total neurons amount × 100%.

## Measurement of Transmission Electron Microscopy (TEM)

The cerebral tissues were prefixed with ice fixative solution for 2 h, and cut into 1 mm × 1 mm × 1 mm blocks. They were collected and fixed for 2 h with 2% cold glutaraldehyde. Then, the blocks were post-fixed with 2% ice osmium tetroxide, dehydrated, and embedded in epon. Ultrathin sections (75 nm-thick) were cut, placed onto colloid-coated copper grids and stained with 0.4% uranyl acetate and 2% lead acetate. Finally, Samples were observed by TEM (Hitachi, Tokyo, Japan).

## Primary Hippocampal Neurons Culture and Oxygen Glucose Deprivation/ Reoxygenation (OGD/R) Model

The primary hippocampal neurons were prepared from brains (within 24 hours of born) of SD rats. Briefly, the hippocampus from newborn rats were separated carefully and placed in D-Hanks' balanced salt solution. After trituration and digestion with trypsase (containing EDTA) for 15 min at 37°C, the cell suspensions were seeded at a density of $1 \times 10^6$/L in 96-well plates or culture dishes in DMEM supplemented with 2% HEPES-buffered salt solution and 10% FBS. Afterward, DMEM culture medium was discarded and changed to neurobasal medium containing 2% B27. After that, change the culture medium every 2°days.

The primary cultured hippocampal neurons were subjected to OGD insult for 2 h and reperfusion for 24 h on day 7. Specifically, the culture medium was changed to glucose-free EBSS, a mixed gas (95% $N_2$ and 5% $CO_2$) was continuously pumped into the incubator for 2 h at 37°C. After the OGD, the culture medium was replaced with regular medium and put back into a normoxic incubator at normal conditions and OMT (5 μg/ml) with or without Rapamycin was added for 24 h. Rapamycin was dissolved in DMSO and the final concentration was 0.2 μg/ml. In the control group, the neurons were cultured under normal conditions without oxygen or glucose deprivation.

## MTT Assay Cell Viability

To determine whether OMT could ameliorate OGD/R-induced neuronal death, Methyl-thiazolyl-diphenyl-tetrazolium bromide (C0009, Beyotime, China) assays were used to evaluate the neuronal viability according to the manufacturer's instructions. Briefly, primary hippocampal neurons were plated in 96-well plates. After reoxygenation for 24 h, 20 μL of MTT solution was added and incubated at 37°C for 4 h. After incubation, the medium was replaced, and the neurons were suspended in dimethyl sulfoxide (DMSO). The optical density (OD) was detected at 490 nm by a microplate reader and the results are expressed as the percentages of cell viability compared to the control group.

## Determination of Mitochondrial Permeablity Transition Pore (mPTP)

Primary hippocampal neurons were underwent OGD/R 24 h later, the determination of mPTP according to the operation of mPTP detection kit. Diluting the dye solution to the desired concentration, and then added 1 ml of staining working fluid to each dish. The neurons were incubated with staining working fluid at 37°C for 15 min. After washing three times with PBS and then imaged with an Olympus fluorescence microscope (Olympus FV1000, Japan) at excitation wavelengths of 488 nm and emission wavelengths of 520 ± 10 nm, respectively.

**TABLE1 |** The primary antibodies in the experiment.

| Antibody | Company | Catalog number | Dilution multiple (*in vivo*/*in vitro*) |
|---|---|---|---|
| PI3K | Cell signaling technology | 20584-1A | 1:1,000/1:500 |
| p-PI3K | Cell signaling technology | 4228S | /1:500 |
| Akt | Abcam | GR242901-30 | 1:2000/1:500 |
| p-Akt | Cell signaling technology | 9271S | /1:500 |
| mTOR | Abcam | GR245538-8 | 1:1,000/ |
| LC3 | Proteintech | 14600-1-AP | 1:500/ |
| Beclin-1 | Proteintech | 11306-1-AP | 1:800/ |
| P62 | Proteintech | 18420-1-AP | 1:1,000/ |
| β-actin | Proteintech | 20536-1-AP | 1:1,000/1:1,000 |

## Monodansylcadaverine (MDC) Staining

After 24 h of OGD/R, neurons were centrifuged at 800 g for 5 minutes and collected after cleaning with 1 × Wash buffer (300 μL). Afterward, the supernatant was sucked out and suspended with equal volume 1 × Wash buffer, the concentration of neuron was adjusted to $10^6$/ml. The 90 μL cell suspension and 10 μL MDC dye solution was mixed evenly and stained at room temperature for 35 minutes. After centrifugation, the neurons were washed again with 300 μL 1×Wash buffer. Subsequently, Collection buffer was added to collect suspended neurons, which added to the slides and observed under an Olympus fluorescence microscope (Olympus FV1000, Japan) at a magnification of 600×.

## Immunofluorescence Analysis

For the immunofluorescence analyses, hippocampal neurons were washed with PBS three times and incubated with 4% paraformaldehyde for 15 min. Afterward, the cells were incubated in goat serum for 60 min at room temperature to block unrelated antigens. The primary anti-*p*-mTOR antibody (1:100, Cell signaling technology, 5536S) was applied to the cells at 4°C overnight and followed by incubation with Rhodamine (TRITC)–conjugated secondary antibody at 37°C for 1 h in the dark. Ultimately, the nuclei were stained with DAPI for 5 min and images were acquired with a fluorescence microscope (Olympus BX-51, Japan) and the fluorescence intensity was analyzed with the ImageJ software.

## Western Blot Analysis

The rats were euthanized by anesthesia with inhaling ether 48 h after HIBD, and the ischemic hemisphere were removed rapidly in ice and stored at −80°C. Primary hippocampal neurons were collected from the culture dishes 24 h after OGD/R. The ischemic hemisphere and primary hippocampal neurons were homogenized in ice-cold lysis buffer in glass homogenizers (Nanjing Jiancheng Bioengineering Institute, Nanjing, China) or epoxide tubes. The homogenate was centrifugated at 12,000 g for 10 min at 4°C to obtain the total protein. The protein concentration of the samples was analyzed by BCA method according to manufacturer's instruction (Nanjing Jiancheng Bioengineering Institute, Nanjing, China). Equal amount of protein lysate (50 μg) in each simple were separated by 10% or 6% sodium dodecyl sulfate polyacrylamide gel electrophoresis (SDS-PAGE) and then transferred onto polyvinylidene fluoride (PVDF) membranes (200 mA, 2 h). Membranes was subsequently blocking with 5% skim milk powder for 2 h at room temperature and incubated with the primary antibodies overnight at 4°C (**Table 1**). After washing with PBST three times (containing 20% Tween-20), the PVDF membranes were incubated with the secondary antibodies (1:2000, SA00001-2; Proteintech) for 2 h at room temperature. The protein bands were observed by a Western blot detection system (Bio-Rad Laboratories, United States). Finally, the gray values of the bands were analyzed by Quantity One software.

## Quantitative Real-Time Polymerase Chain Reaction (Q-PCR)

At 24 h after OGD/R, total RNA of primary hippocampal neurons was extracted in accordance with the previous description (Zhao et al., 2018). Total RNA was then reverse transcribed, amplified and real-time Q-PCR analysis. Ultimately, the PCR products were analyzed quantitatively by using the melting curve. The fold induction ($2^{-\triangle\triangle Ct}$) was represented as the calculated results. Nucleotide sequences of primers utilized are as follows: Beclin1 (forward 5′-AGGAGTTGCCGTTGTACTGTTCTG-3′/reverse 5′-TGCCTC CAGTGTCTTCAATCTTGC-3′; 183 bp, 61.2°C), LC3 (forward 5′-AGCTCTGAAGGCAACAGCAAC-3′/reverse 5′-GCTCCA TGCAGGTAGCAGGAA-3′; 101 bp, 59.8°C), P62 (forward 5′-GGTGTCTGTGAGAGGACGAGGAG-3′/reverse 5′-TCTGGT GATGGAGCCTCTTACTGG-3′; 101 bp, 60.7°C) and β-actin (forward 5′-CCCATCTATGAGGGTTACGC-3′/reverse5′-TCTGGTGATGGAGCCTCTTACTGG-3′; 174 bp, 60.0°C).

## Data Analysis

The apoptosis ratio was analyzed by nonparametric test. The other values were expressed as mean ± SEM, and the statistical analysis of the results was evaluated by one-way ANOVA followed by Dunett's test. $p < 0.05$ was considered statistically significant.

# RESULTS

## OMT Improved HIBD-Induced Neurological Dysfunction

Compared with the Sham group, the rats that were subjected to HI exhibited a prolonged latent period in righting reflex, negative geotaxis and cliff avoidance reflex ($p < 0.01$, **Figures 1A–C**). However, the increased time for above reflexes was reduced

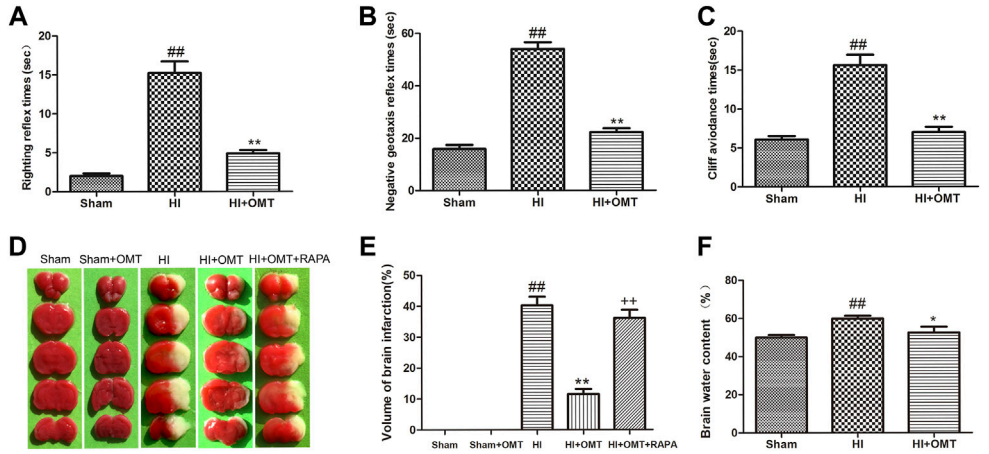


**FIGURE 1 |** Changes in the early neurological reflex performances, infarct volume and water volumes in neonatal rats at 48 h after hypoxia-ischemia brain damage (HIBD). **(A)** The latency of righting reflex. **(B)** The latency of negative geotaxis reflex and **(C)** The latency of n Cliff avoidance reflex. D Representative photographs of the infarct volume identified with 2,3,5-triphenyltetrazoliuM chloride (TTC) staining. **(E)** Measured infarct volumes. **(F)** Assessments of brain water content. The results are expressed as means ± SEM ($n = 6$ per group). $^{\#\#}p < 0.01$ vs. the sham group; $^{*}p < 0.05$, $^{**}p < 0.01$ vs. the HI group; and $^{++}p < 0.01$ vs. the oxymatrine (OMT) group.

significantly ($p < 0.01$, **Figures 1A–C**) in the HI + OMT group than that in HI group.

## OMT Ameliorated HIBD-Induced Cerebral Infarction

2,3,5-Triphenyltetrazolium chloride (TTC) staining is a recognized indicator for evaluating the volume of cerebral infarction. As shown in the images of the TTC staining in **Figure 1D**, the infarct volume was not observed and stained uniformly red in the sham group. The total infarct volume was significantly reduced from 40.32 ± 6.15%–11.60 ± 3.54% ($p < 0.01$) in the HI + OMT group compared with that in the HI group (**Figure 1E**, $p < 0.01$). Rapamycin (RAPA) treatment markedly increased the cerebral infarct volume ($p < 0.01$) compared with the HI + OMT group.

## OMT Decreased HIBD-Induced Cerebral Edema

Brain water content was assessed to evaluate the brain edema (**Figure 1F**). Compared with the sham group, the brain water content increased significantly after cerebral ischemia and hypoxia ($p < 0.01$). However, post-administration with OMT attenuated the brain water content from 59.90 ± 3.20%–52.60 ± 6.61% compared with the HI group ($p < 0.05$).

## OMT Attenuated HIBD-Induced Neuron Pathological Changes and Apoptosis

As shown in **Figure 2A**, neurons were abundant, arranged neatly and stained evenly in the cerebral hippocampus CA1, hippocampus CA3, and cortex in the sham group. Compared with the sham group, the number of cells decreased, the cells became arranged disorderedly, vacuolization, and karyopyknosis were observed in the HI group. After posttreatment with OMT, the expansion of neuronal injury was reversed to a certain extent in the cerebral hippocampus CA1, hippocampus CA3, and cortex (**Figure 2A**). The protective effect of OMT was further determined by TUNEL staining from the ischemic cortex. Virtually rare TUNEL-positive neurons were found in the sham group. By contrast, numerous TUNEL-positive neurons were detected in the HI group. However, compared with the HI group, the neuronal apoptosis was reduced substantially in the posttreatment with OMT (**Figures 2B,C**; $p < 0.01$).

## OMT Inhibited OGD/R-Induced Cell Death, the Openess of mPTP in Cultured Hippocampal Neurons

The results of the MTT assay for cell viability observed for 24 h after oxygen glucose deprivation reoxygenation (OGD/R) are shown in **Figure 3A**. Cell viability was significantly reduced in the OGD/R group compared with the control group ($p < 0.01$). Posttreatment with OMT (5 μg/ml) significantly enhanced the cell viability ($p < 0.01$) compared with that in the OGD/R group. The fluorescence intensity of the mPTP was consistent with that of cell viability. Interestingly, RAPA treatment reversed these effects of OMT (**Figures 3A,C**, $p < 0.05$, $p < 0.01$).

## OMT Reduced the Level of Autophagosome After HIBD and OGD/R

We evaluated the level of autophagy formation in the brain tissue *in vivo* and *in vitro* by tissue ultrastructure and MDC staining, respectively (**Figures 4A,B**). As demonstrated in **Figure 4**, autophagosomes were identified in the HI group but not in the OMT treatment group and sham group. MDC positive staining increased in the primary hippocampal neurons after OGD/R compared with that in the control group. MDC positive staining

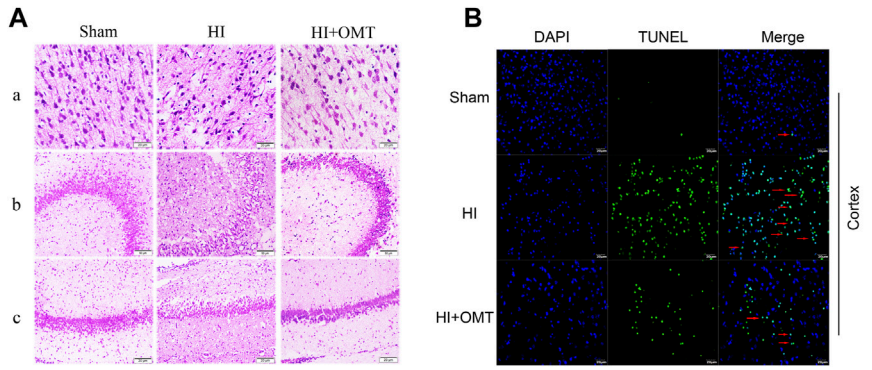


**FIGURE 2 |** Representative photographs of the hematoxylin and eosin (HE) and terminal deoxynucleotidyl transferase-mediated dUTP Nick End Labeling (TUNEL) staining in the hippocampus and cortex for the damaged neurons in the neonatal rats at 48 h after hypoxia-ischemia brain damage (HIBD). **(A)** Representative photographs of the morphological changes identified by HE staining: **(A)** cortex, **(B)** hippocampus CA3, and **(C)** hippocampus CA1. **(B)** Representative photographs of the neuronal apoptosis identified by TUNEL staining. **(C)** Quantitative representation of the expression of apoptotic neurons in the cortex. The results are expressed as mean ± SEM ($n$ = 6 per group). $^{\#\#}p < 0.01$ vs. the sham group; and $^{**}p < 0.01$ vs. the hypoxia-ischemia (HI) group.

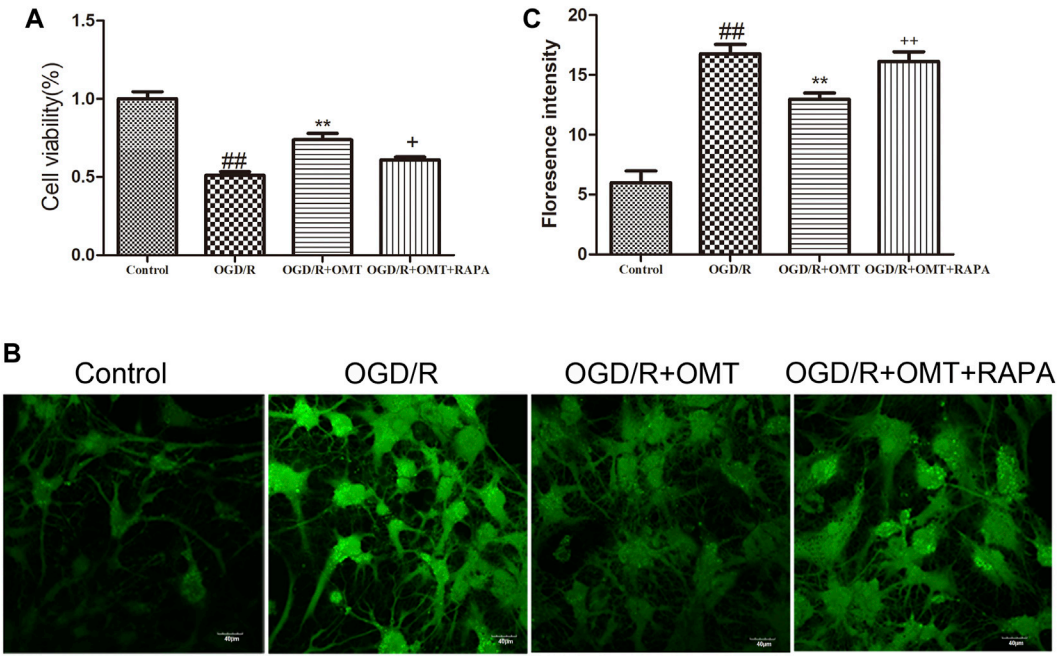


**FIGURE 3 |** Assessments of neuronal death and level of intracellular mitochondrial permeability transition pore (mPTP) in the primary hippocampal neurons at 24 h after oxygen-glucose deprivation reperfusion (OGD/R). **(A)** Cell viability assay. **(B)** Fluorescence micrographs of mPTP. **(C)** mPTP assay. The results are expressed as mean ± SEM ($n$ = 6 per group). $^{\#\#}p < 0.01$ vs. the sham group; $^{**}p < 0.01$ vs. the HI group; and $^{+}p < 0.05$, $^{++}p < 0.01$ vs. the oxymatrine (OMT) group.

decreased with post-administration with OMT. By contrast, posttreatment with RAPA increased the MDC positive staining.

## OMT Regulated the Expression of Autophagy-Related Protein and MRNA Induced HIBD and OGD/R

We further tested the effects of OMT on the mRNA expression of autophagy-related factors, such as Beclin-1, LC3, and P62 protein. As shown in **Figures 4C–E**, the mRNA expression of Beclin-1 and LC3 was significantly increased in the OGD/R group than that in the control group ($p < 0.01$). Post-administration of OMT induced a substantial decrease in the mRNA expression of Beclin-1 and LC3 ($p < 0.01$, $p < 0.05$). The expression of P62 mRNA significantly decreased compared with that in the control group ($p < 0.01$), but, OMT treatment could upregulate markedly its expression ($p < 0.01$). In addition, the expression of the above autophagy-related factors in the OMT could be partially

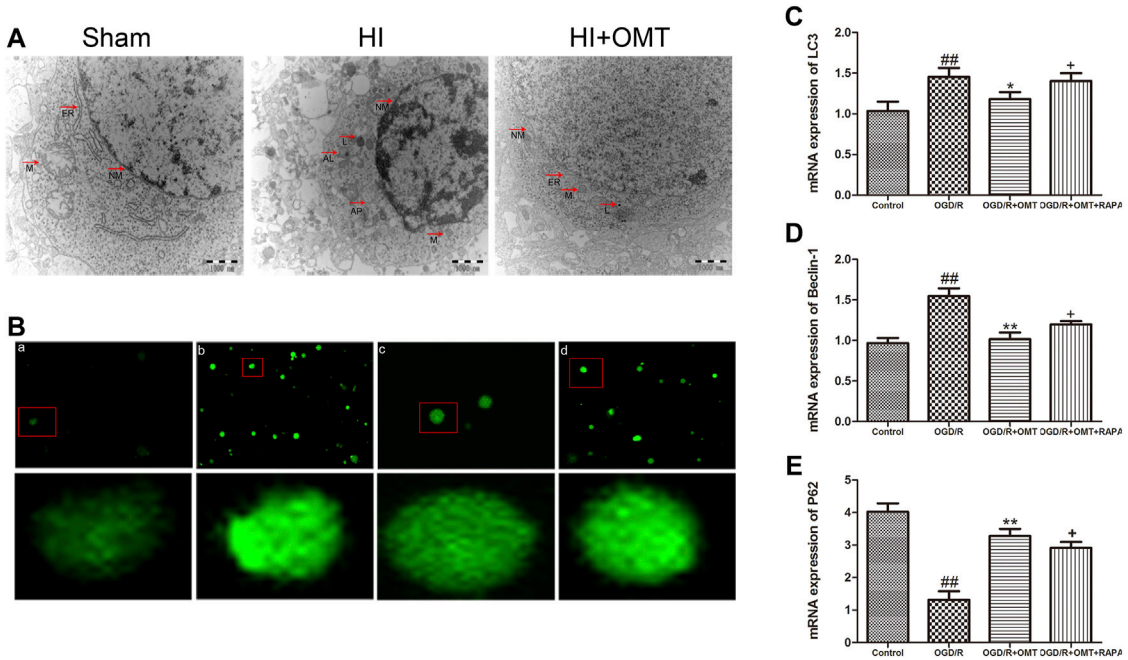


**FIGURE 4 |** Assessments of the level of autophagy *in vivo* and *in vitro*. **(A)** Transmission electron micrographs of the autophagosomes in the neonatal rats at 48 h after hypoxia-ischemia brain damage (HIBD). The arrows represent organelles and autophagosome: N, nucleus; NM, nucleus membrane; M, mitochondrion; ER, endoplasmic reticulum; L, lysosomes; and AP, autophagosome. **(B)** Autophagic vacuoles from each group measured by monodansylcadaverine (MDC) staining. **(C–E)** Levels of microtubule-associated protein 1-light chain 3 (LC3), Beclin-1 and sequestosomel (P62) mRNA in the primary hippocampal neurons measured at 24 h after oxygen-glucose deprivation reperfusion (OGD/R). The results are expressed as means ± SEM ($n = 6$ per group). $^{\#\#}p < 0.01$ vs. the sham group; $^{*}p < 0.05$, $^{**}p < 0.01$ vs. the HI group; and $^{+}p < 0.05$ vs. the oxymatrine (OMT) group.

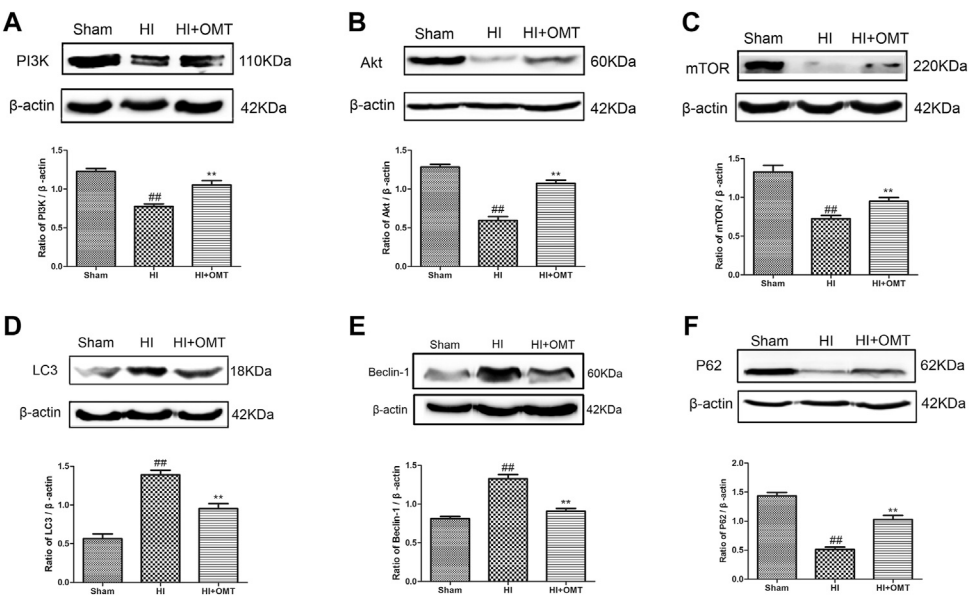


**FIGURE 5 |** Assessment of the protein expression levels of phosphatidylinositol 3-kinase (PI3K), protein kinase B (Akt), mammalian target of rapamycin (mTOR), LC3, Beclin-1 and P62 in the ischemic hemisphere in the neonatal rats at 48 h after hypoxia-ischemia brain damage (HIBD). Representative Western blots and quantitative analyses of the protein expression of **(A)** PI3K, **(B)** Akt, **(C)** mTOR, **(D)** LC3, **(E)** Beclin-1 **(F)** and P62. The results are expressed as means ± SEM ($n = 6$ per group). $^{\#\#}p < 0.01$ vs. the sham group; and $^{**}p < 0.01$ vs. the HI group.

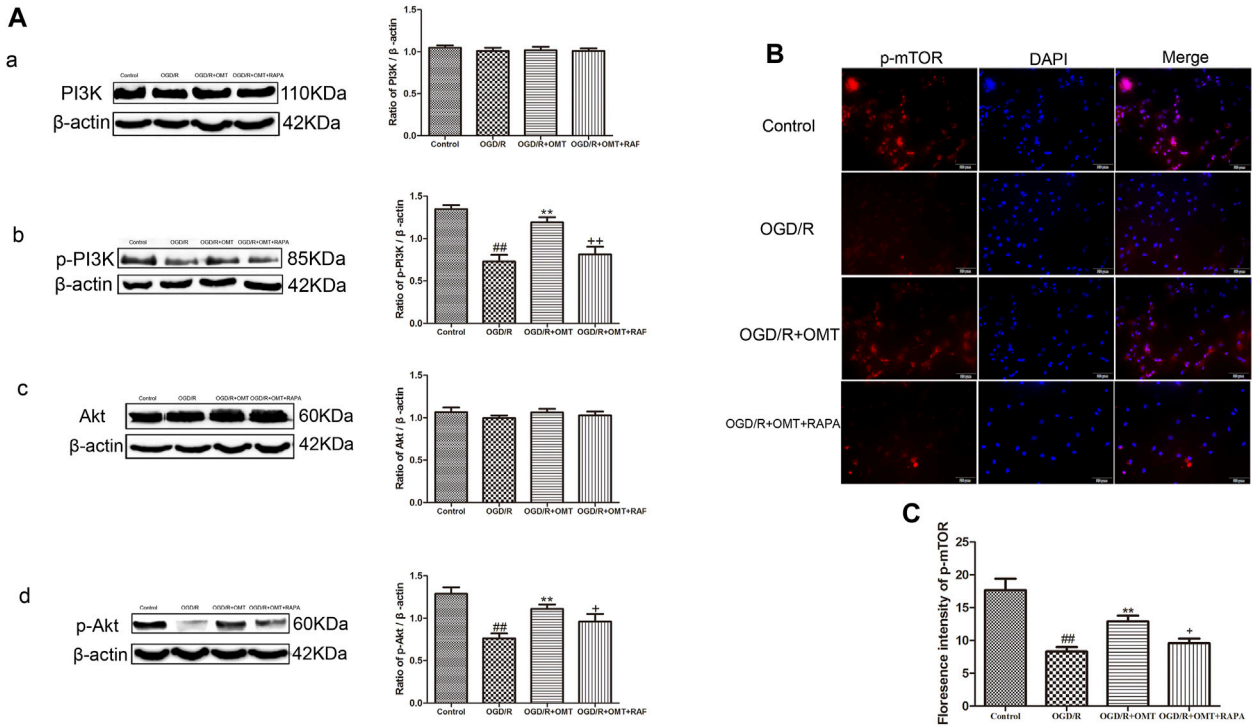


**FIGURE 6 |** Assessment of the expression levels of (*p*)-PI3K (*p*)-Akt, and p-mTOR in the ischemic hemisphere in the neonatal rats at 24 h after oxygen-glucose deprivation reperfusion (OGD/R). **(A)** Representative Western blots and quantitative analyses show the protein expression of **(A**, **B)** PI3K and p-PI3K, and **(C**, **D)** Akt and p-Akt. **(B)** Immunofluorescent-stained p-mTOR in the primary hippocampal neurons at 24 h after OGD/R. **(C)** Analysis of fluorescence intensity of p-mTOR. The results are expressed as mean ± SEM ($n$ = 6 per group). $^{\#\#}p < 0.01$ vs. the sham group; $^{*}p < 0.05$, $^{**}p < 0.01$ vs. the HI group; and $^{+}p < 0.05$ vs. the oxymatrine (OMT) group.

eliminated by RAPA ($p < 0.05$). Interesting, the result of the expression of autophagy-related factor proteins *in vivo* were consistent with those of mRNA expression (**Figures 5D–F**). The results showed that the LC3 and Beclin-1 protein expression levels in the ischemic hemisphere brain were significantly higher ($p < 0.01$, **Figures 5D,E**), whereas the protein expression of P62 was significantly lower in the ischemic hemisphere brain than in the sham group ($p < 0.01$, **Figure 5F**). 120 mg/kg OMT posttreatment can reverse the above protein expression.

## OMT Inhibited Autophagy by Activating PI3K/Akt/mTOR Pathway

These above experiments result preliminarily suggested that OMT could improve HIBD in neonatal rats via regulating autophagy-related protein. To further examine the relationship between the regulative effects of OMT on neuronal autophagy and the PI3K/Akt/mTOR pathway in HIBD, we detected the expression of PI3K, p-PI3K, Akt, *p*-Akt, and *p*-mTOR by Western blot and immunofluorescence analyses (**Figures 5**, **6**). The expression of PI3K, Akt, and mTOR were significantly reduced in the HI group than that in the sham group. Post-administration with OMT could reverse the expression of these kinases ($p < 0.01$). The expression of p-PI3K and p- Akt remained a basal expression under normal condition. OMT significantly enhanced the levels of p-PI3K and *p*-Akt relative to those in the OGD/R group ($p < 0.01$) but no statistically significant difference was observed in the expression of t-PI3K and t-Akt in the above groups ($p > 0.05$, **Figure 6**). Such rise in levels was inhibited by RAPA in the OMT + RAPA group relative to that in the OMT group ($p < 0.01$, $p < 0.05$ and $p < 0.05$, **Figures 6A,C**).

## DISCUSSION

OMT protected against brain injury in a neonatal rat model of HIBD by improving the early neurologic impairments, infarct volume, brain water volume, and neuronal damage and degeneration. OMT also exhibited also neuroprotective effects and reduced OGD/R-mediated cell death and the increase of mPTP in the primary hippocampal neurons. OMT decreased the formation of autophagosome and reversed the levels of autophagy-related factor expression induced by HIBD and OGD/R. OMT promoted the activation of PI3K and Akt and increased the fluorescence intensity of *p*-mTOR under HI. RAPA, an mTOR inhibitor, inhibited the mTOR expression and partially counteracted the neuroprotective effects of OMT. These findings suggest that OMT played a neuroprotective role in treating HIBD, and the

underlying mechanisms may have partly involved the activation of the PI3K/AKT/mTOR signaling pathway.

HIBD is the most common clinical disease of newborn that seriously threatens the physical and mental health of fetus and newborn. Animal model is of great significance to study the pathological mechanism of disease and evaluate the effect of therapeutic intervention. In the present study, we utilized a modified Rice-Vannucci model because the degree of development of the brain tissues of 7-day-old newborn rats is approximately equivalent to that of human fetuses or newborns because both species are in the synapse formation (Dobbing and Sands, 1979; McDonald and Johnston, 1990). In addition, the secondary pathological changes induced by HI in the rat model are similar to those of asphyxiated newborns. The latter is widely used to study neonatal cerebral ischemia–hypoxia injury. Cerebral neurons are extremely vulnerable to HI, because the metabolism of the immature brain is relatively vigorous, and their oxygen consumption accounts for approximately 50% of the total oxygen consumption. These neurons lack the necessary enzyme for effective glycolysis (Li et al., 2017). Once the oxygen and blood in the brain are blocked, which lead to a sharp lack of energy, depolarization of cell membranes occurs, followed by neuronal death. Eventually, a series of lesions, such as edema and infarction, are presented.

It has been reported in the literature that HIBD is accompanied by short-term neurological dysfunction. As expected, we observed that the latencies of the righting reflex, negative geotaxis reflex and cliff avoidance reflex remarkably prolonged subjected to HI in current study. Administering OMT improved these reflexes, revealing that OMT can improve early neurological dysfunction induced by HI in neonatal rats.

Brain edema is a common pathological state of brain tissue under HI. Current studies tend to focus on the cytotoxic brain edema and vasculogenic brain edema (Igor, 1987), which have many similarities in the mechanism of HIBD. Therefore, brain edema can be used as an indirect index to evaluate brain injury. In the present study, 120 mg/kg OMT could significantly ameliorate cerebral water content, which suggested that OMT protected against HIBD by mitigating cerebral water volume. In addition, the HE and TUNEL staining can provide further evidence of the protective effect of OMT.

HI can cause neuronal damage and death. The hippocampus and cortex are the most sensitive regions reflecting HI (Cheng et al., 2012), so we choose these areas to observe neuronal damage and morphological changes. The HE staining results showed that the cell density significantly decreased, became arranged loosely, and were stained unevenly. In addition, a number of vacuoles appeared in cerebral cortex, hippocampal CA3, and CA1 in the HI group compared with the sham group. After intervention with OMT, these symptoms were alleviated. In addition, TUNEL staining results showed that a large number of TUNEL-positive neurons in the ischemic cortex, while OMT treatment promoted the recovery of the injured neurons. These results indicated that OMT alleviated the pathological damage and death of neurons induced by HI.

We also established the OGD/R model *in vivo* to evaluate the cell viability and damage using the MTT method and mitochondrial permeability transition pore (mPTP) assays. The increase in ROS and calcium overload caused by HI could lead to the opening of the mPTP, the disorder of mitochondrial membrane potential, decoupling of respiratory chain, and blockage of ATP synthesis. These processes eventually lead to the swelling, rupture, and death of the mitochondria. Therefore, the degree of neuronal injury is related to the opening of mPTP (Halestrap, 2009). In our current research, OMT attenuated OGD/R-induced neuronal death and inhibited the increase of intracellular mPTP. These results indicate that OMT had a protective effect on the OGD/R-induced hippocampal neuronal damage. Brain infract volume is generally considered as a standard indicator for evaluating the effects of drugs on brain ischemic. RAPA intervention could reverse the remission effect of OMT on the cerebral infarction and neuronal damage induced by HIBD. These results suggest that the protective effect of OMT on HIBD in neonatal rats may be related to the mTOR pathway.

HI cause three types of cell death, namely, apoptosis, necrosis, and autophagy. Autophagy is a precise and orderly process that allows the degradation and recycling of cellular organelles and misfolded proteins under physiological conditions. Several studies have indicated that autophagy plays a significant role in HIBD (Northington et al., 2011), that is, an overactivated autophagy leads to rapid neuronal death (Levine and Yuan, 2005; Koike et al., 2008). Electron microscopy is currently considered to be a gold marker for the formation of autophagosome in tissues, and monodansylcadaverine (MDC) is an eosinophilic fluorescent stain, usually used to detect specific markers for the formation of autophagosome in cells. The results showed that after OMT treatment, the formation level of the autophagosome decreased significantly, and the regulatory effect of OMT on autophagosome formation was partially blocked by the administration of RAPA. The results further suggest that OMT played an antiexcessive autophagy role through the mTOR signaling pathway and participated in maintaining the stability of neurons and the recovery of injury. This process also suggested that regulating the level of autophagy may be one of the roles of OMT in protecting HIBD.

The PI3K/Akt/mTOR pathway is an intracellular signaling pathway involved in regulating cell survival and death. Moreover, as the only autophagic protective pathway, it plays an important role in HIBD (Yu et al., 2018). The mTOR, which belongs to the PI3K protein kinase family, is sensitive to RAPA and participates in regulating cell growth, apoptosis and autophagy (Hu et al., 2015). PI3K/Akt is one of the key upstream regulators of mTOR and plays an important role in regulating mTOR (Gunn and Hailes, 2008). Subsequently, when activated by PI3K, Akt could phosphorylate TSC2, dissociate the TSC1/TSC2 complex and activate mTOR (Pankiv et al., 2007). Finally, mTOR regulated the expression of downstream autophagy-related proteins Beclin1, LC3 and P62 and participated in the regulation of autophagy. LC3 is located on the autophagosome membrane and plays an important role in the formation of complete autophagosome. Beclin-1 plays an important role in lysosome fusion and autophagy formation in autophagy, and is another important autophagy marker. As an index of autophagic flow, some studies have shown that the level of P62 increases and the level of LC3 decreases, indicating that the autophagic flow is complete

(Bockaert and Marin, 2015). Some reports have also demonstrated that promoting mTOR activation can play a neuroprotective role in HIBD (Chen et al., 2012). To further explore the potential protective mechanism of OMT in neonatal rats and primary hippocampal neurons after HI, we verified the expression of PI3K, p-PI3K, Akt, p-Akt, p-mTOR and autophagy-related factors. Consistent with a previous study, the present results showed that the expression of PI3K, Akt, mTOR and P62 in the brain tissue was significantly decreased after HI, while protein expression of LC3 and Beclin-1increased. After the intervention with OMT, the protein expression was significantly reversed. These results suggest that OMT can alleviate the damage of HIBD neurons by up-regulating the expression of PI3K, Akt, mTOR and P62, and down-regulating the expression of LC3 and Beclin-1. At the cellular level, the expression of p-PI3K, *p*-Akt, *p*-mTOR, and P62 significantly decreased, and the expression of LC3 and Beclin-1 significantly increased compared with that of the control group. OMT could significantly reverse the activity of pathway-related factors, reduce the expression of Beclin1 and LC3, increase the expression of P62 and improve the HIBD in neonatal rats. However, in the mTOR inhibitor treatment group, RAPA partially eliminated the effects of OMT on the expression levels of p-PI3K, *p*-Akt, *p*-mTOR, LC3, Beclin-1 and P62. These findings confirm that the neuroprotective effect of OMT on HIBD may be related to the regulation of the PI3K/Akt/mTOR signaling pathway and the inhibition of excessive autophagy. However, besides the PI3K/Akt/mTOR pathway, other factors may be involved in the neuroprotective effect induced by OMT, and related factors need further study.

In conclusion, by performing *in vivo* and *in vitro* experiments, we demonstrated that posttreatment with OMT efficaciously exerted neuroprotective effect against HIBD in the neonatal rats. The underlying mechanisms may include the regulation of the PI3K/Akt/mTOR signaling pathway and inhibition of excessive autophagy of neurons. However, our study had some limitations. First, we did not explore different times to evaluate the optimal therapeutic window of OMT for the neonatal HIBD. Second, accruing studies have shown sex-specific differences in the HIBD model. Further studies are required to explore the differences in the effects of OMT on the HIBD in female and male neonatal rats.

## DATA AVAILABILITY STATEMENT

The original contributions presented in the study are included in the article/Supplementary Material, further inquiries can be directed to the corresponding authors.

## ETHICS STATEMENT

The animal study was reviewed and approved by the Experimental Animal Center of Ningxia Medical University (Animal License Number: SCXK Ningxia 2015-0001).

## AUTHOR CONTRIBUTIONS

WW: Conceptualization, Investigation, Methodology, writing—original draft. ML: Validation. XL: Formal analysis. NL: Visualization. WS: Supervision. AD: Data curation. JY: Project administration. All authors have read and agreed to the published version of the manuscript.

## FUNDING

This study was supported by the National Natural Science Foundation of China (grant 81660261) and the National Natural Science Foundation of China (grant 81960726).

## REFERENCES

Bockaert, J., and Marin, P. (2015). mTOR in brain physiology and pathologies. *Physiol. Rev.* 95 (4), 1157–1187. doi:10.1152/physrev.00038.2014

Bodine, S. C., Stitt, T. N., Gonzalez, M., Kline, W. O., Stover, G. L., Bauerlein, R., et al. (2001). Akt/mTOR pathway is a crucial regulator of skeletal muscle hypertrophy and can prevent muscle atrophy *in vivo*. *Nat. Cell Biol* 3 (11), 1014–1019. doi:10.1038/ncb1101-1014

Chen, H., Xiong, T., Qu, Y., Zhao, F., Ferriero, D., and Mu, D. (2012). mTOR activates hypoxia-inducible factor-1α and inhibits neuronal apoptosis in the developing rat brain during the early phase after hypoxia-ischemia. *Neurosci. Lett.* 507 (2), 118–123. doi:10.1016/j.neulet.2011.11.058

Cheng, O., Li, Z., Han, Y., Jiang, Q., Yan, Y., and Cheng, K. (2012). Baicalin improved the spatial learning ability of global ischemia/reperfusion rats by reducing hippocampal apoptosis. *Brain Res.* 1470, 111–118. doi:10.1016/j.brainres.2012.06.026

Cui, L., Zhang, X., Yang, R., Wang, L., Liu, L., Li, M., et al. (2011). Neuroprotection and underlying mechanisms of oxymatrine in cerebral ischemia of rats. *Neurol. Res.* 33 (3), 319–324. doi:10.1179/016164110x12759951866876

Dobbing, J., and Sands, J. (1979). Comparative aspects of the brain growth spurt. *Early Hum. Dev.* 3 (1), 79–83. doi:10.1016/0378-3782(79)90022-7

Dong, X. Q., Du, Q., Yu, W. H., Zhang, Z. Y., Zhu, Q., Che, Z. H., et al. (2013). Anti-inflammatory effects of oxymatrine through inhibition of nuclear factor-kappa B and mitogen-activated protein kinase activation in lipopolysaccharide-induced BV2 microglia cells. *Iran J. Pharm. Res.* 12 (1), 165–174.

Douglas-Escobar, M., and Weiss, M. D. (2015). Hypoxic-ischemic encephalopathy. *JAMA Pediatr.* 169, 397–403. doi:10.1001/jamapediatrics.2014.3269

Edwards, A. D., Brocklehurst, P., Gunn, A. J., Halliday, H., Juszczak, E., Levene, M., et al. (2010). Neurological outcomes at 18 months of age after moderate hypothermia for perinatal hypoxic ischaemic encephalopathy: synthesis and meta-analysis of trial data. *BMJ* 340, c363. doi:10.1136/bmj.c363

Funaya, N., and Haginaka, J. (2012). Matrine- and oxymatrine-imprinted monodisperse polymers prepared by precipitation polymerization and their applications for the selective extraction of matrine-type alkaloids from *Sophora* flavescens Aiton. *J. Chromatogr. A* 1248, 18–23. doi:10.1016/j.chroma.2012.05.081

Gunn, R. M., and Hailes, H. C. (2008). Insights into the PI3-K-PKB-mTOR signalling pathway from small molecules. *J. Chem. Biol.* 1 (1–4), 49–62. doi:10.1007/s12154-008-0008-0

Halestrap, A. P. (2009). What is the mitochondrial permeability transition pore?. *J. Mol. Cell Cardiol.* 46 (6), 821–31. doi:10.1016/j.yjmcc.2009.02.021

Hu, Z., Yang, B., Mo, X., and Xiao, H. (2015). Mechanism and regulation of autophagy and its role in neuronal diseases. *Mol. Neurobiol.* 52 (3), 1190–1209. doi:10.1007/s12035-014-8921-4

Huang, L., Chen, C., Zhang, X., Li, X., Chen, Z., Yang, C., et al. (2018). Neuroprotective effect of curcumin against cerebral ischemia-reperfusion via mediating autophagy and inflammation. *J. Mol. Neurosci.* 64 (1), 129–139. doi:10.1007/s12031-017-1006-x

Igor, K. (1987). Pathophysiological aspects of brain edema. *Acta Neuropathol.* 72 (3), 236–239. doi:10.1007/BF00691095

Jacobs, S. E., Berg, M., Hunt, R., Tarnow-Mordi, W. O., Inder, T. E., and Davis, P. G. (2013). Cooling for newborns with hypoxic ischaemic encephalopathy. *Cochrane Database Syst. Rev.* 31, CD003311. doi:10.1002/14651858.CD003311.pub3

Koh, S.-H., and Lo, E. H. (2015). The role of the PI3K pathway in the regeneration of the damaged brain by neural stem cells after cerebral infarction. *J. Clin. Neurol.* 11 (4), 297–304. doi:10.3988/jcn.2015.11.4.297

Koike, M., Shibata, M., Tadakoshi, M., Gotoh, K., Komatsu, M., Waguri, S., et al. (2008). Inhibition of autophagy prevents hippocampal pyramidal neuron death after hypoxic-ischemic injury. *Am. J. Pathol.* 172 (2), 454–469. doi:10.2353/ajpath.2008.070876

Lawn, J. E., Cousens, S., and Zupan, J. (2005). 4 million neonatal deaths: when? Where? Why?. *The Lancet* 365 (9462), 891–900. doi:10.1016/s0140-6736(05)71048-5

Levine, B., and Yuan, J. (2005). Autophagy in cell death: an innocent convict?. *J. Clin. Invest.* 115 (10), 2679–2688. doi:10.1172/jci26390

Li, D., Luo, L., Xu, M., Wu, J., Chen, L., Li, J., et al. (2017). AMPK activates FOXO3a and promotes neuronal apoptosis in the developing rat brain during the early phase after hypoxia-ischemia. *Brain Res. Bull.* 132, 1–9. doi:10.1016/j.brainresbull.2017.05.001

Li, Y., Wang, X., Cai, C, Zeng, S., Bai, J., Guo, K., et al. (2019). FGF21 promotes functional recovery after hypoxic-ischemic brain injury in neonatal rats by activating the PI3K/Akt signaling pathway via FGFR1/β-klotho. *Exp. Neurol.* 317, 34–50. doi:10.1016/j.expneurol.2019.02.013

Lin, T. N., He, Y. Y., Wu, G., Khan, M., and Hsu, C. Y. (1993). Effect of brain edema on infarct volume in a focal cerebral ischemia model in rats. *Stroke* 24 (1), 117–121. doi:10.1161/01.str.24.1.117

Liu, H., Sun, X., Gong, X., and Wang, G. (2019). Human umbilical cord mesenchymal stem cells derived exosomes exert antiapoptosis effect via activating PI3K/Akt/mTOR pathway on H9C2 cells. *J. Cell Biochem.* 120 (9), 14455–14464. doi:10.1002/jcb.28705

Martin, A., Karina, Z., Floris, G., Bell, F. V., and Peeters-Scholte, C. P. (2019). Neuroprotective strategies following perinatal hypoxia-ischemia: taking aim at NOS. *Free Radic. Biol. Med.* 142, 123–131. doi:10.1016/j.freeradbiomed.2019.02.025

McDonald, J. W., and Johnston, M. V. (1990). Physiological and pathophysiological roles of excitatory amino acids during central nervous system development. *Brain Res. Rev.* 15 (1), 41–70. doi:10.1016/0165-0173(90)90011-c

Northington, F. J., Chavez-Valdez, R., and Martin, L. J. (2011). Neuronal cell death in neonatal hypoxia-ischemia. *Ann. Neurol.* 69 (5), 743–758. doi:10.1002/ana.22419

Pankiv, S., Clausen, T. H., Lamark, T., Brech, A., Bruun, J.-A., Outzen, H., et al. (2007). p62/SQSTM1 binds directly to Atg8/LC3 to facilitate degradation of ubiquitinated protein aggregates by autophagy. *J. Biol. Chem.* 282, 24131–24145. doi:10.1074/jbc.m702824200

Panthati, M. K., Rao, K. N. V., Sandhya, S., and David, B. (2012). A review on phytochemical, ethnomedical and pharmacological studies on genus *Sophora*. *Fabaceae. Panthati Murali Krishna* 22 (5), 1145–1154. doi:10.1590/S0102-695X2012005000043

Vannucci, R. C., and Vannucci, S. J. (2005). Perinatal hypoxic-ischemic brain damage: evolution of an animal model. *Dev. Neurosci.* 27 (2-4), 81–86. doi:10.1159/000085978

Wang, J., Zhang, D., Fu, X., Lu, Z., Guo, Y., Liu, X., et al. (2018). Carbon monoxide-releasing molecule-3 protects against ischemic stroke by suppressing neuroinflammation and alleviating blood-brain barrier disruption. *J. Neuroinflam* 15 (1), 188. doi:10.1186/s12974-018-1226-1

Wang, S.-B., and Jia, J.-P. (2014). Oxymatrine attenuates diabetes-associated cognitive deficits in rats. *Acta Pharmacol. Sin* 35 (3), 331–338. doi:10.1038/aps.2013.158

Wei, W., Lan, X. B., Liu, N., Yang, J. M., Du, J., Ma, L., et al. (2019). Echinacoside alleviates hypoxic-ischemic brain injury in neonatal rat by enhancing antioxidant capacity and inhibiting apoptosis. *Neurochem. Res.* New York. 44 (7), 1582–1592. doi:10.1007/s11064-019-02782-9

Wu, W., Wei, W., Lu, M., Zhu, X., Liu, N., Niu, Y., et al. (2017). Neuroprotective effect of chitosan oligosaccharide on hypoxic-ischemic brain damage in neonatal rats. *Neurochem. Res.* 42 (11), 3186–3198. doi:10.1007/s11064-017-2356-z

Wu, Y. W., and Gonzalez, F. F. (2015). Erythropoietin: a novel therapy for hypoxic-ischaemic encephalopathy?. *Dev. Med. Child. Neurol.* 57 (Suppl. 3), 34–39. doi:10.1111/dmcn.12730

Yu, Y., Wu, X., Pu, J., Luo, P., Ma, W., Wang, J., et al. (2018). Lycium barbarum polysaccharide protects against oxygen glucose deprivation/reoxygenation-induced apoptosis and autophagic cell death via the PI3K/Akt/mTOR signaling pathway in primary cultured hippocampal neurons. *Biochem. Biophys. Res. Commun.* 495 (1), 1187–1194. doi:10.1016/j.bbrc.2017.11.165

Yıldız, E. P., Ekici, B., Tatlı, B., et al. (2017). Neonatal hypoxic ischemic encephalopathy: an update on disease pathogenesis and treatment. *Expert Rev. Neurother.* 17 (5), 449–459. doi:10.1080/14737175.2017.1259567

Zhao, P., Zhou, R., Li, H. N., Yao, W. X., Qiao, H. Q., Wang, S. J., et al. (2015). Oxymatrine attenuated hypoxic-ischemic brain damage in neonatal rats via improving antioxidant enzyme activities and inhibiting cell death. *Neurochem. Int.* 89, 7–27. doi:10.1016/j.neuint.2015.06.008

Zhao, P., Chang, R.-Y., Liu, N., Wang, J., Zhou, R., Qi, X., et al. (2018). Neuroprotective effect of oxysophocarpine by modulation of MAPK pathway in rat hippocampal neurons subject to oxygen-glucose deprivation and reperfusion. *Cell Mol Neurobiol.* 38 (2), 529–540. doi:10.1007/s10571-017-0501-5

Zhu, W., Gao, Y., Wan, J., Lan, X., Han, X., Zhu, S., et al. (2018). Changes in motor function, cognition, and emotion-related behavior after right hemispheric intracerebral hemorrhage in various brain regions of mouse. *Brain Behav. Immun.* 69, 568–581. doi:10.1016/j.bbi.2018.02.004

**Conflict of Interest:** The authors declare that the research was conducted in the absence of any commercial or financial relationships that could be construed as a potential conflict of interest.

frontiers in Cellular Neuroscience

ORIGINAL RESEARCH
published: 31 May 2021
doi: 10.3389/fncel.2021.644047

# Deciphering *in silico* the Role of Mutated $Na_V1.1$ Sodium Channels in Enhancing Trigeminal Nociception in Familial Hemiplegic Migraine Type 3

*Alina Suleimanova[1], Max Talanov[1], Arn M. J. M. van den Maagdenberg[2,3] and Rashid Giniatullin[4,5]**

[1] *Institute of Information Technology and Intelligent Systems, Kazan Federal University, Kazan, Russia,* [2] *Department of Neurology, Leiden University Medical Center, Leiden, Netherlands,* [3] *Department of Human Genetics, Leiden University Medical Center, Leiden, Netherlands,* [4] *Laboratory of Neurobiology, Kazan Federal University, Kazan, Russia,* [5] *A.I. Virtanen Institute for Molecular Sciences, University of Eastern Finland, Kuopio, Finland*

Familial hemiplegic migraine type 3 (FHM3) is caused by gain-of-function mutations in the *SCN1A* gene that encodes the α1 subunit of voltage-gated $Na_V1.1$ sodium channels. The high level of expression of $Na_V1.1$ channels in peripheral trigeminal neurons may lead to abnormal nociceptive signaling thus contributing to migraine pain. $Na_V1.1$ dysfunction is relevant also for other neurological disorders, foremost epilepsy and stroke that are comorbid with migraine. Here we used computer modeling to test the functional role of FHM3-mutated $Na_V1.1$ channels in mechanisms of trigeminal pain. The activation of Aδ-fibers was studied for two algogens, ATP and 5-HT, operating through P2X3 and 5-HT3 receptors, respectively, at trigeminal nerve terminals. In WT Aδ-fibers of meningeal afferents, $Na_V1.1$ channels efficiently participate in spike generation induced by ATP and 5-HT supported by $Na_V1.6$ channels. Of the various FHM3 mutations tested, the L263V missense mutation, with a longer activation state and lower activation voltage, resulted in the most pronounced spiking activity. In contrast, mutations that result in a loss of $Na_V1.1$ function largely reduced firing of trigeminal nerve fibers. The combined activation of P2X3 and 5-HT3 receptors and branching of nerve fibers resulted in very prolonged and high-frequency spiking activity in the mutants compared to WT. We identified, *in silico,* key determinants of long-lasting nociceptive activity in FHM3-mutated Aδ-fibers that naturally express P2X3 and 5-HT3 receptors and suggest mutant-specific correction options. Modeled trigeminal nerve firing was significantly higher for FHM3 mutations, compared to WT, suggesting that pronounced nociceptive signaling may contribute to migraine pain.

**Keywords: migraine, $Na_V$, meninges, trigeminal nerve, ATP, 5-HT, FHM3, model**

OPEN ACCESS

***Edited by:***
*Daniela Pietrobon, University of Padua, Italy*

***Reviewed by:***
*Luigi Catacuzzeno, University of Perugia, Italy*
*Keith Elmslie, A.T. Still University, United States*

****Correspondence:***
*Rashid Giniatullin*
*rashid.giniatullin@uef.fi*

***Specialty section:***
*This article was submitted to Cellular Neurophysiology, a section of the journal Frontiers in Cellular Neuroscience*

***Received:*** *21 December 2020*
***Accepted:*** *06 May 2021*
***Published:*** *31 May 2021*

***Citation:***
*Suleimanova A, Talanov M, van den Maagdenberg AMJM and Giniatullin R (2021) Deciphering in silico the Role of Mutated $Na_V1.1$ Sodium Channels in Enhancing Trigeminal Nociception in Familial Hemiplegic Migraine Type 3. Front. Cell. Neurosci. 15:644047. doi: 10.3389/fncel.2021.644047*

## INTRODUCTION

The generation of disabling migraine pain involves the activation of the meningeal trigeminovascular system (Moskowitz, 2008; Messlinger, 2009), but the underlying pro-nociceptive mechanisms remain largely unknown. Current data suggest participation of mainly Aδ-fibers of the trigeminal nerve densely innervating the meninges (Melo-Carrillo et al., 2017; Haanes and Edvinsson, 2019).

To unravel molecular mechanisms of migraine pathophysiology, the study of monogenic subtypes of migraine, foremost familial hemiplegic migraine, has been instrumental (Ferrari et al., 2015). Familiar hemiplegic migraine type 3 (FHM3), which is caused by specific missense mutations in the *SCN1A* gene encoding the α1 subunit of voltage-gated $Na_V1.1$ sodium channels (Dichgans et al., 2005; Tolner et al., 2015), allows the specific interrogation of the role mutant $Na_V1.1$ channels in migraine pathophysiology. The observation that incubation at lower temperature and expression in neurons rescued folding/trafficking issues now firmly established that FHM3 is caused by a gain of $Na_V1.1$ function (Dhifallah et al., 2018), whereas earlier studies suggested foremost loss-of-function effects of FHM3 mutations when overexpressed in heterologous expression systems (Dichgans et al., 2005; Kahlig et al., 2008). As $Na_V1.1$ channels are strongly expressed in peripheral Aδ-fibers of the trigeminal nerve (Ho and O'Leary, 2011; Osteen et al., 2016), their modified activity may underlie the activation of peripheral trigeminal neurons leading to migraine pain. It can be expected that a gain-of-function enhances excitability of peripheral nerve fibers expressing modified $Na_V1.1$ channels, providing a high pro-nociceptive activity delivered to second order neurons.

Investigating $Na_V1.1$ channel dysfunction, which are expressed also in central neurons (Ogiwara et al., 2007; Favero et al., 2018; Sakkaki et al., 2020), in relation to changes in neuronal excitability, is also of relevance to various neurological disorders other than migraine, foremost childhood epilepsy (Menezes et al., 2020), autism spectrum disorder (Scheffer and Nabbout, 2019), Alzheimer's disease (Sakkaki et al., 2020), and perhaps less known, transient cerebral ischemia (Zhan et al., 2007). In fact, changes in neuronal hyperexcitability may therefore, at least to certain extent, underlie the comorbidity of several of the disorders with migraine, for instance when they lead to spreading depolarizations, as observed for migraine and stroke (Dreier and Reiffurth, 2015). Unlike for the other disorders, the evidence for a specific role of $Na_V1.1$ channels in cerebral ischemia is limited although voltage-gated cation channels, including sodium channels have been targets for the treatment of stroke (Gribkoff and Winquist, 2005).

The predominant hypothesis for triggering peripheral mechanisms of pain is that trigeminal nerve terminals are activated by local depolarizing stimuli (Julius and Basbaum, 2001; Basbaum, 2002; Giniatullin, 2020). Purinergic and serotonergic mechanisms are among the most powerful triggers of peripheral nociception in meningeal afferents (Yegutkin et al., 2016; Kilinc et al., 2017; Koroleva et al., 2019).

Recently, we presented a mathematical model of the nociceptive neuro-immune synapse in meninges that, by activation with ATP and 5-HT, generates neuronal firing (Suleimanova et al., 2020). Meninges, which are densely innervated by trigeminal nerve fibers, are currently considered a main source of migraine headache (Moskowitz, 2008; Messlinger, 2009; Olesen et al., 2009). The two algesic substances, ATP and 5-HT selected to be modeled in this study produce a powerful and long-lasting activation of meningeal afferents (Yegutkin et al., 2016; Kilinc et al., 2017; Koroleva et al., 2019). The data are consistent with the purinergic hypothesis of migraine suggested earlier by Burnstock (1981). There is strong evidence that serotonin (5-HT) is involved in migraine already because "triptans," serotonin (5-HT1B/1D) agonists, are effective in treating migraine patients (Goadsby, 2007). However, the sources of the two neurotransmitters, the time spent in the extracellular space, the receptor kinetics, and most notably, the speed of desensitization of the transmitters are different, as we presented in our previous model (Suleimanova et al., 2020). Notably, the respective P2X3 and 5-HT3 receptors activated by ATP and 5-HT, respectively, are expressed in Aδ-fibers (Ford, 2012; Kilinc et al., 2017; Sato et al., 2018), thus in the same neurons that express $Na_V1.1$ sodium channels. Combining, in the mathematical model, effects of these triggers with dysfunction of $Na_V1.1$ channels due to mutations identified in patients may serve as a useful platform to explore mechanisms of activation of peripheral nociception relevant to migraine headache.

Therefore, we here assessed, by using *in silico* modeling, how gain- and loss-of-function mutations in the α1 subunit of $Na_V1.1$ channels, as they occur in patients with FHM3 and childhood epilepsy, respectively, might affect peripheral trigeminal nociception in meningeal afferents. To this end, the WT vs. various mutants $Na_V1.1$ channels were *in silico* "co-expressed" along with other types of sodium ($Na_V1.6$, $Na_V1.7$, $Na_V1.8$) and several potassium channel types ($K_V1$, $K_V3$, $K_V4$, and calcium-activated potassium channel $K_{Ca}$) according to published profile of these channels in Aδ-fibers (Tigerholm et al., 2014; Mandge and Manchanda, 2018; Zemel et al., 2018; Zheng et al., 2019). Our data show a large amplification of nociception in meningeal afferents exclusively with gain-of-function mutations providing a scientific framework that a peripheral mechanism of generating migraine pain in patients with FHM3.

# MATERIALS AND METHODS

## The Mathematical Model for Testing of FHM3 Mutations

To model the function of the trigeminal nerve in meninges we used the NEURON environment version 7.8 (Hines and Carnevale, 2003). Our model describes the activity of Aδ-fibers induced by single, or repetitive ATP and 5-HT release events from abundant meningeal mast cells (Theoharides et al., 1995; Levy, 2009; Kilinc et al., 2017). Thus, the Aδ-fiber coupled to a mast cell represent a model of the nociceptive "neuro-immune synapse" (Theoharides et al., 1995; Koroleva et al., 2019; Suleimanova et al., 2020; **Figure 1A**). Within such synapse, locally released ATP or 5-HT activates, at nerve terminals, P2X3 or 5-HT3 receptors, respectively. Both ATP and 5-HT are potent triggers of nociceptive firing in meningeal afferents (Yegutkin et al., 2016; Kilinc et al., 2017; Koroleva et al., 2019). Although P2X2 receptors are co-expressed with P2X3 subunits in rodents (Simonetti et al., 2006), the P2X3 subtype is the predominant ATP receptor subtype in human sensory neurons (Serrano et al., 2012). Therefore, in our model, we used P2X3 receptors as the main target for fast action of ATP on trigeminal meningeal afferents.

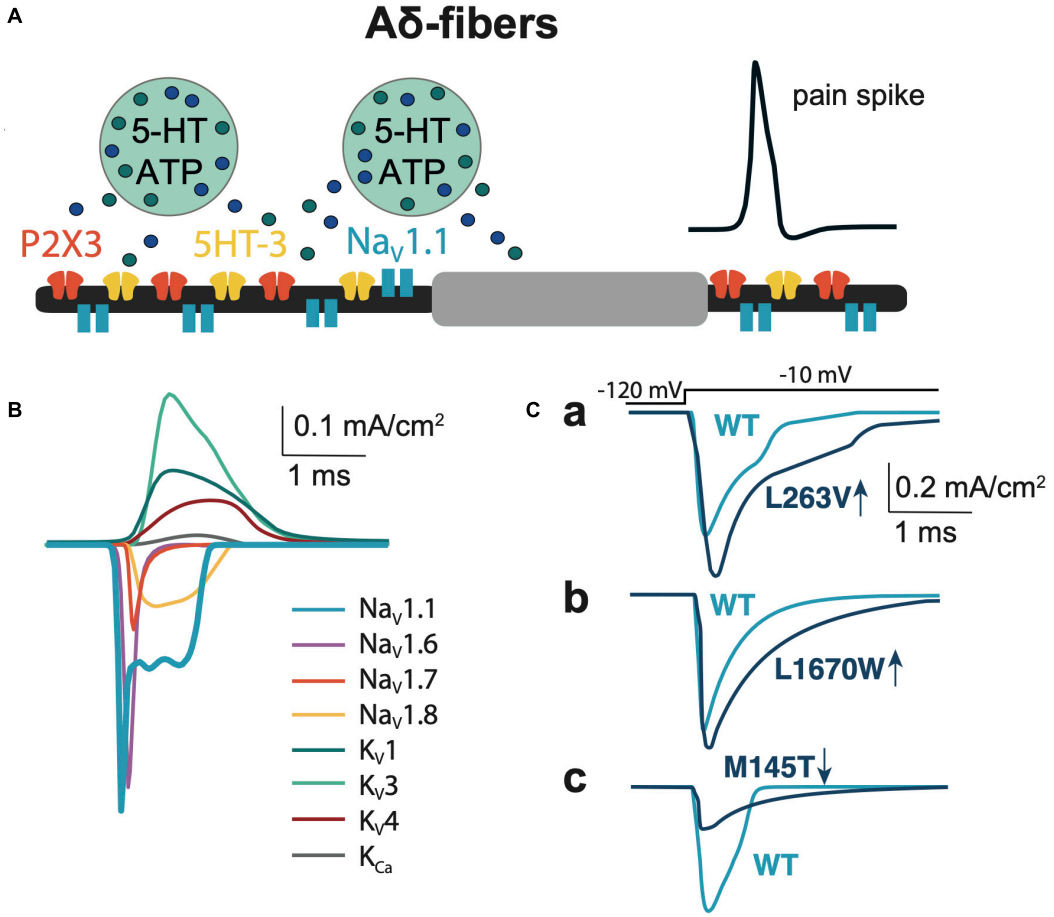


**FIGURE 1 |** Model of Aδ-fiber. **(A)** Schematic presentation of the Aδ-fiber with the diameter 5 μm and node of Ranvier 2 × 2 μm. **(B)** The membrane Na$_V$, K$_V$, and K$_{Ca}$ currents relevant to the model of Aδ-fiber. **(C)** Comparison of Na$_V$1.1 currents, that evoked by a voltage step to -10 mV of WT with the L263V **(Ca)**, L1670W **(Cb)**, and M145T **(Cc)** mutations.

We explored the action of different concentrations of two algogens but for most model trials we used 1 μM ATP and 2 μM 5-HT concentrations to activate receptors, since these values are close to $EC_{50}$ of the respective receptors (Sokolova et al., 2006; Corradi et al., 2009). The kinetics of P2X3 receptors was based on the previously published model of this receptor (Sokolova et al., 2006), whereas the kinetic of 5-HT3 receptors was taken from the study of Corradi et al. (2009). The lifetime of extracellular ATP is determined by fast hydrolysis via multiple ecto-enzymes (Yegutkin, 2008), whereas the profile of 5-HT is controlled by a relatively slow uptake via SERT transporters (Wood et al., 2014). Therefore, we included in our model the partial hydrolysis for ATP and uptake for 5-HT making the model consistent with experimental data on the action of ATP and 5-HT (Suleimanova et al., 2020). The 3D diffusion model suggested by Saftenku (2005) was used to reproduce the time course of transmitters in the nociceptive synapse. We also conducted in the current model experiments in which we varied ATP and 5-HT concentrations to explore the dependence of spike firing on the profile of the neurotransmitters in the meningeal neuro-immune synapse.

The diameter of the Aδ-fiber is 5 μm (West et al., 2015), each segment of the fiber consists of a paranode and a node of Ranvier (McIntyre et al., 2002) that is 2 × 2 μm (width and length; **Figure 1A**). Aδ-fibers highly expressed tetrodotoxin-sensitive (TTX-sensitive) Na$_V$1 channel type (Na$_V$1.1, Na$_V$1.6, Na$_V$1.7), while Na$_V$1.8 was at low level compared to C-fibers (Pinto et al., 2008; Zhang et al., 2013). Most of the input parameters on channel kinetics and voltage dependence of Na$_V$1.6, K$_V$1, K$_V$3, and K$_V$4 ion channels were obtained from somatic recordings (Zheng et al., 2019), whereas the data for the density of ion channels were obtained from axonal measurements (Waxman and Ritchie, 1993; McIntyre et al., 2002). Likewise, we used data from somatic recordings of the contribution of Na$_V$1 channels to $I_{Na}$ current (Zhang et al., 2013) and Na$_V$ channels mRNA levels (Ho and O'Leary, 2011). The WT Na$_V$1.1 channel and FHM3-associated mutations in this channel were modeled based on functional properties obtained in neurons or tsA201 cells (for details see **Table 1**).

To match the natural profile of sodium channels in the Aδ-fiber, we revised our previously used mathematical model (Suleimanova et al., 2020) by adding Na$_V$1.1 and Na$_V$1.6, since

**TABLE 1 |** Biophysical parameters for activation, fast inactivation and slow inactivation of WTs and mutants of $Na_V1.1$ channel.

| Channel | Activation (mV) | | Fast inactivation (mV) | | Slow inactivation (mV) | | $tau_{slow}$ (ms) at −10 mV | | References |
|---|---|---|---|---|---|---|---|---|---|
| | $V_{1/2}$ | k | $V_{1/2}$ | k | $V_{1/2}$ | k | experiment | model | |
| **Familial hemiplegic migraine type 3 (FHM3)** | | | | | | | | | |
| L263V | −24.6 | 7.1 | −54.4 | 6.7 | −54.1 | 5.0 | 3,507 | 3,500 | Kahlig et al., 2008 |
| gain-of-function/WT | −21.5 | 7.2 | −62.2 | 6.4 | −66.8 | 6.3 | 2,100 | 2,100 | |
| Q1478K combined | −24.8 | 9.1 | −60.1 | 7.4 | −77.2 | 7.7 | 938 (−5 mV) | 940 (−5 mV) | Cestele et al., 2008 |
| gain- and loss-of function/WT | −24.5 | 7.9 | −65.1 | 6.0 | −75.8 | 6.2 | 2.090 (−5 mV) | 2,100 (−5 mV) | |
| L1649Q | −22.9 | 7.4 | −34.5 | 7.1 | −57.7 | 8.9 | 1,885 (0 mV) | 1,885 (0 mV) | Cestele et al., 2013 |
| gain-of-function/WT | −21.0 | 6.6 | −54.2 | 5.5 | −59.7 | 9.7 | 2,616 (0 mV) | 2,600 (0 mV) | |
| L1670W | −16.8 | 6.1 | −47.3 | 6.1 | −34.8 | 10.0 | 2,070 | 2,070 | Dhifallah et al., 2018 |
| gain-of-function/WT | −21.6 | 6.6 | −55.6 | 4.9 | −53.5 | 7.6 | 1,310 | 1,300 | |
| **Familial simple febrile seizures** | | | | | | | | | |
| M145T | −11.7 | 7.1 | −65.5 | 9.1 | – | – | – | | Mantegazza et al., 2005 |
| loss-of-function/WT | −21.7 | 6.15 | −64.9 | 8.0 | | | | | |
| **Generalized epilepsy with febrile seizures plus (GEFS +)** | | | | | | | | | |
| R1648H | −19.9 | 8.5 | −61.3 | 7.8 | −68.6 | 6.1 | 3,112 | 3,112 | Kahlig et al., 2006 |
| gain-of-function/WT | −19.4 | 7.9 | −62.7 | 6.9 | −66.7 | 7.8 | 3,029 | 3,000 | |

*$V_{1/2}$ is the voltage of half-maximal activation or inactivation; k is a slope factor; $tau_{slow}$ is kinetics of the development of slow inactivation. Voltage indicated in brackets shows values at which the recordings were performed in the quoted papers and in model studies.*

these fibers express both type of these channels in nodes of Ranvier (Duflocq et al., 2008; Leterrier et al., 2011). We also added $Na_V1.7$ and $Na_V1.8$ channels to our model, as they also support the generation and propagation of nociceptive signals from the periphery (Duflocq et al., 2008; Black et al., 2012; **Figure 1B** and **Supplementary Table 1**). The maximum conductance densities of the TTX-sensitive channels are based on single-channel conductance and channel density values in the range of 1,000 to 2,000 channels/$\mu m^2$ (McIntyre et al., 2002). The density of TTX-resistant Nav1.8 channel is significantly lower since TTX completely blocked spiking activity in Aδ-fiber (Pinto et al., 2008), whereas specific blockers of TTX-resistant channels did not significantly reduce spiking (Tsuchimochi et al., 2011). Of note, we tuned the values to provide a closer similarity to action potential and firing patterns observed in the experimental studies (Cestele et al., 2008, 2013) taking into account the contributions of $Na_V1.1$, $Na_V1.6$, and $Na_V1.7$ to TTX-sensitive current (Zhang et al., 2013) and therespective $Na_V$ channels mRNA level (Ho and O'Leary, 2011). When modeling, we also took into consideration a fiber-specific difference in expression of potassium channels (Zemel et al., 2018; Chien et al., 2007). Thus, our Aδ-fiber model includes voltage-gated potassium channels $K_V1$, Kv3, and Kv4 mediating A-type currents, which are found in axons and nerve endings (Zemel et al., 2018). We recently showed that 4-Aminopyridine, a blocker of A-type current (determined by voltage-gated potassium Kv1 and Kv3 channels) dramatically enhanced the firing of trigeminal afferents in rat meninges promoting appearance of fast large spikes (Andreou et al., 2020), typical for the phenotype of trigeminal Aδ-fibers (MacIver and Tanelian, 1993). We also added to the model calcium-activated potassium large-conductance $K_{Ca}$ channels ($BK_{Ca}$) (Mandge and Manchanda, 2018). The full set of maximum conductance densities of the channels and the kinetics underlying the single action potential is shown in **Supplementary Table 1** and **Figure 1B**, where the current time course for each mutant (L263V, L1670W, and M145T) was compared with the respective WT to fit with experimental results from Mantegazza et al. (2005); Kahlig et al. (2006), and Dhifallah et al. (2018).

Next, we modeled various *SCN1A* mutations by using steady-state voltage dependence and kinetics of channel activation and inactivation as presented in Spampanato et al. (2004). First, we fitted the kinetics of the channels using the three-parameter Gaussian exponential function: $\tau = a \times \exp(((V-V_0)/b)^2)$, where V is the membrane voltage, $V_0$ is the mean voltage around which the Gaussian is positioned, a is the height, and b is the standard deviation. Second, the steady-state voltage dependence of activation was calculated by a Boltzmann function in the form: $m_\infty = 1/(1 + \exp(-(V-V_{1/2})/k))$ and $h_\infty/s_\infty/r_\infty = 1/(1 + \exp((V-V_{1/2})/k))$ for fast ($h_\infty$), slow ($s_\infty$) inactivation and recovery ($r_\infty$), where $V_{1/2}$ is the voltage of half-maximal activation or inactivation, and k is a slope factor. The constants for these calculations are presented in **Table 1**. Third, we used the Hodgkin-Huxley formalism where activation (m) and inactivation (h) states were in the range between 0 and 1 dependent on voltage and time. We used the following equation to define the channel activation state: $dm/dt = (m_\infty - m)/\tau_m$, where $m_\infty$ is referred to as steady-state voltage dependence and $\tau_m$ is the kinetics. In a similar way, we determined the fast and slow inactivation states and recovery. We assume that the slow inactivation and recovery states are independent from other channel gating states since development of slow inactivation and recovery was recorded separately in experimental papers, we added *s*- and *r*-variable to the model. Thus, the sodium current is described by following equation:

$$I_{Na} = m^3 hsrg_{Na} * (V - E_{Na})$$

where $g_{Na}$ is the maximum conductance; $E_{Na}$ is the equilibrium potential for sodium; *m* and *h* are the voltage-dependent activation and inactivation gating states; *s* and *r* are the additional slow inactivation development and recovery voltage-dependent variables.

We modified the activation voltage and the activation speed of WT $Na_V1.1$ channels (Zheng et al., 2019) to recapitulate better the characteristics of a FHM3 mutation. To this end, we decreased the activation voltage of FHM3-associated $Na_V1.1$ channels ($V_{1/2}$ of WT = −21 mV, $V_{1/2}$ of FHM3 = −25 mV; **Figures 2Aa,Ab** and **Table 1**) since L263V-mutated $Na_V1.1$ ($Na_V1.1$-L263V) channels are activated at a lower voltage than WT $Na_V1.1$ channels, although the difference was not significant (Kahlig et al., 2008). The FHM3 L263V mutation shows slower kinetics than WT for both the activation and the inactivation state and an increased "window current" (**Figure 2Aa** and **Supplementary Figure 2A**) due to the shift of the voltage dependence of activation curve to lower voltages and the inactivation curve to higher voltages compared to WT (Kahlig et al., 2008), thus the current peak of $Na_V1.1$-L263V is wide (**Figure 1Ca** and **Supplementary Figure 3**). Second, we modeled the FHM3 L1670W mutation (**Figure 1Cb**), which also exhibits a gain-of-function effect (Dhifallah et al., 2018). This mutation increases the persistent sodium current and shows a positive shift of the inactivation curve and faster recovery from fast inactivation in comparison to WT (**Figures 2Ba,Bb** and **Supplementary Figures 1B, 2B**). Third, the FHM3 L1649Q mutation also enhances persistent sodium current, recovery from slow inactivation, and slightly increased the

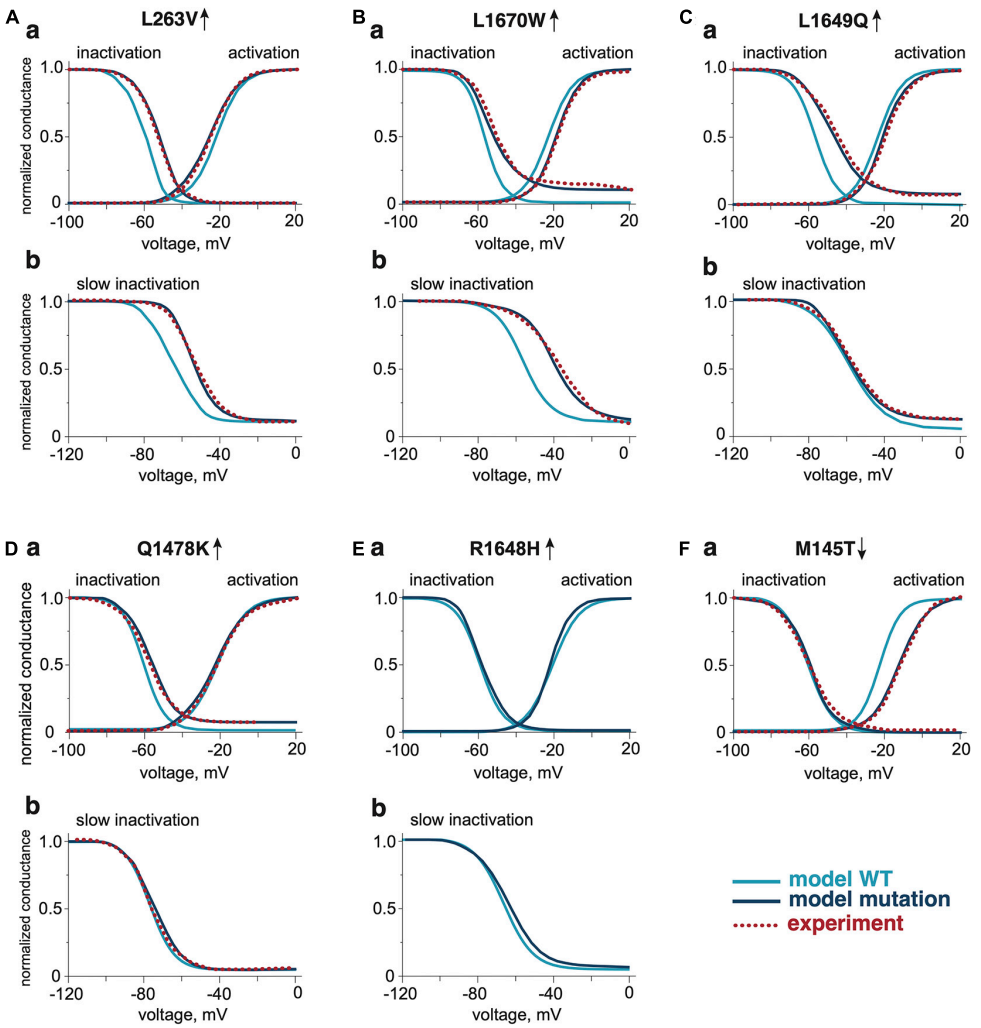


**FIGURE 2 |** The activation and inactivation properties of WT and $Na_V1.1$ mutants. The comparison of voltage dependence of activation and fast inactivation of $Na_V1.1$ WT and mutants L263V **(Aa)**, L1670W **(Ba)**, L1649Q **(Ca)**, Q1478K **(Da)**, R1648H **(Ea)**, and M145T **(Fa)**. The comparison of voltage dependence of slow inactivation development of $Na_V1.1$ WT and gain-of-function mutants L263V **(Ab)**, L1670W **(Bb)**, L1649Q **(Cb)**, Q1478K **(Db)**, and R1648H **(Eb)**. The dotted line shows experimental results from Kahlig et al. (2008) for the L263V mutation, Dhifallah et al. (2018) for the L1670W mutation, Cestele et al. (2008) for the L1649Q mutation, Cestele et al. (2013) for the Q1478K mutation, and Mantegazza et al. (2005) for the M145T mutation. Mutations were compared with the respective WT data from the publication that presented experimental data for the mutations.

time constant for fast inactivation (**Figures 2Ca,Cb** and **Supplementary Figures 1C, 2C**), which can be the reason for the prolonged spiking activity (Cestele et al., 2013). Fourth, the FHM3 Q1478K mutation shows faster recovery, a positive shift of the voltage dependence of inactivation (**Figures 2Da,Db** and **Supplementary Figures 1D, 2D**), and a higher amplitude persistent current (Cestele et al., 2008). Next, we modeled to the model the R1648H mutation (**Figures 2Ea,Eb** and **Supplementary Figures 1E, 2E**) that is associated with childhood epilepsy but exhibits a persistent sodium current as well (Kahlig et al., 2006). Finally, for comparison, we modeled the loss-of-function mutation M145T (**Figures 1Cc, 2Fa**). The comparison of activation and inactivation properties of the WT and mutant $Na_V1.1$ channels are shown in **Figure 2** and **Supplementary Figures 1**, **2**. Using experimental data from Mantegazza et al. (2005); Kahlig et al. (2006, 2008); Cestele et al. (2008, 2013), and Dhifallah et al. (2018) for the mutant and respective WT channel characteristics, we validated our model data with experimental results describing the voltage-dependence of channel activation and inactivation by voltage steps (with increment 10 mV) from −100 to 20 mV. The time constant of development of fast inactivation are shown in **Supplementary Figure 2**. The distribution of tau in our model was compared with time constant from experimental results at the different potentials in the range (−65 to 30 mV). We used median values of normalized conductance at voltage from −100 to 20 mV with a 10-mV step increment. Based on these values, we plotted steady-state curves, using interpolation, and compared results with simulated voltage-dependent steady-states. This comparison indicating a high similarity (*p*-values with Kolmogorov–Smirnov test (K-S test) higher than 0.1 (Boyerinas, 2016) between experimental results and simulation data (**Figure 2**, notice dotted lines for experimental results).

Finally, we took into consideration that the meningeal nerve has a branched structure (Schueler et al., 2014; Barkai et al., 2020; Suleimanova et al., 2020). Therefore, we modified our model to a tree structure with two 1.1 cm long axon branches. In this version of the model, we added two varying concentrations of ATP or 5-HT to activate each of the axon branches. As the junction of branches can block spikes from a branch in the refractory state, we calculated that an interval of 15 ms between applications was sufficient for the propagation of spiking activity.

## Statistical Analysis

We used Kolmogorov–Smirnov test (K-S test) (Boyerinas, 2016) to compare the distribution of inter-spike intervals in experiments with simulation. The ks_2samp function from SciPy library that is implemented in the K-S test statistics was used to compare two samples. With this approach, the *p*-value higher than 0.05, allowed to accept the null hypothesis indicating that the distribution of data in two samples are similar. Experimental data for validation of the model were taken from our publication describing the action of ATP and 5-HT on mouse trigeminal nerves (Koroleva et al., 2019).

# RESULTS

## Role of $Na_V1.1$ and $Na_V1.6$ Channels in ATP-Induced Activation of WT and FHM3 Aδ-Fibers

Aδ-fibers are thought to play an important role in the generation of migraine pain (Melo-Carrillo et al., 2017; Haanes and Edvinsson, 2019). As $Na_V1.1$ and $Na_V1.6$ channels are the major $Na_V$ channel types in Aδ-fibers, we first explored their role in ATP-induced activation of WT and FHM3 nerve fibers. We first used a simplified model of the single trigeminal nerve fiber with one release site for ATP. To address the pure $Na_V1$ phenotype we started with *in silico* "knocking down" the $Na_V1.6$ channel subtype in WT, whereas the conductance of $Na_V1.1$ was set to 0.35 S/cm$^2$. In this case, ATP only induced local receptor potential (**Figures 3Aa,Ba** black lines). Adding $Na_V1.6$, with a conductance of 0.35 S/cm$^2$ was sufficient to generate propagating spikes (**Figures 3Ab,Bb** black lines). Raising the activity of $Na_V1.1$ (conductance 0.5 S/cm$^2$) enhanced the firing with repetitive spikes (**Figures 3Ac,Bc** black lines). In contrast to WT, in the FHM3 model with gain-of-function mutations L263V and L1670W, even $Na_V1.1$ alone was sufficiently effective to generate propagating spikes (**Figures 3Aa,Ba** red lines). Even higher activity was obtained when $Na_V1.6$ (**Figures 3Ab,Bb** red lines) was added or when the conductance of the $Na_V1.1$ channel was increased to 0.5 S/cm$^2$ (**Figures 3Ac,Bc** red lines).

Thus, even in this simple linear model, the activity of FHM3 gain-of-function mutations produced an increased number of nociceptive spikes, suggesting that excitability of the terminals of meningeal afferents was increased. Notably, the L263V mutation caused more spikes than the L1670W mutation when compared with the respective WTs.

## Specific Role of $Na_V1.1$ Channels in the Spiking Activity of WT and FHM3 Aδ-Fibers

As it is known that meningeal afferents are branched (Schueler et al., 2014; Suleimanova et al., 2020), we next modeled the trigeminal nerves with two branches and two ATP release events activating these separate nerve branches (**Figure 4A**). Such model allowed us to explore the role of simultaneous and shifted in time activation of distinct branches and whether this activity may propagate to higher pain centers. We found that in case of the L263V mutation, two simultaneous ATP release events did not change the outcome number of spikes coming to TG (**Figure 4B** red line). However, the final number of spikes was increased by adding a second ATP release with the time interval being 5 ms (**Figure 4C**). With an interval of 10 ms, the number of repetitive spikes further increased from four in WT to eight spikes in L263V (**Figure 4D**). Similar

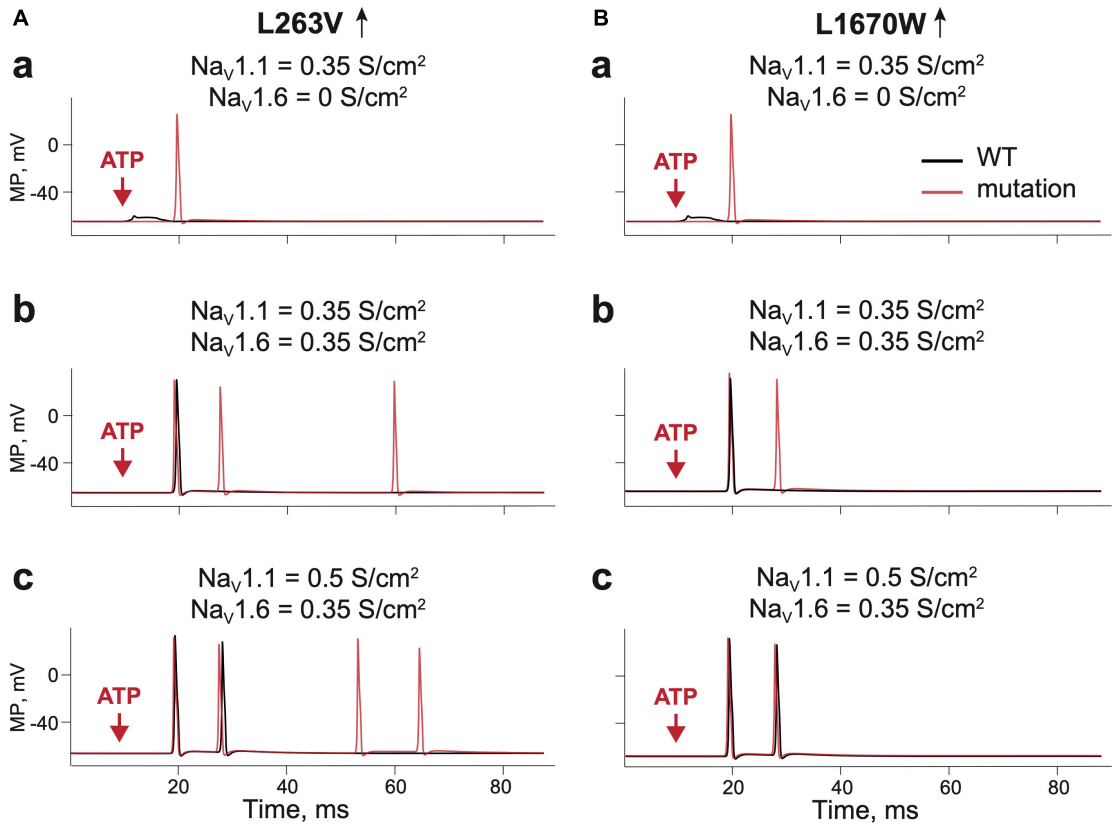


**FIGURE 3 |** Testing the role of $Na_V$ 1.1 and $Na_V1.6$ in firing of Aδ-fiber with one branch and a single ATP release event. **(Aa)** The receptor potential in a single WT (Kahlig et al., 2008) fiber expressing $Na_V1.1$ (black line) and firing in the fiber without $Na_V1.6$. with L263V mutation (red line) of $Na_V1.1$ with conductance 0.35 S/cm$^2$. Of note, there is a membrane potential in the nerve compartment, where ATP is acting, whereas in other panels we present the appearance of the signal to the trigeminal ganglion. **(Ab)** WT (Kahlig et al., 2008) fiber (black line) and the L263V mutation (red line) with $Na_V1.1$ and $Na_V1.6$ (both with conductance 0.35 S/cm$^2$) and; **(Ac)** WT (Kahlig et al., 2008) fiber (black line) and the L263V mutation (red line) with $Na_V1.1$ conductance 0.5 S/cm$^2$ and $Na_V1.6$ conductance 0.35 S/cm$^2$. **(Ba)** The receptor potential in a single WT (Dhifallah et al., 2018) fiber (black line) and L1670W mutation (red line) of $Na_V1.1$ conductance 0.35 S/cm$^2$ and without $Na_V1.6$. **(Bb)** WT (Dhifallah et al., 2018) fiber (black line) and the L1670W mutation (red line) with $Na_V1.1$ conductance 0.35 S/cm$^2$ and $Na_V1.6$ conductance 0.35 S/cm$^2$. **(Bc)** WT (Dhifallah et al., 2018) fiber (black line) and the L1670W mutation (red line) with $Na_V1.1$ conductance 0.5 S/cm$^2$ and $Na_V1.6$ conductance 0.35 S/cm$^2$. ATP signaling is limited by partial hydrolysis.

increase was observed with interval 15 ms (**Figure 4E**). Then, for modeling of other mutant channels, we used a 15-ms interval between ATP release events since a further increase of the interval in the range of 15–100 ms did not change the number of produced spikes. We compared the firing for FHM3 gain-of-function mutations L263V and L1670W, and loss-of-function mutation M145T with the respective WTs. The latter, even modeled from distinct experimental studies (Mantegazza et al., 2005; Kahlig et al., 2008; Dhifallah et al., 2018) generated similar (five for L263V and L1670W and four for M145T, see **Figures 4E–G**) repetitive spikes. We found that the mutation L263V was much more effective in promote firing (eight spikes, **Figure 4E** red line) than WT (five spikes, **Figure 4E** black line). Firing in case of the L1670W mutation was only slightly higher than for WT (**Figure 4F** red line, WT–black line). Instead, the M145T mutation led to a dramatically reduced firing (**Figure 4G**). Thus, FHM3 mutations further increased spike frequency activated by multiple ATP release sites on branched Aδ-fibers. The branching of the single axon enhanced the spiking activity, only when it was combined with asynchronous ATP release (**Figure 4**) because spikes from different branches were efficiently summarized in the primary afferents.

As the concentration of extracellular ATP can vary in the neuro-immune synapse due to expression profile and location of the powerful ATP-degrading ectoenzymes (Yegutkin, 2008), we next explored, in a branched model, the role of different concentrations of ATP in generation of a single spike and on repetitive firing in the most prominent mutant L263V. The dependence of a single-spike probability from concentration of ATP and the role of ATP hydrolysis is shown in **Supplementary Figure 4**. In the range of the tested concentrations, the mutant L263V had a higher probability of the spike generation, with a most visible difference at lower ATP concentrations (**Supplementary Figure 4A**, exemplified in **Supplementary Figure 4C**). In case of a lack of ATP hydrolysis, the difference at low ATP concentrations was more noticeable (**Supplementary Figure 4B**). The repetitive firing

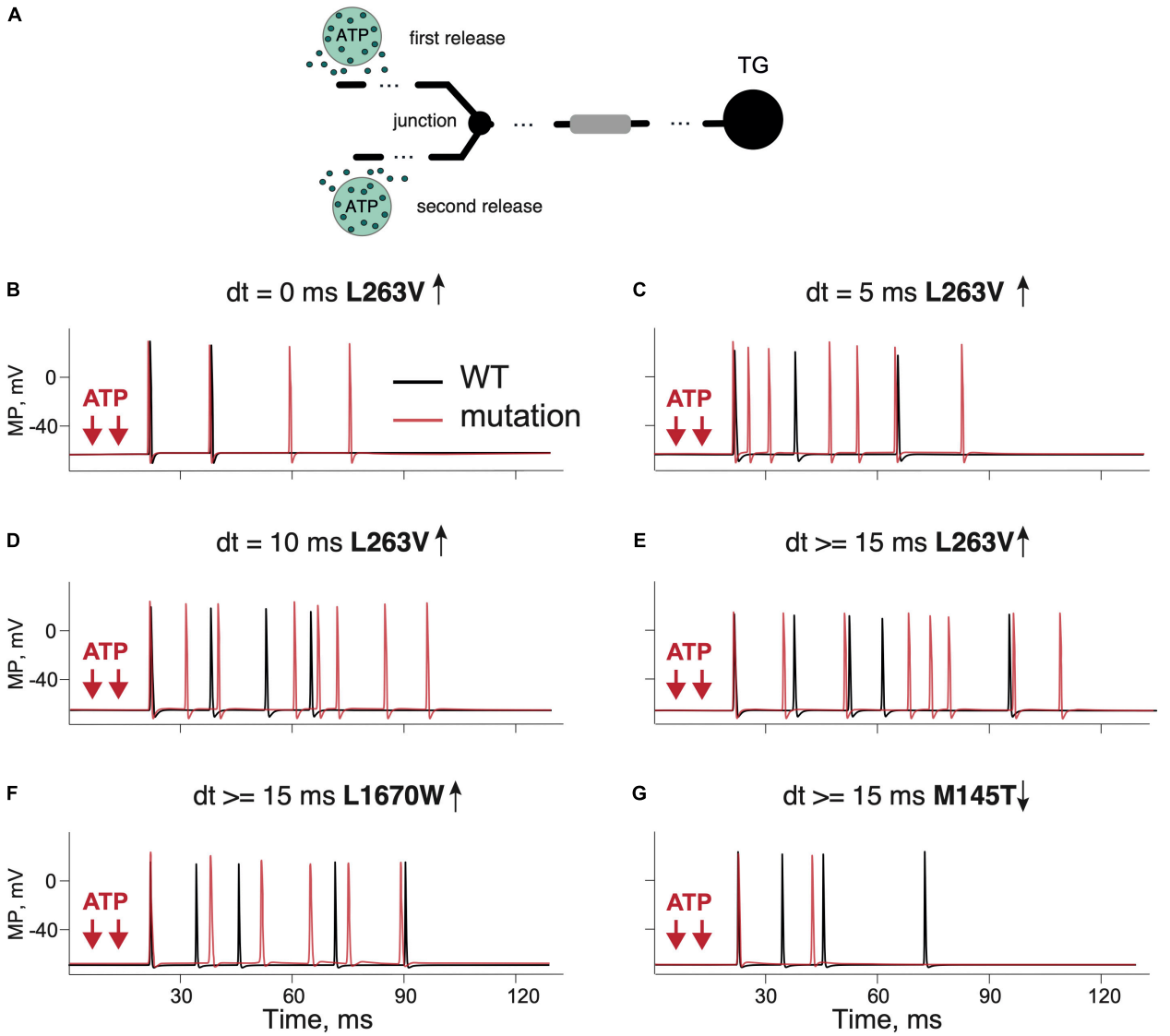


**FIGURE 4 |** Testing the role of branching and multiple ATP release events in firing of the WT and mutant Aδ-fibers. **(A)** Schematic presentation of a dendritic tree with two branches and two ATP release events. **(B)** Firing activity of the L263V $Na_V1.1$ mutant (red line) and WT (Kahlig et al., 2008) fiber (black line) with simultaneous ATP release events. **(C)** The L263V mutant (red line) and WT (Kahlig et al., 2008) fiber (black line) with ATP release with an interval of 5 ms. **(D)** The L263V mutant (red line) and WT (Kahlig et al., 2008) fiber (black line) with an 10-ms interval. **(E)** The L263V mutant (red line) and WT (Kahlig et al., 2008) fiber (black line) with an 15-ms interval. **(F)** The L1670W (red line) and WT (Dhifallah et al., 2018) fiber (black line) with an interval of 15 ms. **(G)** Firing in the loss-of-function mutant M145T (red line) and WT (Mantegazza et al., 2005) fiber (black line) with an ATP release interval of 15 ms. Note that branching and multiple ATP release increased the firing in the case of a gain-of function but reduced in the case of a loss-of-function. ATP signaling is limited by partial hydrolysis.

was less sensitive to the absence or presence of ATP hydrolysis (**Supplementary Figures 4G,H**).

## 5-HT Induced Activation of WT and FHM3 Aδ-Fibers

5-HT is the major neurotransmitter released from meningeal mast cells that can powerfully activate peripheral trigeminal nerve terminals through ligand-gated 5-HT3 receptors (Kilinc et al., 2017; Koroleva et al., 2019). Therefore, we conducted modeling experiments (two branches, two release sites) simulating 5-HT release from mast cells and its action on 5-HT3 receptor in Aδ-fibers meningeal afferents.

Like with ATP, we found that the excitatory action of 5-HT was twice more pronounced with the L263V mutation than with the respective WT (**Figure 5A** L263V–red line, WT–black line). The dependence of a single-spike probability from a concentration of 5-HT in basal conditions or after removal of 5-HT upate for the mutant L263V resembled, in some tests, that of ATP (**Supplementary Figures 4D,E**). In the example shown in **Supplementary Figure 4F**, a concentration of 5-HT as low as 0.6 μM was already able to generate a single spike in the mutant

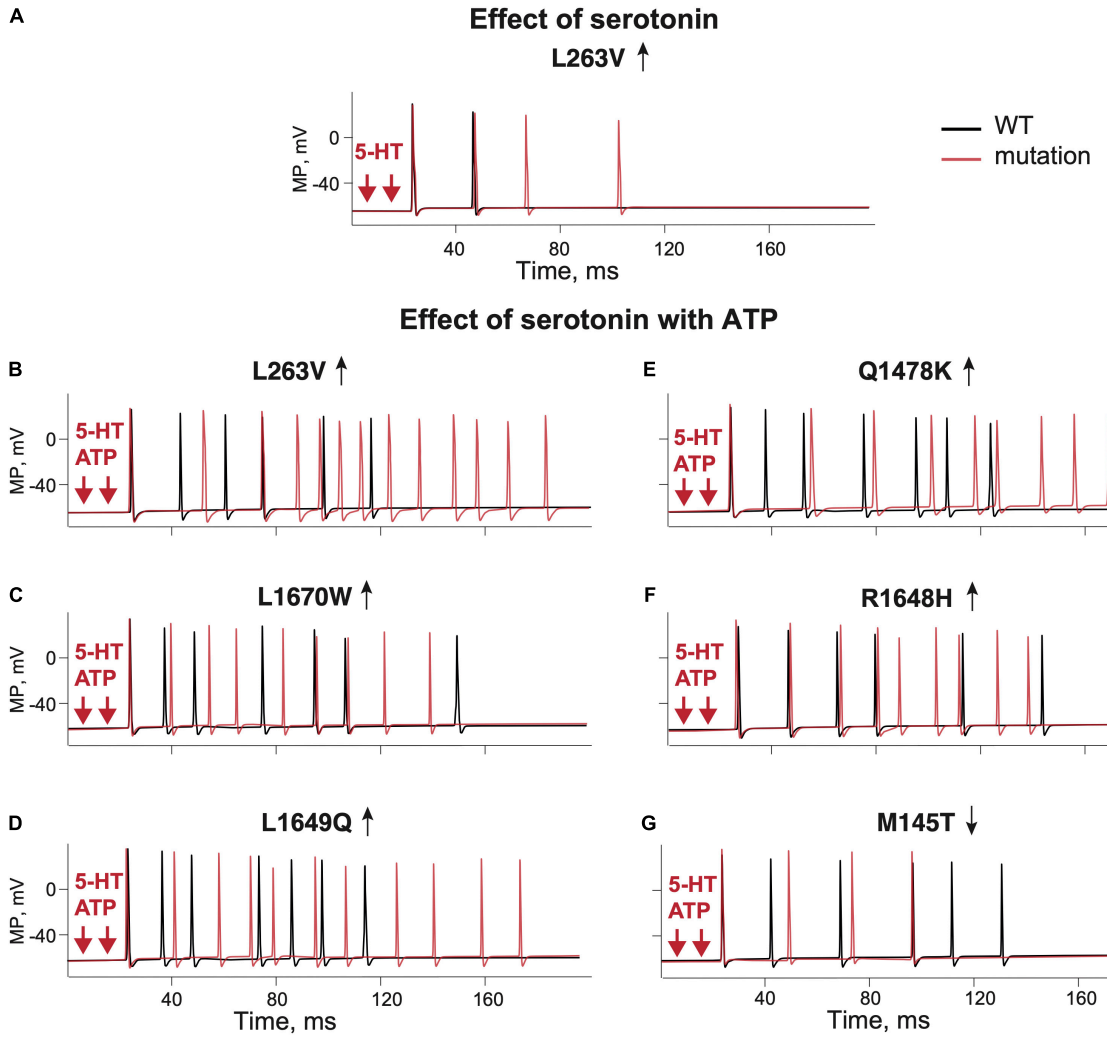


**FIGURE 5 |** The role of 5-HT and combination of ATP and 5-HT release events in firing of the WT and $Na_V1.1$ mutant branching Aδ-fibers. **(A)** Firing of the WT (Kahlig et al., 2008) fibers (black line) and the L263V mutant (red line) activated by two 5-HT release events. **(B)** WT (Kahlig et al., 2008) fibers (black line) and the L263V mutant (red line) activated by ATP + 5-HT release events. **(C)** The L1670W mutant fiber (red line) and WT (Dhifallah et al., 2018) fiber (black line) activated by ATP + 5-HT release events. **(D)** The L1649Q mutant fiber (red line) and WT (Cestele et al., 2008) fiber (black line) activated by ATP + 5-HT release events. **(E)** The Q1478K mutant fiber (red line) and WT (Cestele et al., 2013) fiber (black line) activated by ATP + 5-HT release events. **(F)** The R1648H mutant (red line) and WT (Kahlig et al., 2006) fiber (black line) associated with childhood epilepsy gain-of-function of $Na_V1.1$. **(G)** The M145T $Na_V1.1$ mutant (red line) and WT (Mantegazza et al., 2005) fiber (black line) associated with a loss-of-function mutation of $Na_V1.1$. ATP signaling is limited by partial hydrolysis and 5-HT signals are reduced by specific uptake.

L263V, whereas the same concentration of neurotransmitter in the WT induced only a small receptor potential. We found also an increased repetitive firing with higher 5-HT concentrations for mutant L263V; in particular, when we switched from 2 to 10 μM 5-HT, not only the number of spikes but also the firing frequency rose (**Supplementary Figures 5E,F**). Interestingly, for mutant L263V, increasing the concentration of 5-HT in the micromolar range had a stronger effect on repetitive firing than similar changes in the concentration of ATP (**Supplementary Figures 5B,F** vs. **Supplementary Figures 5A,D**).

As ATP and 5-HT can be co-released during migraine events in the meninges (Suleimanova et al., 2020), we next modeled the simultaneous action of ATP and 5-HT. The combined activation of P2X3 and 5-HT3 receptors in WT produced more spiking activity than ATP or 5-HT alone (**Figures 5B–G** black lines). Then, we extended our approach to compare the firing of *SCN1A* gain- and loss-of-function mutations with their respective control WTs (**Figures 5B–G** red lines). With simultaneous release of ATP and 5-HT, the neuronal firing of WTs was similar (six spikes for L263V, R1648H, M145T, and seven spikes for Q1478K, and L1649Q, **Figures 5B-G**). Again, like in previous modeling conditions, the most pronounced spiking activity was observed with the FHM3 mutations L263V (**Figure 5B**), Q1478K (**Figure 5E**), and L1649Q (**Figure 5D**). The R1648H mutation (**Figure 5F**) that is associated with childhood epilepsy produced less spikes than the L263V mutation but more than WT.

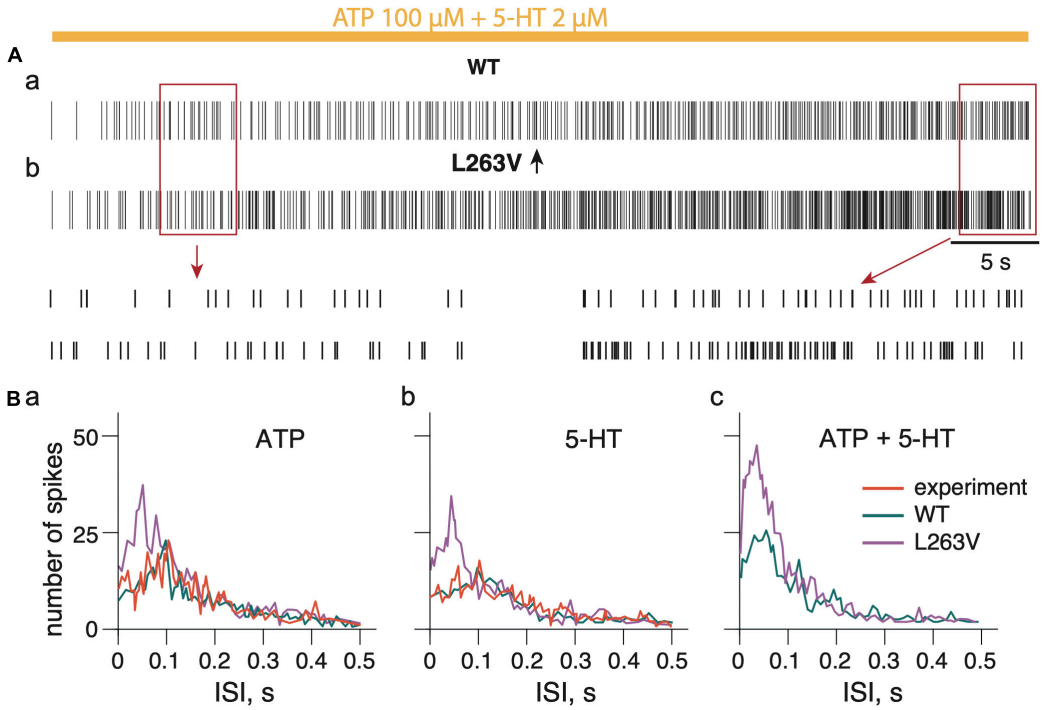


**FIGURE 6 |** Firing activity of whole trigeminal meningeal nerve induced by persistent ATP plus 5-HT. **(Aa)** Firing activity of $Na_V1.1$ WT nerve induced by combined ATP (100 μM) and 5-HT (2 μM) action. **(Ab)** Firing activity induced by combined ATP (100 μM) and 5-HT (2 μM) action on nerve with fibers expressing L263V $Na_V1.1$ mutant channels. Notice details of fitting in insets. **(Ba)** The distribution of the inter-spike intervals (ISI) during action of ATP, 5-HT **(Bb)** and combined ATP + 5-HT action **(Bc).** ATP signaling is limited by partial hydrolysis and 5-HT signals are reduced by specific uptake.

Thus, the updated Aδ-fiber model with simultaneous action of 5-HT and ATP on the branched trigeminal nerve dramatically increased the spiking activity for the FHM3 mutations.

## Modeling the Whole Nerve Activity

Finally, to explore the role of $Na_V1.1$ channels in a more physiological environment, we modeled a WT whole nerve comprising five Aδ-fibers, five C-fibers, and ten inactive (ATP- and 5-HT-insensitive) fibers (schematically presented in **Supplementary Figure 6, left**). In this case, to validate the modeling results with experimental results from rodent meningeal nerves comprised of Aδ- and C-fibers in trigeminal nerves (Levy et al., 2007; Haanes and Edvinsson, 2019), we added simulated C-fibers to the model of the whole nerve, although they do not express $Na_V1.1$ channels, while they express P2X3 and 5-HT receptors (Zeitz et al., 2002; Yegutkin et al., 2016; Kilinc et al., 2017). Details of the C-fiber model are presented in **Supplementary Figure 6**. We added co-expression of P2X2 and P2X3 receptors to the whole nerve model as they are naturally expressed in trigeminal neurons of rodents (Simonetti et al., 2006). A ratio of P2X3/P2X2 was set to 75/25%, since we found in our previous study (Suleimanova et al., 2020) that this ratio closely reproduced the experimental data. The current simulated data for the whole nerve were validated with our previously published experimental results on the activity of ATP and 5-HT in mouse meningeal afferents (Koroleva et al., 2019).

For validation, we compared the inter-spike intervals (ISI) (**Figure 6B**) obtained from experimental data when the spiking activity in meningeal afferents was induced by 100 μM ATP (Koroleva et al., 2019) with the simulated WT model neuronal activity in afferents, also induced by 100 μM ATP (**Supplementary Figure 6Aa**). Likewise, we also modeled the action of 2 μM 5-HT that was also compared with experimental data with 5-HT (Koroleva et al., 2019; **Supplementary Figure 6Ba**). During the simulation experiments, ATP application triggered spiking which spectral profile was almost the same as in the experimental approach (**Figure 6Ba**). The *p*-value of 0.104 in the K-S test indicates the high similarity of the model and experimental results with ATP application. Likewise, with 5-HT, the model approach reproduced the data from the experiment (**Figure 6Bb**). The *p*-value of 0.128 in the K-S test indicates the high similarity of the model and experimental spikes distribution.

To reproduce the role of the FHM3 mutation in the activity of the whole nerve, we selected the L263V mutation as it produced more spikes than any other tested FHM3 mutations. In contrast to WT (**Figure 6Aa**), the model of the nerve with the Aδ-fiber with the L263V mutation showed a much higher neuronal activity with ATP (**Figure 6Ba** and **Supplementary Figure 6Ab**), with 5-HT (**Figure 6Bb** and **Supplementary Figure 6Bb**), and with co-application of ATP together with 5-HT (**Figures 6Ab,Bc**). Notably, with the L263V mutation most spikes were distributed with frequency higher than 10 Hz (ISI 0.1s).

Thus, with a FHM3 mutation an intensive spiking activity was produced in a whole nerve model with shorter intervals which suggested a more powerful nociceptive signaling.

## DISCUSSION

The main result of this study is to provide a mechanistical explanation of peripheral mechanisms of enhanced nociceptive firing activity in trigeminal neurons and the whole nerve when *in silico* modeling the effect of FHM3 mutations. Our computational approach provides a scientific framework for the underlying molecular mechanisms of trigeminal nociceptive firing implicated in this migraine subtype. Our *in silico* approach allowed us to correct ("virtually treat") the abnormal voltage characteristics of mutated channels that resulted in a significant reduction of nociceptive firing. Thus, our data suggest that compounds affecting $Na_V1.1$ channels in Aδ-fibers of peripheral nerves in a mutation-specific manner, may be a promising avenue for novel type analgesic anti-migraine therapy.

### Role of $Na_V1.1$ Channels in the Activation of Aδ-Fibers

Peripheral sensory nerves express a wide range of sodium channels needed for the generation and propagation of nociceptive spikes evoked by mechanical or chemical stimulation of nerve terminals (Basbaum and Woolf, 1999; Julius and Basbaum, 2001; Giniatullin, 2020). Among other $Na_V$ subtypes, the $Na_V1.1$ sodium channel subtype is highly expressed in Aδ-fibers of peripheral nerves (Ho and O'Leary, 2011; Osteen et al., 2016) in addition to in central cortical interneurons (Ogiwara et al., 2007). Their abundance predicts that dysfunction of $Na_V1.1$ channels in Aδ-fibers should affect the transmission of nociceptive signals in a pronounced way. As Aδ-fibers are implicated in the generation of migraine pain (Melo-Carrillo et al., 2017; Haanes and Edvinsson, 2019), this provides a rationale for how pain signals are generated in trigeminal nerves in meninges where migraine pain is generated (Moskowitz, 2008; Messlinger, 2009; Zakharov et al., 2015).

### Trigeminal Neuron Firing in $Na_V1.1$ Channels With FHM3 Mutations

Familial hemiplegic migraine type 3 (FHM3) is caused by gain-of-function mutations in the *SCN1A* gene that encodes the α1 subunit of voltage-gated $Na_V1.1$ sodium channels (Castro et al., 2009). Therefore, in our model, we implemented and tested the functional role of different gain-of-function mutations (L1670W, L263V, L1649Q, and Q1478K), which were previously shown as a genetic cause of disease in patients with FHM3 (Kahlig et al., 2008; Dhifallah et al., 2018). For comparison (as a "negative control"), we also modeled nociceptive firing in trigeminal neurons with the loss-of-function mutation (M145T) in the same α1 subunit of $Na_V1.1$ channels (Mantegazza et al., 2005). The strongest increase of nociceptive firing, a predictive of severe migraine pain, was observed for the L263V mutation, likely due to the increased "window current" (**Figure 2Aa**) because of the shift of the activation in the voltage-dependence curve to lower voltages and the inactivation curve to higher voltages comparing to WT $Na_V1.1$ channels (Kahlig et al., 2008). Although, experimentally, a clear trend, albeit not significant, for increase of voltage dependence of activation ($V_{1/2}$ = −21 mV for WT vs. $V_{1/2}$ = −25 mV for the L263V mutation) was reported by Kahlig et al. (2008), the mutation has a clear effect in our model (**Figure 2A**). It is worth noting that this property was detectable only for the L263V mutant so not with the other tested mutants (**Figure 2**). Our L263V finding maybe not that surprising as even a small shift in activation parameters may provide a sufficiently strong functional effect on excitability, especially near threshold voltage levels when nerve terminals are activated by physiologically relevant low levels of endogenous agonists. Consistent with this, we showed that mutant L263V required less ATP or 5-HT for induction of spiking activity (**Supplementary Figure 4C**), which may translate to a lower pain threshold. Of note, recently, it has been shown in a knock-in mouse model that this mutation facilitated spontaneous cortical spreading depolarization (CSD) events, the likely underlying cause of the migraine aura (Jansen et al., 2020a). However, the effect of the mutation in peripheral trigeminal neurons has not been investigated. Moreover, the observation that mutated $Na_V1.1$ channels can facilitate spontaneous CSD events may also have relevance to, for instance, stroke as relative peri-infarct depolarizations (PID) known to circle around the infarct core (Sukhotinsky et al., 2010), when occurring more easily, may lead to an increase in the infarct size and worse stroke outcome. Although, this has not been demonstrated in the case of FHM3, it was shown that in knock-in mice expressing $Ca_V2.1$ calcium channels with a FHM1 mutation in the α1 subunit (van den Maagdenberg et al., 2004), which results in a gain-of-function and hyperexcitability phenotype (Ferrari et al., 2015), the number of PIDs was greater and the infarct size was larger when infarcts were introduced experimentally (Eikermann-Haerter et al., 2012). A hyperexcitability phenotype in FHM3 is also suggested from overexpression studies in neurons (Cestele et al., 2008; Dhifallah et al., 2018). In the case of the L1670W mutant, when overexpressed in mouse neocortical neurons, a faster recovery of the mutated $Na_V1.1$ channel activity was observed (Dhifallah et al., 2018). Also, for the Q1478K mutant, when expressed in rat neocortical neurons, the gain-of-function leads to hyperexcitability, which, remarkably, was self-limiting meaning that for only a short time high-frequency neuronal discharges were maintained before a depolarizing block occurred (Cestele et al., 2008).

As trigger for receptor potentials, we used ATP and 5-HT, which are among the most powerful agonists of peripheral nociception in meningeal afferents (Yegutkin et al., 2016; Kilinc et al., 2017; Koroleva et al., 2019). The respective P2X3 and 5-HT3 receptors are expressed in Aδ-fibers (Ford, 2012; Kilinc et al., 2017; Sato et al., 2018). For all gain-of-function mutants, which show an increased persistent sodium current (L263V, L1670W, L1649Q, and Q1478K), we found, in our modeling, the activation of Aδ-fibers by ATP or 5-HT was enhanced.

This may explain why migraine pain develops in carriers of *SCN1A* gain-of-function mutations. In contrast, the loss-of-function M145T mutation (Mantegazza et al., 2005), which is associated with febrile seizures dramatically reduce spiking activity of peripheral Aδ-fibers of the trigeminal nerve. The finding of opposite functional outcomes on neuronal activity of the $Na_V1.1$ mutations depending on whether they cause FHM3 or childhood epilepsy indicates that the modeling is a useful discriminating tool to predict disease outcome.

## Role of Factors Amplifying the Effect of *SCN1A* Mutations

Our mathematical model allows a "knock down" or artificial induction of a $Na_V1$ channel subtype that can be used to explore molecular mechanisms that are challenging to achieve in an experimental setting. Moreover, our model allowed dissection in a stepwise approach the contribution of several of these factors, which is highly relevant as they can potentially modify the nociceptive effect of $Na_V1.1$ mutations.

As a first step, we "knocked down" the contribution of the $Na_V1.6$ subtype to leave only the $Na_V1.1$ subtype to study its putative role in nociceptive signaling. Subsequently, we added the $Na_V1.6$ to find out that $Na_V1.6$, which is naturally accompanying $Na_V1.1$, essentially supports the pro-nociceptive role of $Na_V1.1$ in nerve terminals with a FHM3 *SCN1A* mutation.

For the second step, we added a tree structure of nerve branches to reproduce the composition of meningeal afferents more realistically, as shown experimentally (Schueler et al., 2014; Suleimanova et al., 2020) or in model (Barkai et al., 2020). The branching of a single axon combined with multiple ATP and 5-HT release events from mast cells contacting different branches can largely increase the probably of repetitive firing (Suleimanova et al., 2020). A similar amplifying role of branching was shown in the current study (**Figures 4**, **5**). Furthermore, the slow, due to high impedance (Goldstein et al., 2019; Barkai et al., 2020) ATP/5-HT-induced receptor potential in the fine nerve terminal can initiate the persistent current through slowly inactivating $Na_V1.1$. and $Na_V1.8$ channels. A contributing role of $Na_V1.8$ channels to the multiple firing of primary afferents was shown previously in our model of the neuro-immune synapse in meninges (Suleimanova et al., 2020). Moreover, recently we found ATP-gated (but not 5-HT-induced) nociceptive firing not only at peripheral nerve terminals but also in more central parts of trigeminal nerve fibers in rat meninges (Gafurov et al., 2021). The latter suggests that ATP can activate nerve fibers not only at the end points of an axon but also along the fiber and that this probability is higher for ATP than for 5-HT. These factors could be essential for the increased agonist-induced multiple firing of meningeal afferents. Together, our study demonstrated that branching, multiple asynchronous ATP/5-HT release events together with persistent sodium $Na_V1.1$ and the presence of $Na_V1.8$ currents collectively enhance repetitive nociceptive firing in Aδ-fibers, most notable in FHM3-associated mutants.

For the third step, we conducted modeling experiments with 5-HT, which is a major nociceptive mediator in meninges, likely released from mast cells during migraine attacks, and that can strongly activate meningeal fibers through 5-HT3 receptors (Kilinc et al., 2017; Koroleva et al., 2019). However, unlike seen for the combined action of ATP and 5-HT, which induces very pronounced and long-term spiking activity, 5-HT alone induced firing that was not as strong as seen with ATP, likely due to a lower amplitude of 5-HT3 receptor-mediated generator potential at nerve terminals.

Notably, the concentration of ATP and 5-HT released within the meningeal neuro-immune synapse has a different time profile (Suleimanova et al., 2020). In the case of ATP, the time course is primarily determined by enzymatic hydrolysis of this endogenous purinergic transmitter by numerous ectoATPases (Yegutkin, 2008). Therefore, ATP-induced excitation depends on the spatial distribution of these enzymes in the neuro-immune synapse. Any mismatch between the ATP release site and the presence of ectoATPases in the synapse would increase the excitatory nociceptive action of this purinergic transmitter due to reduced transmitter hydrolysis as shown in the current study for the case of absence of ectoATPases activity in the meningeal synapse. Interestingly, in experimental migraine-like conditions induced by the migraine mediator CGRP, the level of endogenous ATP in the rat meninges is significantly enhanced (Yegutkin et al., 2016) by increasing purinergic drive for nociceptive excitation.

In contrast to ATP, released 5-HT is removed from the neuro-immune synapse by a relatively slow uptake (Suleimanova et al., 2020). This is specific for the 5-HT transport system and can be blocked by selective serotonin reuptake inhibitors (SSRIs), commonly used in patients with depression. The inhibition of specific transporters can increase the level of serotonin in the extracellular space and potentially amplify the pro-nociceptive action of 5-HT in meninges. In opposite, an increased expression of serotonin transporters is expected to provide an anti-nociceptive effect, specifically when switching off the serotonergic drive for excitation of nerve terminals via 5-HT3 receptors (Kilinc et al., 2017).

We also explored the effect of ATP and 5-HT concentrations as they could vary in migraine-relevant conditions. In the meningeal neuro-immune synapse, the concentration and the time profile for these two potential triggers of nociceptive firing is very different as determined by distinct elimination mechanisms such as enzymatic degradation and uptake, respectively (Yegutkin, 2008; Wood et al., 2014; Suleimanova et al., 2020). Indeed, we found that the shift from basal conditions with partial ATP hydrolysis and functional 5-HT uptake (**Supplementary Figures 4G,I**) to complete prevention of ATP hydrolysis and removal of 5-HT uptake (**Supplementary Figures 4H,J**) significantly increased repetitive firing of meningeal afferents. Consistent with this, the number of spikes was also increased when enhancing the concentration of both these algogens from 2 to 10 μM, but it was more noticeable with 5-HT (**Supplementary Figures 4C–F**).

In our next step, we simulated the more realistic multi-fiber complex nerve model to compare the computational outcome with results from experiments performed previously (Koroleva et al., 2019). Notably, in the model of the whole nerve, ATP and 5-HT produced a powerful long-lasting firing in in analogy to results observed with firing that was induced

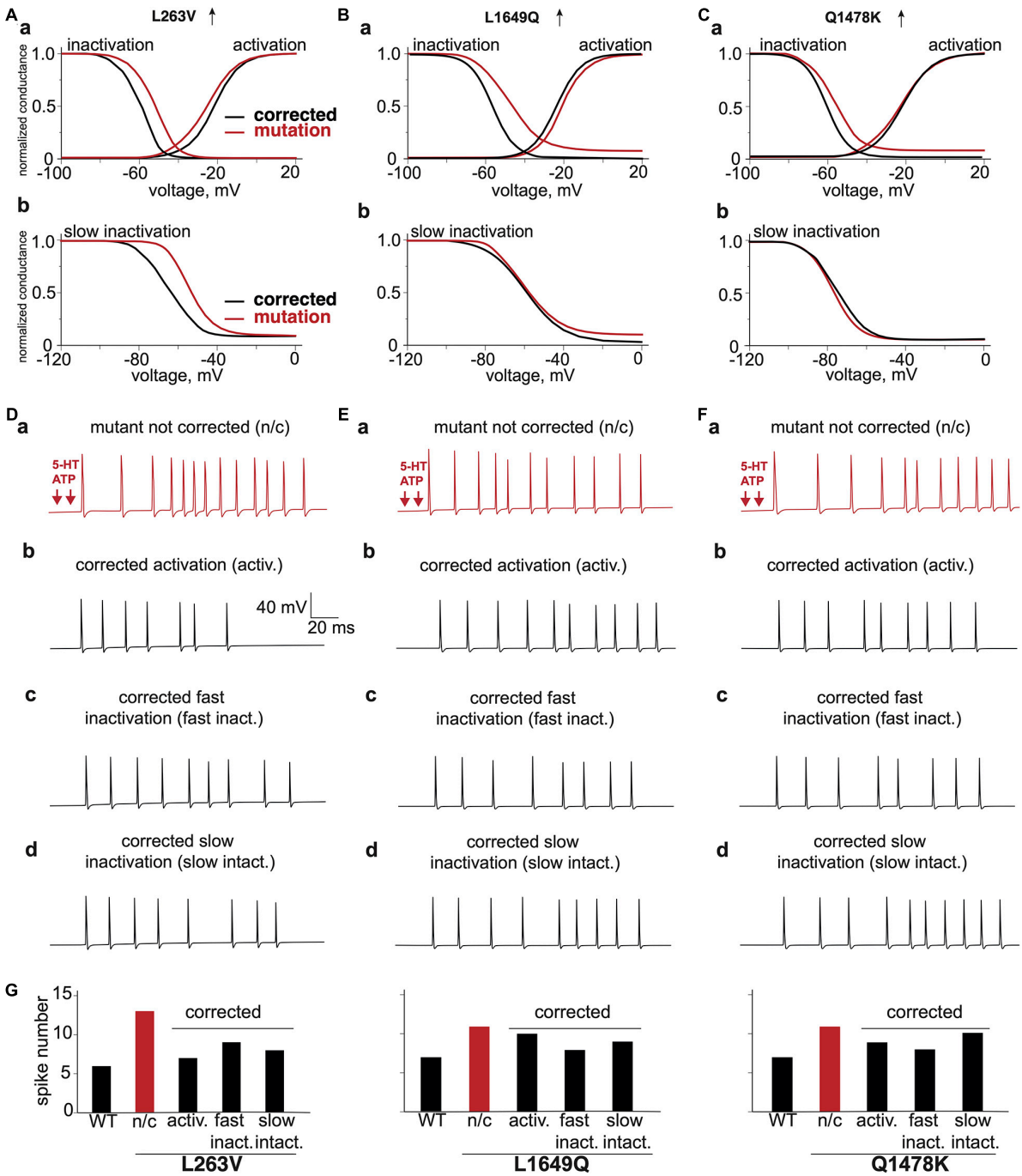


**FIGURE 7 |** The virtual correction of the abnormal phenotype via modification of voltage characteristics of mutated channels. The comparison of voltage dependence of corrected activation, fast inactivation and mutation **(Aa)** L263V, **(Ba)** L1649Q, **(Ca)** Q1478K. The comparison of voltage dependence of corrected slow inactivation and mutation **(Ab)** L263V, **(Bb)** L1649Q, and **(Cb)** Q1478K. **(Da)** L263V mutant fiber activated by ATP + 5-HT release events, **(Db)** with corrected activation, **(Dc)** with corrected fast inactivation, **(Dd)** with corrected slow inactivation. **(Ea)** L1649Q mutant fiber activated by ATP + 5-HT release events, **(Eb)** with corrected activation, **(Ec)** with corrected fast inactivation, **(Ed)** with corrected slow inactivation. **(Fa)** Q1478K mutant fiber activated by ATP + 5-HT release events, **(Fb)** with corrected activation, **(Fc)** with corrected fast inactivation, **(Fd)** with corrected slow inactivation. **(G)** The spike number of WT fiber and L263V, L1649Q, and Q1478K mutations with correction of activation and inactivation. ATP signaling is limited by partial hydrolysis and 5-HT signals are reduced by specific uptake.

by ATP and 5-HT in the experimental condition in mouse meninges. Most relevant to this study, nociceptive spiking of the whole nerve activity largely increased when a FHM3 mutation was introduced in the model of the Aδ-fibers, indicating that our model properly reproduces an enhanced nociceptive firing in FHM3.

## Virtual Treatment *in silico* of Carriers of *SCN1A* Mutations

Since different mutations exhibit distinct changes in the voltage dependence such as activation, fast or slow inactivation (**Figure 2**), we next set out to correct *in silico* the pathological phenotype. To this end, we used as an indicator of "treatment efficiency" the reduction of spiking in meningeal afferents and compared the result with the firing in the WT model (**Figure 7G**).

We observed for mutant L263V that its nociceptive phenotype was associated with abnormal changes of activation, fast and slow inactivation (**Figures 7Aa,Ab,Da**). The best improvement was obtained with corrected activation (**Figure 7Db**), since mutant L263V is activated at a more negative voltage than WT that showed in **Figures 2Aa**, **7Aa** as a shift of the voltage-dependence activation curve to the left and shows a delayed entry into fast inactivation state. Besides, this mutation accelerated recovery, and reduced depolarizing shift in the voltage dependence of both fast and slow inactivation. However, the correction of fast and slow inactivation states in L263V less efficiently reduced spiking activity (**Figures 7Dc,Dd,G**). In the case of mutants L1649Q and Q1478K (**Figures 7Ea,Fa**), which profoundly exhibit a positive shift in fast inactivation (**Figures 7Ba,Ca**), the number of spikes, as expected, was most strongly decreased when we corrected the fast inactivation (**Figures 7Ec,Fc,G**). Since there were no significant alterations in the slow inactivation state for mutants L1649Q and Q1678K (**Figures 7Bb,Cb**) correction of this state did not significantly change the neuronal spiking activity (**Figures 7Ed,Fd**).

Our data suggest that treatment of FHM3 patients that exhibit headache as a main complaint, but due to a different $Na_V1.1$ mutation, may be achieved through two distinct effects of possibly different drugs, as in some cases, the most efficient correction was based on improvement of activation (L263V), whereas in other cases, the best results was obtained with correction of the inactivation state (L1649Q and Q1478K). In addition to direct correction of the genetic defect, there might be alternative pharmacological mechanisms to limit the FHM3-associated enhanced repetitive firing in trigeminal neurons. One possibility may be the activation of potassium-mediated $K_V7$/M-currents, which contribute to the stabilization of the membrane potential and can be activated by the analgesic drugs, such as paracetamol (Ray et al., 2019).

In our modeling approach, we did not simulate the outcome of changes in $Na_V1.1$ in central neurons where these channels are expressed in interneurons (Favero et al., 2018; Sakkaki et al., 2020). Recently, computer modeling of various neuron types, similar to our whole nerve paradigm, was used to predict functional outcome of an FHM3 mutation on the central neuronal network of transgenic Dravet mice, in which $Na_V1.1$ channels were ablated in hippocampus and cortex (Jansen et al., 2020b). One could model the role of $Na_V1.1$ channels in CSD events associated with FHM3 or analogous PID in stroke to assess brain recovery after ischemia (Sukhotinsky et al., 2010). The proposed modeling approach can also actively guide the development of selective activators or inhibitors of $Na_V1.1$ channels to treat diseases such as hemiplegic migraine, seizures and stroke.

In summary, our data demonstrated a long-term intensive spiking activity in meningeal afferents, with various gain-of-function mutations of sodium channels associated with FHM3 in patients. Improvement of high nociceptive activity was obtained in a mutation-specific manner, being in some cases based on correction of the activation process (**Figures 7Db,Eb,Fb**), whereas, in others, a better result was obtained after adjustment of both the fast and slow inactivation of mutated $Na_V1.1$ channels (**Figures 7Dc,Dd,Ec,Ed,Fc,Fd**). Such modeling provides a new tool for the exploration of peripheral mechanisms in trigeminal pain and suggests that molecules reducing, probably in a mutation-specific manner, the excessive activity of $Na_V1.1$ channels could present a novel type of analgesic therapy for patients with migraine.

## DATA AVAILABILITY STATEMENT

The raw data supporting the conclusions of this article will be made available by the authors, without undue reservation.

## AUTHOR CONTRIBUTIONS

AS and MT contributed to modeling, analysis and writing the manuscript. AMJMvdM contributed to design of the study, interpretation, writing the manuscript, and the final editing. RG contributed to the study design and supervision, writing the manuscript, and the final editing. All authors approved the final version of the manuscript.

## FUNDING

The study was supported by RFBR KOMFI (Grant No. 17-00-00053) and Kazan Federal University (Grant No. 0671-2020-0059). Kazan Federal University was supported by the Russian Government Program of Competitive Growth.

## SUPPLEMENTARY MATERIAL

The Supplementary Material for this article can be found online at: https://www.frontiersin.org/articles/10.3389/fncel.2021.644047/full#supplementary-material

## REFERENCES

Andreou, A. P., Leese, C., Greco, R., Demartini, C., Corrie, E., Simsek, D., et al. (2020). Double-binding botulinum molecule with reduced muscle paralysis: evaluation in in vitro and in vivo models of migraine. *Neurotherapeutics* doi: 10.1007/s13311-020-00967-7 [Online ahead of print],

Barkai, O., Butterman, R., Katz, B., Lev, S., and Binshtok, A. M. (2020). The input-output relation of primary nociceptive neurons is determined by the

morphology of the peripheral nociceptive terminals. *J. Neurosci.* 40, 9346–9363. doi: 10.1523/JNEUROSCI.1546-20.2020

Basbaum, A. I. (2002). Pain physiology: basic science. *Can. J. Anaesth.* 49, R1–R3.

Basbaum, A. I., and Woolf, C. J. (1999). Pain. *Curr. Biol.* 9, R429–R431. doi: 10.1016/s0960-9822(99)80273-5

Black, J. A., Frézel, N., Dib-Hajj, S. D., and Waxman, S. G. (2012). Expression of Nav1.7 in DRG neurons extends from peripheral terminals in the skin to central preterminal branches and terminals in the dorsal horn. *Mol. Pain* 8:82. doi: 10.1186/1744-8069-8-82

Boyerinas, B. M. (2016). Determining the Statistical Power of the Kolmogorov-Smirnov and Anderson-Darling goodness-of-fit Tests via Monte Carlo Simulation. CNA Occasional Paper No. CNA-DOP-2016-U-014638-Final-2.

Burnstock, G. (1981). Pathophysiology of migraine: a new hypothesis. *Lancet* 317, 1397–1399. doi: 10.1016/s0140-6736(81)92572-1

Castro, M.-J., Stam, A., Lemos, C., de Vries, B., Vanmolkot, K., Barros, J., et al. (2009). First mutation in the voltage-gated Nav1.1 subunit gene SCN1A with co-occurring familial hemiplegic migraine and epilepsy. *Cephalalgia* 29, 308–313. doi: 10.1111/j.1468-2982.2008.01721.x

Cestele, S., Scalmani, P., Rusconi, R., Terragni, B., Franceschetti, S., and Mantegazza, M. (2008). Self-limited hyperexcitability: functional effect of a familial hemiplegic migraine mutation of the Nav1.1 (SCN1A) Na+ Channel. *J. Neurosci.* 28, 7273–7283. doi: 10.1523/JNEUROSCI.4453-07.2008

Cestele, S., Schiavon, E., Rusconi, R., Franceschetti, S., and Mantegazza, M. (2013). Nonfunctional Nav1.1 familial hemiplegic migraine mutant transformed into gain-of-function by partial rescue of folding defects. *Proc. Natl. Acad. Sci. U.S.A.* 110, 17546–17551. doi: 10.1073/pnas.1309827110

Chien, L. Y., Cheng, J. K., Chu, D., Cheng, C. F., and Tsaur, M. L. (2007). Reduced expression of A-type potassium channels in primary sensory neurons induces mechanical hypersensitivity. *J. Neurosci.* 27, 9855–9865. doi: 10.1523/JNEUROSCI.0604-07.2007

Corradi, J., Gumilar, F., and Bouzat, C. (2009). Single-channel kinetic analysis for activation and desensitization of homomeric 5-HT3A receptors. *Biophys. J.* 97, 1335–1345. doi: 10.1016/j.bpj.2009.06.018

Dhifallah, S., Lancaster, E., Merrill, S., Leroudier, N., Mantegazza, M., and Cestèle, S. (2018). Gain of Function for the SCN1A/hNav1.1-L1670W mutation responsible for familial hemiplegic migraine. *Front. Mol. Neurosci.* 11:232. doi: 10.3389/fnmol.2018.00232

Dichgans, M., Freilinger, T., Eckstein, G., Babini, E., Lorenz-Depiereux, B., Biskup, S., et al. (2005). Mutation in the neuronal voltage-gated sodium channel SCN1A in familial hemiplegic migraine. *Lancet* 366, 371–377. doi: 10.1016/S0140-6736(05)66786-4

Dreier, J. P., and Reiffurth, C. (2015). The stroke-migraine depolarization continuum. *Neuron* 86, 902–922. doi: 10.1016/j.neuron.2015.04.004

Duflocq, A., Le Bras, B., Bullier, E., Couraud, F., and Davenne, M. (2008). Nav1.1 is predominantly expressed in nodes of Ranvier and axon initial segments. *Mol. Cell. Neurosci.* 39, 180–192. doi: 10.1016/j.mcn.2008.06.008

Eikermann-Haerter, K., Lee, J. H., Yuzawa, I., Liu, C. H., Zhou, Z., Shin, H. K., et al. (2012). Migraine mutations increase stroke vulnerability by facilitating ischemic depolarizations. *Circulation* 125, 335–345. doi: 10.1161/CIRCULATIONAHA.111.045096

Favero, M., Sotuyo, N. P., Lopez, E., Kearney, J. A., and Goldberg, E. M. (2018). A transient developmental window of fast-spiking interneuron dysfunction in a mouse model of dravet syndrome. *J. Neurosci.* 38, 7912–7927. doi: 10.1523/JNEUROSCI.0193-18.2018

Ferrari, M. D., Klever, R. R., Terwindt, G. M., Ayata, C., and van den Maagdenberg, A. M. (2015). Migraine pathophysiology: lessons from mouse models and human genetics. *Lancet Neurol.* 14, 65–80. doi: 10.1016/S1474-4422(14)70220-0

Ford, A. P. (2012). P2X3 antagonists: novel therapeutics for afferent sensitization and chronic pain. *Pain Manag.* 2, 267–277. doi: 10.2217/pmt.12.16

Gafurov, O., Koroleva, K., and Giniatullin, R. (2021). Antidromic spike propagation and dissimilar expression of P2X, 5-HT, and TRPV1 channels in peripheral vs. central sensory axons in meninges. *Front Cell. Neurosci.* 14:623134. doi: 10.3389/fncel.2020.623134

Giniatullin, R. (2020). Ion channels of nociception. *Int. J. Mol. Sci.* 21:3553. doi: 10.3390/ijms21103553

Giniatullin, R., Nistri, A., and Fabbretti, E. (2008). Molecular mechanisms of sensitization of pain-transducing P2X3 receptors by the migraine mediators CGRP and NGF. *Mol. Neurobiol.* 37, 83–90. doi: 10.1007/s12035-008-8020-5

Goadsby, P. J. (2007). Serotonin receptor ligands: treatments of acute migraine and cluster headache. *Handb. Exp. Pharmacol.* 177, 129–143. doi: 10.1007/978-3-540-33823-9_5

Goldstein, R. H., Barkai, O., Íñigo-Portugués, A., Katz, B., Lev, S., and Binshtok, A. M. (2019). location and plasticity of the sodium spike initiation zone in nociceptive terminals in vivo. *Neuron* 102, 801.e–812.e. doi: 10.1016/j.neuron.2019.03.005

Gribkoff, V. K., and Winquist, R. J. (2005). Voltage-gated cation channel modulators for the treatment of stroke. *Expert Opin. Investig. Drugs* 14, 579–592. doi: 10.1517/13543784.14.5.579

Haanes, K. A., and Edvinsson, L. (2019). Pathophysiological mechanisms in migraine and the identification of new therapeutic targets. *CNS Drugs* 33, 525–537. doi: 10.1007/s40263-019-00630-6

Hines, M., and Carnevale, N. (2003). The neuron simulation environment. *Neural Comput.* 9, 1179–1209. doi: 10.1162/neco.1997.9.6.1179

Ho, C., and O'Leary, M. E. (2011). Single-cell analysis of sodium channel expression in dorsal root ganglion neurons. *Mol. Cell. Neurosci.* 46, 159–166. doi: 10.1016/j.mcn.2010.08.017

Jansen, N. A., Dehghani, A., Linssen, M. M., Breukel, C., Tolner, E. A., and van den Maagdenberg, A. M. (2020a). First FHM3 mouse model shows spontaneous cortical spreading depolarizations. *Ann. Clin. Transl. Neurol.* 7, 132–138. doi: 10.1002/acn3.50971

Jansen, N. A., Perez, C., Schenke, M., van Beurden, A. W., Dehghani, A., Voskuyl, R. A., et al. (2020b). Impaired theta-gamma coupling indicates inhibitory dysfunction and seizure risk in a Dravet syndrome mouse model. *J. Neurosci.* 41, 524–537. doi: 10.1523/JNEUROSCI.2132-20.2020

Julius, D., and Basbaum, A. I. (2001). Molecular mechanisms of nociception. *Nature* 413, 203–210. doi: 10.1038/35093019

Kahlig, K. M., Misra, S. N., and George, A. L. (2006). Impaired inactivation gate stabilization predicts increased persistent current for an epilepsy-associated SCN1A mutation. *J. Neurosci.* 26, 10958–10966. doi: 10.1523/JNEUROSCI.3378-06.2006

Kahlig, K. M., Rhodes, T. H., Pusch, M., Freilinger, T., Pereira-Monteiro, J. M., Ferrari, M. D., et al. (2008). Divergent sodium channel defects in familial hemiplegic migraine. *Proc. Natl. Acad. Sci. U.S.A.* 105, 9799–9804. doi: 10.1073/pnas.0711717105

Kilinc, E., Guerrero-Toro, C., Zakharov, A., Vitale, C., Gubert-Olive, M., Koroleva, K., et al. (2017). Serotonergic mechanisms of trigeminal meningeal nociception: implications for migraine pain. *Neuropharmacology* 116, 160–173. doi: 10.1016/j.neuropharm.2016.12.024

Koroleva, K., Gafurov, O., Guselnikova, V. V., Nurkhametova, D., Giniatullina, R., Matilla, O., et al. (2019). Meningeal mast cells contribute to ATP-induced nociceptive firing in trigeminal nerve terminals: direct and indirect purinergic mechanisms triggering migraine pain. *Front. Cell. Neurosci.* 13:195. doi: 10.3389/fncel.2019.00195

Leterrier, C., Brachet, A., Dargent, B., and Vacher, H. (2011). Determinants of voltage-gated sodium channel clustering in neurons. *Semin. Cell Dev. Biol.* 22, 171–177. doi: 10.1016/j.semcdb.2010.09.014

Levy, D. (2009). Migraine pain, meningeal inflammation, and mast cells. *Curr. Pain Head. Rep.* 13, 237–240. doi: 10.1007/s11916-009-0040-y

Levy, D., Burstein, R., Kainz, V., Jakubowski, M., and Strassman, A. M. (2007). Mast cell degranulation activates a pain pathway underlying migraine headache. *Pain* 130, 166–176. doi: 10.1016/j.pain.2007.03.012

MacIver, M. B., and Tanelian, D. L. (1993). Structural and functional specialization of A delta and C fiber free nerve endings innervating rabbit corneal epithelium. *J. Neurosci.* 13, 4511–4524. doi: 10.1523/JNEUROSCI.13-10-04511.1993

Mandge, D., and Manchanda, R. (2018). A biophysically detailed computational model of bladder small DRG neuron soma. *PLoS Comput. Biol.* 14:e1006293. doi: 10.1371/journal.pcbi.1006293

Mantegazza, M., Gambardella, A., Rusconi, R., Schiavon, E., Annesi, F., Cassulini, R. R., et al. (2005). Identification of an Nav1.1 sodium channel (SCN1A) loss-of-function mutation associated with familial simple febrile seizures. *Proc. Natl. Acad. Sci. U.S.A.* 102, 18177–18182. doi: 10.1073/pnas.0506818102

McIntyre, C. C., Richardson, A. G., and Grill, W. M. (2002). Modeling the excitability of mammalian nerve fibers: influence of afterpotentials on the recovery cycle. *J. Neurophysiol.* 87, 995–1006. doi: 10.1152/jn.00353.2001

Melo-Carrillo, A., Strassman, A. M., Nir, R. R., Schain, A. J., Noseda, R., Stratton, J., et al. (2017). Fremanezumab—a humanized monoclonal anti-CGRP

antibody—inhibits thinly myelinated (Aδ) but not unmyelinated (C) meningeal nociceptors. *J. Neurosci.* 37, 10587–10596. doi: 10.1523/JNEUROSCI.2211-17.2017

Menezes, L. F. S., Sabiá Júnior, E. F., Tibery, D. V., Carneiro, L. D. A., and Schwartz, E. F. (2020). Epilepsy-related voltage-gated sodium channelopathies: a review. *Front. Pharmacol.* 11:1276. doi: 10.3389/fphar.2020.01276

Messlinger, K. (2009). Migraine: where and how does the pain originate? *Exp. Brain Res.* 196, 179–193. doi: 10.1007/s00221-009-1756-y

Moskowitz, M. A. (2008). Defining a pathway to discovery from bench to bedside: the trigeminovascular system and sensitization. *Headache* 48, 688–690. doi: 10.1111/j.1526-4610.2008.01110.x

Ogiwara, I., Miyamoto, H., Morita, N., Atapour, N., Mazaki, E., Inoue, I., et al. (2007). Nav1.1 localizes to axons of parvalbumin-positive inhibitory interneurons: a circuit basis for epileptic seizures in mice carrying an Scn1a gene mutation. *J. Neurosci.* 27, 5903–5914. doi: 10.1523/jneurosci.5270-06.2007

Olesen, J., Burstein, R., Ashina, M., and Tfelt-Hansen, P. (2009). Origin of pain in migraine: evidence for peripheral sensitisation. *Lancet Neurol.* 8, 679–690. doi: 10.1016/S1474-4422(09)70090-0

Osteen, J. D., Herzig, V., Gilchrist, J., Emrick, J. J., Zhang, C., Wang, X., et al. (2016). Selective spider toxins reveal a role for the Nav1.1 channel in mechanical pain. *Nature* 534, 494–499. doi: 10.1038/nature17976

Pinto, V., Derkach, V. A., and Safronov, B. V. (2008). Role of TTX-sensitive and TTX-resistant sodium channels in Adelta- and C-fiber conduction and synaptic transmission. *J. Neurophysiol.* 99, 617–628. doi: 10.1152/jn.00944.2007

Ray, S., Salzer, I., Kronschläger, M. T., and Boehm, S. (2019). The paracetamol metabolite N-acetylp-benzoquinone imine reduces excitability in first- and second-order neurons of the pain pathway through actions on KV7 channels. *Pain* 160, 954–964. doi: 10.1097/j.pain.0000000000001474

Saftenku, E. (2005). Modeling of slow glutamate diffusion and AMPA receptor activation in the cerebellar glomerulus. *J. Theor. Biol.* 234, 363–382. doi: 10.1016/j.jtbi.2004.11.036

Sakkaki, S., Barrière, S., Bender, A. C., Scott, R. C., and Lenck-Santini, P. P. (2020). Focal dorsal hippocampal Nav1.1 knock down alters place cell temporal coordination and spatial behavior. *Cereb. Cortex* 30, 5049–5066. doi: 10.1093/cercor/bhaa101

Sato, M., Ogura, K., Kimura, M., Nishi, K., Ando, M., Tazaki, M., et al. (2018). Activation of mechanosensitive transient receptor potential/piezo channels in odontoblasts generates action potentials in cocultured isolectin B4–negative medium-sized trigeminal ganglion neurons. *J. Endod.* 44, 984–991. doi: 10.1016/j.joen.2018.02.020

Scheffer, I. E., and Nabbout, R. (2019). SCN1A-related phenotypes: epilepsy and beyond. *Epilepsia* 60(Suppl. 3), S17–S24. doi: 10.1111/epi.16386

Schueler, M., Neuhuber, W. L., De Col, R., and Messlinger, K. (2014). Innervation of rat and human dura mater and pericranial tissues in the parieto-temporal region by meningeal afferents. *Headache* 54, 996–1009. doi: 10.1111/head.12371

Serrano, A., Mo, G., Grant, R., Pare, M., O'Donnell, D., Yu, X. H., et al. (2012). Differential expression and pharmacology of native P2X receptors in rat and primate sensory neurons. *J. Neurosci.* 32, 11890–11896. doi: 10.1523/JNEUROSCI.0698-12.2012

Simonetti, M., Fabbro, A., D'Arco, M., Zweyer, M., Nistri, A., Giniatullin, R., et al. (2006). Comparison of P2X and TRPV1 receptors in ganglia or primary culture of trigeminal neurons and their modulation by NGF or serotonin. *Mol. Pain* 2:11. doi: 10.1186/1744-8069-2-11

Sokolova, E., Skorinkin, A., Igor, M., Agrachev, A., Nistri, A., and Giniatullin, R. (2006). Experimental and modeling studies of desensitization of P2X3 receptors. *Mol. Pharmacol.* 70, 373–382. doi: 10.1124/mol.106.023564

Spampanato, J., Aradi, I., Soltesz, I., and Goldin, A. L. (2004). Increased neuronal firing in computer simulations of sodium channel mutations that cause generalized epilepsy with febrile seizures plus. *J. Neurophysiol.* 91, 2040–2050. doi: 10.1152/jn.00982.2003

Sukhotinsky, I., Yaseen, M. A., Sakadzic, S., Ruvinskaya, S., Sims, J. R., Boas, D. A., et al. (2010). Perfusion pressure-dependent recovery of cortical spreading depression is independent of tissue oxygenation over a wide physiologic range. *J. Cereb. Blood Flow Metab.* 30, 1168–1177. doi: 10.1038/jcbfm.2009.285

Suleimanova, A., Talanov, M., Gafurov, O., Gafarov, F., Koroleva, K., Virenque, A., et al. (2020). Modeling a nociceptive neuro-immune synapse activated by ATP and 5-HT in meninges: novel clues on transduction of chemical signals into persistent or rhythmic neuronal firing. *Front. Cell. Neurosci.* 14:135. doi: 10.3389/fncel.2020.00135

Theoharides, T. C., Spanos, C., Pang, X., Alferes, L., Ligris, K., Letourneau, R., et al. (1995). Stress-induced intracranial mast cell degranulation: a corticotropin-releasing hormone-mediated effect. *Endocrinology* 136, 5745–5750. doi: 10.1210/endo.136.12.7588332

Tigerholm, J., Petersson, M. E., Obreja, O., Lampert, A., Carr, R., Schmelz, M., et al. (2014). Modeling activity-dependent changes of axonal spike conduction in primary afferent C-nociceptors. *J. Neurophysiol.* 111, 1721–1735. doi: 10.1152/jn.00777.2012

Tolner, E. A., Houben, T., Terwindt, G. M., de Vries, B., Ferrari, M. D., and van den Maagdenberg, A. M. (2015). From migraine genes to mechanisms. *Pain* 156(Suppl. 1), S64–S74.

Tsuchimochi, H., McCord, J. L., Leal, A. K., and Kaufman, M. P. (2011). Dorsal root tetrodotoxin- resistant sodium channels do not contribute to the augmented exercise pressor reflex in rats with chronic femoral artery occlusion. *Am. J. Physiol Heart Circ. Physiol.* 300, H652–H663. doi: 10.1152/ajpheart.00859.2010

van den Maagdenberg, A. M., Pietrobon, D., Pizzorusso, T., Kaja, S., Broos, L. A., Cesetti, T., et al. (2004). A cacna1a knockin migraine mouse model with increased susceptibility to cortical spreading depression. *Neuron* 41, 701–710. doi: 10.1016/s0896-6273(04)00085-6

Waxman, S., and Ritchie, J. (1993). Molecular dissection of the myelinated axon. *Ann. Neurol.* 33, 121–136. doi: 10.1002/ana.410330202

West, S. J., Bannister, K., Dickenson, A. H., and Bennett, D. L. (2015). Circuitry and plasticity of the dorsal horn–toward a better understanding of neuropathic pain. *Neuroscience* 300, 254–275. doi: 10.1016/j.neuroscience.2015.05.020

Wood, K. M., Zeqja, A., Nijhout, H. F., Reed, M. C., Best, J., and Hashemi, P. (2014). Voltammetric and mathematical evidence for dual transport mediation of serotonin clearance in vivo. *J. Neurochem.* 130, 351–359. doi: 10.1111/jnc.12733

Yegutkin, G. G. (2008). Nucleotide- and nucleoside-converting ectoenzymes: important modulators of purinergic signalling cascade. *Biochim. Biophys. Acta* 1783, 673–694. doi: 10.1016/j.bbamcr.2008.01.024

Yegutkin, G. G., Guerrero-Toro, C., Kilinc, E., Koroleva, K., Ishchenko, Y., Abushik, P., et al. (2016). Nucleotide homeostasis and purinergic nociceptive signaling in rat meninges in migraine-like conditions. *Purinergic Signal.* 12, 561–574. doi: 10.1007/s11302-016-9521-8

Zakharov, A., Vitale, C., Kilinc, E., Koroleva, K., Fayuk, D., Shelukhina, I., et al. (2015). Hunting for origins of migraine pain: cluster analysis of spontaneous and capsaicin-induced firing in meningeal trigeminal nerve fibers. *Front. Cell. Neurosci.* 9:287. doi: 10.3389/fncel.2015.00287

Zeitz, K. P., Guy, N., Malmberg, A. B., Dirajlal, S., Martin, W. J., Sun, L., et al. (2002). The 5-HT3 subtype of serotonin receptor contributes to nociceptive processing via a novel subset of myelinated and unmyelinated nociceptors. *J. Neurosci.* 22, 1010–1019. doi: 10.1523/jneurosci.22-03-01010.2002

Zemel, B. M., Ritter, D. M., Covarrubias, M., and Muqeem, T. (2018). A-type Kv channels in dorsal root ganglion neurons: diversity, function, and dysfunction. *Front. Mol. Neurosci.* 11:253. doi: 10.3389/fnmol.2018.00253

Zhan, R. Z., Nadler, J. V., and Schwartz-Bloom, R. D. (2007). Impaired firing and sodium channel function in CA1 hippocampal interneurons after transient cerebral ischemia. *J. Cereb. Blood Flow Metab.* 27, 1444–1452. doi: 10.1038/sj.jcbfm.9600448

Zhang, M. M., Wilson, M. J., Gajewiak, J., Rivier, J. E., Bulaj, G., Olivera, B. M., et al. (2013). Pharmacological fractionation of tetrodotoxin-sensitive sodium currents in rat dorsal root ganglion neurons by μ-conotoxins. *Br. J. Pharmacol.* 169, 102–114. doi: 10.1111/bph.12119

Zheng, Y., Liu, P., Bai, L., Trimmer, J. S., Bean, B. P., and Ginty, D. D. (2019). Deep sequencing of somatosensory neurons reveals molecular determinants of intrinsic physiological properties. *Neuron* 103, 598–616.

**Conflict of Interest:** The authors declare that the research was conducted in the absence of any commercial or financial relationships that could be construed as a potential conflict of interest.

frontiers in Neuroscience

BRIEF RESEARCH REPORT
published: 03 November 2021
doi: 10.3389/fnins.2021.740639

# Sex Differences in Risk Profile, Stroke Cause and Outcome in Ischemic Stroke Patients With and Without Migraine

*Katie M. Linstra[1,2], Hendrikus J. A. van Os[1], Ynte M. Ruigrok[3], Paul J. Nederkoorn[4], Ewoud J. van Dijk[5], L. Jaap Kappelle[3], Peter J. Koudstaal[6], Marieke C. Visser[4], Michel D. Ferrari[1], Antoinette MaassenVanDenBrink[2], Gisela M. Terwindt[1] and Marieke J. H. Wermer[1]* on behalf of the Dutch Parelsnoer Institute Stroke Study Group*

[1] Department of Neurology, Leiden University Medical Center, Leiden, Netherlands, [2] Division of Pharmacology and Vascular Medicine, Department of Internal Medicine, Erasmus MC, Rotterdam, Netherlands, [3] Department of Neurology and Neurosurgery, UMC Utrecht Brain Center, University Medical Center Utrecht, Utrecht, Netherlands, [4] Department of Neurology, Amsterdam University Medical Center, Amsterdam, Netherlands, [5] Department of Neurology, Radboud University Medical Center, Nijmegen, Netherlands, [6] Department of Neurology, Erasmus Medical Center, Rotterdam, Netherlands

OPEN ACCESS

**Edited by:**
*Jukka Jolkkonen, University of Eastern Finland, Finland*

**Reviewed by:**
*Roshni Thakkar, University of Miami, United States*
*Jukka Putaala, Helsinki University Central Hospital, Finland*

***Correspondence:**
*Marieke J. H. Wermer*
*m.j.h.wermer@lumc.nl*

**Specialty section:**
*This article was submitted to Neuropharmacology, a section of the journal Frontiers in Neuroscience*

**Received:** *13 July 2021*
**Accepted:** *28 September 2021*
**Published:** *03 November 2021*

**Citation:**
*Linstra KM, van Os HJA, Ruigrok YM, Nederkoorn PJ, van Dijk EJ, Kappelle LJ, Koudstaal PJ, Visser MC, Ferrari MD, MaassenVanDenBrink A, Terwindt GM and Wermer MJH (2021) Sex Differences in Risk Profile, Stroke Cause and Outcome in Ischemic Stroke Patients With and Without Migraine. Front. Neurosci. 15:740639. doi: 10.3389/fnins.2021.740639*

**Background:** An increased risk of stroke in patients with migraine has been primarily found for women. The sex-dependent mechanisms underlying the migraine–stroke association, however, remain unknown. This study aims to explore these sex differences to improve our understanding of pathophysiological mechanisms behind the migraine–stroke association.

**Methods:** We included 2,492 patients with ischemic stroke from the prospective multicenter Dutch Parelsnoer Institute Initiative study, 425 (17%) of whom had a history of migraine. Cardiovascular risk profile, stroke cause (TOAST classification), and outcome [modified Rankin scale (mRS) at 3 months] were compared with both sexes between patients with and without migraine.

**Results:** A history of migraine was not associated with sex differences in the prevalence of conventional cardiovascular risk factors. Women with migraine had an increased risk of stroke at young age (onset $<$ 50 years) compared with women without migraine (RR: 1.7; 95% CI: 1.3–2.3). Men with migraine tended to have more often stroke in the TOAST category other determined etiology (RR: 1.7; 95% CI: 1.0–2.7) in comparison with men without migraine, whereas this increase was not found in women with migraine. Stroke outcome was similar for women with or without migraine (mRS $\geq$ 3 RR 1.1; 95% CI 0.7–1.5), whereas men seemed to have a higher risk of poor outcome compared with their counterparts without migraine (mRS $\geq$ 3 RR: 1.5; 95% CI: 1.0–2.1).

**Conclusion:** Our results indicate possible sex differences in the pathophysiology underlying the migraine–stroke association, which are unrelated to conventional cardiovascular risk factors. Further research in larger cohorts is needed to validate these findings.

**Keywords: sex differences, migraine, stroke outcome, stroke subtype, cardiovascular risk factors**

## INTRODUCTION

Migraine is a prevalent brain disorder and important risk factor for cardiovascular disease (CVD), including stroke. The increased risk is especially evident in women and less clear in men (Schurks et al., 2009). In addition, sex differences in ischemic stroke are increasingly acknowledged. Women more often suffer from ischemic stroke compared with men, especially after menopause, and have an increased risk of poor outcome (Gall et al., 2012; Bushnell et al., 2014). Although it has been recognized that cardiovascular pathophysiology is partly different between women and men, the role of sex in the migraine–stroke association remains poorly understood (Reeves et al., 2008; Schurks et al., 2009; Haast et al., 2012). Missing gaps in the association are the role of conventional and non-conventional vascular risk factors, the relation with underlying stroke cause, and the effect of migraine susceptibility on brain tissue recovery after ischemia. Until now, it is unknown how sex affects these factors.

This explorative study aims to investigate differences in cardiovascular risk profiles, stroke cause, and stroke outcome between men and women to improve our understanding of pathophysiological mechanisms underlying the migraine–stroke association.

## MATERIALS AND METHODS

We selected patients with ischemic stroke for whom information on a history of migraine was available from the prospective registry and biobank "Dutch Parelsnoer Institute Cerebrovascular Accident (PSI-CVA) Initiative" in eight university hospitals in the Netherlands (Nederkoorn et al., 2015). The PSI-CVA registry is a large cohort of stroke patients in which comprehensive clinical data, detailed phenotyping of stroke, imaging data, and biomaterials were prospectively and uniformly collected. The registry started in 2009 and ended in 2019. The Ethics Committees of all participating centers approved the PSI-CVA Initiative.

Data on cardiovascular risk profile (conventional risk factors including smoking, diabetes mellitus, hyperlipidemia, previous stroke, myocardial infarction, atrial fibrillation, BMI $\geq$ 25, and hypertension) and stroke classification were obtained prospectively upon hospital admission. Ischemic stroke was defined according to the WHO criteria and confirmed on CT or MRI and further specified according to the trial of ORG 10172 in acute stroke treatment (TOAST) classification in the subcategories large-artery atherosclerosis, cardioembolism, small-vessel occlusion, stroke of other determined etiology, and stroke of undetermined etiology (Adams et al., 1993). The modified Rankin Scale (mRS) was used to grade stroke outcome. A poor outcome was defined as mRS at 3 months after discharge $\geq$ 3.

Migraine history was prospectively obtained at hospital admission using a short, validated questionnaire that was specially developed to establish migraine diagnosis in patients with stroke (MISS questionnaire, see **Supplementary Material**; van der Willik et al., 2016).

We performed a complete case analysis with respect to migraine status. Poisson regression analysis was performed to calculate risk ratios (RR) including 95% confidence intervals (CI) for the associations between age of stroke onset, cardiovascular risk factors, stroke subtype and outcome, and migraine diagnosis, for all patients and for each sex separately. The analyses were adjusted for potential confounders.

## RESULTS

In total 6,259 participants were included in the PSI-CVA database, of whom 4,273 had ischemic stroke and 2,492 (40% women) also with information on migraine status. A lifetime history of migraine was present in 425/2,492 (17% overall, 10% in men, and 27% in women) of the participants. Age, sex, and cardiovascular risk profile were similar between patients with or without available information about migraine status.

There were no differences in cardiovascular risk factor profile in stroke patients with vs. without migraine overall or between sexes (**Table 1**).

Women with migraine had their stroke on average 7 years ($p < 0.0001$) and men 5 years earlier than stroke patients without migraine ($p < 0.0001$). Stroke onset < 50 years occurred more often in women with than in women without migraine (RR: 1.7; 95% CI: 1.3–2.3, **Table 1** and **Figure 1**). This increased risk could not be confirmed in men (RR: 1.4; 95% CI: 0.9–2.1).

Men with migraine tended to have a higher risk for stroke of other determined etiology compared with men without migraine (RR: 1.7; 95% CI: 1.0–2.7), whereas no differences in this TOAST category were found in women (RR: 0.9; 95% CI: 0.6–1.4, **Table 2** and **Figure 1**). Other stroke subtypes were comparable with men and women with and without migraine, although the effect estimate had an opposite direction for the category small vessel occlusion.

Outcome after stroke seemed to be comparable with women regardless of migraine diagnosis (RR: 1.1; 95% CI: 0.7–1.5), whereas men tended to have a worse outcome compared with their counterparts without migraine (RR: 1.5; 95% CI: 1.0–2.1, **Table 3** and **Figure 1**).

## DISCUSSION

Our explorative study suggests that sex differences in stroke pathophysiology in patients with migraine cannot be explained by differences in conventional vascular risk factors. Women with migraine had a higher risk for stroke under the age of 50. Men tended to more often have stroke of other determined etiology and a worse outcome compared with men without migraine.

Evidence in the literature about the relationship between conventional vascular risk factors and migraine is conflicting, and rarely, data of men and women are analyzed separately (Sacco et al., 2015). In general, the association between migraine and

**TABLE 1 |** Demographics and cardiovascular risk factors.

| | All | | | | Women | | | | Men | | | |
|---|---|---|---|---|---|---|---|---|---|---|---|---|
| | **Migraine** | **No migraine** | **RR** | **aRR[a]** | **Migraine** | **No migraine** | **RR** | **aRR[b]** | **Migraine** | **No migraine** | **RR** | **aRR[b]** |
| **Demographics** | | | | | | | | | | | | |
| Number | 425 (1) | 2,067 (83) | – | – | 264 (62) | 730 (35) | – | – | 161 (38) | 1,337 (65) | – | – |
| Age, years | 61 ± 15 | 67 ± 14* | – | – | 61 ± 17 | 68 ± 15* | – | – | 61 ± 13 | 66 ± 14* | – | – |
| Age of onset < 50 | 93 (22) | 266 (13) | 1.7 (1.3–2.1) | – | 65 (25) | 105 (14) | 1.7 (1.3–2.3) | – | 28 (17) | 161 (12) | 1.4 (0.9–2.1) | – |
| Age of onset ≥ 50 | 332 (78) | 1,801 (87) | 0.8 (0.8–0.9) | – | 199 (75) | 625 (86) | 0.9 (0.7–1.0) | – | 133 (83) | 1,176 (88) | 0.9 (0.8–1.1) | – |
| Pre-stroke mRS | 29 (7) | 164 (9) | 0.8 (0.5–1.2) | 0.9 (0.6–1.3) | 21 (8) | 82 (12) | 0.7 (0.4–1.1) | 0.8 (0.5–1.3) | 8 (5) | 82 (7) | 0.8 (0.4–1.5) | 0.9 (0.4–1.8) |
| **CV risk factors** | | | | | | | | | | | | |
| Hypertension[c] | 226 (54) | 1,115 (54) | 1.0 (0.9–1.1) | 1.1 (1.0–1.3) | 138 (53) | 412 (57) | 0.9 (0.8–1.1) | 1.1 (0.9–1.3) | 88 (55) | 703 (53) | 1.0 (0.8–1.3) | 1.1 (0.9–1.4) |
| DM[d] | 58 (14) | 304 (15) | 0.9 (0.7–1.2) | 1.1 (0.8–1.4) | 35 (13) | 113 (16) | 0.9 (0.6–1.2) | 1.0 (0.7–1.5) | 23 (14) | 191 (14) | 1.0 (0.6–1.5) | 1.1 (0.7–1.7) |
| Hyperlipidemia[e] | 145 (35) | 752 (37) | 0.9 (0.8–1.1) | 1.1 (0.9–1.3) | 89 (34) | 240 (34) | 1.0 (0.8–1.3) | 1.2 (0.9–1.5) | 56 (35) | 512 (39) | 0.9 (0.7–1.2) | 1.0 (0.7–1.3) |
| Previous Stroke | 115 (28) | 515 (26) | 1.1 (0.9–1.3) | 1.2 (1.0–1.5) | 69 (27) | 169 (24) | 1.1 (0.9–1.5) | 1.3 (1.0–1.7) | 46 (29) | 346 (27) | 1.1 (0.8–1.5) | 1.2 (0.9–1.6) |
| History of MI | 34 (8) | 262 (13) | 0.6 (0.4–0.9) | 0.9 (0.6–1.3) | 15 (6) | 57 (8) | 0.7 (0.4–1.3) | 0.9 (0.5–1.6) | 19 (12) | 205 (16) | 0.8 (0.5–1.2) | 1.0 (0.6–1.5) |
| Atrial fibrillation | 42 (10) | 259 (13) | 0.8 (0.6–1.1) | 1.1 (0.8–1.6) | 22 (9) | 81 (11) | 0.8 (0.5–1.2) | 1.0 (0.6–1.7) | 20 (13) | 178 (14) | 0.9 (0.6–1.5) | 1.2 (0.8–2.0) |
| Smoking ever[f] | 25 (6) | 186 (9) | 0.7 (0.4–1.0) | 0.8 (0.5–1.2) | 15 (6) | 50 (7) | 0.8 (0.5–1.4) | 0.9 (0.5–1.7) | 10 (6) | 136 (10) | 0.6 (0.3–1.1) | 0.7 (0.3–1.3) |
| BMI ≥ 25 | 258 (62) | 1,267 (64) | 1.0 (0.8–1.1) | 1.1 (0.9–1.2) | 147 (57) | 349 (51) | 1.1 (0.9–1.4) | 1.1 (0.9–1.3) | 111 (69) | 918 (71) | 1.0 (0.8–1.2) | 1.0 (0.8–1.2) |

*mRS, modified Rankin Scale; CV, cardiovascular; DM, diabetes mellitus; MI, myocardial infarction; BMI, body mass index (kg/m$^2$).*
*Data are represented as mean ± SD or number of subjects (%).*
**Migraine vs. no migraine: $p < 0.001$.*
*[a]Adjusted for age and sex.*
*[b]Adjusted for age.*
*[c]Ever or current diagnosis or treatment with antihypertensive drugs.*
*[d]Ever or current diagnosis or treatment with antidiabetic drugs.*
*[e]Total cholesterol > 3.5 mmol/L, low-density lipoprotein cholesterol > 2.5 mmol/L or treatment with lipid-lowering agents.*
*[f]Current smokers and smokers who stopped smoking > 6 months ago.*

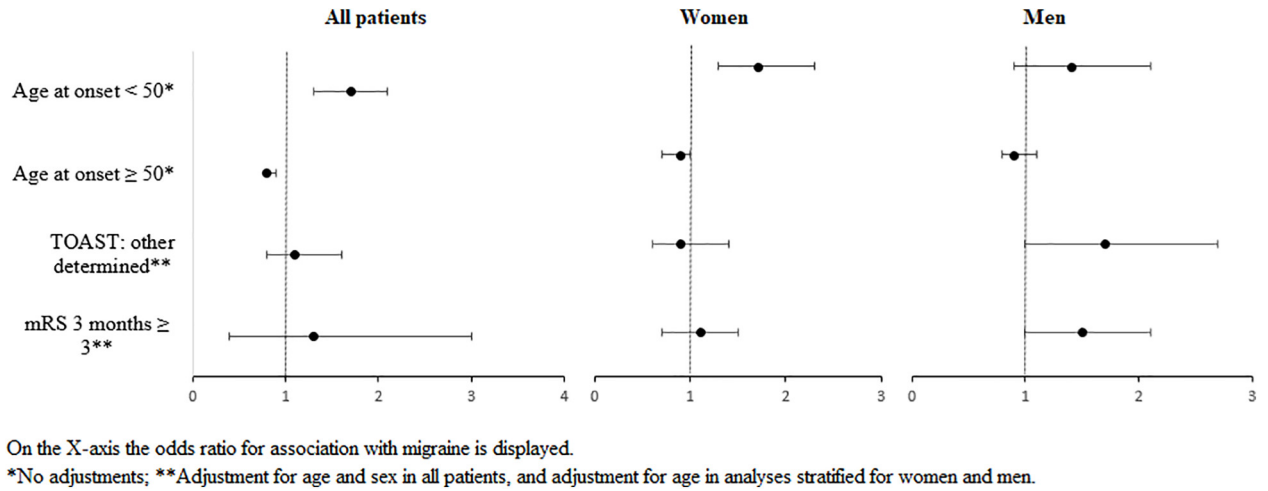


**FIGURE 1 |** Forest plot of the most important findings on associations between migraine and risk factors, etiology, or outcome of stroke, stratified for sex.

stroke is thought to be more prominent in patients without a traditional vascular risk profile and with a lower Framingham Risk Score (Li et al., 2015; Sacco et al., 2015). Only little is known about the association between migraine and sex-specific cardiovascular risk factors. Unfortunately, our PSI-CVA database did not contain all factors needed to construct Framingham Risk score. Also, our database did not include non-conventional sex-dependent vascular risk factors such as (pre)-eclampsia, sex hormone disorders, or use of hormones. Future studies are therefore needed to investigate the effect of these non-conventional risk factors. A younger age at stroke onset in patients with migraine in general, has been reported previously (Schurks et al., 2009; Li et al., 2015).

Previous studies on stroke etiology reported lower frequencies of large vessel and cardio-embolic stroke etiology in female migraine patients and more infarcts of unknown origin in migraine patients in general (Rist et al., 2010; Li et al., 2015). In a recent study, migraine with aura was strongly associated with cryptogenic stroke, whereas such association was not found in migraine without aura (Martinez-Majander et al., 2021). The association of migraine with aura with stroke was independent of vascular risk factors or patent foramen ovale. The association was present in both women and men, although the odds ratios were higher in women. We observed an increase in stroke of other determined etiology only in men with migraine (with and without aura combined). Sex differences in migraine pathophysiology are likely multifactorial and may reflect genetic and hormonal sex differences. In addition, migraine is associated with cerebral hyperexcitability and spreading depolarization (SD), the neurophysiological correlate of migraine aura. SD is associated with neurovascular uncoupling and can also be found in the penumbra of cerebral ischemia (Ferrari et al., 2015). These mechanisms may be associated with a sex-specific systemic vascular pathology in migraine patients (Sacco et al., 2015). Since the increased stroke risk in migraine patients is not associated with enhanced atherosclerosis, alternative pathology, including micro-embolisms, vasospasms in the microvasculature and endothelial dysfunction, may be involved (Tietjen, 2009; Stam et al., 2013; Ferrari et al., 2015; van Os et al., 2017). These "non-conventional" mechanisms may explain the higher proportion of other determined causes in men with migraine. We have no good explanation why the higher risk was only found in men and not in women with migraine.

Existing literature on functional stroke outcome in patients with migraine is limited to the Women's Health Study, which only included female health care employees and reported a relatively favorable mRS at hospital discharge after ischemic stroke for women with migraine with aura (Sacco et al., 2015). In general, female sex has been associated with a less favorable stroke outcome in terms of disability and mortality (Reeves et al., 2008; Haast et al., 2012). Our study found no differences in outcome between women with and without migraine but did not investigate women with migraine aura separately. In men with migraine, our data cautiously suggested a worse outcome compared with their counterparts without migraine. As these are the first data on stroke outcome in men specifically, further research is needed to confirm these findings and investigate underlying causes.

Strengths of our study are the relatively large sample size, prospective design, and the use of standardized definitions of cardiovascular risk factor and stroke characteristics. Also, we compared men and women with stroke directly with their counterparts without migraine. Migraine diagnosis was established with a validated questionnaire, and migraine prevalence was as expected for this population. Our study also has limitations. First, the MISS questionnaire has only moderate positive predictive value for aura symptoms. Therefore, we did not distinguish between migraine with and without aura, although the migraine–stroke connection is particularly apparent

**TABLE 2 |** Stroke subtype according to TOAST classification.

| | All | | | | Women | | | | Men | | | |
|---|---|---|---|---|---|---|---|---|---|---|---|---|
| | **Migraine** | **No migraine** | **RR** | **RR[a]** | **Migraine** | **No migraine** | **RR** | **RR[b]** | **Migraine** | **No migraine** | **RR** | **RR[b]** |
| LAA | 84 (20) | 530 (26) | 0.8 (0.6–1.0) | 0.9 (0.7–1.2) | 45 (17) | 147 (21) | 0.8 (0.6–1.2) | 0.9 (0.7–1.3) | 39 (24) | 383 (29) | 0.8 (0.6–1.1) | 0.9 (0.7–1.3) |
| Cardioembolism | 50 (12) | 296 (15) | 0.8 (0.6–1.1) | 0.9 (0.7–1.2) | 32 (12) | 102 (14) | 0.7 (0.6–1.3) | 1.0 (0.7–1.5) | 18 (11) | 194 (15) | 0.8 (0.5–1.2) | 0.8 (0.5–1.3) |
| SVO | 72 (17) | 373 (18) | 0.9 (0.7–1.2) | 0.9 (0.7–1.2) | 43 (17) | 158 (22) | 0.8 (0.5–1.0) | 0.8 (0.6–1.1) | 29 (18) | 215 (16) | 1.1 (0.7–1.6) | 1.1 (0.7–1.6) |
| Other determined | 47 (11) | 137 (7) | 1.7 (1.2–2.3) | 1.1 (0.8–1.6) | 27 (10) | 59 (8) | 1.3 (0.8–2.0) | 0.9 (0.6–1.4) | 20 (12) | 78 (6) | 2.1 (1.3–3.4) | 1.7 (1.0–2.7) |
| Undetermined | 167 (40) | 692 (34) | 1.2 (1.0–1.4) | 1.1 (0.9–1.3) | 113 (43) | 250 (35) | 1.2 (1.0–1.6) | 1.2 (0.9–1.5) | 54 (34) | 442 (34) | 1.0 (0.8–1.3) | 1.0 (0.7–1.3) |

*TOAST, Trial of ORG 10172 in acute stroke treatment; LAA, large-artery atherosclerosis; SVO, small-vessel occlusion.*
*Data are represented as mean ± SD or number of subjects (%).*
*[a]Adjusted for age and sex.*
*[b]Adjusted for age.*

**TABLE 3 |** Stroke severity and outcome.

| | All | | | | Women | | | | Men | | | |
|---|---|---|---|---|---|---|---|---|---|---|---|---|
| | **Migraine** | **No migraine** | **RR** | **RR[a]** | **Migraine** | **No migraine** | **RR** | **RR[b]** | **Migraine** | **No Migraine** | **RR** | **RR[b]** |
| NIHSS ≥ 7[C] | 67 (17) | 340 (18) | 0.9 (0.7–1.2) | 0.9 (0.7–1.2) | 36 (15) | 131 (20) | 0.7 (0.5–1.1) | 0.8 (0.5–1.1) | 31 (21) | 209 (17) | 1.2 (0.8–1.1) | 1.2 (0.8–1.8) |
| mRS discharge ≥ 3 | 102 (30) | 238 (32) | 1.0 (0.8–1.2) | 1.1 (0.9–1.4) | 59 (28) | 184 (32) | 0.9 (0.7–1.2) | 1.2 (0.8–1.6) | 43 (33) | 307 (32) | 1.1 (0.8–1.4) | 1.2 (0.8–1.6) |
| mRS 3 months ≥ 3 | 73 (20) | 368 (20) | 1.0 (0.7–1.2) | 1.3 (0.9–1.7) | 41 (18) | 142 (22) | 0.8 (0.6–1.1) | 1.1 (0.7–1.5) | 32 (23) | 226 (19) | 1.2 (0.8–1.7) | 1.5 (1.0–2.1) |

*NIHSS, National Institute of Health Stroke Scale; mRS, modified Rankin Scale.*
*Data are represented as mean ± SD or number of subjects (%).*
*[a]Adjusted for pre-stroke mRS, NIHSS at admission (for mRS at discharge and at 3 months), age, and sex.*
*[b]Adjusted for pre-stroke mRS, NIHSS at admission (for mRS at discharge and at 3 months) and age.*
*[c]NIHSS on admission.*

in migraine with aura. Second, from 4,273 participants with ischemic stroke in our cohort, only 2,492 had complete data on migraine. Not all PSI-CVA study centers participated in our migraine study. We consider this selection to be random and assume that it did not result in selection bias. Third, we did not correct for multiple comparisons. Finally, although our study included almost 2,500 stroke patients, the sample size in several sub-analyses was low, and therefore, our study should be considered explorative and hypothesis generating. To confirm our findings and to study sex differences in migraine with aura patients separately, studies with far, with over 10 thousands of stroke patients will be necessary (because of the relative low prevalence of migraine with aura). Future studies are also needed to study sex-specific non-conventional cardiovascular risk factors and investigate stroke causes in more detail to enable sex-specific prevention of strokes in patients with migraine.

## DATA AVAILABILITY STATEMENT

The datasets presented in this article are not readily available because anonymized data may be requested for the sole purpose of replicating procedures and results presented in the article and only after agreement of the Dutch Parelsnoer Institute Cerebrovascular Accident (PSI-CVA) Initiative committee. Requests to access the datasets should be directed to corresponding author.

## ETHICS STATEMENT

The studies involving human participants were reviewed and approved by the ethics committees of all participating medical centres. The patients/participants provided their written informed consent to participate in this study.

## AUTHOR CONTRIBUTIONS

MW, KL, HO, AM, and GT contributed to conception and design of the study. YR, MW, and KL organized the database extraction. KL and HO performed the statistical analysis. KL wrote the first draft of the manuscript. MW, HO, MF, MV, LK, PK, AM, and GT wrote sections of the manuscript. All authors contributed to manuscript revision, read, and approved the submitted version.

## FUNDING

This work was supported by a grant of the Dutch Hearth Foundation (grant no. 2013T083) (KL, MW, AM, and GT).

## SUPPLEMENTARY MATERIAL

The Supplementary Material for this article can be found online at: https://www.frontiersin.org/articles/10.3389/fnins.2021.740639/full#supplementary-material

## REFERENCES

Adams, H. P. Jr., Bendixen, B. H., Kappelle, L. J., Biller, J., Love, B. B., Gordon, D. L., et al. (1993). Classification of subtype of acute ischemic stroke. Definitions for use in a multicenter clinical trial. Toast. Trial of org 10172 in acute stroke treatment. *Stroke* 24, 35–41. doi: 10.1161/01.STR.24.1.35

Bushnell, C., McCullough, L. D., Awad, I. A., Chireau, M. V., Fedder, W. N., Furie, K. L., et al. (2014). Guidelines for the prevention of stroke in women: a statement for healthcare professionals from the american heart association/american stroke association. *Stroke* 45, 1545–1588. doi: 10.1161/01.str.0000442009.06663.48

Ferrari, M. D., Klever, R. R., Terwindt, G. M., Ayata, C., and van den Maagdenberg, A. M. (2015). Migraine pathophysiology: lessons from mouse models and human genetics. *Lancet Neurol.* 14, 65–80. doi: 10.1016/S1474-4422(14)70220-0

Gall, S. L., Tran, P. L., Martin, K., Blizzard, L., and Srikanth, V. (2012). Sex differences in long-term outcomes after stroke: functional outcomes, handicap, and quality of life. *Stroke* 43, 1982–1987. doi: 10.1161/STROKEAHA.111.632547

Haast, R. A., Gustafson, D. R., and Kiliaan, A. J. (2012). Sex differences in stroke. *J. Cereb. Blood Flow Metab.* 32, 2100–2107. doi: 10.1038/jcbfm.2012.141

Li, L., Schulz, U. G., Kuker, W., Rothwell, P. M., and Oxford Vascular, S. (2015). Age-specific association of migraine with cryptogenic tia and stroke: population-based study. *Neurology* 85, 1444–1451. doi: 10.1212/WNL.0000000000002059

Martinez-Majander, N. A. V., Ylikotila, P., von Sarnowski, B., Waje-Andreassen, U., Yesilot, N., et al. (2021). Association between migraine and cryptogenic ischemic stroke in young adults. *Ann. Neurol.* 89, 242–253. doi: 10.1002/ANA.25937

Nederkoorn, P. J., van Dijk, E. J., Koudstaal, P. J., Luijckx, G. J., van Oostenbrugge, R. J., Visser, M. C., et al. (2015). The dutch string-of-pearls stroke study: protocol of a large prospective multicenter genetic cohort study. *Int. J. Stroke* 10, 120–122. doi: 10.1111/ijs.12359

Reeves, M. J., Bushnell, C. D., Howard, G., Gargano, J. W., Duncan, P. W., Lynch, G., et al. (2008). Sex differences in stroke: epidemiology, clinical presentation, medical care, and outcomes. *Lancet Neurol.* 7, 915–926. doi: 10.1016/S1474-4422(08)70193-5

Rist, P. M., Buring, J. E., Kase, C. S., Schurks, M., and Kurth, T. (2010). Migraine and functional outcome from ischemic cerebral events in women. *Circulation* 122, 2551–2557. doi: 10.1161/CIRCULATIONAHA.110.977306

Sacco, S., Pistoia, F., Degan, D., and Carolei, A. (2015). Conventional vascular risk factors: their role in the association between migraine and cardiovascular diseases. *Cephalalgia* 35, 146–164. doi: 10.1177/0333102414559551

Schurks, M., Rist, P. M., Bigal, M. E., Buring, J. E., Lipton, R. B., and Kurth, T. (2009). Migraine and cardiovascular disease: systematic review and meta-analysis. *BMJ* 339, b3914. doi: 10.1136/bmj.b3914

Stam, A. H., Weller, C. M., Janssens, A. C., Aulchenko, Y. S., Oostra, B. A., Frants, R. R., et al. (2013). Migraine is not associated with enhanced atherosclerosis. *Cephalalgia* 33, 228–235. doi: 10.1177/0333102412466966

Tietjen, G. E. (2009). Migraine as a systemic vasculopathy. *Cephalalgia* 29, 987–996. doi: 10.1111/j.1468-2982.2009.01937.x

van der Willik, D., Pelzer, N., Algra, A., Terwindt, G. M., and Wermer, M. J. (2016). Assessment of migraine history in patients with a transient ischemic attack or

stroke; validation of a migraine screener for stroke. *Eur. Neurol.* 77, 16–22. doi: 10.1159/000449425

van Os, H. J. A., Mulder, I. A., Broersen, A., Algra, A., van der Schaaf, I. C., Kappelle, L. J., et al. (2017). Migraine and cerebrovascular atherosclerosis in patients with ischemic stroke. *Stroke* 48, 1973–1975. doi: 10.1161/STROKEAHA.116.016133

**Conflict of Interest:** The authors declare that the research was conducted in the absence of any commercial or financial relationships that could be construed as a potential conflict of interest.

**Publisher's Note:** All claims expressed in this article are solely those of the authors and do not necessarily represent those of their affiliated organizations, or those of the publisher, the editors and the reviewers. Any product that may be evaluated in this article, or claim that may be made by its manufacturer, is not guaranteed or endorsed by the publisher.

frontiers in Cellular Neuroscience

SYSTEMATIC REVIEW
published: 11 November 2021
doi: 10.3389/fncel.2021.711604

# Sex Differences in Hemostatic Factors in Patients With Ischemic Stroke and the Relation With Migraine—A Systematic Review

*Nelleke van der Weerd[1,2]*, Hine J. A. van Os[1], Mariam Ali[3], Jan W. Schoones[4], Arn M. J. M. van den Maagdenberg[1,2], Nyika D. Kruyt[1,5], Bob Siegerink[6] and Marieke J. H. Wermer[1,5]*

[1] Department of Neurology, Leiden University Medical Centre, Leiden, Netherlands, [2] Department of Human Genetics, Leiden University Medical Centre, Leiden, Netherlands, [3] Department of Neurology, Amsterdam University Medical Centre, Vrije Universiteit Amsterdam, Amsterdam, Netherlands, [4] Directorate of Research Policy, Leiden University Medical Centre, Leiden, Netherlands, [5] Department of Neurology, University Neurovascular Centre, The Hague, Netherlands, [6] Department of Clinical Epidemiology, Leiden University Medical Centre, Leiden, Netherlands

**Background:** Women are more affected by stroke than men. This might, in part, be explained by sex differences in stroke pathophysiology. The hemostasis system is influenced by sex hormones and associated with female risk factors for stroke, such as migraine.

**Aim:** To systematically review possible sex differences in hemostatic related factors in patients with ischemic stroke in general, and the influence of migraine on these factors in women with ischemic stroke.

**Results:** We included 24 studies with data on sex differences of hemostatic factors in 7247 patients with ischemic stroke (mean age 57–72 years, 27–57% women) and 25 hemostatic related factors. Levels of several factors were higher in women compared with men; FVII:C (116% ± 30% vs. 104% ± 30%), FXI (0.14 UI/mL higher in women), PAI-1 (125.35 ± 49.37 vs. 96.67 ± 38.90 ng/mL), D-dimer (1.25 ± 0.31 vs. 0.95 ± 0.24 μg/mL), and aPS (18.7% vs. 12.0% positive). In contrast, protein-S (86.2% ± 23.0% vs. 104.7% ± 19.8% antigen) and P-selectin (48.9 ± 14.4 vs. 79.1 ± 66.7 pg/mL) were higher in men. Most factors were investigated in single studies, at different time points after stroke, and in different stroke subtypes. Only one small study reported data on migraine and hemostatic factors in women with ischemic stroke. No differences in fibrinogen, D-dimer, t-PA, and PAI-1 levels were found between women with and without migraine.

**Conclusion:** Our systematic review suggests that sex differences exist in the activation of the hemostatic system in ischemic stroke. Women seem to lean more toward increased levels of procoagulant factors whereas men exhibit increased levels of coagulation inhibitors. To obtain better insight in sex-related differences in hemostatic factors, additional studies are needed to confirm these findings with special attention for different stroke phases, stroke subtypes, and not in the least women specific risk factors, such as migraine.

**Keywords: male, female, risk factor, migraine, coagulation, plasma, serum**

OPEN ACCESS

***Edited by:***
*Michael Fleischer, Essen University Hospital, Germany*

***Reviewed by:***
*Dennis Qing Wang, Southern Medical University, China*
*Gretchen E. Tietjen, University of Toledo, United States*

****Correspondence:***
*Nelleke van der Weerd*
*n.van_der_weerd@lumc.nl*

***Specialty section:***
*This article was submitted to Cellular Neuropathology, a section of the journal Frontiers in Cellular Neuroscience*

***Received:*** *18 May 2021*
***Accepted:*** *13 October 2021*
***Published:*** *11 November 2021*

***Citation:***
*van der Weerd N, van Os HJA, Ali M, Schoones JW, van den Maagdenberg AMJM, Kruyt ND, Siegerink B and Wermer MJH (2021) Sex Differences in Hemostatic Factors in Patients With Ischemic Stroke and the Relation With Migraine—A Systematic Review. Front. Cell. Neurosci. 15:711604. doi: 10.3389/fncel.2021.711604*

## INTRODUCTION

Stroke is the third most disabling disease worldwide. Women are particularly affected because of a higher stroke incidence and a worse outcome compared with men (Girijala et al., 2017). Evidence accumulates that these differences might, in part, be explained by sex-specific pathophysiological mechanisms underlying stroke (Demel et al., 2018).

Multiple mechanisms and pathways are involved in the pathophysiology of stroke. More precise atherosclerosis, oxidative stress, endothelial and mitochondrial dysfunction, inflammation, complement activation, and hemostatic factors are associated with ischemic stroke (Periayah et al., 2017; Liu et al., 2018; Ma et al., 2019; Shao et al., 2020).

In addition to traditional vascular risk factors, women have specific stroke risk factors, such as the presence of reproductive disorders, the use of oral contraceptives, and the co-occurrence of migraine with aura. Especially the comorbidity between ischemic stroke and cardiovascular disease with migraine is recognized already for decades (Kurth et al., 2012; Sacco et al., 2017; Adelborg et al., 2018; Demel et al., 2018). Both men and women with migraine with aura have an approximately twofold increased risk of ischemic stroke (Adelborg et al., 2018). However, the point estimates of the association between migraine and stroke seem to be higher in women and the risk is further increased to sevenfold in women who use oral contraceptives (Etminan et al., 2005; Schürks et al., 2009) and even ninefold when they are also smoking (Schürks et al., 2009). A vascular mechanistic link between migraine and ischemic stroke has been proposed, linking the increased risk and underlying disease mechanisms (Kurth et al., 2012). A possible link between hemostatic factors for migraine and ischemic stroke has previously been shown in genetic studies. For instance, prothrombotic genotypes factor V Leiden and prothrombin G20210A were more frequently present in young patients with ischemic stroke and a history of migraine with aura compared with young patients with migraine without aura or no history of migraine (Pezzini et al., 2011). Furthermore, in a mendelian randomization study, genetically determined increased levels of hemostatic factors FVIII, von Willebrand factor (vWF), phosphorylated fibrinopeptide A, and a decrease of fibrinogen seemed causally related to susceptibility for migraine, especially migraine with aura (Guo Y. et al., 2021).

Sex differences in hemostatic factors, alone or in combination with female risk factors, could increase the risk of ischemic stroke in women (Siegerink et al., 2010; Sacco et al., 2017). The hemostatic system can be divided into primary hemostasis (platelet activation and aggregation), secondary hemostasis (coagulation cascade), and the fibrinolytic pathway. A systematic review suggested that some factors of the hemostatic system, for example vWF, FXI, prothrombin fragment 1 + 2 (F1.2), D-dimer, plasminogen activator inhibitor 1 (PAI-1) and anti-phosphatidyl serine antibodies (aPS), are related to poor clinical outcome after ischemic stroke. However, it is yet unclear whether these factors could be used as predictors for stroke outcome (Donkel et al., 2019). Also it is unknown whether they have additional value above other known prognostic factors in stroke (Deng et al., 2018; Li et al., 2019, 2020; Chang et al., 2021; Chen et al., 2021; Montellano et al., 2021). Female sex hormones can influence hemostatic factors causing the hemostasis system to function differently for men and women (Abou-Ismail et al., 2020). Sex differences in levels of hemostatic factors could therefore be a missing link in understanding sex differences in ischemic stroke risk and outcome.

Many hemostatic factors have previously been reviewed in relation to ischemic stroke, but sex differences have not yet been systemically evaluated (Periayah et al., 2017). We aimed to review possible sex differences of the hemostatic system, and the influence of migraine, by performing a systematic search on sex differences in plasma and/or serum levels of hemostatic related factors in ischemic stroke, and hemostatic related factors in women with ischemic stroke and migraine.

## METHODS

This systematic review was performed conform the Preferred Reporting Items for Systematic Reviews and Meta-analysis (PRISMA) guidelines (Shamseer et al., 2015).

### Information Sources and Search Strategy

In cooperation with a trained librarian (JS), we composed two search strategies. The primary query consisted of the combination of three subjects: (1) stroke, (2) coagulation, platelet activation, hemostasis, primary hemostatic factors, and secondary hemostatic factors, and (3) sex differences. In the second query, we added to the subjects: (1) stroke, (2) coagulation platelet activation, hemostasis, primary hemostatic factors, and secondary hemostatic factors, the subject (3) migraine and changed sex differences to the subject (4) women, as migraine is a risk factor for stroke in women specifically. For the different concepts, all relevant keyword variations were used, not only keyword variations in the controlled vocabularies of the various databases, but the free text word variations of these concepts as well. The search strategy was optimized for all consulted databases, taking into account the differences of the various controlled vocabularies as well as the differences of database-specific technical variations (e.g., the use of quotation marks). Both searches were performed on January 2nd 2020 in the following databases: Pubmed, Embase (OVID-version), Emcare (OVID-version), Web of Science, and the Cochrane Library. Full details of the search strategies can be found in **Supplementary Appendix 1**.

### Eligibility Criteria

We included studies with ischemic stroke patients aged ≥18 years. For the first query on sex differences, single-sex studies were excluded. For both queries studies with specific criteria for patient selection (other than age ≥18 years) were excluded. Studies types included were: (1) study cohort, (2) case-control study, (3) cross-sectional study, (4) nested case-control study, and (5) clinical trials. Studies excluded were: (1) case reports, (2) case series, (3) reviews, and (4) meta-analyses. Included studies had to report on plasma and/or serum levels of

hemostatic factors. When multiple publications on one cohort were found, they were all included when the studies investigated different factors. Otherwise the most recent one was included. Articles had to be written in English or Dutch.

## Study Selection

Two independent reviewers (NW and MA) first screened publications on title and abstract, followed by a second screening on full text. Disagreements were discussed in a consensus meeting with a third reviewer (HO). Titles and abstracts were screened based on: (1) population criteria, and (2) outcome (plasma levels in concentration and antiphospholipids as positive or negative). Population for query on sex differences screened for inclusion of both men and women, ≥18 years old, with ischemic stroke, query on stroke and migraine screened for inclusion of women, >18 years old, with ischemic stroke and migraine. Selection for full-text screening was based on: (1) results reported for men and women separately, and (2) ischemic stroke diagnosis confirmed by clinical and neuro-imaging (CT or MRI) assessments.

## Data Extraction

We collected the following baseline information from the selected papers: number of patients (per sex), age, risk factors (smoking, diabetes mellitus, hypertension, and BMI), ischemic stroke etiology, and timing of blood draw after stroke. In addition, concentrations of serum and/or plasma levels of hemostatic factors were collected. Factors were divided into primary hemostasis, secondary hemostasis, fibrinolytic pathway, and other factors. We defined the group "other factors" as a group of factors that influence hemostasis directly but are not hemostatic factors. Risk of bias was assessed using Grading of Recommendations Assessment, Development, and Evaluation (GRADE).

# RESULTS

## Study Characteristics Sex Differences in Hemostatic Factors

The first query on sex differences in ischemic stroke resulted in 1132 studies, of which 24 were included (**Figure 1**) with data on a total of 7217 patients. The number of patients per study ranged from 30 to 3342, with a median of 152. The proportion of women in all included studies ranged from 27 to 57%. Mean age ranged from 57 to 77 years across included studies. The characteristics of the included articles are summarized in **Supplementary Table 1**. Most often reported vascular risk factors in the articles were smoking, hypertension, diabetes mellitus, and BMI (**Supplementary Table 2**). Large differences in these risk factors were seen between the studies, except for BMI (between 24 and 26). Smoking ranging from 18 to 62%, hypertension ranging from 44 to 84%, and diabetes mellitus ranging from 13 to 60%.

A total of 25 different factors were reported: seven primary hemostatic factors, nine secondary hemostatic factors, four fibrinolytic pathway factors, and five other factors related to hemostasis. All primary and secondary hemostatic factors were investigated in only one study. Fibrinolytic pathway factors and other factors involved in hemostasis were investigated in multiple studies. A meta-analysis could not be performed due to the many single studies and large heterogeneity between the studies.

Risk of bias was assessed for each article (**Supplementary Table 3**). No risk of bias was found for selection of men and women as they were always selected from the same stroke population. For 23 of the 24 articles, study populations were included from a single center or region, therefore only partly representative for the whole ischemic stroke population. In most cases (20 of 24), the confidence in the assessment of outcome is high, with most studies specifically addressing the timing of blood sampling. However, in only 14 of 24 studies timing of blood sampling was similar for both men and women. Another concern was the assessment and adjustment for confounding, with most studies (19 of 24) adjusting for very few or no confounding factors at all.

## Sex Differences in Primary Hemostasis

Seven primary hemostatic related factors were reported in five articles, with a total of 1115 patients (**Table 1**). No sex differences were found for glutamate (Meng et al., 2014) and phospholipase A2 (PLA2) (Elkind et al., 2006) within 72h after stroke, thromboxane 2 (TXA2), prostaglandin I2 (PGI2), adenosine diphosphate (ADP) within 2 weeks after stroke (Lee et al., 1987), and vWF (Kain et al., 2001) 3 months after stroke. P-selectin plasma levels were lower in women than in men at day 1 (79.1 ± 66.7 vs. 48.9 ± 15.4 in pg/mL) but not on day 4 (113.6 ± 82.6 vs. 83.5 ± 46.4 in pg/mL) after stroke (Blum et al., 2012).

## Sex Differences in Secondary Hemostasis

Nine secondary hemostatic factors were reported in eight articles, with a total of 1031 patients (**Table 2**). No sex differences were found for antithrombin III (AT III) (Haapaniemi et al., 2002), thrombin-antithrombin (Haapaniemi et al., 2004), and protein C (Haapaniemi et al., 2002), at four time points, β-antithrombin within 2 days after stroke (de la Morena-Barrio et al., 2015), and FXIIa 3 months after stroke (Kain et al., 2001). Women had higher FVII:ag (114% ± 34% vs. 99% ± 31%) 3 months after stroke (Kain et al., 2001) and FXIc levels (1.13 ± 0.32; with difference of 0.14 UI/mL) 1 month after stroke (Santamaria et al., 2007) compared with men. Protein S antigen percentages were reported to be lower in women than men in the first 2 days (86.2% ± 23.0% vs. 104.7% ± 19.8%), 1 week (72.3% ± 34.2% vs. 87.8% ± 4.3%), 1 month (80.6% ± 32.8% vs. 85.5% ± 28.5%), and 3 months (73.5% ± 28.0% vs. 91.2% ± 31.1%) after stroke (Haapaniemi et al., 2002). Four studies (Carter et al., 1997; Kain et al., 2001; Skoloudik et al., 2010; Kisialiou et al., 2012) did not report sex differences for fibrinogen levels. One study found higher fibrinogen levels in women with cortical infarcts of the anterior circulation [4.90 g/L (95% CI 4.48–5.32)] than in women with lacunar infarcts (4.04 g/L [95% CI 3.73–4.37)] in the first

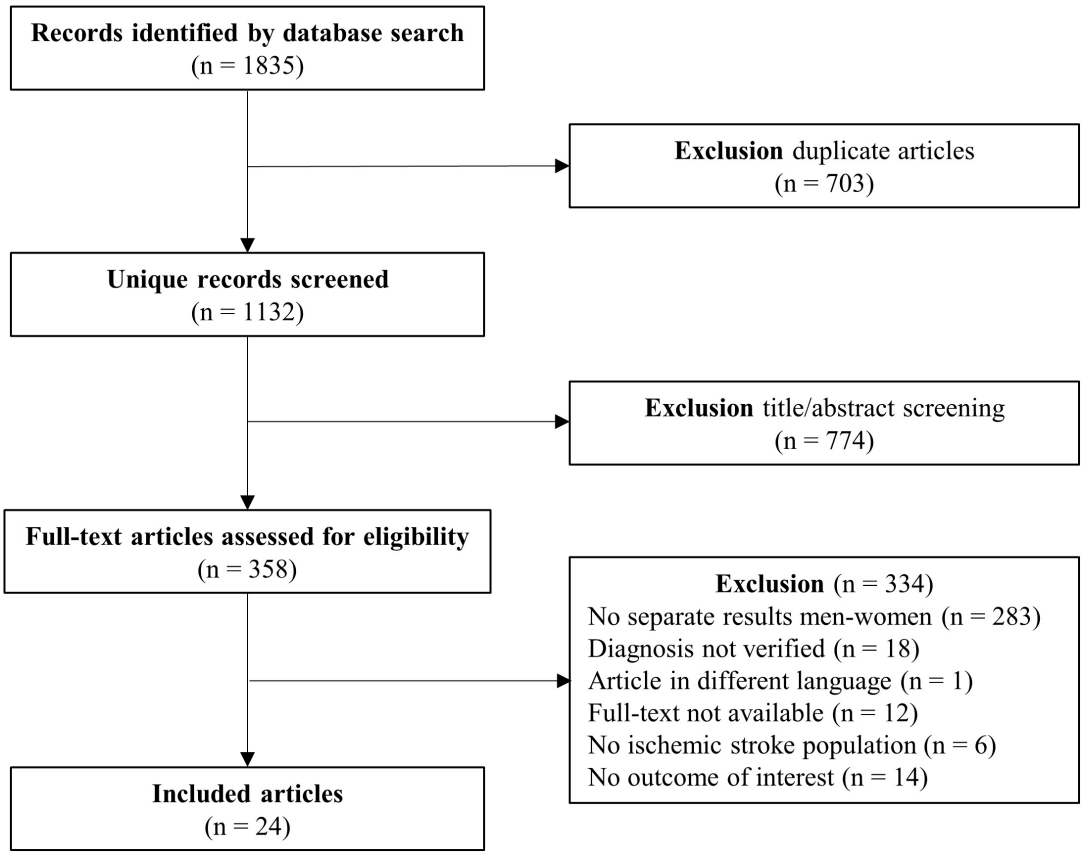


**FIGURE 1 |** PRISMA flow chart study selection sex differences in ischemic stroke.

**TABLE 1 |** Primary hemostatic factors.

| | Men [mean ± SD median (IQR)] | Women [mean ± SD median (IQR)] | Sex difference | Study |
|---|---|---|---|---|
| **TXA2 (pg/mL)*** | <2w<br>*n* = 31: 105.01 ± 92.56<br>*n* = 31: 94.90 ± 76.18<br>*n* = 20: 96.96 ± 57.39<br>*n* = 20: 92.18 ± 56.97 | <2w<br>*n* = 25: 81.43 ± 64.05<br>*n* = 20: 84.84 ± 82.49<br>*n* = 11: 94.54 ± 56.57<br>*n* = 13: 84.05 ± 44.18 | NS | Lee et al., 1987 |
| **PGI2 (pg/mL)*** | <2w<br>*n* = 8: 42.25 ± 20.30<br>*n* = 7: 36.10 ± 10.77 | <2w<br>*n* = 8: 43.38 ± 17.85<br>*n* = 7: 37.87 ± 18.63 | NS | Lee et al., 1987 |
| **ADP threshold concentration (μM)*** | <2w<br>*n* = 40: 4.20 ± 2.77<br>*n* = 44: 4.58 ± 3.05<br>*n* = 20: 4.53 ± 2.83<br>*n* = 23: 4.86 ± 3.32 | <2w<br>*n* = 28: 4.08 ± 2.47<br>*n* = 28: 4.47 ± 2.81<br>*n* = 13: 4.48 ± 2.17<br>*n* = 13: 4.15 ± 2.87 | NS | Lee et al., 1987 |
| **vWF (IU/mL)** | 3m: 1.8 ± 0.8 | 3m: 1.9 ± 0.8 | NS | Kain et al., 2001 |
| **Glutamate (μM)** | <72h: 187 (128–267) | | NS | Meng et al., 2014 |
| **P-selectin (pg/mL)** | 1d: 79.1 ± 66.7<br>4d: 113.6 ± 82.6 | 1d: 48.9 ± 15.4<br>4d: 83.5 ± 46.4 | *p* = 0.02<br>*p* = 0.08 | Blum et al., 2012 |
| **PLA2 (ng/mL)** | <72h: 326.8 ± 112.9 | <72h: 336.1 ± 132.7 | NS | Elkind et al., 2006 |

**Patients were divided in four groups to compare effect of a drug. The numbers shown here are the baseline measurements before any drug was administered.*

**TABLE 2 |** Secondary hemostatic factors.

| | Men [mean ± SD median (IQR)] | Women [mean ± SD median (IQR)] | Sex difference | Study |
|---|---|---|---|---|
| **FVII:C (%)** | 3m: 104 ± 30 | 3m: 116 ± 30 | $p = 0.04$ | Kain et al., 2001 |
| **FVII:ag (%)** | 3m: 99 ± 31 | 3m: 114 ± 34 | $p = 0.01$ | |
| **FXIIa (ng/mL)** | 3m: 2.2 ± 1.0 | 3m: 2.4 ± 1.1 | NS | Kain et al., 2001 |
| **FXI (UI/mL)** | 1m: 1.13 ± 0.32 (0.14 higher in women than in men) | | 95%CI: 0.09–0.19 | Santamaria et al., 2007 |
| **AT III (% activity)** | <2d: 102.5 ± 12.4<br>1w: 106.1 ± 13.8<br>1m: 113.5 ± 15.7<br>3m: 113.3 ± 12.5 | <2d: 103.6 ± 16.9<br>1w: 114.4 ± 16.6<br>1m: 112.8 ± 12.5<br>3m: 112.6 ± 13.2 | NS | Haapaniemi et al., 2002 |
| **β-antithrombin (% activity)** | <2d: 105.9 ± 17.4 | | NS | de la Morena-Barrio et al., 2015 |
| **Thrombin-antithrombin (mg/L)** | <2d: 7.9 ± 9.1<br>1w: 6.6 ± 8.6<br>1m: 4.5 ± 3.3<br>3m: 6.0 ± 6.2 | | NS | Haapaniemi et al., 2004 |
| **protein S (% antigen)** | <2d: 104.7 ± 19.8<br>1w: 87.8 ± 4.3<br>1m: 85.5 ± 28.5<br>3m: 91.2 ± 31.1 | <2d: 86.2 ± 23.0<br>1w: 72.3 ± 34.2<br>1m: 80.6 ± 32.8<br>3m: 73.5 ± 28.0 | $p < 0.05$<br>NS<br>NS<br>$p < 0.01$ | Haapaniemi et al., 2002 |
| **Protein C (% activity)** | <2d: 118.6 ± 28.4<br>1w: 108.3 ± 42.4<br>1m: 109.0 ± 35.7<br>3m: 109.0 ± 43.5 | <2d: 116.0 ± 30.6<br>1w: 125.8 ± 44.1<br>1m: 119.8 ± 44.7<br>3m: 111.7 ± 40.6 | NS | Haapaniemi et al., 2002 |
| **Fibrinogen (g/L)** | <10d: 4.57 (4.37–4.78)<br>3m: 3.86 (3.63–4.12) | <10d: 4.40 (4.22–4.58)<br>3m: 3.82 (3.64–4.02) | ↑ in women with TACI ($p = 0.021$) | Carter et al., 1997 |
| **Fibrinogen (g/L)** | 3m: 3.8 ± 1.3 | 3m: 3.7 ± 1.3 | NS | Kain et al., 2001 |
| **Fibrinogen (g/L)** | 3h: 3.4 ± 0.8<br>6h: 3.1 ± 0.8<br>24h: 3.4 ± 0.8 | | NS | Skoloudik et al., 2010 |
| **Fibrinogen (g/L)** | <24h: 3.9 ± 1.2 | <24h: 4.0 ± 1.8 | NS | Kisialiou et al., 2012 |

10 days after stroke, but not 3 months after stroke. This effect was not observed in men (Carter et al., 1997).

## Sex Differences in the Fibrinolytic Pathway

Four factors of the fibrinolytic pathway were reported in nine articles, with a total of 1343 patients (**Table 3**). No sex differences were found for tissue plasminogen activator (t-PA) plasma levels (Jeppesen et al., 1998; Mansfield et al., 1998; Kain et al., 2001; Haapaniemi et al., 2004; Saidi et al., 2007) (decreases thrombotic tendency) and F1.2 (Furie et al., 2004; Haapaniemi et al., 2004) (increases thrombotic tendency), while varying results were reported for D-dimer and PAI-1 (both increase thrombotic tendency). Two studies found no sex differences for D-dimer levels within 24h after stroke (Skoloudik et al., 2010) or 3 months after stroke (Haapaniemi et al., 2004). One study found higher levels in women than in men (1.25 ± 0.31 vs. 0.95 ± 0.24 in μg/mL), but did not report how long after stroke blood was drawn (Li et al., 2018). Four of five articles reported higher PAI-1 levels 3 months after stroke in women compared with men [15.7 (95% CI 13.7–18.1) vs. 11.4 (10.2–12.7) in U/mL] (Mansfield et al., 1998), (18.2 ± 13.5 vs. 13.3 ± 11.0 in U/mL) (Kain et al., 2001), (16.2 ± 2.1 vs. 11.1 ± 2.4 in U/mL) (Kain et al., 2002), and (125.35 ± 49.37 vs. 96.67 ± 38.90 in U/mL) (Saidi et al., 2007). One study found no sex differences in PAI-1 activity at four different time points (Haapaniemi et al., 2004).

## Sex Differences in Other Hemostasis Associated Factors

Five other factors, that directly influence hemostasis, were reported in six articles, with a total of 4143 patients (**Table 4**). No sex differences were reported for plasma levels of tissue inhibitor metalloproteinase 1 (TIMP-1) (Zhong et al., 2019) and insulin-like growth factor 1 (IGF-1) (Dong et al., 2014; Zhang et al., 2018) 1 day after stroke, matrix metalloproteinase 2 (MMP2) within 2 days after stroke (Montaner et al., 2001), and matrix metalloproteinase 9 (MMP9) 2 days (Montaner et al., 2001; Zhong et al., 2019) and 1 month after stroke (Abdelnaseer et al., 2017). One study found higher aPS titers (18.7% vs. 12.0% positive) in women compared with men 5 days after ischemic stroke, however, this did not reach statistical significance (Tuhrim et al., 1999).

## Studies on Hemostatic Factors in Women With Ischemic Stroke and Migraine

The second query on ischemic stroke and migraine in women specifically resulted in 2772 studies, of which only one study

**TABLE 3 |** Fibrinolysis factors.

| | Men [mean ± SD median (IQR)] | Women [mean ± SD median (IQR)] | Sex difference | Study |
|---|---|---|---|---|
| **D-dimer (μg/mL)** | <2d: 0.66 ± 0.56<br>1w: 1.61 ± 3.18<br>1m: 0.79 ± 0.89<br>3m: 0.49 ± 0.42 | | NS | Haapaniemi et al., 2004 |
| **D-dimer (μg/mL)** | 3h: 0.31 ± 0.40<br>6h: 0.86 ± 1.04<br>24h: 0.59 ± 1.00 | | NS | Skoloudik et al., 2010 |
| **D-dimer (μg/mL)** | 0.95 ± 0.24* | 1.25 ± 0.31* | $p < 0.001$ | Li et al., 2018 |
| **PAI-1 (U/mL)** | 3m: 11.4 (10.2–12.7) | 3m: 15.7 (13.7–18.1) | $p = 0.001$ | Mansfield et al., 1998 |
| **PAI-1 activity U/mL)**<br>**PAI-1:ag (U/mL)** | 3m: 16.1 ± 11.7<br>3m: 13.3 ± 11.0 | 3m: 19.3 ± 10.8<br>3m: 18.2 ± 13.5 | $p = 0.04$<br>$p = 0.04$ | Kain et al., 2001 |
| **PAI-1 activity (U/mL)**<br>**PAI-1:ag (U/mL)** | 3m: 14.1 ± 2.0<br>3m: 11.1 ± 2.4 | 3m: 19.2 ± 1.7<br>3m: 16.2 ± 2.1 | $p < 0.05$<br>$p < 0.05$ | Kain et al., 2002 |
| **PAI-1 (AU/mL)** | <2d: 17.2 ± 7.8<br>1w:11.2 ± 9.2<br>1m: 14.4 ± 7.9<br>3m: 15.8 ± 8.4 | | NS | Haapaniemi et al., 2004 |
| **PAI-1 (ng/mL)** | 96.7 ± 38.9* | 125.4 ± 49.4* | $p < 0.05$** | Saidi et al., 2007 |
| **t-PA:ag (ng/mL)** | <2w: 9.4 (6.7–12.1)<br>6m: 10.3 (9.1–14.6) | <2d: 10.1 (7.4–12.6)<br>6m: 10.9 (7.3–15.3) | NS | Jeppesen et al., 1998 |
| **t-PA:ag (ng/mL)** | 3m: 11.5 (10.7–12.2) | 3m: 11.7 (10.8–12.6) | NS | Mansfield et al., 1998 |
| **t PA:ag (ng/mL)** | 3m: 11.4 ± 1.6 | 2m: 12.0 ± 1.7 | NS | Kain et al., 2001 |
| **t-PA:ag (ng/mL)** | 0.8 ± 0.4* | 0.7 ± 0.3* | NS | Saidi et al., 2007 |
| **t-PA:ag (ng/mL)** | <2d: 8.8 ± 4.2<br>1w: 8.4 ± 3.4<br>1m: 8.3 ± 3.2<br>3m: 8.7 ± 4.3 | | NS | Haapaniemi et al., 2004 |
| **F1.2 (ng/mL)** | 3–6m: 0.9 (0.3–2.4) | 3–6m: 1.0 (0.4–2.8) | $p = 0.02$ | Furie et al., 2004 |
| **F1.2 (nmol/L)** | <2d: 1.7 ± 0.9<br>1w: 1.7 ± 1.1<br>1m: 1.4 ± 0.8<br>3m: 1.6 ± 1.4 | | NS | Haapaniemi et al., 2004 |

**Unknown in which phase blood was drawn.*

***Increased in women with ischemic stroke compared to controls, no difference in men between ischemic stroke patients and controls.*

was included (**Figure 2**). Sixteen women (mean age 37 years) with lacunar stroke were included, of whom 44% had migraine. Migraine patients were more often smokers (57% vs. 33%) and users of oral contraceptives (29% vs. 0%) (Salobir et al., 2002). Four hemostatic factors (fibrinogen, D-dimer, t-PA, and PAI-1) were investigated in the chronic phase after stroke. No clear differences were found between patients with and without migraine (Salobir et al., 2002).

## DISCUSSION

We found sex differences for several hemostatic factors in patients with ischemic stroke. In women, levels of FVII (Kain et al., 2001), FXI (Santamaria et al., 2007), PAI-1 (Mansfield et al., 1998; Kain et al., 2001, 2002; Saidi et al., 2007), and D-dimer (Li et al., 2018) were higher compared with men. In contrast, levels of P-selectin (Blum et al., 2012) and protein S (Haapaniemi et al., 2002) were lower in women. We found no differences for hemostatic factors in women with ischemic stroke with or without migraine (Salobir et al., 2002) but only one study fulfilled our inclusion criteria.

Previous reviews on women with stroke have been performed but mainly addressed hemostatic factors in relation to oral contraceptives use (Lete et al., 2015) and menopause status (Sowers et al., 2005). Our review specifically focused on sex differences in ischemic stroke patients in general, and the influence of migraine on hemostatic factors in women with ischemic stroke. Overall, the sex differences in our review indicate that women with ischemic stroke lean more toward increased levels of procoagulant factors, whereas men lean more toward increased levels of coagulation inhibitors. FVII and FXI are involved in the activation of thrombin *via* the coagulation cascade of secondary hemostasis. Activation of thrombin leads to platelet activation and fibrin formation (Periayah et al., 2017). D-dimer is released when fibrin is crosslinked to form a clot. Increased D-dimer levels thus indicate activation of thrombin (Furie et al., 2004; Skoloudik et al., 2010), conform the higher levels of FVII and FXI. Further, FXI activation helps stabilize fibrin clots and makes the clot more resistant to fibrinolysis (Santamaria et al., 2007). The fibrinolysis pathway is inhibited by PAI-1, further increasing the thrombotic tendency (Saidi et al., 2007). Only two factors were higher in men of which protein S inhibits coagulation factors V and VIII (Haapaniemi et al., 2002) and

**TABLE 4 |** Other factors involved in hemostasis.

| | Men [mean ± SD median (IQR)] | Women [mean ± SD median (IQR)] | Sex difference | Study |
|---|---|---|---|---|
| **MMP2 (ng/mL)** | 0h: 752.5 ± 210.9<br>12h: 668.8 ± 254.6<br>24h: 599.0 ± 195.4<br>48h: 580.1 ± 188.0<br>mean: 644.2 ± 185.8 | | NS | Montaner et al., 2001 |
| **MMP9 (ng/mL)** | 0h: 147.1 ± 118.6<br>12h: 140.4 ± 120.7<br>24h: 172.6 ± 139.0<br>48h: 144.5 ± 127.6<br>mean: 149.6 ± 99.0 | | NS | Montaner et al., 2001 |
| **MMP9 (ng/mL)** | <24h: 668.9 (415.0–1022.0) | | NS | Zhong et al., 2019 |
| **MMP9 (ng/mL)** | 24h: 998.8 ± 154.7<br>1m: 800.3 ± 156.4 | | NS | Abdelnaseer et al., 2017 |
| **TIMP-1 (ng/mL)** | <24h: 198.6 (163.7–241.2) | | NS | Zhong et al., 2019 |
| **IGF-1 (ng/mL)** | <24h: 129 (109–153) | | NS | Dong et al., 2014 |
| **IGF-1 (ng/mL)** | <24h: 112 (92–142) | | NS | Zhang et al., 2018 |
| **Antiphosphatidyl serine (% positive)** | <5d: 12.0 | <5d: 18.7 | NS | Tuhrim et al., 1999 |

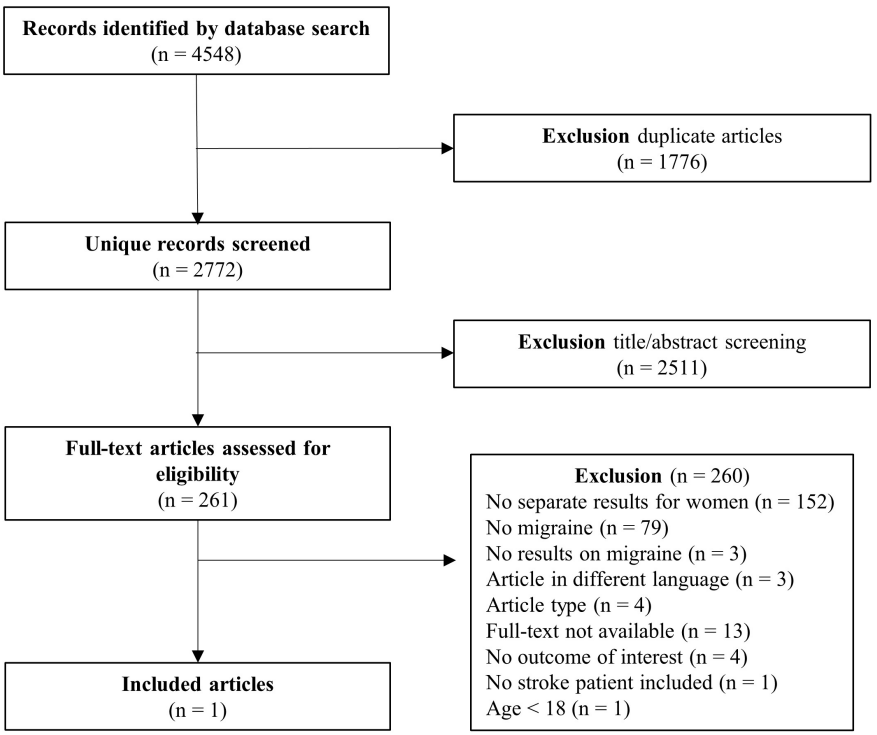


**FIGURE 2 |** PRISMA flow chart study selection ischemic stroke and migraine in women.

P-selectin is released by activated platelets and endothelial cells (Blum et al., 2012). Fibrinogen is an acute phase reactant. We found no sex differences in levels of fibrinogen between men and women, but in women fibrinogen levels differed between cortical and lacunar location which could point to differences in underlying disease mechanisms. Interestingly, high levels of some of these factors (FXI, D-dimer, PAI-1, and aPS) have previously been associated with impaired clinical outcome after ischemic stroke (Donkel et al., 2019). Therefore, sex differences in the hemostatic system might contribute to both an increased risk as to a worse outcome after stroke in women compared with men (Girijala et al., 2017).

Another aspect of sex differences in ischemic stroke are the women specific risk factors, such as migraine, especially in combination with the use of oral contraceptives. We found only one study investigating the influence of migraine history on hemostatic factors in female stroke patients. This study included only 16 patients and found no influence on fibrinogen, D-dimer, t-PA, and PAI-1 (Salobir et al., 2002). Previous research has shown some evidence for a genetic predisposition for hypercoagulability in patients with migraine with aura (Guo Y. et al., 2021). Hypercoagulability and microemboli have been suggested to have a potential role in the association of migraine with aura with ischemic stroke. The increased risk of stroke in women with migraine using oral contraceptives further supports the hypothesis, since estrogen is associated with increase of FII, FVII, FX, prothrombin, and fibrinogen (Tietjen and Collins, 2018). Phosphorylated fibrinopeptide A is a marker for coagulation activity, and has been shown to be associated with susceptibility for migraine with aura (Guo Y. et al., 2021). In addition, ischemic stroke patients with a history of migraine with aura more often had prothrombotic genotypes (factor V Leiden and prothrombin G20210A) than ischemic stroke patients without history of migraine or migraine without aura (Pezzini et al., 2011). To further unravel the pathophysiological connection between migraine and stroke more studies investigating the influence of migraine on hemostatic factors are urgently needed.

Ischemic stroke and migraine are associated with the presence of white matter hyperintensities (WMH), which might be part of the underlying pathophysiology (Kruit et al., 2010; Ghaznawi et al., 2021). Several hemostatic factors are associated with WMH, showing possible mechanisms of hemostatic factor involvement in pathophysiology of ischemic stroke and migraine besides hypercoagulability. Increased fibrinogen levels have been associated with more severe WMH (You et al., 2018; Guo X. et al., 2021), as well as PLA2 (Zhu et al., 2019). Furthermore, increased t-PA activity was associated with progression of WMH in lacunar stroke (van Overbeek et al., 2016).

Increased levels of hemostatic factors can be both cause or consequence of acute ischemic stroke. Most factors for which a sex difference was found, were measured 1–3 months after stroke (FVII, FXI, PAI-1, and Protein S) (Mansfield et al., 1998; Kain et al., 2001, 2002; Haapaniemi et al., 2002; Saidi et al., 2007; Santamaria et al., 2007) and are, therefore, not severely influenced by the acute phase of ischemic stroke. Only two of the factors with a sex difference, aPS and P-selectin, were measured in the first week after stroke (Tuhrim et al., 1999; Blum et al., 2012). This indicates that the levels of these factors could be a direct consequence of ischemic stroke and a different response between men and women. Unfortunately, the timing of measurement was unknown for the study showing higher D-dimer levels in women (Li et al., 2018).

The reported sex differences should be interpreted with caution as many were only investigated in a limited number of studies. Most factors were measured in a single study, or in multiple studies with large heterogeneity. First, some studies did not provide information about risk factors (especially diabetes mellitus and smoking affect the hemostatic balance) for ischemic stroke and/or whether reported results were adjusted for those risk factors. Second, most studies did not provide information on the medication that patients received before or after stroke. Since all blood samples were collected after stroke, patients likely already received medication that can influence the levels of hemostatic factors such as anticoagulants. Because of this heterogeneity, a formal meta-analysis was unfortunately not possible.

To interpret the generalizability of this systematic review several factors need to be considered. First, studies included patients with varying etiologies of ischemic stroke. The underlying mechanisms of stroke might be related to (sex) differences in hemostatic factors. Some studies took differences of hemostatic factors for stroke etiologies or stroke location into account. However, the majority of them did not report results separately for men and women and had to be excluded from this review. Second, most patients were older than 50 years whereas (sex differences in) hemostatic factors may be especially important in young ischemic stroke patients, when estrogen and other sex hormones have the most influence on hemostasis related factors (Abou-Ismail et al., 2020). Third, women specific risk factors were often not reported in studies on hemostatic factors, such as pre-eclampsia and migraine. Both pre-eclampsia and migraine are associated with an inflammatory and hypercoagulable state, increasing the risk of ischemic stroke (Sacco et al., 2017; Demel et al., 2018). Only one study investigated the role of migraine on hypercoagulability in women with stroke (Salobir et al., 2002), showing the lack of research on this common women specific risk factor.

## CONCLUSION

Sex differences appear to exist for several hemostatic factors after ischemic stroke, with women leaning more toward increased procoagulant factors, and men leaning more toward increased coagulant inhibitors. Future research on hemostatic factors in ischemic stroke should also include young ischemic stroke patients, stratify for stroke etiology, report medication use, report results for men and women separately, include migraine as risk factor (including migraine subtype), and take women specific risk factors into account. This could improve insights about differences in mechanisms underlying ischemic stroke between men and women.

## DATA AVAILABILITY STATEMENT

The original contributions presented in the study are included in the article/**Supplementary Material**, further inquiries can be directed to the corresponding author/s.

## AUTHOR CONTRIBUTIONS

NW, HO, MW, BS, and JS designed the systematic search strategy. NW, MA, and HO collected the data. All authors

contributed to drafting the article or revisions and approved the final version for publication.

## FUNDING

This review was supported by the personal ZonMw VIDI grant (91717337) and Aspasia grant of the Netherlands Organization for Scientific Research and a Westerdijk Grant from Leiden University to MW.

## SUPPLEMENTARY MATERIAL

The Supplementary Material for this article can be found online at: https://www.frontiersin.org/articles/10.3389/fncel.2021.711604/full#supplementary-material

## REFERENCES


Abdelnaseer, M. M., Elfauomy, N. M., Esmail, E. H., Kamal, M. M., and Elsawy, E. H. (2017). Matrix Metalloproteinase-9 and Recovery of Acute Ischemic Stroke. *J. Stroke Cerebrovasc. Dis.* 26, 733–740. doi: 10.1016/j.jstrokecerebrovasdis.2016.09.043

Abou-Ismail, M. Y., Citla Sridhar, D., and Nayak, L. (2020). Estrogen and thrombosis: a bench to bedside review. *Thromb. Res.* 192, 40–51. doi: 10.1016/j.thromres.2020.05.008

Adelborg, K., Szépligeti, S. K., Holland-Bill, L., Ehrenstein, V., Horváth-Puhó, E., Henderson, V. W., et al. (2018). Migraine and risk of cardiovascular diseases: danish population based matched cohort study. *BMJ* 360:k96. doi: 10.1136/bmj.k96

Blum, A., Vaispapir, V., Keinan-Boker, L., Soboh, S., Yehuda, H., and Tamir, S. (2012). Endothelial dysfunction and procoagulant activity in acute ischemic stroke. *J. Vasc. Interv. Neurol.* 5, 33–39.

Carter, A. M., Catto, A. J., Bamford, J. M., and Grant, P. J. (1997). Gender-specific associations of the fibrinogen B beta 448 polymorphism, fibrinogen levels, and acute cerebrovascular disease. *Arterioscler. Thromb. Vasc. Biol.* 17, 589–594. doi: 10.1161/01.atv.17.3.589

Chang, Z., Zou, H., Xie, Z., Deng, B., Que, R., Huang, Z., et al. (2021). Cystatin C is a potential predictor of unfavorable outcomes for cerebral ischemia with intravenous tissue plasminogen activator treatment: a multicenter prospective nested case-control study. *Eur. J. Neurol.* 28, 1265–1274. doi: 10.1111/ene.14663

Chen, Z., Li, M., Wu, Z., Zhang, M., Weng, G., Li, M., et al. (2021). Cerebral Circulation Time Is a Potential Predictor of Disabling Ischemic Cerebrovascular Events in Patients With Non-disabling Middle Cerebral Artery Stenosis. *Front. Neurol.* 12:653752. doi: 10.3389/fneur.2021.653752

de la Morena-Barrio, M. E., Garcia, A., Martinez-Martinez, I., Minano, A., Padilla, J., Navarro-Fernandez, J., et al. (2015). A new method to quantify beta-antithrombin glycoform in plasma reveals increased levels during the acute stroke event. *Thromb. Res.* 136, 634–641. doi: 10.1016/j.thromres.2015.06.039

Demel, S. L., Kittner, S., Ley, S. H., McDermott, M., and Rexrode, K. M. (2018). Stroke Risk Factors Unique to Women. *Stroke* 49, 518–523. doi: 10.1161/strokeaha.117.018415

Deng, Q. W., Li, S., Wang, H., Lei, L., Zhang, H. Q., Gu, Z. T., et al. (2018). The Short-term Prognostic Value of the Triglyceride-to-high-density Lipoprotein Cholesterol Ratio in Acute Ischemic Stroke. *Aging Dis.* 9, 498–506. doi: 10.14336/ad.2017.0629

Dong, X., Chang, G., Ji, X. F., Tao, D. B., and Wang, Y. X. (2014). The relationship between serum insulin-like growth factor I levels and ischemic stroke risk. *PLoS One* 9:e94845. doi: 10.1371/journal.pone.0094845

Donkel, S. J., Benaddi, B., Dippel, D. W. J., Ten Cate, H., and de Maat, M. P. M. (2019). Prognostic Hemostasis Biomarkers in Acute Ischemic Stroke. *Arterioscler. Thromb. Vasc. Biol.* 39, 360–372. doi: 10.1161/atvbaha.118.312102

Elkind, M. S., Tai, W., Coates, K., Paik, M. C., and Sacco, R. L. (2006). High-sensitivity C-reactive protein, lipoprotein-associated phospholipase A2, and outcome after ischemic stroke. *Arch. Intern. Med.* 166, 2073–2080. doi: 10.1001/archinte.166.19.2073

Etminan, M., Takkouche, B., Isorna, F. C., and Samii, A. (2005). Risk of ischaemic stroke in people with migraine: systematic review and meta-analysis of observational studies. *BMJ* 330:63. doi: 10.1136/bmj.38302.504063.8F

Furie, K. L., Rosenberg, R., Thompson, J. L., Bauer, K., Mohr, J. P., Rosner, B., et al. (2004). Thrombin generation in non-cardioembolic stroke subtypes: the Hemostatic System Activation Study. *Neurology* 63, 777–784. doi: 10.1212/01.wnl.0000137032.20456.df

Ghaznawi, R., Geerlings, M. I., Jaarsma-Coes, M., Hendrikse, J., and de Bresser, J. (2021). Association of White Matter Hyperintensity Markers on MRI and Long-term Risk of Mortality and Ischemic Stroke: the SMART-MR Study. *Neurology* 96, e2172–e2183. doi: 10.1212/wnl.0000000000011827

Girijala, R. L., Sohrabji, F., and Bush, R. L. (2017). Sex differences in stroke: review of current knowledge and evidence. *Vasc. Med.* 22, 135–145. doi: 10.1177/1358863X16668263

Guo, X., Deng, B., Zhong, L., Xie, F., Qiu, Q., Wei, X., et al. (2021). Fibrinogen is an Independent Risk Factor for White Matter Hyperintensities in CADASIL but not in Sporadic Cerebral Small Vessel Disease Patients. *Aging Dis.* 12, 801–811. doi: 10.14336/ad.2020.1110

Guo, Y., Rist, P. M., Sabater-Lleal, M., de Vries, P., Smith, N., Ridker, P. M., et al. (2021). Association Between Hemostatic Profile and Migraine: a Mendelian Randomization Analysis. *Neurology* 96, e2481–e2487. doi: 10.1212/wnl.0000000000011931

Haapaniemi, E., Soinne, L., Syrjala, M., Kaste, M., and Tatlisumak, T. (2004). Serial changes in fibrinolysis and coagulation activation markers in acute and convalescent phase of ischemic stroke. *Acta Neurol. Scand.* 110, 242–247. doi: 10.1111/j.1600-0404.2004.00304.x

Haapaniemi, E., Tatlisumak, T., Soinne, L., Syrjälä, M., and Kaste, M. (2002). Natural anticoagulants (antithrombin III, protein C, and protein S) in patients with mild to moderate ischemic stroke. *Acta Neurol. Scand.* 105, 107–114. doi: 10.1034/j.1600-0404.2002.1o112.x

Jeppesen, L. L., Jørgensen, H. S., Nakayama, H., Raaschou, H. O., Olsen, T. S., and Winther, K. (1998). Tissue plasminogen activator is elevated in women with ischemic stroke. *J. Stroke Cerebrovasc. Dis.* 7, 187–191. doi: 10.1016/s1052-3057(98)80005-0

Kain, K., Catto, A. J., Carter, A. M., Young, J., Bamford, J., Bavington, J., et al. (2001). Decreased fibrinolytic potential in South Asian women with ischaemic cerebrovascular disease. *Br. J. Haematol.* 114, 155–161. doi: 10.1046/j.1365-2141.2001.02916.x

Kain, K., Young, J., Bamford, J., Bavington, J., Grant, P. J., and Catto, A. J. (2002). Determinants of plasminogen activator inhibitor-1 in South Asians with ischaemic stroke. *Cerebrovasc. Dis.* 14, 77–83. doi: 10.1159/000064732

Kisialiou, A., Pelone, G., Carrizzo, A., Grillea, G., Trimarco, V., Marino, M., et al. (2012). Blood biomarkers role in acute ischemic stroke patients: higher is worse or better? *Immun. Ageing* 9:22. doi: 10.1186/1742-4933-9-22

Kruit, M. C., van Buchem, M. A., Launer, L. J., Terwindt, G. M., and Ferrari, M. D. (2010). Migraine is associated with an increased risk of deep white matter lesions, subclinical posterior circulation infarcts and brain iron accumulation: the population-based MRI CAMERA study. *Cephalalgia* 30, 129–136. doi: 10.1111/j.1468-2982.2009.01904.x

Kurth, T., Chabriat, H., and Bousser, M. G. (2012). Migraine and stroke: a complex association with clinical implications. *Lancet Neurol.* 11, 92–100.

Lee, T. K., Chen, Y. C., and Kuo, T. L. (1987). Comparison of the effect of acetylsalicylic acid on platelet function in male and female patients with ischemic stroke. *Thromb. Res.* 47, 295–304. doi: 10.1016/0049-3848(87)90143-5

Lete, I., Chabbert-Buffet, N., Jamin, C., Lello, S., Lobo, P., Nappi, R. E., et al. (2015). Haemostatic and metabolic impact of estradiol pills and drospirenone-containing ethinylestradiol pills vs. levonorgestrel-containing ethinylestradiol pills: a literature review. *Eur. J. Contracept. Reprod. Health Care* 20, 329–343. doi: 10.3109/13625187.2015.1050091

Li, J., Gu, C., Li, D., Chen, L., Lu, Z., Zhu, L., et al. (2018). Effects of serum N-terminal pro B-type natriuretic peptide and D-dimer levels on patients with acute ischemic stroke. *Pak. J. Med. Sci.* 34, 994–998. doi: 10.12669/pjms.344.15432

Li, W., Qi, Z., Kang, H., Qin, X., Song, H., Sui, X., et al. (2020). Serum Occludin as a Biomarker to Predict the Severity of Acute Ischemic Stroke, Hemorrhagic Transformation, and Patient Prognosis. *Aging Dis.* 11, 1395–1406. doi: 10.14336/ad.2020.0119

Li, X., Lin, S., Chen, X., Huang, W., Li, Q., Zhang, H., et al. (2019). The Prognostic Value of Serum Cytokines in Patients with Acute Ischemic Stroke. *Aging Dis.* 10, 544–556. doi: 10.14336/ad.2018.0820

Liu, F., Lu, J., Manaenko, A., Tang, J., and Hu, Q. (2018). Mitochondria in Ischemic Stroke: new Insight and Implications. *Aging Dis.* 9, 924–937. doi: 10.14336/ad.2017.1126

Ma, Y., Liu, Y., Zhang, Z., and Yang, G. Y. (2019). Significance of Complement System in Ischemic Stroke: a Comprehensive Review. *Aging Dis.* 10, 429–462. doi: 10.14336/ad.2019.0119

Mansfield, M. W., Catto, A. J., Carter, A. M., and Grant, P. J. (1998). Fibrinolytic measurements in type 2 diabetic patients with acute cerebral infarction. *Diabet. Med.* 15, 953–957.

Meng, X.-E., Li, N., Guo, D.-Z., Pan, S.-Y., Li, H., and Yang, C. (2014). High Plasma Glutamate Levels are Associated with Poor Functional Outcome in Acute Ischemic Stroke. *Cell. Mol. Neurobiol.* 35, 159–165. doi: 10.1007/s10571-014-0107-0

Montaner, J., Alvarez-Sabín, J., Molina, C., Anglés, A., Abilleira, S., Arenillas, J., et al. (2001). Matrix metalloproteinase expression after human cardioembolic stroke: temporal profile and relation to neurological impairment. *Stroke* 32, 1759–1766. doi: 10.1161/01.str.32.8.1759

Montellano, F. A., Ungethüm, K., Ramiro, L., Nacu, A., Hellwig, S., Fluri, F., et al. (2021). Role of Blood-Based Biomarkers in Ischemic Stroke Prognosis: a Systematic Review. *Stroke* 52, 543–551. doi: 10.1161/strokeaha.120.029232

Periayah, M. H., Halim, A. S., and Mat Saad, A. Z. (2017). Mechanism Action of Platelets and Crucial Blood Coagulation Pathways in Hemostasis. *Int. J. Hematol. Oncol. Stem Cell Res.* 11, 319–327.

Pezzini, A., Grassi, M., Lodigiani, C., Patella, R., Gandolfo, C., Casoni, F., et al. (2011). Predictors of migraine subtypes in young adults with ischemic stroke: the italian project on stroke in young adults. *Stroke* 42, 17–21. doi: 10.1161/strokeaha.110.592246

Sacco, S., Merki-Feld, G. S., Ægidius, K. L., Bitzer, J., Canonico, M., Kurth, T., et al. (2017). Hormonal contraceptives and risk of ischemic stroke in women with migraine: a consensus statement from the European Headache Federation (EHF) and the European Society of Contraception and Reproductive Health (ESC). *J. Headache Pain* 18:108. doi: 10.1186/s10194-017-0815-1

Saidi, S., Slamia, L. B., Mahjoub, T., Ammou, S. B., and Almawi, W. Y. (2007). Association of PAI-1 4G/5G and -844G/A gene polymorphism and changes in PAI-1/tPA levels in stroke: a case-control study. *J. Stroke Cerebrovasc. Dis.* 16, 153–159. doi: 10.1016/j.jstrokecerebrovasdis.2007.02.002

Salobir, B., Sabovic, M., Peternel, P., Stegnar, M., and Grad, A. (2002). Classic risk factors, hypercoagulability and migraine in young women with cerebral lacunar infarctions. *Acta Neurol. Scand.* 105, 189–195. doi: 10.1034/j.1600-0404.2002.1o108.x

Santamaria, A., Oliver, A., Borrell, M., Belvis, R., Marti-Fabregas, J., Mateo, J., et al. (2007). Higher risk of ischaemic stroke associated with factor XI levels in dyslipidaemic patients. *Int. J. Clin. Pract.* 61, 1819–1823. doi: 10.1111/j.1742-1241.2007.01388.x

Schürks, M., Rist, P. M., Bigal, M. E., Buring, J. E., Lipton, R. B., and Kurth, T. (2009). Migraine and cardiovascular disease: systematic review and meta-analysis. *BMJ* 339:b3914. doi: 10.1136/bmj.b3914

Shamseer, L., Moher, D., Clarke, M., Ghersi, D., Liberati, A., Petticrew, M., et al. (2015). Preferred reporting items for systematic review and meta-analysis protocols (PRISMA-P) 2015: elaboration and explanation. *BMJ* 350:g7647. doi: 10.1136/bmj.g7647

Shao, A., Lin, D., Wang, L., Tu, S., Lenahan, C., and Zhang, J. (2020). Oxidative Stress at the Crossroads of Aging, Stroke and Depression. *Aging Dis.* 11, 1537–1566. doi: 10.14336/ad.2020.0225

Siegerink, B., Govers-Riemslag, J. W., Rosendaal, F. R., Ten Cate, H., and Algra, A. (2010). Intrinsic coagulation activation and the risk of arterial thrombosis in young women: results from the Risk of Arterial Thrombosis in relation to Oral contraceptives (RATIO) case-control study. *Circulation* 122, 1854–1861. doi: 10.1161/circulationaha.110.943738

Skoloudik, D., Bar, M., Sanak, D., Bardon, P., Roubec, M., Langova, K., et al. (2010). D-dimers increase in acute ischemic stroke patients with the large artery occlusion, but do not depend on the time of artery recanalization. *J. Thromb. Thrombolysis* 29, 477–482. doi: 10.1007/s11239-009-0372-9

Sowers, M. R., Matthews, K. A., Jannausch, M., Randolph, J. F., McConnell, D., Sutton-Tyrrell, K., et al. (2005). Hemostatic factors and estrogen during the menopausal transition. *J. Clin. Endocrinol. Metab.* 90, 5942–5948. doi: 10.1210/jc.2005-0591

Tietjen, G. E., and Collins, S. A. (2018). Hypercoagulability and Migraine. *Headache* 58, 173–183. doi: 10.1111/head.13044

Tuhrim, S., Rand, J. H., Wu, X., Horowitz, D. R., Weinberger, J., Goldman, M. E., et al. (1999). Antiphosphatidyl serine antibodies are independently associated with ischemic stroke. *Neurology* 53, 1523–1527. doi: 10.1212/wnl.53.7.1523

van Overbeek, E. C., Staals, J., Knottnerus, I. L., ten Cate, H., and van Oostenbrugge, R. J. (2016). Plasma tPA-Activity and Progression of Cerebral White Matter Hyperintensities in Lacunar Stroke Patients. *PLoS One* 11:e0150740. doi: 10.1371/journal.pone.0150740

You, C. J., Liu, D., Liu, L. L., Liu, Q. Q., and Li, G. Z. (2018). Correlation between Fibrinogen and White Matter Hyperintensities among Nondiabetic Individuals with Noncardiogenic Ischemic Stroke. *J. Stroke Cerebrovasc. Dis.* 27, 2360–2366. doi: 10.1016/j.jstrokecerebrovasdis.2018.04.025

Zhang, W., Wang, W., and Kuang, L. (2018). The relation between insulin-like growth factor 1 levels and risk of depression in ischemic stroke. *Int. J. Geriatr. Psychiatry* 33, e228–e233. doi: 10.1002/gps.4774

Zhong, C., Wang, G., Xu, T., Zhu, Z., Guo, D., Zheng, X., et al. (2019). Tissue inhibitor metalloproteinase-1 and clinical outcomes after acute ischemic stroke. *Neurology* 93, e1675–e1685. doi: 10.1212/WNL.0000000000008389

Zhu, S., Wei, X., Yang, X., Huang, Z., Chang, Z., Xie, F., et al. (2019). Plasma Lipoprotein-associated Phospholipase A2 and Superoxide Dismutase are Independent Predicators of Cognitive Impairment in Cerebral Small Vessel Disease Patients: diagnosis and Assessment. *Aging Dis.* 10, 834–846. doi: 10.14336/ad.2019.0304

**Conflict of Interest:** The authors declare that the research was conducted in the absence of any commercial or financial relationships that could be construed as a potential conflict of interest.

**Publisher's Note:** All claims expressed in this article are solely those of the authors and do not necessarily represent those of their affiliated organizations, or those of the publisher, the editors and the reviewers. Any product that may be evaluated in this article, or claim that may be made by its manufacturer, is not guaranteed or endorsed by the publisher.

frontiers in Cellular Neuroscience

ORIGINAL RESEARCH
published: 26 November 2021
doi: 10.3389/fncel.2021.761423

# New Insights and Methods for Recording and Imaging Spontaneous Spreading Depolarizations and Seizure-Like Events in Mouse Hippocampal Slices

*Yi-Ling Lu*[1] *and Helen E. Scharfman*[1,2,3,4]*

[1] Center for Dementia Research, The Nathan Kline Institute for Psychiatric Research, Orangeburg, NY, United States,
[2] Department of Child and Adolescent Psychiatry, New York University Langone Health, New York, NY, United States,
[3] Department of Neuroscience and Physiology, New York University Langone Health, New York, NY, United States,
[4] Department of Psychiatry, New York University Langone Health, New York, NY, United States

Spreading depolarization (SD) is a sudden, large, and synchronous depolarization of principal cells which also involves interneurons and astrocytes. It is followed by depression of neuronal activity, and it slowly propagates across brain regions like cortex or hippocampus. SD is considered to be mechanistically relevant to migraine, epilepsy, and traumatic brain injury (TBI), but there are many questions about its basic neurophysiology and spread. Research into SD in hippocampus using slices is often used to gain insight and SD is usually triggered by a focal stimulus with or without an altered extracellular buffer. Here, we optimize an *in vitro* experimental model allowing us to record SD without focal stimulation, which we call spontaneous. This method uses only an altered extracellular buffer containing 0 mM $Mg^{2+}$ and 5 mM $K^{+}$ and makes it possible for simultaneous patch and extracellular recording in a submerged chamber plus intrinsic optical imaging in slices of either sex. We also add methods for quantification and show the quantified optical signal is much more complex than imaging alone would suggest. In brief, acute hippocampal slices were prepared with a chamber holding a submerged slice but with flow of artificial cerebrospinal fluid (aCSF) above and below, which we call interface-like. As soon as slices were placed in the chamber, aCSF with 0 $Mg^{2+}$/5 $K^{+}$ was used. Most mouse slices developed SD and did so in the first hour of 0 $Mg^{2+}$/5 $K^{+}$ aCSF exposure. In addition, prolonged bursts we call seizure-like events (SLEs) occurred, and the interactions between SD and SLEs suggest potentially important relationships. Differences between rats and mice in different chambers are described. Regarding optical imaging, SD originated in CA3 and the pattern of spread to CA1 and the dentate gyrus was similar in some ways to prior studies but also showed interesting differences. In summary, the methods are easy to use, provide new opportunities to study SD, new insights, and are inexpensive. They support previous suggestions that SD is diverse, and also suggest that participation by the dentate gyrus merits greater attention.

**Keywords: spreading depression, intrinsic optical signal, seizures, epilepsy, experimental model, migraine, traumatic brain injury, dentate gyrus**

OPEN ACCESS

***Edited by:***
*Rustem Khazipov, Institut National de la Santé et de la Recherche Médicale (INSERM), France*

***Reviewed by:***
*R. David Andrew, Queen's University, Canada*
*Eszter Farkas, University of Szeged, Hungary*

***Correspondence:**
*Helen E. Scharfman*
*Helen.Scharfman@NKI.rfmh.org*

***Specialty section:***
*This article was submitted to Cellular Neuropathology, a section of the journal Frontiers in Cellular Neuroscience*

***Received:*** *19 August 2021*
***Accepted:*** *04 October 2021*
***Published:*** *26 November 2021*

***Citation:***
*Lu Y-L and Scharfman HE (2021) New Insights and Methods for Recording and Imaging Spontaneous Spreading Depolarizations and Seizure-Like Events in Mouse Hippocampal Slices. Front. Cell. Neurosci. 15:761423. doi: 10.3389/fncel.2021.761423*

## INTRODUCTION

Increased neuronal excitability is a common feature underlying several neurological disorders, including but not limited to migraine, epilepsy, traumatic brain injury (TBI), and stroke (Eikermann-Haerter et al., 2013; Noseda and Burstein, 2013; Rogawski, 2013; Kim et al., 2014; Bugay et al., 2020). Although seizures may be the best-known example that results from increased neuronal excitability, spreading depolarization (SD) is another example.

Spreading depolarization is a group of cells that depolarize dramatically and typically begin to fire numerous action potentials (APs). Ultimately firing ceases, neurons appear to lose normal intrinsic electrophysiological properties such as input resistance, and there is a loss of the normal ion gradients across the membrane (Czéh et al., 1993; Somjen, 2001; Hartings et al., 2017). The activity of the subset of neurons is almost synchronous so when electrical activity is monitored extracellularly, the initial depolarization is associated with a significant negative potential shift in an extracellular recording [direct current (DC) recording]. At the peak of the depolarization, action potential firing stops and neurons are silent. This period is associated with a suppression in the extracellular recording and is followed by a slow recovery. During the recovery, glia and ion pumps restore normal ionic gradients (Lian and Stringer, 2004; Dreier, 2011; Varga et al., 2020).

Leão (1944) first reported SD after focal electrical stimulation and its slow spread across the cortex of the anesthetized rabbit. He coined the term "spreading depression (SD)." However, it should be noted that SD sometimes involves a phase of depression that precedes, rather than follows, depolarization (Dreier, 2011; Ayata and Lauritzen, 2015).

There is extensive influx of sodium and calcium, and large efflux of potassium that leads to the loss of ion gradients (Somjen, 2001; Dreier, 2011; Ayata and Lauritzen, 2015). The inflow of cations brings water inside the neuron, which leads to swelling and alters the light transmission through tissue (Dreier, 2011). Therefore, the change in light transmission has been used as a method to monitor SD-associated swelling and the propagation of SD from one brain area to the next (e.g., Obeidat and Andrew, 1998; Anderson and Andrew, 2002; Buchheim et al., 2002).

To gain a better understanding of mechanisms underlying SD, past hippocampal studies have typically used slice models and rats. Many of these studies were conducted in an interface chamber (e.g., Snow et al., 1983; Scharfman, 1997; Buchheim et al., 2002; Reyes-Garcia et al., 2018). In an interface chamber, brain slices lie on a mesh at the interface between artificial cerebrospinal fluid (aCSF) and air. Warm, humidified $O_2$ or 95% $O_2$/5% $CO_2$ is vented over the slices (Schwartzkroin, 1975; Haas et al., 1979; Scharfman et al., 2001). Although interface chambers are widely used to study SD, lack of a powerful microscope limits visualization (but see Case and Broberger, 2013). On the other hand, a submerged chamber that is typically used with a high-resolution microscope allows visualization of neurons. Visualization is an advantage because it facilitates patch clamp recordings and optical imaging.

In both types of recording chambers, SDs are often initiated by electrical stimulation or focal application of concentrated potassium solutions, sometimes with a change in the ionic milieu to increase excitability (e.g., Czéh et al., 1993; Buchheim et al., 2002; Lindquist and Shuttleworth, 2012; Eickhoff et al., 2014; Martens-Mantai et al., 2014). When a different approach is used to increase excitability, such as reducing $Mg^{2+}$ in aCSF, afferent stimuli is typically needed to elicit SD (Mody et al., 1987). Spontaneous SD is rare and delayed (Mody et al., 1987). In a submerged chamber, SD is not found (Anderson et al., 1986; Lewis et al., 1990; Churn et al., 1991; Kojima et al., 1991). Therefore, methods using a submerged chamber would be beneficial. Moreover, use of a low concentration of $[Mg^{2+}]_o$ is advantageous to study SD because it is typically a powerful inhibitor of SD (Santos et al., 2016). Indeed, one reason some past studies have had difficulty in producing SD could be due to a relatively high $Mg^{2+}$ level in the aCSF, which is often done to preserve slices during the dissection. Finally, focal stimulation may not always be effective in eliciting SD. In the dentate gyrus, for example, afferent stimulation can lead to frequency depression, not facilitation (Sloviter, 1991; Scharfman et al., unpublished observations). If the GC axons are stimulated, CA3 does not exhibit SD under normal conditions (Scharfman, 1997).

Here, we report methods to achieve this goal and new findings. Regarding new methods, we used a submerged chamber with flow above and below the slice, and compared results to a classic submerged chamber with more limited flow. When slices were placed in the recording chamber, we began to use aCSF containing 0 mM $Mg^{2+}$ and 5 mM $K^+$. We refer to this aCSF as "0 $Mg^{2+}$/5 $K^+$ aCSF." SD was recorded in the majority of slices and we refer to SD that occurred, without a time-locked focal stimulus, as "spontaneous" SD. These spontaneous SDs appeared to be spontaneous because they had an unpredictable delay before SD ultimately occurred. Spontaneous SD is usually rare in slices, rare in adult mouse, and rare in a submerged chamber, providing a potentially useful and new approach to complement others. Our methods allowed us to record spontaneous SDs, bursts, and trains of bursts we call SLEs, which is valuable because these different types of epileptiform activity occur in humans. We added intrinsic optical imaging and developed methods to quantify the imaging results, finding a spatiotemporal complexity the quantification identified that was not evident by observation of video. These methods provided additional insight about SD beyond what is known and provide new analysis opportunities to extend our understanding of the dynamics of cell swelling in SD. In our slices, each subfield showed good viability so we followed SD from CA3 not only to CA1 but also the dentate gyrus. Interestingly, the delay and invasion of SD in the dentate gyrus was complex. We suggest that these methods and novel observations provide further advances in understanding SD as well as providing a preparation that may be useful to preclinical drug screening.

## MATERIALS AND METHODS

The experimental procedures were carried out in accordance with the National Institutes of Health guidelines and were

approved by the Institutional Animal Care and Use Committee in The Nathan Kline Institute. All chemicals were obtained from Millipore-Sigma unless otherwise specified.

## Animals and Husbandry

A total of 10 Sprague–Dawley rats (all males, age 21–45 days) and 26 C57BL/6 mice (14 males and 12 females, age 20–36 days) were used in the current study (**Table 1**). The maximum number of animals housed per cage was three for rats and four for mice. All animals were housed using a 12 h light/dark cycle. Food (Purina 5001 Chow, W. F. Fisher) and water were available *ad libitum*. Numbers of animals that were used in each experimental condition are listed in the **Table 1**.

## Terminology

Definitions of the terms described below were defined based on past studies of SD and our data. Extracellularly, **SD** was defined as an event that consists of a negative DC shift with a slow recovery. In our model, SD almost always began with a series of high frequency bursts and then proceeded to a negative DC shift. Intracellularly, SD began with a large depolarization with superimposed high frequency firing of APs at the onset. Subsequently, firing ceased and there was a slow repolarization.

A **SLE** was defined by multiple criteria to distinguish it as abnormal and seizure-like. Extracellularly, SLEs were defined as multiple bursts of population spikes superimposed on short-lasting positive waves. In slices, where spontaneous population spikes are not normally present, SLEs were easy to distinguish. SLEs were referred to as seizure-like because they showed more bursts than the 1–2 bursts referred to as an epileptiform discharges. SLEs also were composed of bursts at high frequency (>1 Hz) and some bursts were prolonged (Borck and Jefferys, 1999). Intracellularly, an SLE corresponded to an initial depolarization with APs at the peak, somewhat like a paroxysmal depolarization shift (PDS; Borck and Jefferys, 1999). The SLEs observed in our preparation resembled events that have been called ictaform or ictal events/activity in the past (Anderson et al., 1986; Avoli et al., 2002).

## Slice Preparation and Electrophysiological Recording

Rats or mice were deeply anesthetized using isoflurane (Patterson Veterinary) and then decapitated. Brains were quickly removed and immersed in ice-cold sucrose-containing aCSF (sucrose aCSF, ingredient in mM: 90 sucrose, 80 NaCl, 2.5 KCl, 1.25 $NaH_2PO_4$, 25 $NaHCO_3$, 10 D-glucose, 4.5 $MgSO_4$, and 0.5 $CaCl_2$, pH = 7.3–7.4). Horizontal hippocampal slices (350 μm thick) were obtained using an oscillating tissue slicer (Microm, HM650V, Thermo Fisher Scientific, or VT1200 S, Leica). Brain slices were then transferred to a holding chamber (made in-house) containing sucrose aCSF. This chamber allowed slices to sit on a mesh several inches from the base of the chamber but still below the surface of aCSF, and the aCSF circulated around the slices. The holding chamber with brain slices was placed in a water bath and temperature was gradually increased to 35°C. Afterward, the temperature of the water bath was maintained at 35°C for 45 min ("recovery"). After recovery, slices were maintained at room temperature in sucrose aCSF for the rest of the day (**Figure 1A**). All aCSF for slicing and recording was constantly oxygenated using carbogen (95% $O_2$ and 5% $CO_2$).

Brain slices were transferred from the holding chamber to a recording chamber for data collection. Two types of recording chambers were used in the current study: a "classic" submerged chamber (classic chamber, RC-26GLP, Harvard Apparatus, **Figure 1B**) and a chamber we call "interface-like" (**Figure 1B**). The interface-like chamber is a submerged chamber but flow is both above and below the slice, making it different from the classic chamber where flow is only above the slice. For this reason the chamber that we call interface-like is more like an interface chamber and it is often called that (interface-like chamber, RC-27LD, Harvard Apparatus, **Figure 1B**). When slices were placed in the recording chamber, we used aCSF with 0 mM $MgSO_4$ and 5 mM KCl (0 $Mg^{2+}$/5 $K^+$ aCSF) as follows (in mM): 130 NaCl, 5 KCl, 1.25 $NaH_2PO_4$, 25 $NaHCO_3$, 10 D-glucose, 0 $MgSO_4$, and 2.4 $CaCl_2$. Recordings were performed at 32 ± 1°C with 5–7 mL/min flow rate.

It should be noted that recording at 32°C was chosen because higher temperature led to reduced viability, particularly in the

**TABLE 1 |** Conditions tested for the development of SD and SLEs using 0 $Mg^{2+}$/5 $K^+$ aCSF.

| Species | Sex | # of animals | Age (day) | Age range (day) | # of slices | Incidence of SD (# slices with SD/total # slices tested) | Incidence of SLE (# slices with SLE/total # slices tested) |
|---|---|---|---|---|---|---|---|
| **Classic submerged style chamber** | | | | | | | |
| Mouse | M | 2 | 26 ± 2 | 24–27 | 8 | 1/8[a] | 2/8 |
| | F | 2 | 27 ± 1 | 26–28 | 8 | 2/8[b] | 2/8 |
| | Total | 4 | 26 ± 1 | 24–27 | 16 | 3/16[c] | 4/16 |
| **Interface-like submerged style chamber** | | | | | | | |
| Mouse | M | 12 | 26 ± 1[e] | 20–30 | 22 | 18/22[a,d] | 14/22 |
| | F | 10 | 27 ± 1 | 21–36 | 23 | 18/23[b] | 8/23 |
| | Total | 22 | 26 ± 1 | 20–36 | 45 | 36/45[c] | 22/45 |
| Rat | M | 10 | 35 ± 3[e] | 21–45 | 20 | 0/20[d] | 15/20 |

*Comparison of conditions used for eliciting SD and SLEs in two types of recording chambers. Statistical comparisons with significantly differences ($p < 0.05$) are noted by superscript letters a–e. Tests were Fisher's exact (superscript a–d) or unpaired t-test (superscript e).*

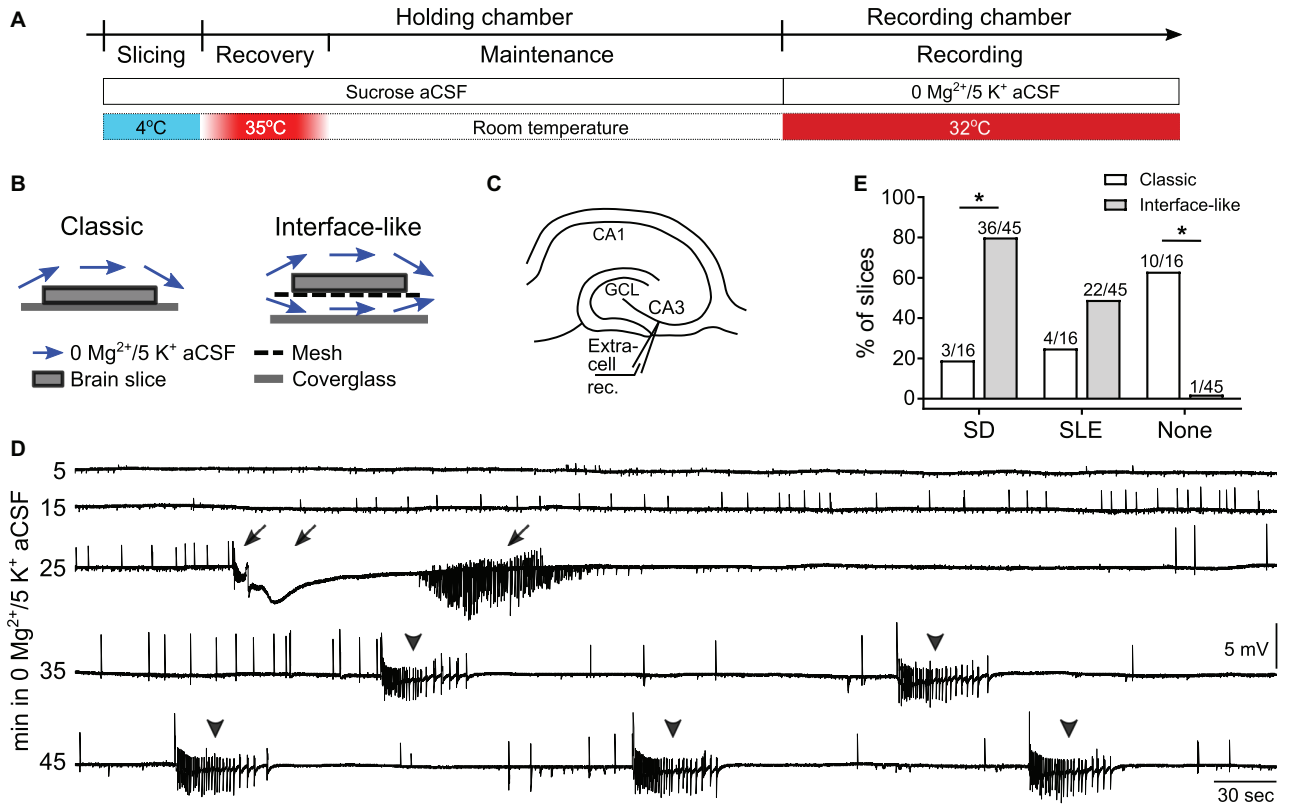


**FIGURE 1 |** Spreading depolarization (SD) and seizure-like events (SLEs) developed in 0 $Mg^{2+}$/5 $K^+$ aCSF in an interface-like submerged chamber. **(A)** Experimental timeline. Hippocampal slices were prepared in ice-cold sucrose-based artificial cerebrospinal fluid (sucrose aCSF). Slices were incubated at 35°C for 45 min and then maintained at room temperature in sucrose aCSF before being transferred to the recording chambers for recording at 32°C. **(B)** Illustration of classic (single superfusion) and interface-like (dual superfusion) recording chambers. **(C)** Schematic of extracellular recording in CA3 of hippocampus. **(D)** A representative trace shows a continuous recording of extracellular activity in CA3 in 0 mM $[Mg^{2+}]_o$/5 mM $[K^+]_o$ aCSF (0 $Mg^{2+}$/5 $K^+$ aCSF). The slice was recorded in an interface-like recording chamber. Both SD and SLEs, and either one could precede the other. Arrows point to a single SD and its after discharges. Arrowheads point to five SLEs. **(E)** Percentage of SDs, SLEs, and neither event (none) that developed in classic (white bars) or interface-like (gray bars) recording chambers within the first hour of 0 $Mg^{2+}$/5 $K^+$ aCSF exposure. Slices recorded in an interface-like recording chamber showed a higher percentage of SD than in a classic recording chamber (two-sided Fisher's exact test, $p < 0.0001$ asterisk indicates $p < 0.05$). Nighty-eight percent of slices recorded in an interface-like chamber developed SD and/or SLEs.

hilus of the DG. Ensuring viability in all parts of the slice was important to ensure that spread of SD was unaffected by tissue damage that can occur in slice preparation. In the past, when an interface recording chamber was used without infrared differential interference contrast (IR-DIC), recordings from different cell areas and cell types allowed us to judge viability. In the classic submerged or interface-like chamber, viability was addressed by confirming that the general morphology of cells prior to patch clamping was normal using IR-DIC at 40×.

Notably, at 32°C, SD and epileptiform activity may be less likely, and some aspects of SD such as cell swelling may be reduced because lower temperatures are protective. In rat slices, reducing temperature clearly inhibited SD caused by oxygen and glucose deprivation (Obeidat et al., 2000). On the other hand, when we tested temperatures from 30–35°C using an interface chamber without IR-DIC, electrophysiology was quite similar.

Recording electrodes were pulled (P-97, Sutter Instruments) from borosilicate glass (1.5 mm outer diameter, 0.86 mm inner diameter, Sutter Instruments). An extracellular recording electrode containing 0 $Mg^{2+}$/5 $K^+$ aCSF (resistance 3–7 MΩ) was placed in CA3 stratum pyramidale to record field potentials. For two simultaneous extracellular recordings, a second recording electrode was placed in either CA1 or the granule cell (GC) layer (GCL) at the crest of the dentate gyrus. In some slices, a second recording electrode (resistance 5–8 MΩ) was used to make whole-cell recordings of individual CA3 pyramidal cells simultaneously. The internal solution for whole-cell recording contained (in mM) 120 K-gluconate, 10 HEPES, 20 KCl, 2 $MgCl_2$, 0.2 EGTA, 4 Mg-ATP, 0.3 $Na_2$-GTP, 7 Tris-phosphocreatine, and 0.5% biocytin. Data were amplified (MultiClamp 700B, Molecular Devices), digitized at 10 kHz (Digidata1440A or 1550B, Molecular Devices), and acquired using pClamp (v. 10.7 or 11, Molecular Devices).

## Biocytin Labeling

Immediately after recording, hippocampal slices were rinsed in 0.9% saline (all solutions used deionized water; $dH_2O$) and then preserved in 4% paraformaldehyde in 0.1 M phosphate buffer

(pH 7.4). Slices were stored at 4°C until they were processed. Procedures were conducted using free-floating sections at room temperature with mild agitation using a clinical rotator (The Belly Dancer, Stovall Life Science Inc.) unless otherwise specified. For the following steps, all buffers were prepared in 0.1 M Tris buffer (TB, pH 7.6). First, slices were incubated in 1% Triton-X 100 (Triton) for an hour to make cell membranes more permeable to reagents. Then endogenous peroxidase activity was suppressed by incubating slices in 0.1% $H_2O_2$ for 30 min. After three rinses (10 min each) with 0.25% Triton, slices were incubated in an avidin-biotin complex solution (ABC Elite Kit, Vector Laboratories) overnight at 4°C with gentle rotation. Slices were pretreated with 0.05% 3,3′-diaminobenzidine (DAB) with 1 mM $NiCl_2$ for 30 min followed by incubation of 0.05% DAB with 0.0075% $H_2O_2$ (diluted in $dH_2O$) until biocytin-filled cells were clearly visualized. The DAB reaction was terminated by three 10 min washes in TB. Slices were equilibrated with increasing concentrations of glycerol (15 min each, 25%, 40%, 55%, 70%, 85%, 100%) (Hamam and Kennedy, 2003). Slices were coverslipped in 100% glycerol and edges of coverslip were sealed using nail polish. Brightfield images were taken using a charge-coupled device (CCD) camera (Retiga R2000, Teledyne QImaging) and an upright microscope (BX61, Olympus) with a 10× objective (UPlanSApo, 0.40 N.A., Olympus). ImagePro 7 Plus (Media Cybernetics) software was used for image acquisition. Brightfield images from different focal plans were stacked using CombineZP software (Hadley, 2010; Botterill et al., 2017) or the Stack Focuser plug-in in ImageJ (Umorin, 2002; Schneider et al., 2012).

## Intrinsic Optical Imaging

Spontaneous SD and SLEs in CA3 were continuously monitored using field potential recordings. Recording of intrinsic optical signals was started manually as soon as electrophysiological manifestations of SD were observed. The time of the beginning of the imaging was recorded and matched with electrophysiological recordings. One slice was excluded from imaging analysis because the imaging was started after the beginning of SD.

Intrinsic optical signals were captured using continuous white light (halogen bulb) and a 775 nm band pass filter. Time-lapse images were taken at one or two frames per second. All images covered each of the major subfields in hippocampus (dentate gyrus, CA3, CA2, CA1, subiculum) and some of the cortex. The first image of an event was used as a baseline for comparisons of changes in intrinsic optical signals within the event. This method to define a baseline was chosen because the first three images showed minimal or no change in intrinsic optical signals.

Time-lapse images were acquired every 0.5 s for 11 slices and 1 s for 2 slices. The overall propagation patterns of imaged SDs were similar whether acquisition was 0.5 or 1 s/image, so the data using the two different acquisition rates were pooled. A CCD camera (Retiga Electro, Teledyne Photometrics) mounted on an upright microscope (BX51, Olympus) with a 4× objective was used for image acquisition. No multiplier was used between objective and the camera. A 775 nm filter was used to allow red/far red light to pass through the recorded slice. The light intensity was determined at the time when a slice was transferred into the recording chamber without saturated pixels. The same light intensity was used throughout the recording of a given event. Exposure time of each image was 10 ms. MicroManager (Edelstein et al., 2010, 2014) or Ocular (Teledyne Photometrics) was used for image acquisition. Images were stored in stacks and analyzed using ImageJ or Fiji (Schindelin et al., 2012; Schneider et al., 2012).

To visualize changes in light transmission in pseudocolor, several steps were taken. First, images during an event (SD or SLE) were subtracted from the baseline image. Specifically, Image Calculator in ImageJ was used to calculate the difference between an image stack of an event (Event Stack) and an image stack generated from the event's baseline image (Baseline Stack). The result was a stack of images that showed the difference from the baseline in light intensity (Result Stack). Next, images from Result Stack were pseudocolored for better visualization where warmer and cooler colors indicated higher and lower light transmission, respectively. The Event Stack was later combined with its Result Stack side by side for presentation (Combined Stack). The Combined Stack was saved as a video file and replayed to review the propagation of SD across hippocampal subfields (**Supplementary Video 1**).

Changes in light transmission were quantified using ImageJ. The quantification procedure is illustrated in **Supplementary Figure 3**. In short, a square box of 50 by 50 pixels was used to sample part of a cell layer of a subfield. The box size was chosen so that it enclosed a representative part of the cell layer with minimal overlap with adjacent layers. Each box was a region of interest (ROI) that was marked and added to the ROI Manager function in ImageJ. These regions included the CA3 cell layer (at or close to the electrophysiological recording site), GCL upper blade, GCL crest, GCL lower blade, and CA1. The Multi Measure function was used to obtain the mean gray value of each ROI (**Supplementary Figure 3**). Data were visualized in RStudio (v. 1.1.456[1]).

## Calculation of Spreading Depolarization Propagation Speed

Spreading depolarization propagation speed was calculated by dividing the length of the SD propagation path (in mm) by the timespan (in min) between two ROIs. An SD propagation path was drawn based on the observations of optical imaging. Because SD propagated from CA3 to CA1 like a wave, and the path followed the curvature of the pyramidal cell layer, the distance between CA3 and CA1 was measured along the curved cell layer and used to calculate the propagation speed. The distance between CA3 and the crest of GCL was measured in a different way because the wave front shown in the intrinsic optical images appeared to first move from CA3 to the upper blade in a linear path and then from upper to lower blade in a path following the curvature of the GCL. Therefore, the distance between CA3 and the crest of GCL was defined as the sum of two segments: (1) a straight line between the origin in CA3 and the tip of upper blade, and (2) a curved line along the GCL from the tip of upper blade to the crest. A timespan between two ROIs were determined

[1]http://www.rstudio.com/

by the number of images and the image sampling frequency (every 0.5 or 1 s).

## Quantification

Electrophysiological recordings were quantified using Clampfit software (v. 10.7 or 11.1.0.23, Molecular Devices). **Supplementary Figure 1A** illustrates how an SD was measured. When an SD was observed, its **onset** was the beginning of the train of bursts just before the DC negative shift. As mentioned above, a burst consisted of at least one population spike superimposed on a positivity. A 5–10 s period before the beginning of the train of bursts was defined as the **baseline**. The **amplitude** of an SD was measured from the baseline to the maximal negative deflection. **Additional synchronized activity** that occurred during the end of the recovery phase, also called afterdischarges, contained negative-going, fast spike-like events in extracellular recordings. This additional synchronized activity was documented in a binary fashion, i.e., slices either had or did not have them. SD **half duration** was the time from the onset of the negative DC shift to the timepoint when the recovery reached 1/2 of the peak amplitude of the negative DC shift.

**Supplementary Figure 1B** shows how SLEs were quantified. Similar to an SD, the **onset** of a SLE was the beginning of the train of bursts. There was no large DC negative shift like SD but there could be a small slow DC shift superimposed by bursts during a SLE. The **Amplitude** of this small DC shift during a SLE was defined by the difference between the baseline potential and the most negative deflection. Population spikes were not considered in this measurement. A 5–10 s period before the beginning of the train of bursts was defined as the baseline. The **duration** of a SLE was the onset of the first burst to the time when the last burst ceased.

## Statistical Analysis

Statistical analyses were performed using Prism (GraphPad) or RStudio (v. 1.1.463, see text footnote 1). Data were first examined for their normality using the Shapiro–Wilk test. Homogeneity of variance was tested using the *F* test. An unpaired *t*-test was used to compare means between two groups when data were normally distributed and without significant inhomogeneity of variance. When data were normally distributed with unequal variances, an unpaired *t*-test with Welch's correction was used. When data violated the assumption of normality, a Mann–Whitney *U* test was conducted for comparison of two groups. Maximal light change of SD and SLE in CA3 and CA1 was analyzed using a two-way ANOVA with event type and subregion as between-subject variables. Tukey's *post hoc* analysis was followed when the main test reached significance. The incidence of SD and SLE were compared using a Fisher's exact test. Differences were considered significant when $p < 0.05$. Prism, RStudio, Inkscape (v. 0.92[2]), and GNU Image Manipulation Program (GIMP, v. 2.10.18[3]) were used for preparation of figures.

[2]http://www.inkscape.org/

[3]http://www.gimp.org

# RESULTS

## An Interface-Like Chamber Promotes the Development of Spreading Depolarization and Seizure-Like Event in 0 $Mg^{2+}$/5 $K^+$ Artificial Cerebrospinal Fluid

Spreading depolarization in area CA3 occurs in an interface chamber when aCSF contains 0 $Mg^{2+}$/5 $K^+$ (Mody et al., 1987; Scharfman, 1997). To examine SD in submerged mouse hippocampal slices, we first used a classic submerged chamber commonly used in patch clamp recording (**Figure 1B**). Recordings were made in area CA3 and used extracellular recording methods (**Figure 1C**) because this was done in prior studies using interface chambers. Many slices (10/16 or 63% of all slices tested, n = 4 mice) did not show any SD or SLE within 60 min of 0 $Mg^{2+}$/5 $K^+$ aCSF exposure. However, some slices exhibited SD (3/16) and some showed SLEs (4/16; **Table 1**).

Because most slices did not exhibit SD or SLEs, and previous reports showed that network activity is facilitated when aCSF flows above and below submerged slices (Hájos and Mody, 2009; Hájos et al., 2009; Morris et al., 2016), we tested an interface-like chamber (**Figure 1B**) using the same slice preparation and recording methods. **Figure 1D** demonstrates a representative recording in the interface-like chamber. The recording shows the initial period of exposure (specifically from minute 5 to 50 after the start of exposure) of a mouse slice to 0 $Mg^{2+}$/5 $K^+$ aCSF. In this example, one SD (arrow) and five SLEs (arrowhead) occurred. Typically, we found one SD and many SLEs (discussed further below). Almost all slices developed SD and/or SLEs (44/45 slices, 22 mice). There were significantly more slices that developed SD in the interface-like chamber than in the classic chamber (Fisher's exact test, $p = 0.0009$; **Figure 1E**; **Table 1**).

In prior studies of SD in a submerged chamber, there is often an external stimulus to induce SD such as local application of high potassium or electrical stimulation (Lindquist and Shuttleworth, 2012; Steffensen et al., 2015). To the best of our knowledge, our results are the first to show SD in submerged slices using 0 $Mg^{2+}$/5 $K^+$ aCSF.

## Characteristics of Spreading Depolarization and Seizure-Like Events in 0 $Mg^{2+}$/5 $K^+$ Artificial Cerebrospinal Fluid

### Spreading Depolarization

In rat slices, SD did not develop in the interface-like chamber (20 slices, 10 rats, **Table 1**). Among mouse slices tested in the interface-like chamber, 80% of slices developed SD (36/45 slices, 22 mice; **Table 1**). The majority of slices showed one SD and the most SDs that were observed were three, and that was only found in one slice. The first SD developed after 33.6 ± 1.4 min exposure of 0 $Mg^{2+}$/5 $K^+$ aCSF (36 slices, 19 mice). In the slice that developed three SDs, the intervals between onsets of SDs were 12.1 and 13.3 min. The time between the onset of SD and the

beginning of the characteristic negative DC shift was 10.7 ± 0.8 s (36 slices, 19 mice).

The negative DC shift consisted of one or two peaks. Seventy-seven percent of slices that developed SD showed two peaks (27/35 slices, 18 mice; 1 slice was not included due to a technical problem that occurred during the recording). The time from the beginning of the negative DC shift to the first peak was 2.2 ± 0.2 s and to the second peak was 22.6 ± 1.9 s (27 slices, 18 mice). The peak amplitude of the first and the second peaks were −3.1 ± 0.4 and −3.5 ± 0.4 mV, respectively (27 slices, 18 mice). The amplitude difference between the two peaks was mostly within one standard deviation with only three exceptions, where two slices had a larger second peak and one slice had a larger first peak. It is notable that these amplitudes were small relative to those recorded in rat slices from an interface chamber with similar electrophysiological equipment. There, SD may be 10× larger or more (Scharfman, 1997; Scharfman et al., 2003; Skucas et al., 2013) but the smaller size in submerged chambers is common for all field potentials, and attributed to the more limited current flow.

For slices that developed only one SD, the timespan from the beginning to the peak of negative DC shift was 22.6 ± 12.7 s (8/35 slices, 7 mice).

The half duration of SD was 53.0 ± 4.7 s (35 slices, 19 mice). During the recovery phase, 29/36 slices showed additional synchronized activity. The synchronized activity lasted for 102.9 ± 6.1 s (29 slices, 17 mice). No sex difference was observed in the measurements of incidence of SD, number of SD, SD onset, and maximal SD amplitude (**Supplementary Figure 2**).

In a subset of experiments, simultaneous whole-cell recording was performed to examine the activity of individual CA3 pyramidal cells (PCs) during SD (five cells, five mice; **Figure 2A**). Recorded cells were filled with biocytin, and the cell type was confirmed later to have the morphological characteristics of CA3 PCs, such as a prominent apical dendritic tree, basal dendrites, and spiny dendrites (Lorente De Nó, 1934; **Figure 2B**). The electrophysiological characteristics also were consistent with a PC, such as an AP with a time course similar to a "regular spiking" neuron and an absence of the characteristic large afterhyperpolarizations of GABAergic neurons (Scharfman, 1993a,b, 1995).

In the five recorded PCs, a sudden, large depolarization that occurred at the start of SD was 21.5 ± 2.4 mV. After the cessation of cell firing, a second larger depolarization of 39.5 ± 3.7 mV followed. Therefore, the peak of the depolarizations was close to 0 mV. As expected for SD, the depolarization phase corresponded to the negative DC shift observed in the extracellular recording (**Figure 2C**). Cells repolarized and then hyperpolarized for 7.4 ± 3.2 mV before returning to their resting membrane potentials. Additional synchronized activity observed in extracellular recordings corresponded to large amplitude depolarizations and/or AP firing (**Figure 2C**).

## Seizure-Like Events

In 45 tested mouse slices, 49% of slices developed SLEs within the 60 min of exposure to 0 $Mg^{2+}$/5 $K^+$ aCSF (22/45 slices, 22 mice; **Table 1**). Among 22 slices that showed SLEs, 8 of them developed only SLEs and the other 14 slices developed both SD and SLEs. More SLEs developed in slices without an SD (without SD, 8 slices, 10 ± 1 SLEs; with SD, 14 slices, 5 ± 1 SLEs; unpaired *t*-test, $t(20) = 2.743$, $p = 0.01$), suggesting a negative interaction between SD and SLEs.

The average duration of SLEs was 41.4 ± 4.0 s (22 slices, 14 mice). Although the duration of SLEs was indifferent with or without an SD (without SD, 8 slices, 42.8 ± 2.8 s; with SD, 14 slices, 40.7 ± 6.2 s; unpaired *t*-test with Welch's correction, $t(17.42) = 0.3069$, $p = 0.76$), SLEs with SD showed greater variation than SLEs without SD (*F* test, $F = 8.8$, $p = 0.0079$). This result supports the idea mentioned above that SDs interfere with SLEs.

During SLEs, an extremely small negativity developed. The average negativity was −0.7 ± 0.1 mV (21 slices, 14 mice). The average negativity of SLEs did not appear to depend on appearance of SD (without SD, eight slices, −0.7 ± 0.1 mV; with SD, 13 slices, −0.7 ± 0.1 mV; unpaired *t*-test, $t(19) = 0.2455$, $p = 0.81$).

For seven cells in five mice, intracellular recordings were made simultaneous to extracellular recordings and showed the components of SLEs (**Figure 2D**). The trains of bursts during SLEs were qualitatively similar to the initial train of bursts at the onset of SD (**Figure 2C**). However, the duration of the train of bursts of an SLE was longer than the train of bursts at SD onset (SLEs, 40.9 ± 4.2 s, 21 slices, 13 mice; train of bursts at SD onset, 9.3 ± 0.8 s, 33 slices, 18 mice; Mann–Whitney test, $U = 3$, $p < 0.001$). The similarity in the trains of bursts of SLEs and SDs suggest that an SLE was a failure of bursts to trigger SD.

## Comparisons Between Spreading Depolarization and Seizure-Like Events

### *Incidence*

During the first 60 min of exposure to 0 $Mg^{2+}$/5 $K^+$ aCSF, 31% of mouse slices developed both SD and SLE (14/45 slices, 22 mice) while 49% of slices developed only SD (22/45 slices), and 18% of slices developed only SLEs (8/45 slices). The differences were significant, with more slices exhibiting SD than SLE (SD, 36/45 slices; SLE, 22/45 slices, Fisher's exact test, $p = 0.0039$, **Figure 2E1**). Each slice developed significantly fewer SDs than SLEs (SD, 0.8 ± 0.1; SLE, 3.2 ± 0.7; 45 slices, Wilcoxon matched pairs signed rank test, $p = 0.049$; **Figure 2E2**).

### *Onset of Spreading Depolarization and Seizure-Like Event*

The first SD occurred 33.6 ± 1.4 min after the slice was transferred into the recording chamber with 0 $Mg^{2+}$/5 $K^+$ aCSF (36 slices, 22 mice), which was not different from the first SLE (37.1 ± 2.4 min, 22 slices, 21 mice; unpaired *t*-test, $t(56) = 1.348$, $p = 0.18$; **Figure 2E3**). Among 14 slices that showed both SD and SLEs, SD was more likely to develop before a SLE (SD as the first event, 11/14 slices, SLE as the first event, 3/14 slices; Fisher's exact test, $p = 0.0027$). Thus, the onset of SD and SLE was similar, but an SD was more likely to be the first event in our 0 $Mg^{2+}$/5$K^+$ aCSF preparation.

### *Amplitude and Half-Duration*

When the DC shift was measured (for Methods, see **Supplementary Figure 1**), SDs showed an average of a 4.7 times larger negative shift than SLEs (SD, −3.3 ± 0.4 mV, 36

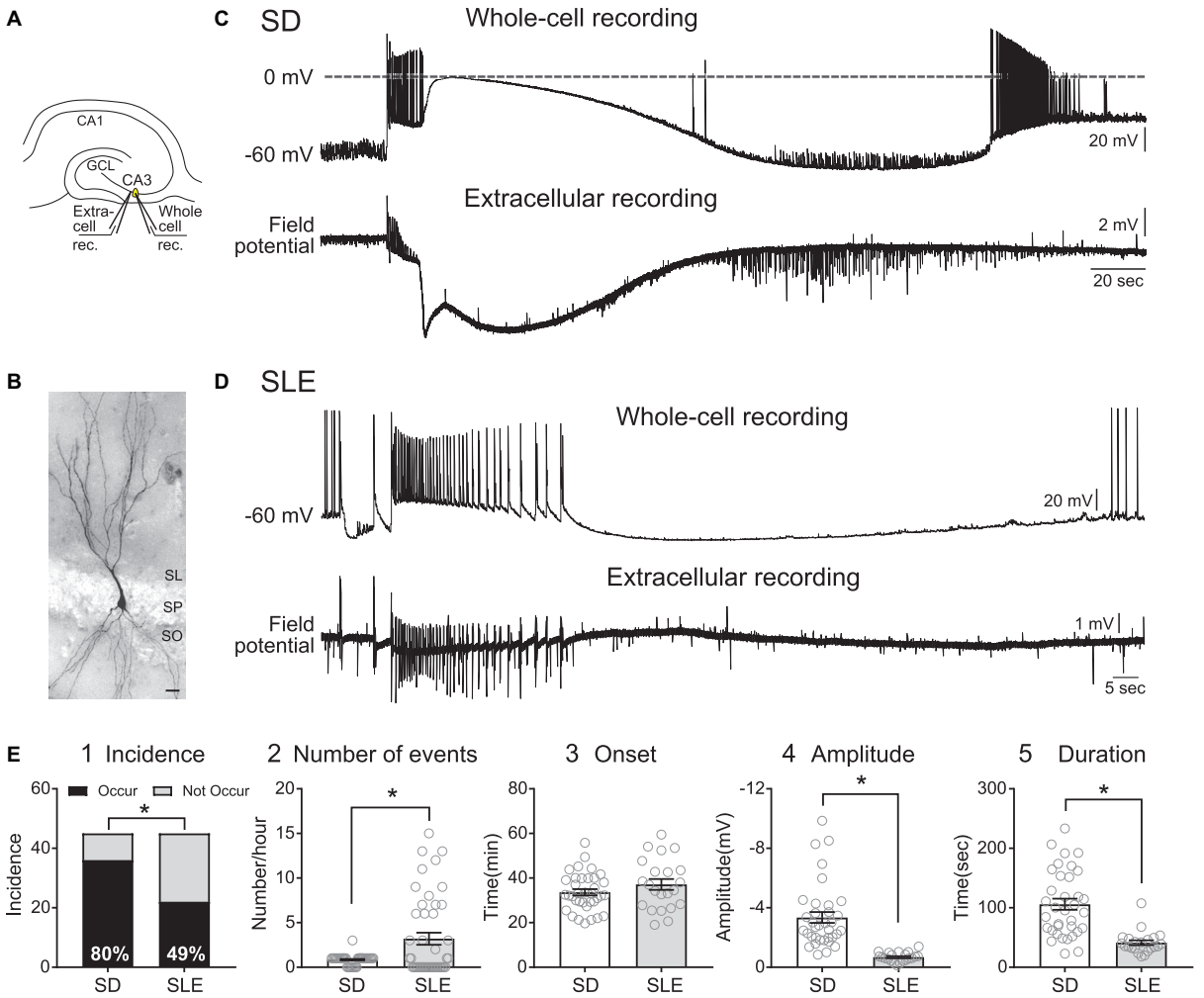


**FIGURE 2 |** SD and SLEs are two main types of events with distinct characters in the 0 $Mg^{2+}$/5 $K^+$ aCSF slice model. **(A)** Schematic illustrates the recording sites for simultaneous field potential and whole-cell recordings in CA3. **(B)** A representative image of a recorded and biocytin-filled CA3 pyramidal cell. SL, stratum lucidum; SP, stratum pyramidale; SO, stratum oriens. Scale bar, 20 μm. **(C)** Example of an SD. The intracellular and extracellular characteristics of SD are shown. **(D)** Example of a SLE. The intracellular recording shows characteristics such as a sudden depolarization and extensive firing. **(E)** Comparisons between SD and SLEs. (E1) In a 60-min recording period. SD showed a higher incidence than SLEs (two-sided Fisher's exact test, $p = 0.02$; asterisk indicates $p < 0.05$. (E2) In a 60-min recording period, more SLEs occurred than SDs (Wilcoxon test, $p = 0.01$). (E3) The onset of the first SD and SLE was not significantly different (unpaired $t$-test, $p = 0.18$). (E4) SD triggered a larger negative deflection than SLEs (Mann–Whitney test, $p < 0.0001$). (E5) SDs had a longer duration than SLEs (Mann–Whitney test, $p < 0.0001$). No sex difference was observed (**Supplementary Figure 2**).

slices, 19 mice; SLEs, −0.7 ± 0.1 mV, 22 slices, 14 mice; Mann–Whitney test, $U = 12$, $p < 0.0001$; **Figure 2E4**). When an SD's duration was estimated by doubling SD's half-duration, SD had duration more than twice the duration of SLEs (SD, 106 ± 9 s, 36 slices, 19 mice; SLE, 41 ± 4 s, 22 slices, 14 mice; Mann–Whitney test, $U = 12$, $p < 0.0001$, **Figure 2E5**). No sex difference was observed in these measures (**Supplementary Figure 2**).

## Spreading Depolarization Propagation

### Spreading Depolarization Spread to CA1 vs. Dentate Gyrus

Propagation across gray matter is an important feature of SD. When 0 $Mg^{2+}$/5 $K^+$ aCSF was used in the past, it was suggested that SD that begins in CA3 appears to spread to CA1 in hippocampus (Mody et al., 1987). Other studies using rabbit hippocampal slices and focal $K^+$ to elicit SD came to a similar conclusion (Haglund and Schwartzkroin, 1984). A spread to the dentate gyrus from CA3 through the upper blade has been reported when SDs are induced near CA2 using a local application of $K^+$ (Buchheim et al., 2002). Note the site is somewhat unclear because a diagram and text states CA1 but the depiction and images show CA2 or CA3a, depending on the septotemporal level, because the boundaries change with the septotemporal axis. However, spread from this general area to the dentate gyrus has not been studied before using 0 $Mg^{2+}$/5 $K^+$ aCSF. Therefore, we first confirmed that the SDs we observed did spread and then asked how they spread. The site of origin of SD in our experiments was CA3 regardless of the septotemporal level.

### *Extracellular Recordings*

We began by electrophysiological recording in two locations using extracellular methods. First, we examined the propagation of SD from CA3 to CA1 in 0 $Mg^{2+}$/5 $K^{+}$ aCSF. Extracellular recording electrodes were placed in the CA3b (where onset of SD was exhibited) and CA1b regions (**Figure 3A1**). In seven slices, five developed an SD in CA3. In two of these slices, CA1 showed an SD. Consistent with past reports, the onset of the negative DC shift in CA1 was delayed from CA3 by an average of 8 s (range 5–11 s, **Figure 3A2**) whereas the initial train of bursts occurred at similar time (<10 ms). These data are interesting because they suggest neuronal activity can occur with short a delays but the

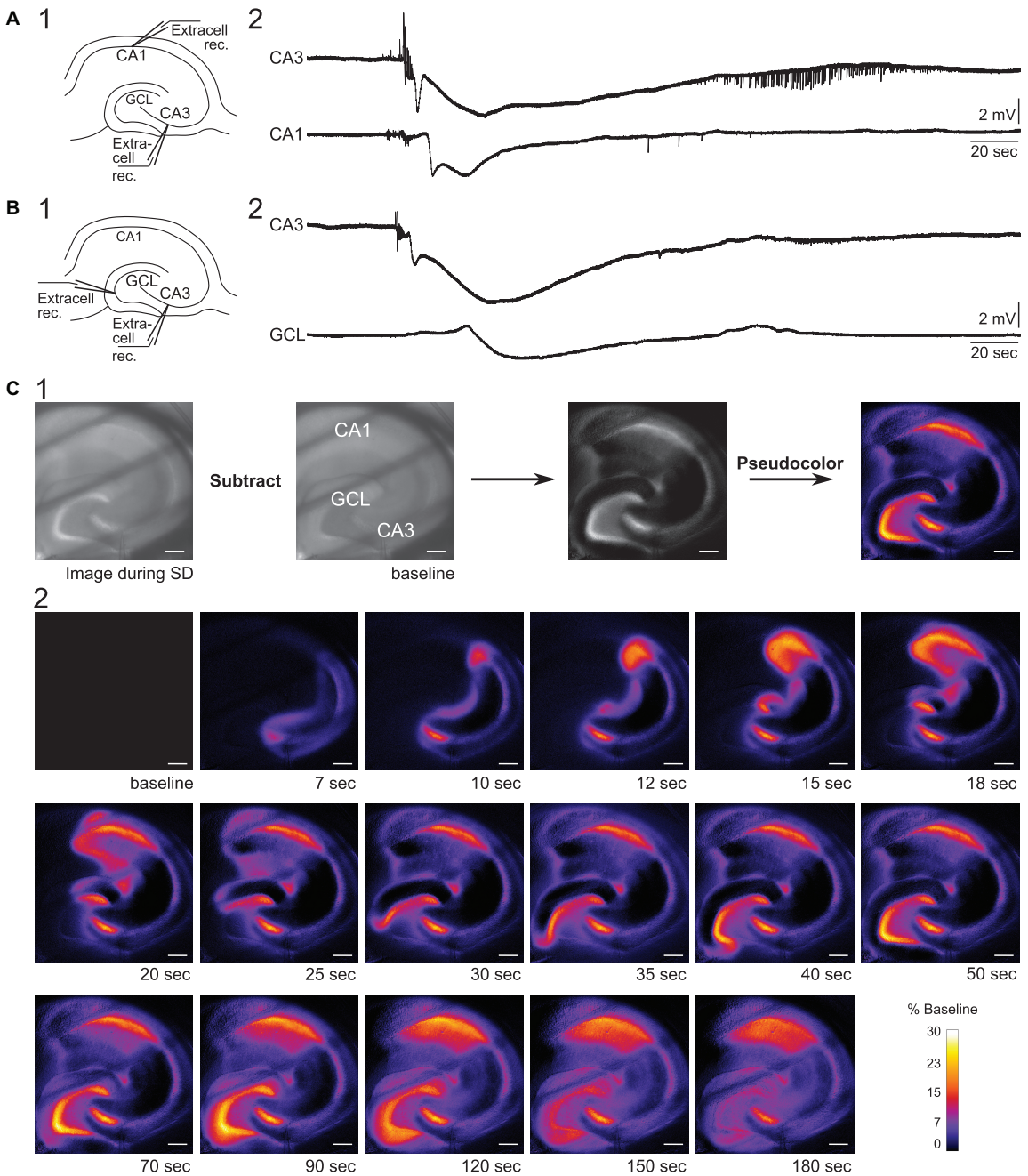


**FIGURE 3 |** Propagation of SD in mouse hippocampus. **(A1)** Schematic of dual field recordings in the CA3 and CA1. **(A2)** An SD propagated from CA3 to CA1. The electrical recordings show a significant delay between CA3 and CA1 DC shift, corresponding to the delay in the optical image in **(C)**. **(B1)** Schematic of dual field recordings in the CA1 and the GCL. **(B2)** An SD propagated from CA3 to the GCL with a delay. **(C1)** An SD was accompanied by a changed in the intrinsic optical signal. The difference in light transmission was calculated by subtracting a baseline image from the image acquired during SD. **(C2)** Consecutive images illustrate the propagation of an SD. Diagonal dark lines were from the mesh underneath the brain slice. GCL, granule cell layer. Scale bar, 200 μm.

large cell depolarization, occurring during the negative DC shift, is first in CA3 and very slowly propagates to CA1.

Next, we examined the propagation of SD from CA3 to the dentate gyrus. Extracellular recording electrodes were placed in the CA3 PCL and GCL at the crest of the dentate gyrus, which was chosen because it is the furthest point from CA3 in the GCL (**Figures 3B1,B2**). In two slices with these recording locations, both slices showed SD in the GCL with a long delay of 26.7 s (range 24.9–28.5 s, two slices from two different mice). Our data suggest that SD that develops in CA3 during superfusion of 0 $Mg^{2+}$/5 $K^+$ aCSF can propagate to both CA1 and dentate gyrus and with different delays, and the delay from CA3 to the dentate gyrus appears to be longer than the delay from CA3 to CA1.

### *Intrinsic Optical Imaging*

Spreading depolarization-induced neuronal swelling changes the light transmission. Specifically, the light transmission increases when an upright brightfield microscope is used (**Figure 3C1**, Buchheim et al., 2002; Mané and Müller, 2012). We used this characteristic of SD to examine the path of the SD wavefront across hippocampal subregions in our slice preparation.

To capture changes in light transmission that reflected SD propagation, images of SDs were taken and subtracted from the baseline image (see Methods and **Figure 3C1**). **Figure 3C2** shows images selected in temporal order throughout an SD. In 9/11 imaged slices the wave fronts of the SDs all emerged from CA3 (**Figure 4**). SDs of the exceptional two slices were not fully imaged so the emergence of their wavefronts was unclear. Within the nine slices, 44% of SDs propagated into both CA1 and the whole dentate gyrus (4/9 slices). Other SDs propagated either only into the whole dentate gyrus (2/9 slices), or only into hilus (2/9 slices), or only into CA1 (1/9 slices). The direction of SD propagation was either toward CA1 or toward the dentate gyrus or both. No association between propagation pattern and dorsoventral axis of hippocampus was observed.

To quantify the propagation speed of SDs, we measured the length of the SD traveling path among our defined regions of interests (see section "Calculation of Spreading Depolarization Propagation Speed") and the time that elapsed from the start of the path to its end. The propagation speed from CA3 to CA1 was 4.4 ± 1.6 mm/min (range 2.6–8.6 mm/min, five slices, three mice). The propagation speed from CA3 to the crest of the GCL in the dentate gyrus was 2.7 ± 0.5 mm/min (range 1.8–4.6 mm/min, nine slices, four mice). Propagation speed from CA3 to CA1 was not statistically different from the speed from CA3 to GCL [unpaired *t*-test with Welch's correction, $t(4.706) = 2.284$, $p = 0.07$].

The **Supplementary Video 1** shows the emergence, propagation, and recovery of an SD using original brightfield and pseudocolored images. Taken together, these results show that most SD wave fronts emerge from CA3 in 0 $Mg^{2+}$/5 $K^+$ aCSF. SD then spreads both in the direction of the trisynaptic circuit, i.e., to CA1, and in the opposite direction of the trisynaptic circuit, i.e., to the dentate gyrus. The speeds are similar and consistent with past studies (Obeidat and Andrew, 1998; Buchheim et al., 2002).

## Spreading Depolarization Spread From Upper to Lower Blades of the Dentate Gyrus

When SDs in CA3 propagated toward the dentate gyrus, 25% of SDs (3/12 slices, 6 mice) reached the hilus and/or upper blade of GCL but then stopped spreading to the other parts of the dentate gyrus. The rest of the SDs (9/12 slices, 6 mice) traveled to the upper blade and then spread to the crest and finally the lower blade (**Figure 5A**).

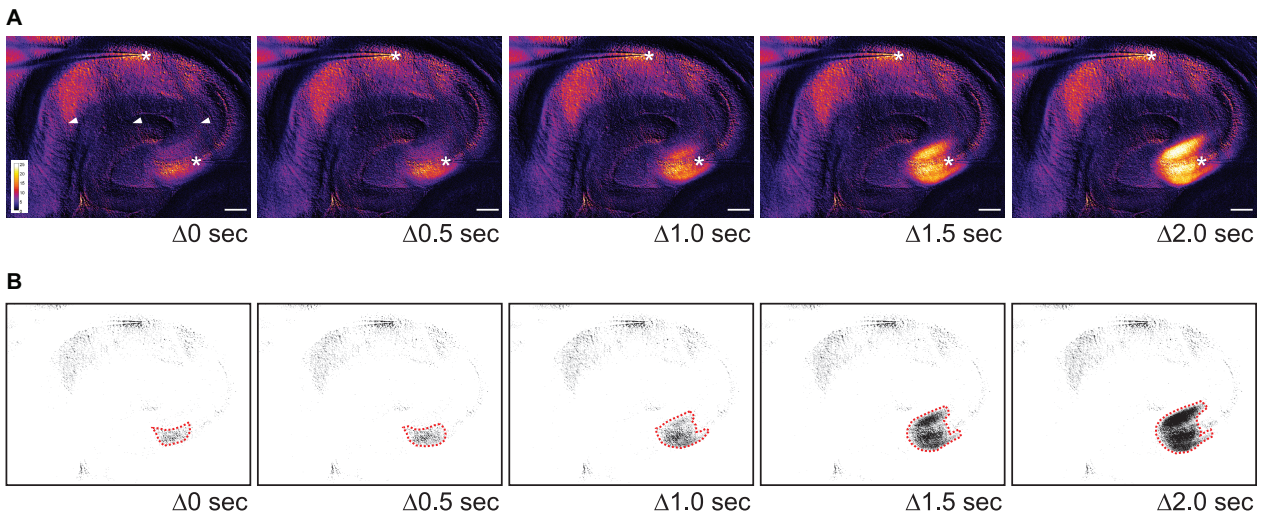


**FIGURE 4 |** The initial wave of SD often begins in CA3 in 0 $Mg^{2+}$/5 $K^+$ aCSF. **(A)** Time lapse images show the initiation site of an SD in CA3. The images during SD were first subtracted from a baseline image and then pseudocolored. Warmer color indicates higher light transmission and cooler color reflects lower light transmission. The increase in light transmission began in both SP and SL of CA3 before a wave front became prominent. Stars: recording sites in CA3 and CA1. Arrowheads: dark areas reflecting the mesh underneath the slice. Scale bar, 200 μm. **(B)** Same images from panel **(A)** were thresholded so that areas with the greatest change in light transmission in CA3 could be distinguished (dashed red lines).

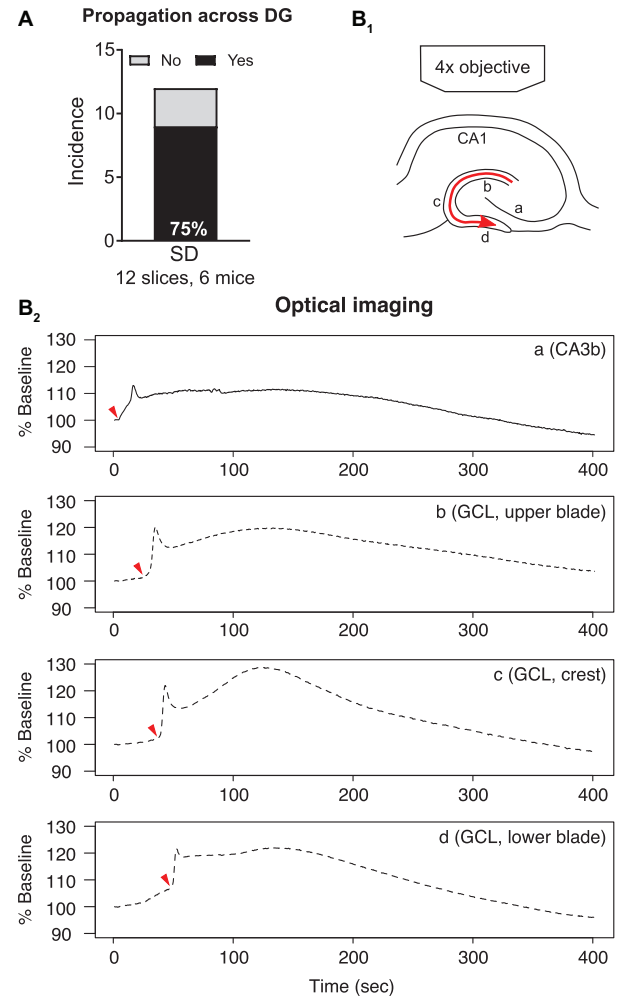


**FIGURE 5 |** Propagation of SD within the dentate gyrus. **(A)** SD that propagated from upper to lower blades occurred in the majority (77.8%) of optically recorded slices. **(B1)** A schematic of SD propagation. The red arrow indicates the observed direction of SD propagation. **(B2)** Representative traces of light changes in CA3b (a), GCL, upper blade (b), GCL, crest (c), and GCL, lower blade (d). Red arrowheads indicate the time when light transmission began the most rapid change, and shows the propagation of SD schematized in **(B1)**.

Spreading depolarizations we observed entered the dentate gyrus in two separate waves: into the hilus and into the lateral tip of upper blade (**Figure 3C2**). Although the lateral tip of lower blade of GCL was also approached by the wave front (**Figure 4**), it seemed to occur with entry into the hilus, which spread into the entire area between both blades rapidly. The wave front stopped at the boundary of hilus with the GCL. The wave front that entered the upper blade moved through the GCL and molecular layer together and followed the curvature of the GCL so that it traveled from upper blade to crest to lower blade in a slow continuous wave (**Figure 5B1**).

Quantification of light transmission supported the propagation pattern of SD wave front. The onset of sharp rise of light transmission happened in sequence among CA3b (**Figure 5B2a**), GCL upper blade (**Figure 5B2b**), GCL crest (**Figure 5B2c**), and GCL lower blade (**Figure 5B2d**). Interestingly, after the first peak in light transmission there was a short drop of light transmission followed by an increase of light transmission in the GCL and molecular layers (**Figure 5B2**, **Supplementary Video 1**). This secondary increase in light transmission was also observed in CA3 and CA1, and the underlying cellular correlates remain unclear.

To quantify the speed of propagation within the dentate gyrus, we measured the length of SD propagation by following SD's traveling path, and the time spent from upper blade, crest to lower blade (see section "Calculation of Spreading Depolarization Propagation Speed"). The speed of propagation was 2.8 ± 0.5 mm/min (range 1.4–4.0 mm/min, seven slices, four mice).

## Seizure-Like Events Showed Increased but Weak Intrinsic Optical Signals

Next, we quantified changes in light transmission of SLEs. **Figure 6** compares the change in light transmission of SDs to SLEs. In contrast to SD (**Figure 6A2**), the change in light transmission during the SLEs was minimal (**Figure 6B2**. However, although changes in light transmission in SLEs were small, they were significantly greater than baseline [one sample *t*-test, CA3, $t(6) = 4.75$, $p = 0.0032$; CA1, $t(6) = 3.96$, $p = 0.0075$].

It was not surprising that the percent change of maximal light transmission of SD was greater than SLEs [two-way ANOVA, SD vs. SLEs, $F(1,34) = 12.69$, $p = 0.0011$; CA3 vs. CA1, $F(1,34) = 0.34$, $p = 0.3376$; interaction, $F(1,34) = 0.3585$, $p = 0.5533$; **Figure 6C**]. This was true for CA1 (SD, 118.4 ± 4.7%, 12 SDs in 12 slices, 6 mice vs. SLEs, 104.0 ± 1.0%; 7 SLEs in 7 slices, 3 mice; $p = 0.03$, Tukey's multiple comparison test) but not for CA3 (SD, 113.0 ± 2.1%, 12 SDs in 12 slices, 6 mice vs. SLEs, 102.7 ± 0.6%; 7 SLEs in 7 slices, 3 mice; $p = 0.18$, Tukey's multiple comparison test). These data suggest that electrical recordings are quantitatively more sensitive than light transmissions.

In summary, SLEs showed a very small but detectable change in light transmission. The data are consistent with studies showing an increase in light transmission associated with an increase in neuronal activity (MacVicar and Hochman, 1991; D'Arcangelo et al., 2001).

# DISCUSSION

## Summary

In the present study, we first addressed methods to use mouse slices to study SD and SLEs during exposure to 0 $Mg^{2+}$/5 $K^{+}$ aCSF. We made several new insights (**Table 2**). We recorded these events using extracellular recording, whole-cell recording, and intrinsic optical imaging, which was advantageous both temporarily and spatially. We found that the chamber mattered: SD was more likely to develop in submerged mouse slices in an interface-like than in a classic submerged chamber. Species also mattered: mouse hippocampal slices developed SD and rat slices did not show SD. However, both species showed SLEs. Notably,

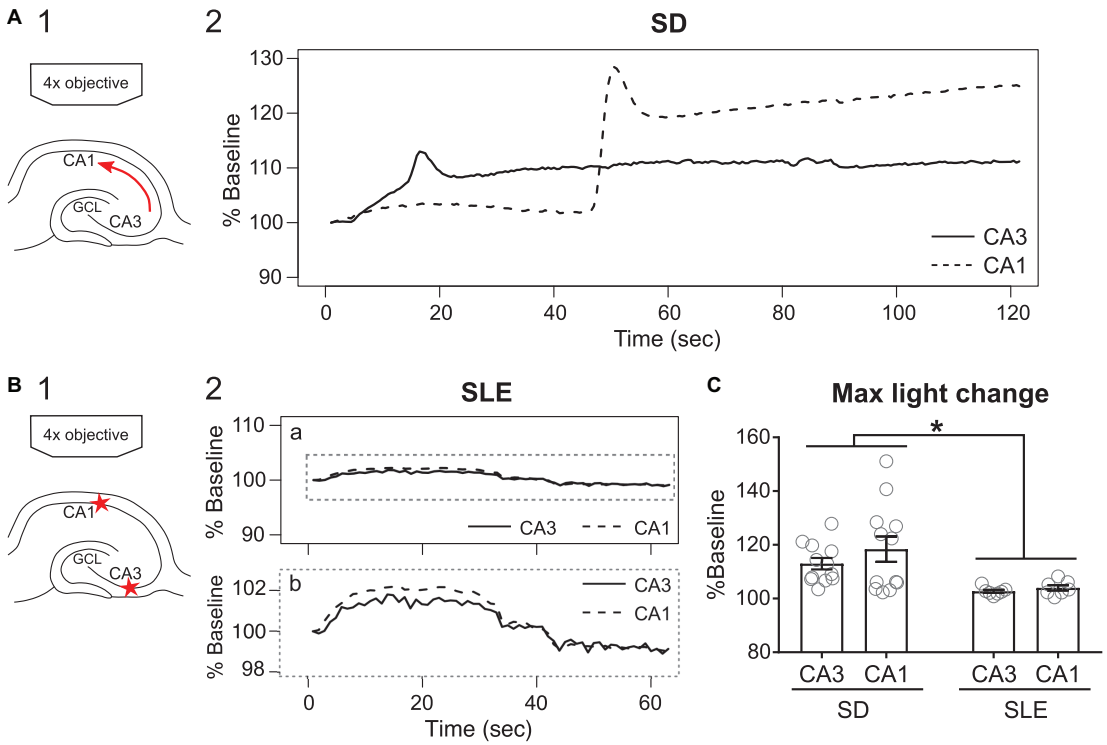


**FIGURE 6 |** SDs but not SLEs, show prominent changes in light transmission. **(A1)** Schematic of the path of light transmission in panel A2. Arrow indicates the propagation of the observed SD. **(A2)** Change of light transmission initiated in CA3 (solid line) and then followed by CA1 (dashed line) with a delay. **(B1)** Schematic of the region of interests (stars) in panel B2. **(B2)** A SLE showed subtle changes in light transmission (expanded in **b**) without a long delay between CA3 (solid line) and CA1 (dashed line). **(C)** SDs had significantly higher changes in light transmission than SLEs [two-way ANOVA, SD vs. SLEs, $F(1,34) = 12.69$, $p = 0.0011$; CA3 vs. CA1, $F(1,34) = 0.34$, $p = 0.3376$; interaction, $F(1,34) = 0.3585$, $p = 0.5533$].

**TABLE 2 |** Summary of new insights.

- Spontaneous SD following exposure to 0 $Mg^{2+}$/5 $K^{+}$ aCSF in submerged mouse slices occurs in the majority of slices but occurs only once or twice in the first hour of recording. SD does not appear to depend on an immature age or sex.
- Trains of bursts or what we call SLEs occurred in a robust manner, usually after SD, and occurred repetitively for the first hour of recording. SLEs were stereotypical in morphology, and associated with a change in optical transmission, but optical transmission changes were minimal relative to SD.
- SD began with a flurry of bursts followed by the large negative DC shift that is typical of SD. The flurry of bursts was similar to the trains of bursts that comprised SLEs, suggesting they may be related. Upon recovery there were often trains of synchronized activity (usually called afterdischarges).
- The fact that SD occurred and usually SLEs followed suggests that SDs could delay, interfere, or inhibit SLEs. The fact that SLEs occurred after SD and SD rarely repeated suggests that SLEs may have inhibited SD.
- Like focal stimulation to an area near CA2 (Buchheim et al., 2002), spread to the dentate gyrus from CA3 followed a path that typically involved slow invasion of the upper blade GCL and molecular layer from lateral tip to crest and then lower blade. Spread could also involve the entire hilar region, which has not been reported before. The optical transmission changes obeyed the GCL/hilar border in all cases, suggesting a novel aspect of the GCL/hilar border.
- Spread to CA1 from CA3 was delayed for the negative DC shift but minimal delay occurred for the initial electrical activity. In the dentate gyrus both were significantly delayed.
- Quantification of the optical transmission changes showed fluctuations during SD that were not observed by eye. These fluctuations varied from subfield to subfield, suggesting different dynamics of cell swelling that quantification can show better than the typical pseudocolor analyses.

*A summary of new insights gained from the Results are listed. These are discussed in the "Results and Discussion" sections.*

recording and imaging both SD and SLEs provided a chance to examine them in ways that have rarely been done in the past.

Intrinsic optical imaging allowed us to examine the emergence of the SD wave front and SD propagation without investing in additional dyes, transgenic mice, or equipment. Within hippocampus, we found that the majority of SDs initiated in CA3. Because of our imaging field only covered the hippocampus with limited cortical areas, we cannot exclude that SDs initiated in the small part of the cortex attached to the hippocampus (Martens-Mantai et al., 2014). Interestingly, when we recorded extracellular electrical activity in CA3 and CA1 simultaneously, the SDs began with a train of bursts with less than 10 ms delay between CA3 and CA1. However, the negative DC shift in CA3 immediately followed the train whereas in CA1 it was clearly delayed. The concurrent trains of bursts may have propagated synaptically from CA3 to CA1 but the drastic

cell depolarization that underlies the DC shift relies on other mechanisms. Alternatively, the entorhinal cortex (EC) innervates both CA3 and CA1 pyramidal cells (Witter et al., 2017) and may trigger trains of bursts.

In hippocampus, SD propagated along the direction of classic trisynaptic circuit into CA1 and in the opposite direction into dentate gyrus. Among SDs that propagated into dentate gyrus, they traveled in a way that is not consistent with the idea that SD spreads in all directions by a simple process. Instead, SDs propagated in two separate waves—one moved into hilus and the other moved along molecular layer and GCL. The wave front that propagated into hilus obeyed the boundary between GCL and hilus, and it dissipated in hilus. The wave front that moved into molecular layer and GCL propagated from upper blade to crest, and then lower blade. The wave front encompassed the entire molecular layer without involving adjacent layers in CA1 or the hilus.

Other researchers have also studied the DG, although with different methods. Obeidat and Andrew (1998) found that oxygen and glucose deprivation led to changes in light transmission in CA1 and the DG at a similar time. In contrast, focal application of high potassium to an area near the CA1 border with CA2 led to more of a change in the adjacent CA1 only. One limitation was the area near the lower blade was cropped so it was not visible for the reader.

The results of oxygen and glucose deprivation were striking. Interestingly, their images of the DG suggest a distinct pattern of spread in some ways and similarities to our data in other ways. The differences included invasion first of the upper blade molecular layer, which was not fully invaded. At that time the GCL did not appear to have light transmission changes but after that time the GCL showed striking changes and did so throughout the upper blade GCL. This pattern is quite different from what we found, where both the molecular layer and adjacent part of the GCL showed optical transmission changes at the same time. Furthermore, there was initiation at the lateral tip of the upper blade and then movement to the center of the upper blade, border with the crest region, the crest, and finally the lower blade. Another difference was a general lack of invasion of the hilus when oxygen and glucose deprivation was studied. However, there was a general pattern of spread from upper to lower blade in both models of SD. The differences could be partly explained by generation of SD in CA1 by oxygen and glucose deprivation and generation in CA3 for our work. Also, lack of hilar participation could simply be due to a larger hilar area in our horizontally prepared sections compared to transverse sections used for oxygen and glucose deprivation. Hilar involvement would also be more likely with CA3 playing a major role in SD initiation because of the CA3 backprojecting axons to the hilus (Scharfman, 2007).

Another group also provided a beautiful study of how the DG is invaded by SD (Buchheim et al., 2002). Buchheim et al. (2002) used local pressure application of 1M KCl in an area they stated was CA1 but could be CA2 or CA3a from the information in the figures. They found spread of SD into CA3 and then the upper blade, with subsequent spread toward the lower blade. The example that was shown had the lower blade clipped partially and at low power, so the hilus and GCL border were not entirely clear and some of the lower blade was absent entirely. There was late activity that could be part of the lower blade of the lower hilus - it is hard to say. One notable difference from our findings is invasion of the hilus seems absent except for the possibility of the late activity in the lower hilus. Our findings showed invasion could occur in the hilus extensively. The reason may be the septotemporal level of the slice, which was somewhat dorsal in the example of Buchheim et al. (2002). The backprojection from CA3 to the hilus is not as prominent in the dorsal hippocampus (Scharfman, 2007). Another noteworthy distinction is that the perforant path innervation of the DG is more robust in the horizontal plane in temporal sections (Witter et al., 2017). Dorsal sections transect the connections more. Thus, EC SD can spread to the DG readily in some ventral slices but not dorsally. Indeed, Buchheim et al. (2002) include a very nice diagram that shows spread from CA3 to the EC but no spread from the EC to the DG.

Our report is distinct in the ways described above, and the first one to show the SD propagation pattern in the DG using 0 $Mg^{2+}$/5 $K^{+}$ aCSF.

The consistent direction of SD propagation across different SD induction models suggests that a common structural factor, e.g., the components of the neuropil like the extracellular matrix and vasculature which is not necessarily homogeneous. In particular, the GCL/hilar border has a very different milieu, which makes it subject to injury (Soltesz et al., 1995).

In addition to SD, SLEs developed in 0 $Mg^{2+}$/5 $K^{+}$ aCSF. SD and SLE had distinct characteristics: (1) the negative DC shift of SDs were more than 5× that of SLEs'; (2) SDs were approximately 6× longer than SLEs; and (3) SDs had approximately 7× larger changes in light transmission than SLEs. However, the trains of bursts underlying SLEs were quite similar to those before SD. These results suggest that once a SLE is initiated in CA3, it could complete as a SLE or trigger an SD. Possible factors that could switch the progression of a SLE into an SD may be related to the degree the slice preparation preserves the recurrent collaterals of CA3 PCs, which would allow greater synchrony and in turn, greater local accumulation of ions. The mossy fiber pathway may also be a factor, because it can vary in the degree it is maintained in a slice also; if well maintained its normally high concentration of glutamate can be released onto CA3 PCs to a greater extent, facilitating SD. Although our data do not suggest major variations in these factors, slices can vary from one to the next and from one animal to another.

Taken together, our optimized model with 0 $Mg^{2+}$/5 $K^{+}$ aCSF led to a slow development of both SD and SLEs, which provides an opportunity to study these events without the typical trigger where the stimulus is immediately followed by SD. Additionally, our preparation also provided great temporal and spatial resolution by combining electrophysiological recording and optical imaging. We therefore think that this experimental model has many uses to advance our understanding of mechanisms of SD and interactions between SD and SLEs. Also, one could use the approach for validating preclinical drug candidates by taking advantage of a controlled *ex vivo* environment and relevance to disease mechanisms of migraine, TBI, stroke, etc.

## The Importance of the Recording Chamber

Submerged slices seem to be a suboptimal condition for SD and even the development of epileptiform activity when compared to slices situated at an interface of oxygenated solution and air. Thus, slices maintained in an interface chamber from rats showed both SD and epileptiform bursts in 0 $Mg^{2+}$ aCSF (3–5 mM $K^+$; Mody et al., 1987; Gloveli et al., 1995; Kovács et al., 1999), but only bursts were reported in submerged rat hippocampal slices in 0 $Mg^{2+}$ aCSF (2–5 mM $K^+$; Lewis et al., 1989, 1990; Neuman et al., 1989; Churn et al., 1991; Kojima et al., 1991; Billard et al., 1997; Wahab et al., 2009). When rat slices in a classic submerged chamber were compared with rat slices in an interface chamber, using experimental conditions that were otherwise the same, fewer submerged slices showed epileptiform bursts than slices in the interface chamber (Schuchmann et al., 2002).

Regarding anoxia-induced SD (hypoxia with normal glucose concentrations), SD occurred in an interface chamber but not in a classic submerged chamber (Croning and Haddad, 1998). Our data are consistent with these findings. On the other hand, when oxygen and glucose deprivation are used to induce SD, it has been shown that submerged slices exhibit SD (Juzekaeva et al., 2020; Grube et al., 2021).

Both SD and SLEs both have components of synchronized activity. An *in vitro* environment that supports synchronized activity would aid the development of SD and SLEs, and oxygen supply could be a critical player. The oxygen in interface chambers is supplied from carbogen-saturated humidified air and aCSF, while carbogen-saturated aCSF is the sole oxygen resource in submerged chambers. Since only a limited amount of oxygen can dissolve in aCSF, the direct contact with humidified air in an interface chamber has been considered as a more efficient way to supply oxygen than slices that obtain all oxygen from aCSF in a submerged chamber (Aitken et al., 1995). In interface chambers, rat brain slices showed *in vivo*-like rhythmic oscillations generated by synchronized cell activity (von Krosigk et al., 1993; Sanchez-Vives and McCormick, 2000; Case and Broberger, 2013). In submerged chambers, however, similar observations of synchronized activity seem possible only when oxygen supply is increased by superfusing aCSF above and below slices and using a fast flow rate (Hájos and Mody, 2009; Hájos et al., 2009). We found that the likelihood of developing SD in mouse slices significantly increased in an interface-like chamber, where 80% of mouse slices developed SD in an interface-like recording chamber when compared to 19% of slices in a classic recording chamber. Our results agree with previous findings that synchronous activity appears to be better supported in interface chambers. Furthermore, our results support the hypothesis that oxygen supply is important in SD and SLEs.

## Species Differences in the Development of Spreading Depolarization in 0 $Mg^{2+}$/5 $K^+$ Artificial Cerebrospinal Fluid

When mouse and rat slices were compared in the same preparation (interface-like chamber, fast flow, and 0 $Mg^{2+}$/5 $K^+$ aCSF), we found that SLEs were observed in slices from both species while SDs were exclusively in mouse slices, at least for SDs and SLEs following 0 $Mg^{2+}$/5 $K^+$ aCSF exposure. The discrepancy may be explained by the preservation of circuit components. We prepared both mouse and rat hippocampal slices using the same thickness (350 μm). When using the same thickness, others have been proposed that mouse slices are likely to preserve more connections and circuit properties than rat slices (Heinemann et al., 2006). This argument is based on the idea that, as similar brain circuitry is compressed in the mouse relative to the rat, the compression would force more elements into a smaller volume in mouse compared to rat. In support, it was stated that epileptiform activity is more readily elicited in mouse than rat (Heinemann et al., 2006). However, our experience is distinct from Heinemann et al. (2006) because we do not necessarily find epileptiform activity more readily elicited in mouse. For example, when mouse slices were exposed to a buffer than increased excitability, the latency to spontaneous epileptiform activity in the EC was longer than rat (Duffy et al., 2015).

It is also possible that the rat slices need more oxygen because they are larger in surface area, despite the same thickness as the mouse slices. Another possibility to explain the species difference could be related to age. The ranges of ages overlapped but the youngest mice were younger than the youngest rats. On the other hand, we tested very young rats and mice (postnatal day 21–22) and we obtained similar results—rat slices did not exhibit SD, but mouse slices did. Therefore, age did not appear to be a factor in species differences.

## Spreading Depolarization vs. Seizure-Like Events in 0 $Mg^{2+}$/5 $K^+$ Artificial Cerebrospinal Fluid

In slices that developed both types of events, 73% of slices developed SD first. Most slices exhibited only one SD (32 of 33 slices; the exceptional slice had three SDs) in the first hour of 0 $Mg^{2+}$/5 $K^+$ aCSF incubation. On the other hand, a slice could show multiple (1–16) SLEs with or without developing SD. These results are consistent with the suppression, interference, or delay of neural activity after SD. For example, in rat slices in an interface chamber, SDs occur spontaneously after 0 $Mg^{2+}$/5 $K^+$ aCSF exposure but only every 15 min. For minutes after an SD, responses to afferent stimulation in CA3 were weak (Scharfman, unpublished observations).

Both SD and SLEs developed in CA3 of mouse hippocampal slices in 0 $Mg^{2+}$/5 $K^+$ aCSF. When we examined the onset of SD, we found trains of bursts that were very similar to SLEs, but shorter. Why these bursts are followed by SD sometimes, but otherwise they do not appear to do so, is not clear. It could be the bursts are triggered by different mechanisms, one due to entorhinal cortical input and one intrinsic to CA3. These different mechanisms may recruit feedforward or feedback inhibition more for SLEs and less for SD. Another possibility is that SLEs sometimes trigger SD and sometimes do not. This hypothesis is consistent with the idea that SD can be a natural anti-seizure mechanism where a seizure triggers SD and then SD suppresses activity for some time afterward (Tamim et al., 2021).

## Propagation of Spreading Depolarization

We found that SD typically began in CA3. We used two methods to identify this: electrical recording from more than one location and intrinsic optical imaging. Since our imaging field was limited, our method did not allow us to determine if SD began in an extrahippocampal area but use of a lower power objective could do so in the future. An increase of light transmittance propagated toward both CA1 and dentate gyrus with up to 30% transmittance change locally. Interestingly, SLEs only showed subtle changes in the intrinsic optical signals (2%) but it was possible to visualize the small changes. It is possible that more detail might be clear with other wavelengths, such as 460–560 nm used previously (Mané and Müller, 2012). However, our recording at 775 nm was certainly sufficient.

Our analysis of SD propagation to the dentate gyrus is one of the few studies that have examined this issue. We found that SD propagated from CA3 to the dentate gyrus in a pattern that was unlike a unidirectional wave which approached the upper and lower blade simultaneously before the wavefront reached crest. Instead, SD circled around the dentate gyrus through upper blade, crest, and then lower blade. This pattern of SD spread from upper to lower blade was described before in response to SD elicited by focal $K^+$ stimulation to site near CA2 (Buchheim et al., 2002). Spread from upper to lower blade was also noted by Obeidat and Andrew (1998).

The reason for spread from upper to lower blade is not completely clear. There was no evidence that the lower blade had lower viability or better viability in our slices, based on viewing the cells in the slice with IR-DIC at 40×. Patched GCs from the lower blade were healthy and similar to the GCs in the upper blade.

## Advantages and Disadvantages of Our Methods

There are several advantages to the methods that we used. One advantage is to use the potent ability of reduced levels of $[Mg^{2+}]_o$ to release its normal inhibition of SD (Santos et al., 2016). To preserve our slices during dissection and recovery, we used $Mg^{2+}$ in the aCSF, but during recording and imaging it was removed. Use of this model is relevant to SD because there is a reduced $Mg^{2+}$ block of the NMDA receptor, which is a receptor that becomes unblocked by depolarization as well as removal of $Mg^{2+}$ from the aCSF. Depolarization occurs during the insult to the brain during TBI, seizures, and NMDA receptors are likely to become less blocked. Therefore, reducing $[Mg^{2+}]_o$ helps simulate the events during SD that occur during TBI and seizures. However, reducing $[Mg^{2+}]_o$ also has other effects. As noted before, the dynamics of intracellular $Ca^{2+}$ and frequency facilitation are affected, with facilitation promoted (Mody et al., 1987).

Regarding $[K^+]_o$, our model also was advantageous in that raising $[K^+]_o$ simulates the slow rise in $[K^+]_o$ after ischemic injury that leads to SD (Erdemli et al., 1998). In epilepsy, a rise in $[K^+]_o$ occurs at the onset of seizures and is thought to play a role in generation of the ictal state (Scharfman, 2015) which is typically followed by SD (Ssentongo et al., 2017). Therefore, by raising $[K^+]_o$ we simulated some of the changes that occur during SD *in vivo* in clinically relevant conditions.

On the other hand, as pointed out by Maslarova et al. (2011), in epileptic tissue there can be a resistance to SD and this was suggested to be due to a relatively high level of $[K^+]_o$ to foster SD. The threshold concentration of $[K^+]_o$ to facilitate SD in control slices was significantly lower than epileptic slices. Remarkably, the $[K^+]_o$ thresholds in that study were far above 10 mM whereas in our tissue we raised $[K^+]_o$ from 3.5 to 5 mM, much less of a change. There were several differences in the studies that could explain the discrepancies in concentrations of $[K^+]_o$ required to promote SD, such as use of neocortex and human tissue, and other factors such as 500 μm-thick slices.

Use of 0 $Mg^{2+}$/5 $K^+$ aCSF is also useful as a comparison to osmotic stress or oxygen and glucose deprivation. A very comprehensive recent study compared osmotic stress, oxygen/glucose deprivation, and focal methods using normal aCSF (Frank et al., 2021). Both osmotic stress and oxygen/glucose deprivation led to spontaneous SD, and SD had incomplete recovery and injury compared to SD induced by focal methods in normal aCSF. There was greater spread of SD induced by osmotic stress and oxygen/glucose deprivation than the SD induced by focal methods in normal aCSF. In the present study, 0 $Mg^{2+}$/5 $K^+$ aCSF induced SD that appeared to recover completely and extensive neural injury did not seem to occur. One reason may be that there is less risk of injury with 0 $Mg^{2+}$/5 $K^+$ aCSF because of the relative lack of osmotic stress and presence of oxygen and glucose. If that is true, the 0 $Mg^{2+}$/5 $K^+$ aCSF provides a method to induce spontaneous SD that is not as severe in consequences, something that may be relevant to SD in migraine where neurons may not become damaged despite repetitive migraines. On the other hand, osmotic stress and oxygen/glucose deprivation may be more relevant to TBI and stroke that lead to severe damage.

Our slice model provides a method to expand the repertoire of a patch clamp rig to study spatiotemporal dynamics of both SD and SLEs without costly investments. While we found limitations with the classic submerged chamber, a slight modification to use a design more like an interface chamber circumvented the problem. This interface-like design can be fabricated or, as was the case in our study, purchased. The cost of a chamber was one of the few investments our methods required. Using a fast flow rate seemed important and is highly feasible.

Although rat slices could be used with the interface-like chamber, SD was not common. This might be circumvented by a mini-slice (if the problem is the large size of the slice, mentioned above), but then all subfields could not be imaged. Therefore, rat studies of SD are feasible with our methods but will require more animals to sample SD enough for statistical comparisons.

One advantage of our methods was that SD occurred faster than in prior studies using a classic interface chamber. SD only spontaneously developed after 2 h of 0 $Mg^{2+}$/5 $K^+$ aCSF exposure in a previous study and that spontaneous SD only was mentioned as occurring once (Mody et al., 1987). In comparison, we observed spontaneously developed SD within the first hour of 0 $Mg^{2+}$/5 $K^+$ aCSF incubation.

The methods can potentially be used with ways to induce SD other than 0 $Mg^{2+}$/5 $K^{+}$ aCSF, such as local high K application, low calcium, ouabain, etc. It also can be used with transgenic mice, optogenetics, chemogenetics, and other methods currently used in research. Pharmacology is more readily used with the submerged chamber designs due to a smaller volume in the chamber compared to classic interface chambers. Therefore, drug studies and preclinical studies are facilitated by our methods.

The ability to induce both SD and SLEs is also useful for future studies of neuronal excitability and preclinical studies for epilepsy. For example, when a drug will be inhibitory to SD but facilitate SLEs is important to identify. The opposite, a drug that inhibits SLEs but leads to more SD is important.

Although we found no sex differences in the development of SD in mouse hippocampal slices, this may simply be due to the fact that the mice had not yet reached sexual maturity (Bell, 2018). Extending our findings into adulthood will be valuable in the future because of sex differences and hormonal regulation of in SD (Scharfman et al., 2003; Harte-Hargrove et al., 2013; Skucas et al., 2013; Scharfman and MacLusky, 2014). This topic has important translational implications because of sex differences in migraine and epilepsy (Scharfman and MacLusky, 2008, 2014; Vetvik and MacGregor, 2017).

There are also some disadvantages to the methods that we used. Although we were able to examine SD without a focal stimulus, the unpredictability of these SDs made it hard to trigger the start of video at the baseline before SD occurred. One method to circumvent the issue is to record throughout exposure to 0 $Mg^{2+}$/5 $K^{+}$ aCSF, and as digital acquisition and storage improve such prolonged recording is likely to be easier.

## CONCLUSION

Spreading depolarization and seizure-like events are both products of hypersynchronized activity of brain cells. We optimized a classic 0 $Mg^{2+}$/5 $K^{+}$ aCSF model for submerged hippocampal slices so both SD and SLEs are spontaneously developed within the first hour of 0 $Mg^{2+}$/5 $K^{+}$ aCSF exposure. We also extended our ability to record intrinsic optical signals without additional costs. With the relevance of SD and seizure activity to many pathological conditions and neurological disorders, this optimized model provides an opportunity to study SD with temporal and spatial advantages. It could also address how SD and SLEs interact with each other in a controlled environment. We suggest that this model could be useful in testing mechanisms and validating treatment targets in pre-clinical studies.

## DATA AVAILABILITY STATEMENT

The raw data supporting the conclusions of this article will be made available by the authors, without undue reservation.

## ETHICS STATEMENT

The animal study was reviewed and approved by the Institutional Animal Care and Use Committee of The Nathan Kline Institute.

## AUTHOR CONTRIBUTIONS

Y-LL and HES conceived and designed the study and wrote the manuscript. Y-LL performed the experiments and analyzed the data. Both authors contributed to the article and approved the submitted version.

## ACKNOWLEDGMENTS

This study was supported by NIH grants AG-055328, MH-109305, NS-037562, NS-081203, Pyramid Biosciences, and the NY State Office of Mental Health. We thank Karim Elayouby for the technical support in immunolabeling experiments. We are grateful to (by alphabetical order) Elissavet Chartampila, Kasey Gerencer, Swati Jain, John LaFrancois, and David Alcantara-Gonzalez, Hannah Bernstein, Justin Botterill, Chiara Criscuolo, Áine Duffy, and Christos Lisgaras for their experimental supports and valuable discussions and feedback on the manuscript.

## SUPPLEMENTARY MATERIAL

The Supplementary Material for this article can be found online at: https://www.frontiersin.org/articles/10.3389/fncel.2021.761423/full#supplementary-material

## REFERENCES

Aitken, P. G., Breese, G. R., Dudek, F. F., Edwards, F., Espanol, M. T., Larkman, P. M., et al. (1995). Preparative methods for brain slices: a discussion. *J. Neurosci. Methods* 59, 139–149. doi: 10.1016/0165-0270(94)00204-T

Anderson, T. R., and Andrew, R. D. (2002). Spreading depression: imaging and blockade in the rat neocortical brain slice. *J. Neurophysiol.* 88, 2713–2725. doi: 10.1152/jn.00321.2002

Anderson, W. W., Anderson, W. W., Lewis, D. V., Scott Swartzwelder, H., and Wilson, W. A. (1986). Magnesium-free medium activates seizure-like events in the rat hippocampal slice. *Brain Res.* 398, 215–219. doi: 10.1016/0006-8993(86)91274-6

Avoli, M., D'Antuono, M., Louvel, J., Köhling, R., Biagini, G., Pumain, R., et al. (2002). Network and pharmacological mechanisms leading to epileptiform synchronization in the limbic system in vitro. *Prog. Neurobiol.* 68, 167–207. doi: 10.1016/S0301-0082(02)00077-1

Ayata, C., and Lauritzen, M. (2015). Spreading depression, spreading depolarizations, and the cerebral vasculature. *Physiol. Rev.* 95, 953–993. doi: 10.1152/physrev.00027.2014

Bell, M. R. (2018). Comparing postnatal development of gonadal hormones and associated social behaviors in rats, mice, and humans. *Endocrinology* 159, 2596–2613. doi: 10.1210/en.2018-00220

Billard, J. M., Jouvenceau, A., Lamour, Y., and Dutar, P. (1997). NMDA receptor activation in the aged rat: electrophysiological investigations in the CA1 area

of the hippocampal slice ex vivo. *Neurobiol. Aging* 18, 535–542. doi: 10.1016/S0197-4580(97)00104-8

Borck, C., and Jefferys, J. G. R. (1999). Seizure-like events in disinhibited ventral slices of adult rat hippocampus. *J. Neurophysiol.* 82, 2130–2142. doi: 10.1152/jn.1999.82.5.2130

Botterill, J. J., Nogovitsyn, N., Caruncho, H. J., and Kalynchuk, L. E. (2017). Selective plasticity of hippocampal GABAergic interneuron populations following kindling of different brain regions. *J. Comp. Neurol.* 525, 389–406. doi: 10.1002/cne.24071

Buchheim, K., Weissinger, F., Siegmund, H., Holtkamp, M., Schuchmann, S., and Meierkord, H. (2002). Intrinsic optical imaging reveals regionally different manifestation of spreading depression in hippocampal and entorhinal structures in vitro. *Exp. Neurol.* 175, 76–86. doi: 10.1006/exnr.2002.7893

Bugay, V., Bozdemir, E., Vigil, F. A., Chun, S. H., Holstein, D. M., Elliott, W. R., et al. (2020). A mouse model of repetitive blast traumatic brain injury reveals post-trauma seizures and increased neuronal excitability. *J. Neurotrauma* 37, 248–261. doi: 10.1089/neu.2018.6333

Case, L., and Broberger, C. (2013). A method for visually guided whole-cell recordings in brain slices exhibiting spontaneous rhythmic activity. *J. Neurosci. Methods* 212, 64–71. doi: 10.1016/j.jneumeth.2012.09.014

Churn, S. B., Anderson, W. W., and DeLorenzo, R. J. (1991). Exposure of hippocampal slices to magnesium-free medium produces epileptiform activity and simultaneously decreases calcium and calmodulin-dependent protein kinase II activity. *Epilepsy Res.* 9, 211–217. doi: 10.1016/0920-1211(91)90054-J

Croning, M. D., and Haddad, G. G. (1998). Comparison of brain slice chamber designs for investigations of oxygen deprivation in vitro. *J. Neurosci. Methods* 81, 103–111. doi: 10.1016/S0165-0270(98)00023-5

Czéh, G., Aitken, P. G., and Somjen, G. G. (1993). Membrane currents in CA1 pyramidal cells during spreading depression (SD) and SD-like hypoxic depolarization. *Brain Res.* 632, 195–208. doi: 10.1016/0006-8993(93)91154-K

D'Arcangelo, G., Tancredi, V., and Avoli, M. (2001). Intrinsic optical signals and electrographic seizures in the rat limbic system. *Neurobiol. Dis.* 8, 993–1005. doi: 10.1006/nbdi.2001.0445

Dreier, J. P. (2011). The role of spreading depression, spreading depolarization and spreading ischemia in neurological disease. *Nat. Med.* 17, 439–447. doi: 10.1038/nm.2333

Duffy, ÁM., Morales-Corraliza, J., Bermudez-Hernandez, K. M., Schaner, M. J., Magagna-Poveda, A., Mathews, P. M., et al. (2015). Entorhinal cortical defects in Tg2576 mice are present as early as 2-4 months of age. *Neurobiol. Aging* 36, 134–148. doi: 10.1016/j.neurobiolaging.2014.07.001

Edelstein, A., Amodaj, N., Hoover, K., Vale, R., and Stuurman, N. (2010). Computer control of microscopes using μManager. *Curr. Protoc. Mol. Biol.* 14, 1–17. doi: 10.1002/0471142727.mb1420s92

Edelstein, A. D., Tsuchida, M. A., Amodaj, N., Pinkard, H., Vale, R. D., and Stuurman, N. (2014). Advanced methods of microscope control using μManager software. *J. Biol. Methods* 1:e10. doi: 10.14440/jbm.2014.36

Eickhoff, M., Kovac, S., Shahabi, P., Ghadiri, M. K., Dreier, J. P., Stummer, W., et al. (2014). Spreading depression triggers ictaform activity in partially disinhibited neuronal tissues. *Exp. Neurol.* 253, 1–15. doi: 10.1016/j.expneurol.2013.12.008

Eikermann-Haerter, K., Negro, A., and Ayata, C. (2013). Spreading depression and the clinical correlates of migraine. *Rev. Neurosci.* 24, 353–363. doi: 10.1515/revneuro-2013-0005

Erdemli, G., Xu, Y. Z., and Krnjević, K. (1998). Potassium conductance causing hyperpolarization of CA1 hippocampal neurons during hypoxia. *J. Neurophysiol.* 80, 2378–2390. doi: 10.1152/jn.1998.80.5.2378

Frank, R., Bari, F., Menyhárt, Á, and Farkas, E. (2021). Comparative analysis of spreading depolarizations in brain slices exposed to osmotic or metabolic stress. *BMC Neurosci.* 22:33. doi: 10.1186/s12868-021-00637-0

Gloveli, T., Albrecht, D., and Heinemann, U. (1995). Properties of low Mg2+ induced epileptiform activity in rat hippocampal and entorhinal cortex slices during adolescence. *Dev. Brain Res.* 87, 145–152. doi: 10.1016/0165-3806(95)00069-P

Grube, P., Heuermann, C., Rozov, A., Both, M., Draguhn, A., and Hefter, D. (2021). Transient oxygen-glucose deprivation causes region- and cell type-dependent functional deficits in the mouse hippocampus in vitro. *eNeuro* 8:2021. doi: 10.1523/ENEURO.0221-21.2021

Haas, H. L., Schaerer, B., and Vosmansky, M. (1979). A simple perfusion chamber for the study of nervous tissue slices in vitro. *J. Neurosci. Methods* 1, 323–325. doi: 10.1016/0165-0270(79)90021-9

Hadley, A. (2010). *CombineZP Image Stacking Software*. Available online at: http://micropics.org.uk/

Haglund, M. M., and Schwartzkroin, P. A. (1984). Seizure-like spreading depression in immature rabbit hippocampus in vitro. *Brain Res.* 316, 51–59.

Hájos, N., Ellender, T. J., Zemankovics, R., Mann, E. O., Exley, R., Cragg, S. J., et al. (2009). Maintaining network activity in submerged hippocampal slices: importance of oxygen supply. *Eur. J. Neurosci.* 29, 319–327. doi: 10.1111/j.1460-9568.2008.06577.x

Hájos, N., and Mody, I. (2009). Establishing a physiological environment for visualized in vitro brain slice recordings by increasing oxygen supply and modifying aCSF content. *J. Neurosci. Methods* 183, 107–113. doi: 10.1016/j.jneumeth.2009.06.005

Hamam, B. N., and Kennedy, T. E. (2003). Visualization of the dendritic arbor of neurons in intact 500 μm thick brain slices. *J. Neurosci. Methods* 123, 61–67. doi: 10.1016/S0165-0270(02)00341-2

Harte-Hargrove, L. C., Maclusky, N. J., and Scharfman, H. E. (2013). Brain-derived neurotrophic factor-estrogen interactions in the hippocampal mossy fiber pathway: implications for normal brain function and disease. *Neuroscience* 239, 46–66. doi: 10.1016/j.neuroscience.2012.12.029

Hartings, J. A., Shuttleworth, C. W., Kirov, S. A., Ayata, C., Hinzman, J. M., Foreman, B., et al. (2017). The continuum of spreading depolarizations in acute cortical lesion development: examining Leão's legacy. *J. Cereb. Blood Flow Metab.* 37, 1571–1594. doi: 10.1177/0271678X16654495

Heinemann, U., Kann, O., and Schuchmann, S. (2006). "An overview of in vitro seizure models in acute and organotypic slices," in *Models of Seizures and Epilepsy*, eds A. Pitkänen, P. A. Schwartzkroin, and S. L. Moshé (Cambridge: Elsevier Academic Press), 35–44.

Juzekaeva, E., Gainutdinov, A., Mukhtarov, M., and Khazipov, R. (2020). Reappraisal of anoxic spreading depolarization as a terminal event during oxygen-glucose deprivation in brain slices in vitro. *Sci. Rep.* 10:18970. doi: 10.1038/s41598-020-75975-w

Kim, Y. K., Yang, E. J., Cho, K., Lim, J. Y., and Paik, N. J. (2014). Functional recovery after ischemic stroke is associated with reduced gabaergic inhibition in the cerebral cortex: a GABA PET study. *Neurorehabil. Neural Repair* 28, 576–583. doi: 10.1177/1545968313520411

Kojima, H., Kowada, M., and Bragdon, A. C. (1991). Mechanism of electrographic seizure generation in the rat brain slice in low magnesium medium: modulatory effect of interictal bursting on seizure generation. *Jpn. J. Psychiatry Neurol.* 45, 279–283. doi: 10.1111/j.1440-1819.1991.tb02472.x

Kovács, R., Gutiérrez, R., Kivi, A., Schuchmann, S., Gabriel, S., and Heinemann, U. (1999). Acute cell damage after low Mg2+-induced epileptiform activity in organotypic hippocampal slice cultures. *Neuroreport* 10, 207–213. doi: 10.1097/00001756-199902050-00002

Leão, A. A. P. (1944). Spreading depression of activity in the cerebral cortex. *J. Neurophysiol.* 7, 359–390. doi: 10.1152/jn.1944.7.6.359

Lewis, D. V., Jones, L. S., and Mott, D. D. (1990). Hippocampal epileptiform activity induced by magnesium-free medium: differences between areas CA1 and CA2-3. *Epilepsy Res.* 6, 95–101. doi: 10.1016/0920-1211(90)90083-8

Lewis, D. V., Jones, L. S., and Swartzwelder, H. S. (1989). The effects of baclofen and pertussis toxin on epileptiform activity induced in the hippocampal slice by magnesium depletion. *Epilepsy Res.* 4, 109–118. doi: 10.1016/0920-1211(89)90015-6

Lian, X. Y., and Stringer, J. L. (2004). Astrocytes contribute to regulation of extracellular calcium and potassium in the rat cerebral cortex during spreading depression. *Brain Res.* 1012, 177–184. doi: 10.1016/j.brainres.2004.04.011

Lindquist, B. E., and Shuttleworth, C. W. (2012). Adenosine receptor activation is responsible for prolonged depression of synaptic transmission after spreading depolarization in brain slices. *Neuroscience* 223, 365–376. doi: 10.1016/j.neuroscience.2012.07.053

Lorente De Nó, R. (1934). Studies on the structure of the cerebral cortex II. Continuation of the study of the ammonic system. *J. Psychol. Neurol.* 46, 113–177.

MacVicar, B. A., and Hochman, D. (1991). Imaging of synaptically evoked intrinsic optical signals in hippocampal slices. *J. Neurosci.* 11, 1458–1469. doi: 10.1523/jneurosci.11-05-01458.1991

Mané, M., and Müller, M. (2012). Temporo-Spectral imaging of intrinsic optical signals during hypoxia-induced spreading depression-like depolarization. *PLoS One* 7:e43981. doi: 10.1371/journal.pone.0043981

Martens-Mantai, T., Speckmann, E. J., and Gorji, A. (2014). Propagation of cortical spreading depression into the hippocampus: the role of the entorhinal cortex. *Synapse* 68, 574–584. doi: 10.1002/syn.21769

Maslarova, A., Alam, M., Reiffurth, C., Lapilover, E., Gorji, A., and Dreier, J. P. (2011). Chronically epileptic human and rat neocortex display a similar resistance against spreading depolarization in vitro. *Stroke* 42, 2917–2922. doi: 10.1161/STROKEAHA.111.621581

Mody, I., Lambert, J. D., and Heinemann, U. (1987). Low extracellular magnesium induces epileptiform activity and spreading depression in rat hippocampal slices. *J. Neurophysiol.* 57, 869–888. doi: 10.1152/jn.1987.57.3.869

Morris, G., Jiruska, P., Jefferys, J. G. R., and Powell, A. D. (2016). A new approach of modified submerged patch clamp recording reveals interneuronal dynamics during epileptiform oscillations. *Front. Neurosci.* 10:519. doi: 10.3389/fnins.2016.00519

Neuman, R. S., Cherubini, E., and Ben-Ari, Y. (1989). Endogenous and network bursts induced by N-methyl-D-aspartate and magnesium free medium in the CA3 region of the hippocampal slice. *Neuroscience* 28, 393–399. doi: 10.1016/0306-4522(89)90186-3

Noseda, R., and Burstein, R. (2013). Migraine pathophysiology: anatomy of the trigeminovascular pathway and associated neurological symptoms, cortical spreading depression, sensitization, and modulation of pain. *Pain* 154, S44–S53. doi: 10.1016/j.pain.2013.07.021

Obeidat, A. S., and Andrew, R. D. (1998). Spreading depression determines acute cellular damage in the hippocampal slice during oxygen/glucose deprivation. *Eur. J. Neurosci.* 10, 3451–3461. doi: 10.1046/j.1460-9568.1998.00358.x

Obeidat, A. S., Jarvis, C. R., and Andrew, R. D. (2000). Glutamate does not mediate acute neuronal damage after spreading depression induced by O2/glucose deprivation in the hippocampal slice. *J. Cereb. Blood Flow Metab.* 20, 412–422. doi: 10.1097/00004647-200002000-00024

Reyes-Garcia, S. Z., Scorza, C. A., Araújo, N. S., Ortiz-Villatoro, N. N., Jardim, A. P., Centeno, R., et al. (2018). Different patterns of epileptiform-like activity are generated in the sclerotic hippocampus from patients with drug-resistant temporal lobe epilepsy. *Sci. Rep.* 8:7116. doi: 10.1038/s41598-018-25378-9

Rogawski, M. A. (2013). "Migraine and epilepsy-shared mechanisms within the family of episodic disorders," in *Jasper's Basic Mechanisms of the Epilepsies*, eds J. L. Noebels, M. Avoli, M. A. Rogawski, R. W. Olsen, and A. V. Delgado-Escueta (Bethesda: National Center for Biotechnology Information), 930–944.

Sanchez-Vives, M. V., and McCormick, D. A. (2000). Cellular and network mechanisms of rhytmic recurrent activity in neocortex. *Nat. Neurosci.* 3, 1027–1034. doi: 10.1038/79848

Santos, E., León, F., Silos, H., Sanchez-Porras, R., Shuttleworth, C. W., Unterberg, A., et al. (2016). Incidence, hemodynamic, and electrical characteristics of spreading depolarization in a swine model are affected by local but not by intravenous application of magnesium. *J. Cereb. Blood Flow Metab.* 36, 2051–2057. doi: 10.1177/0271678X16671317

Scharfman, H. E. (1993a). Characteristics of spontaneous and evoked EPSPs recorded from dentate spiny hilar cells in rat hippocampal slices. *J. Neurophysiol.* 70, 742–757. doi: 10.1152/jn.1993.70.2.742

Scharfman, H. E. (1993b). Spiny neurons of area CA3c in rat hippocampal slices have similar electrophysiological characteristics and synaptic responses despite morphological variation. *Hippocampus* 3, 9–28. doi: 10.1002/hipo.450030103

Scharfman, H. E. (1995). Electrophysiological evidence that dentate hilar mossy cells are excitatory and innervate both granule cells and interneurons. *J. Neurophysiol.* 74, 179–194. doi: 10.1152/jn.1995.74.1.179

Scharfman, H. E. (1997). Hyperexcitability in combined entorhinal/hippocampal slices of adult rat after exposure to brain-derived neurotrophic factor. *J. Neurophysiol.* 78, 1082–1095. doi: 10.1152/jn.1997.78.2.1082

Scharfman, H. E. (2007). The CA3 "backprojection" to the dentate gyrus. *Prog Brain Res.* 63, 627–637. doi: 10.1016/S0079-6123(07)63034-9

Scharfman, H. E. (2015). "Epilepsy," in *Neurobiology of Brain Disorders: Biological Basis of Neurological and Psychiatric Disorders*, eds M. J. Zigmond, L. P. Rowland, and J. T. Coyle (Amsterdam: Elsevier Inc.), 236–261.

Scharfman, H. E., and MacLusky, N. J. (2008). Estrogen-growth factor interactions and their contributions to neurological disorders. *Headache* 48, S77–S89. doi: 10.1111/j.1526-4610.2008.01200.x

Scharfman, H. E., and MacLusky, N. J. (2014). Sex differences in the neurobiology of epilepsy: a preclinical perspective. *Neurobiol. Dis.* 72, 180–192. doi: 10.1016/j.nbd.2014.07.004

Scharfman, H. E., Mercurio, T. C., Goodman, J. H., Wilson, M. A., and MacLusky, N. J. (2003). Hippocampal excitability increases during the estrous cycle in the rat: a potential role for brain-derived neurotrophic factor. *J. Neurosci.* 23, 11641–11652.

Scharfman, H. E., Smith, K. L., Goodman, J. H., and Sollas, A. L. (2001). Survival of dentate hilar mossy cells after pilocarpine-induced seizures and their synchronized burst discharges with area CA3 pyramidal cells. *Neuroscience* 104, 741–759. doi: 10.1016/S0306-4522(01)00132-4

Schneider, C. A., Rasband, W. S., and Eliceiri, K. W. (2012). NIH Image to ImageJ: 25 years of image analysis. *Nat. Methods* 9, 671–675. doi: 10.1038/nmeth.2089

Schindelin, J., Arganda-Carreras, I., Frise, E., Kaynig, V., Longair, M., Pietzsch, T., et al. (2012). Fiji: an open-source platform for biological-image analysis. *Nat. Methods* 9, 676–82. doi: 10.1038/nmeth.2019

Schuchmann, S., Meierkord, H., Stenkamp, K., Breustedt, J., Windmüller, O., Heinemann, U., et al. (2002). Synaptic and nonsynaptic ictogenesis occurs at different temperatures in submerged and interface rat brain slices. *J. Neurophysiol.* 87, 2929–2935. doi: 10.1152/jn.2002.87.6.2929

Schwartzkroin, P. A. (1975). Characteristics of CA1 neurons recorded intracellularly in the hippocampal in vitro slice preparation. *Brain Res.* 85, 423–436. doi: 10.1016/0006-8993(75)90817-3

Skucas, V. A., Duffy, ÁM., Harte-Hargrove, L. C., Magagna-Poveda, A., Radman, T., Chakraborty, G., et al. (2013). Testosterone depletion in adult male rats increases mossy fiber transmission, LTP, and sprouting in area CA3 of Hippocampus. *J. Neurosci.* 33, 2338–2355. doi: 10.1523/jneurosci.3857-12.2013

Sloviter, R. S. (1991). Permanently altered hippocampal structure, excitability, and inhibition after experimental status epilepticus in the rat: the "dormant basket cell" hypothesis and its possible relevance to temporal lobe epilepsy. *Hippocampus* 1, 41–66. doi: 10.1002/hipo.450010106

Soltesz, I., Smetters, D. K., and Mody I. (1995). Tonic inhibition originates from synapses close to the soma. *Neuron* 14, 1273–1283. doi: 10.1016/0896-6273(95)90274-0

Snow, R. W., Taylor, C. P., and Dudek, F. E. (1983). Electrophysiological and optical changes in slices of rat hippocampus during spreading depression. *J. Neurophysiol.* 50, 561–572. doi: 10.1152/jn.1983.50.3.561

Somjen, G. G. (2001). Mechanisms of spreading depression and hypoxic spreading depression-like depolarization. *Physiol. Rev.* 81, 1065–1096. doi: 10.1152/physrev.2001.81.3.1065

Ssentongo, P., Robuccio, A. E., Thuku, G., Sim, D. G., Nabi, A., Bahari, F., et al. (2017). A Murine Model to Study Epilepsy and SUDEP Induced by Malaria Infection. *Sci. Rep.* 7:43652. doi: 10.1038/srep43652

Steffensen, A. B., Sword, J., Croom, D., Kirov, S. A., and MacAulay, N. (2015). Chloride cotransporters as a molecular mechanism underlying spreading depolarization-induced dendritic beading. *J. Neurosci.* 35, 12172–12187. doi: 10.1523/JNEUROSCI.0400-15.2015

Tamim, I., Chung, D. Y., de Morais, A. L., Loonen, I. C. M., Qin, T., Misra, A., et al. (2021). Spreading depression as an innate antiseizure mechanism. *Nat. Commun.* 12:2206. doi: 10.1038/s41467-021-22464-x

Umorin, M. (2002). *Stack Focuser*. Available online at: https://imagej.nih.gov/ij/plugins/stack-focuser.html.

Varga, D. P., Menyhárt, Á, Pósfai, B., Császár, E., Lénárt, N., Cserép, C., et al. (2020). Microglia alter the threshold of spreading depolarization and related potassium uptake in the mouse brain. *J. Cereb. Blood Flow Metab.* 40, S67–S80. doi: 10.1177/0271678X19900097

Vetvik, K. G., and MacGregor, E. A. (2017). Sex differences in the epidemiology, clinical features, and pathophysiology of migraine. *Lancet Neurol.* 16, 76–87. doi: 10.1016/S1474-4422(16)30293-9

von Krosigk, M., Bal, T., and McCormick, D. A. (1993). Cellular mechanisms of a synchronized oscillation in the thalamus. *Science* 261, 361–364. doi: 10.1126/science.8392750

Wahab, A., Heinemann, U., and Albus, K. (2009). Effects of γ-aminobutyric acid (GABA) agonists and a GABA uptake inhibitor on pharmacoresistant seizure like events in organotypic hippocampal slice cultures. *Epilepsy Res.* 86, 113–123. doi: 10.1016/j.eplepsyres.2009.05.008

Witter, M. P., Doan, T. P., Jacobsen, B., Nilssen, E. S., and Ohara, S. (2017). Architecture of the entorhinal cortex a review of entorhinal anatomy in rodents with some comparative notes. *Front. Syst. Neurosci.* 11:46. doi: 10.3389/fnsys.2017.00046

**Conflict of Interest:** The authors declare that the research was conducted in the absence of any commercial or financial relationships that could be construed as a potential conflict of interest.

**Publisher's Note:** All claims expressed in this article are solely those of the authors and do not necessarily represent those of their affiliated organizations, or those of the publisher, the editors and the reviewers. Any product that may be evaluated in this article, or claim that may be made by its manufacturer, is not guaranteed or endorsed by the publisher.

frontiers in Cellular Neuroscience

REVIEW
published: 10 February 2022
doi: 10.3389/fncel.2022.837650

# Migraine Aura, Transient Ischemic Attacks, Stroke, and Dying of the Brain Share the Same Key Pathophysiological Process in Neurons Driven by Gibbs–Donnan Forces, Namely Spreading Depolarization

*Coline L. Lemale[1,2], Janos Lückl[1,3,4], Viktor Horst[1], Clemens Reiffurth[1,2], Sebastian Major[1,2,5], Nils Hecht[6], Johannes Woitzik[7] and Jens P. Dreier[1,2,5,8,9]**

[1] Center for Stroke Research Berlin, Berlin Institute of Health, Charité – Universitätsmedizin Berlin, Corporate Member of Freie Universität Berlin, Humboldt-Universität zu Berlin, Berlin, Germany, [2] Department of Experimental Neurology, Berlin Institute of Health, Charité – Universitätsmedizin Berlin, Corporate Member of Freie Universität Berlin, Humboldt-Universität zu Berlin, Berlin, Germany, [3] Department of Medical Physics and Informatics, University of Szeged, Szeged, Hungary, [4] Department of Neurology, University of Szeged, Szeged, Hungary, [5] Department of Neurology, Berlin Institute of Health, Charité – Universitätsmedizin Berlin, Corporate Member of Freie Universität Berlin, Humboldt-Universität zu Berlin, Berlin, Germany, [6] Department of Neurosurgery, Berlin Institute of Health, Charité – Universitätsmedizin Berlin, Corporate Member of Freie Universität Berlin, Humboldt-Universität zu Berlin, Berlin, Germany, [7] Department of Neurosurgery, Evangelisches Krankenhaus Oldenburg, University of Oldenburg, Oldenburg, Germany, [8] Bernstein Center for Computational Neuroscience Berlin, Berlin, Germany, [9] Einstein Center for Neurosciences Berlin, Berlin, Germany

OPEN ACCESS

**Edited by:**
*Rustem Khazipov, Institut National de la Santé et de la Recherche Médicale (INSERM), France*

**Reviewed by:**
*Hulya Karatas, Hacettepe University, Turkey*
*Oscar Herreras, Spanish National Research Council (CSIC), Spain*

***Correspondence:**
*Jens P. Dreier*
*jens.dreier@charite.de*

**Specialty section:**
*This article was submitted to Cellular Neurophysiology, a section of the journal Frontiers in Cellular Neuroscience*

**Received:** *16 December 2021*
**Accepted:** *19 January 2022*
**Published:** *10 February 2022*

**Citation:**
*Lemale CL, Lückl J, Horst V, Reiffurth C, Major S, Hecht N, Woitzik J and Dreier JP (2022) Migraine Aura, Transient Ischemic Attacks, Stroke, and Dying of the Brain Share the Same Key Pathophysiological Process in Neurons Driven by Gibbs–Donnan Forces, Namely Spreading Depolarization. Front. Cell. Neurosci. 16:837650. doi: 10.3389/fncel.2022.837650*

Neuronal cytotoxic edema is the morphological correlate of the near-complete neuronal battery breakdown called spreading depolarization, or conversely, spreading depolarization is the electrophysiological correlate of the initial, still reversible phase of neuronal cytotoxic edema. Cytotoxic edema and spreading depolarization are thus different modalities of the same process, which represents a metastable universal reference state in the gray matter of the brain close to Gibbs–Donnan equilibrium. Different but merging sections of the spreading-depolarization continuum from short duration waves to intermediate duration waves to terminal waves occur in a plethora of clinical conditions, including migraine aura, ischemic stroke, traumatic brain injury, aneurysmal subarachnoid hemorrhage (aSAH) and delayed cerebral ischemia (DCI), spontaneous intracerebral hemorrhage, subdural hematoma, development of brain death, and the dying process during cardio circulatory arrest. Thus, spreading depolarization represents a prime and simultaneously the most neglected pathophysiological process in acute neurology. Aristides Leão postulated as early as the 1940s that the pathophysiological process in neurons underlying migraine aura is of the same nature as the pathophysiological process in neurons that occurs in response to cerebral circulatory arrest, because he assumed that spreading depolarization occurs in both conditions. With this in mind, it is not surprising that patients with migraine with aura

have about a twofold increased risk of stroke, as some spreading depolarizations leading to the patient percept of migraine aura could be caused by cerebral ischemia. However, it is in the nature of spreading depolarization that it can have different etiologies and not all spreading depolarizations arise because of ischemia. Spreading depolarization is observed as a negative direct current (DC) shift and associated with different changes in spontaneous brain activity in the alternating current (AC) band of the electrocorticogram. These are non-spreading depression and spreading activity depression and epileptiform activity. The same spreading depolarization wave may be associated with different activity changes in adjacent brain regions. Here, we review the basal mechanism underlying spreading depolarization and the associated activity changes. Using original recordings in animals and patients, we illustrate that the associated changes in spontaneous activity are by no means trivial, but pose unsolved mechanistic puzzles and require proper scientific analysis.

**Keywords: migraine aura, traumatic brain injury, circulatory arrest, subarachnoid hemorrhage, spreading depolarization, spreading depression, brain death, brain ischemia**

## INTRODUCTION

The brain is the most complex structure known in the universe. In this electrochemical organ, consciousness arises in a hitherto unknown way, which can perceive, feel, think and react, and which is periodically switched off and on again. Compared with these complex phenomena, the nature of the basic electrochemical process that occurs when neurons in the gray matter of the brain die under severe oxygen and glucose deprivation is relatively simple and, in effect, no different from the dying process in other cells of the body under the same conditions. Nevertheless, in the brain gray matter this electrochemical process has some interesting features that could result from the special structures that neurons have for processing information. These peculiarities include, for example, that this electrochemical process does not proceed slowly and steadily to completion as in other body cells, but abruptly reaches 90% within a few seconds about 1–5 min after the onset of severe energy deficiency, then apparently pauses for a while, and finally proceeds to completion unless the supply of oxygen and glucose resumes in time and recovery takes place. Another peculiarity is that it typically propagates slowly at a rate of 2–9 mm/min through the tissue in the form of a giant wave (Woitzik et al., 2013; Kaufmann et al., 2017; Milakara et al., 2017). Moreover, a similar giant wave can also occur in almost normal brain gray matter for largely unexplained reasons spontaneously. Under this condition, the event is only of short duration and causes comparatively mild neurological deficits. These mild deficits are referred to in neurology as migraine aura and usually disappear again without any long-term sequelae (Dreier and Reiffurth, 2015). Because neurons die faster than other body cells, it has been hypothesized that this giant wave could facilitate cell death (Gill et al., 1992; Mies et al., 1993; Busch et al., 1996; Takano et al., 1996; Dreier et al., 2007). However, definitive proof of this has yet to be provided and it is important that the wave is typically reversible at first (Luckl et al., 2018; Dreier et al., 2022). With a grain of salt (see below), the continuum from initially transient, reversible giant waves to the terminal wave can be experimentally triggered by flooding the tissue with increasing concentrations of the $Na^+/K^+$-ATPase inhibitor ouabain (Balestrino et al., 1999; Jarvis et al., 2001; Major et al., 2017). The neurons can remain in the wave state for some time without immediately dying. However, if this lasts for too long, they will die even though there is no deficiency of oxygen and glucose (Bignami and Palladini, 1966; Cornog et al., 1967; Lees and Leong, 1996). Conversely, the same giant wave can also be triggered when the $Na^+/K^+$-ATPase can no longer be activated due to a lack of oxygen, glucose and ultimately ATP (Jarvis et al., 2001; Somjen, 2001). However, if oxygen and glucose are reintroduced into the neural tissue shortly after the onset of the giant wave, ATP production starts up again, the $Na^+/K^+$-ATPase can thus be activated and the neurons survive (Ayad et al., 1994; Nozari et al., 2010; Luckl et al., 2018). The Brazilian physiologist Aristides Leão was the first to propose that this giant wave, now termed spreading depolarization, occurs in both migraine aura and cerebral circulatory arrest and is "*of the same nature*" in both conditions. He published the relevant papers on this translational hypothesis as early as 1945 and 1947 on the basis of animal observations, having described traces of the underlying phenomenon and its normal neurovascular response in animal experiments already in 1944

**Abbreviations:** AC, alternating current; aSAH, aneurysmal subarachnoid hemorrhage; ACSF, artificial cerebrospinal fluid; $[K^+]_{ACSF}$, artificial cerebrospinal fluid with an elevated $K^+$ concentration; BOLD, blood oxygen level-dependent; CNS, central nervous system; COSBID, Co-Operative Studies on Brain Injury Depolarizations; DCI, delayed cerebral ischemia; DW, diffusion-weighted; DC, direct current; ECoG, electrocorticography; EEG, electroencephalography; $[Ca^{2+}]_o$, extracellular $Ca^{2+}$ concentration; $[K^+]_o$, extracellular $K^+$ concentration; $[Na^+]_o$, extracellular $Na^+$ concentration; FHM, familial hemiplegic migraine; IEE, ictal epileptic events; $[K^+]_i$, intracellular $K^+$ concentration; $[Ca^{2+}]_i$, intraneuronal $Ca^{2+}$ concentration; $[Na^+]_i$, intraneuronal $Na^+$ concentration; IOS, intrinsic optical signal; MRI, magnetic resonance imaging; MCAO, middle cerebral artery occlusion; NUP, negative ultraslow potential; L-NNA, $N^G$-nitro-L-arginine; NO, nitric oxide; NOS, nitric oxide synthase; ROS, reactive oxygen species; rCBF, regional cerebral blood flow; SPECT, single-photon emission computed tomography; SDEA, spreading depolarization with epileptiform activity; $p_{ti}O_2$, tissue partial pressure of oxygen; TIA, transient ischemic attack; TBI, traumatic brain injury.

(Leão, 1944a,b, 1947; Leão and Morison, 1945). In particular, the experiments he describes in his 1947 paper are of refreshing intellectual clarity, as relevant today as they were more than 70 years ago, and a must read for anyone scientifically or clinically concerned with migraine aura and stroke. Specifically, Leão and Morison wrote in their 1945 paper (Leão and Morison, 1945): "Much has been written about vascular phenomena both in clinical epilepsy and the presumably related condition of migraine. The latter disease with the . . . slow march of scotomata in the visual or somatic sensory sphere is suggestively similar to the experimental phenomenon [the spreading depression] here described." Leão (1947) wrote: "The results seem to indicate that in the spreading depression of activity, a change of the same nature as one resulting from prolonged interruption of the circulation, occurs in the cerebral cortex. The electrical sign of this change is the negative voltage variation."

More than 70 years later, we have reached the point where numerous studies including five meta-analyses have confirmed the expected epidemiologic association between migraine with aura and ischemic stroke based on Leão's original hypothesis (Etminan et al., 2005; Schurks et al., 2009; Spector et al., 2010; Hu et al., 2017; Mahmoud et al., 2018; Oie et al., 2020). The relative risk of ischemic stroke is doubled in people with migraine with aura compared with those with neither migraine with aura nor migraine without aura. In contrast, it is uncertain whether the risk of ischemic stroke is altered in migraine patients without aura (Oie et al., 2020), which is one of the arguments that migraine with aura and migraine without aura share the same headache type but generally do not share the spreading-depolarization process. Regarding the pro and con arguments in this controversy, we would like to refer to the following more comprehensive account (Dreier and Reiffurth, 2015). Most importantly, the entire spreading-depolarization continuum from short duration, to intermediate duration, to terminal waves has now been clearly demonstrated electrocorticographically in patients in all its facets and peculiarities during symptoms of migraine aura (Major et al., 2020), alternating with electrographic seizures [=ictal epileptic events (IEE)] during status epilepticus (Fabricius et al., 2008; Dreier et al., 2012; Revankar et al., 2017), in ischemic stroke (Dohmen et al., 2008; Woitzik et al., 2013; Schumm et al., 2021; Sueiras et al., 2021), in traumatic brain injury (TBI) (Strong et al., 2002; Fabricius et al., 2006; Hartings et al., 2011b), in aneurysmal subarachnoid hemorrhage (aSAH) and delayed cerebral ischemia (DCI) (Dreier et al., 2006, 2009; Bosche et al., 2010; Oliveira-Ferreira et al., 2010; Hartings et al., 2017b; Luckl et al., 2018; Sugimoto et al., 2018), including both delayed transient ischemic attacks (TIA) (Dreier et al., 2022) and delayed ischemic stroke (Luckl et al., 2018), during spontaneous intracerebral hemorrhage (Fabricius et al., 2006; Helbok et al., 2017), during subdural hematoma (Mohammad et al., 2020), during the development of brain death (Carlson et al., 2019; Dreier et al., 2019, 2022) and during the dying process from circulatory arrest (Dreier et al., 2018b, 2022). In a prospective, observational, multicenter cohort study in 138 TBI patients, the occurrence of spreading depolarization clusters was independently associated with poor outcome (Hartings et al., 2020). In DISCHARGE-1, a recent prospective, observational, multicenter, cohort, diagnostic phase III trial in 180 aSAH patients, spreading depolarization variables were included in each multiple regression model for longitudinal neuroimaging-proven early, delayed, and total brain damage, outcome at 7 months, and patient death (Dreier et al., 2022). These statistical results strongly suggest that spreading depolarizations are an independent biomarker of progressive brain injury, which is not astonishing given that spreading depolarization experimentally represents the injury potential of the brain's gray matter (Major et al., 2020).

Surprisingly, it was not realized during several decades that there is no contradiction between the so-called vascular hypothesis of migraine by Harold Wolff and the neuronal hypothesis of Aristides Leão (see above) (Leão and Morison, 1945; Dreier et al., 2007; Dreier and Reiffurth, 2015). Wolff's vascular hypothesis posited that migraine aura arises from intracranial vasoconstriction and migraine headache from extracranial vasodilation (Blau, 2004). It is generally assumed today that extracranial vasodilation is neither necessary nor sufficient for migraine headache (Charles and Baca, 2013; Pietrobon and Moskowitz, 2014). However, with respect to migraine aura, this traditional controversy between the vascular and neuronal theory dissolved when it became clear that epipial, i.e., abluminal, application of the vasoconstrictor polypeptide endothelin-1 is currently the most potent trigger of spreading depolarization in rodents *in vivo* and that endothelin-1 has this effect because of its vasoconstrictor properties, causing an imbalance between energy supply and demand of neurons (Dreier et al., 2002a). These findings have contributed significantly to the hypothesis that endothelial dysfunction could be one of the different etiologies leading to spreading depolarization and migraine aura in certain circumstances (Kleeberg et al., 2004; Dreier et al., 2007; Ducros, 2012; Dreier and Reiffurth, 2015; Liman et al., 2015; Oliveira-Ferreira et al., 2020; Paolucci et al., 2021). In recent clinical studies, intravenous infusion of endothelin-1 induced aura symptoms neither in healthy volunteers nor in patients with a history of migraine aura (Hougaard et al., 2020a,b). However, these clinical findings do not in any way contradict the assumption that endothelin-1 could be involved in the development of migraine auras, because endothelin-1 does not cross the blood–brain barrier and becomes a vasodilator when applied intraluminally instead of abluminally, since it causes the release of nitric oxide (NO) under this condition (Kobari et al., 1994a,b). In addition to ischemia, of course, there are countless other more or less harmful triggers for spreading depolarization. Thus, the fact that some migraine auras have a vascular etiology does not mean that all migraine auras have a vascular etiology (van den Maagdenberg et al., 2004; Leo et al., 2011; Brennan et al., 2013; Dreier and Reiffurth, 2015; Jansen et al., 2020). It has been particularly well established clinically and in animal experiments for familial hemiplegic migraine (FHM) types 1 and 3 as examples of primary neuronal disorders (Vahedi et al., 2000; Ducros et al., 2001; van den Maagdenberg et al., 2004; Dichgans et al., 2005; Jansen et al., 2020) and for FHM type 2 as an example of a primary astrocytic disorder (De Fusco et al., 2003; Jurkat-Rott et al., 2004; Dreier et al., 2005; Leo et al., 2011; Reiffurth et al., 2020; Smith et al., 2020; Parker et al., 2021) that not only primary vascular but

also primary neuronal and primary astrocytic dysfunctions can lead to spreading depolarization. Indeed, it was already known before the discovery of FHM mutations that primary astrocytic dysfunction is a potent trigger of spreading depolarization (Largo et al., 1996b).

For many decades, spreading depolarization was considered by leading neurologists as a purely animal and experimental phenomenon, whose transferability to humans fell into the realm of "neuromythology" (Blau, 1992, 2004). Only a few have at least assumed that it could occur in migraine aura, but at the same time have often blanked out the fact that the occurrence of spreading depolarization in migraine aura is only the tip of the iceberg and spreading depolarizations have infinitely more implications in neurology. Ultimately, Leão was correct in highlighting the importance of spreading depolarization for both human migraine aura and human cerebral circulatory disorders based on his animal experiments (Leão and Morison, 1945; Leão, 1947). And, in retrospect, it is quite incomprehensible why this prime mechanism of acute cerebral injury in the brain's gray matter was virtually always ignored in the preclinical preparation of the myriad, consistently negative clinical neuroprotection trials (Ginsberg, 2008). We now know that spreading depolarization ends up being the phenomenon that can be reliably reproduced across all species higher than mollusks (Spong et al., 2017; Robertson et al., 2020), and in all models with preserved cytoarchitecture (Kunkler et al., 2004; Pomper et al., 2006), and plays a key role in the mammalian brain, including the human brain, as a universal reference state in the cascades of acute neuronal injury and damage development. Once again, the dictum of Max Planck seems to prove true: "*A new scientific truth does not triumph by convincing its opponents and making them see the light, but rather because its opponents eventually die and a new generation grows up that is familiar with it*" (Planck, 1968). Many minds have contributed to the recognition of the importance of spreading depolarizations to neurology, most notably the Co-Operative Studies on Brain Injury Depolarizations (COSBID[1]), founded in 2003, which were based on a paper by Strong et al. (2002) who showed that spreading depressions of cortical activity can be recorded using subdural electrode strips in TBI patients. A particularly valuable source of inspiration for understanding the underlying mechanisms of spreading depolarization in physiological and energy-depleted tissues remains George Somjen's book, Ions in the Brain (Somjen, 2004a).

## THE SPREADING-DEPOLARIZATION CONTINUUM

Spreading depolarization is observed as a negative direct current (DC) shift using electrocorticography (ECoG) (Dreier, 2011; Herreras and Makarova, 2020). The spreading-depolarization continuum describes the spectrum from transient waves with negative DC shifts of intermediate to short duration in less ischemic or adequately supplied tissue, to terminal waves in severely ischemic tissue characterized by long-lasting DC shifts and transition of the neurons from the state of acute injury to cell death (Dreier and Reiffurth, 2015; Hartings et al., 2017a). The concept of the spreading-depolarization continuum is important to understand why spreading depolarization is a prime pathophysiological process in acute neurology. The continuum is particularly easy to trace in focal cerebral ischemia secondary to proximal cerebral artery occlusion. For example, in **Figure 1**, the spreading depolarization continuum is shown in progressively shorter negative DC shifts along an imaginary path from the ischemic core across the penumbra to normally perfused tissue after middle cerebral artery occlusion (MCAO) (Koroleva and Bures, 1996; Dijkhuizen et al., 1999; Nallet et al., 1999). Thus, the development of cell damage in focal cerebral ischemia is characterized by wave-like exacerbations alternating with partial recoveries (Dreier et al., 2018a). The simplified and frequently used conceptual model postulates the existence of an ischemic core in which neurons die more or less immediately. In reality, however, energetic failure and spreading depolarization initiating the neuronal damage occur along a dynamic continuum in space and time (del Zoppo et al., 2011). Importantly, in focal cerebral ischemia, at least 15 min must elapse during which neurons are in the state of spreading depolarization before the first neurons in the ischemic core begin to die (Heiss and Rosner, 1983; Memezawa et al., 1992; Shen et al., 2005; Pignataro et al., 2007; Nozari et al., 2010; Luckl et al., 2018). This means that when the animals are sacrificed 72 h later, no necrotic neurons are found in the ischemic core if the ischemic core was reperfused within 15 min, even though perfusion was very low and neurons were persistently in the state of spreading depolarization during the ischemic period (Luckl et al., 2018). Around the persistently depolarized ischemic core, there is a spatially distinct region of ischemic penumbra with functionally challenged neurons that survive longer than those in the ischemic core (Hossmann, 1996). However, recurrent spreading depolarizations in the penumbra may result in increased metabolic demand, additional regional cerebral blood flow (rCBF) reduction and delayed spatial expansion of the irreversibly damaged zone that typically follows an onion-skin-like growth pattern (Gyngell et al., 1995; Busch et al., 1996; Takano et al., 1996; Dreier et al., 2007). The mechanism that ultimately leads to neuronal death can vary. In general, an extreme lack of energy causes necrotic cell death with a delay of minutes up to tens of minutes, while a milder lack of energy is more likely to result in apoptotic cell death with a delay of hours up to several days. Similar to practically all relevant mechanisms of stroke, it also applies to necrosis and apoptosis that they are not strictly separable processes, but are on a continuum, partially sharing common pathways. Furthermore, non-apoptotic regulated cell death may also contribute to the final tissue damage in stroke (Tang et al., 2019). The cell death continuum becomes apparent when cell death is followed from the ischemic core into the penumbra (Charriaut-Marlangue et al., 1996). The words 'ischemic core' and 'penumbra' thus represent gross simplifications that squeeze the high spatial and temporal complexity and variability of stroke development into a handy concept that is suitable for many practical applications in the clinic, but has unfortunately led to the misperception in scientific

[1] www.cosbid.org

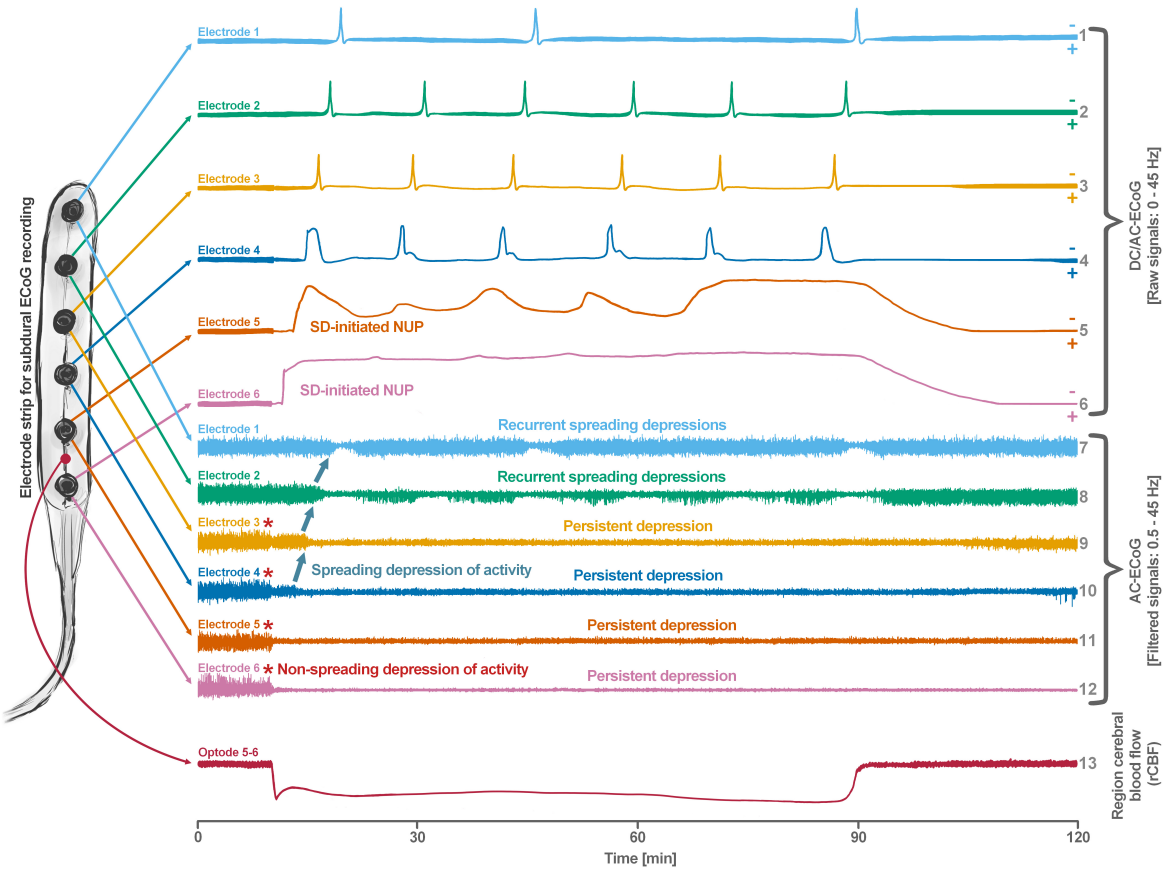


**FIGURE 1 |** Schematic representation of the spreading depolarization (SD) continuum associated with different spontaneous brain activity changes after middle cerebral artery occlusion (MCAO). Traces 1–6 from top to bottom give the direct current (DC)/alternating current (AC)-electrocorticography (ECoG) recordings (band-pass: 0–45 Hz) where spreading depolarizations are recorded as large negative DC shifts. The ECoG traces are oriented with negativity upward and positivity downward according to the electroencephalography (EEG) convention. The following 6 traces (7–12) show the high frequency band (AC-ECoG, band-pass: 0.5–45 Hz) were changes in the spontaneous brain activity can be assessed. The last trace (13) represents the regional cerebral blood flow (rCBF) recorded with an optode for laser-Doppler flowmetry located between electrodes 5 and 6. From these recordings, we can retrieve both temporal information (*x*-axis: time) and spatial information [*y*-axis: the electrode strip is composed of 6 electrodes overlying brain cortex from the ischemic center (electrode 6) to the adequately perfused periphery (electrode 1)]. Along the *x*-axis, the first prominent event is the drop in rCBF as a result of MCAO (trace 13). A few seconds after this focal drop in rCBF, the first signs of non-spreading activity depression begin at electrodes 6–3, with the non-spreading depression being most pronounced in the ischemic center below electrode 6 (red asterisks at AC-ECoG traces 12–9). Approximately 1 min after the drop in rCBF, the first spreading depolarization begins in the ischemic center at electrode 6 and spreads concentrically from electrode 6 to electrode 1 (first negative DC shift in the DC/AC-ECoG traces 6–1). Importantly, the first spreading depolarization begins long before cell death develops, which is ultimately a consequence of toxic changes in the intraneuronal environment due to persistent spreading depolarization. Thus, the first spreading depolarization initiates a high-amplitude negative ultraslow potential (NUP) in the DC/AC-ECoG traces of electrodes 6 and 5 (traces 6 and 5), defining the later ischemic core region. In the AC-ECoG traces of electrodes 4–1, the first spreading depolarization induces spreading depression of activity (dark green arrows between traces 10–7). Note that spreading depolarization-induced spreading depression at electrode 3 (trace 9) similar to that at electrode 4 (trace 10) results in persistent activity depression, although electrode 3, unlike electrode 4, lies outside the actual ischemic penumbra (Oliveira-Ferreira et al., 2010). Spreading depolarizations in persistently depressed tissue are called isoelectric spreading depolarizations (traces 5–3 and 11–9) (Hartings et al., 2011a; Dreier et al., 2017). The first spreading depolarization at electrodes 6 and 5 cannot induce spreading depression of activity because the activity has already been suppressed by non-spreading depression of activity. Not all spreading depolarizations reach tissue remote from the ischemic center. In this example, electrode 1 only recorded three of the six spreading depolarizations. The occluded MCA is reopened after 90 min immediately followed by reperfusion (trace 13). Although necrosis develops in the ischemic core region if reperfusion occurs later than 15–20 min after the onset of ischemia (Luckl et al., 2018), the DC potential often still shows some recovery from negativity if reperfusion occurs after 90 min. Later in the course, there may even be a transient return to extremely low-amplitude spontaneous activity in the region of the ischemic core.

analysis of stroke that the pathophysiological processes in the core of ischemia are fundamentally different from the processes in the penumbra.

Only if spreading depolarization outlasts a threshold duration, the so-called commitment point, neurons will die (Somjen, 2004b). The commitment point is not a universal value but is modified by additional factors. First of all, it varies between different types of neurons involved (Heiss and Rosner, 1983; Pulsinelli, 1985). Moreover, it depends on age, local temperature, prior injury, preconditioning and the level of the remaining perfusion (Steen et al., 1979; Dreier et al., 2013b). For example, when cerebral circulation ceases completely, as

after a complete cardiac arrest, and normal body temperature prevails, the commitment point shifts closer to the onset of spreading depolarization and is usually reached in less than 10 min (Steen et al., 1979; Ayad et al., 1994; Somjen, 2004b). Thus, dogs could survive only 8–9 min of complete global ischemia with return of normal neurological functions, but rCBF above 0% and below 10% of control values already prolonged the commitment point to 10–12 min, underscoring the importance of chest compressions in cardiac arrest to increase the chance of successful resuscitation (Steen et al., 1979).

By definition, a terminal spreading depolarization has two components. On the one hand, there is the initial, still reversible spreading depolarization component and, on the other hand, a late potential component, which is termed negative ultraslow potential (NUP) (**Figure 1**) (Oliveira-Ferreira et al., 2010; Drenckhahn et al., 2012; Hartings et al., 2017b; Dreier et al., 2018b, 2019; Luckl et al., 2018; Carlson et al., 2019). The NUP of a terminal spreading depolarization is thus experimentally defined by three typical properties: (i) that it is preceded by the initial spreading-depolarization component, (ii) that the ion shifts and cell edema do not fully recover during this extremely long DC negativity, and (iii) the death of neurons (Dreier, 2011; Dreier et al., 2013a; Luckl et al., 2018). One difficulty with this operational definition of the NUP is that the precise distinction between a NUP and a prolonged spreading depolarization that has not yet reached the commitment point and has not yet resulted in cell death cannot be made on the basis of electrophysiological criteria alone. A more detailed discussion of this can be found in the following account (Dreier et al., 2019). In human recordings with platinum/iridium electrodes, there is the additional special problem that part of the NUP is due to the interference of the electrode material with factors such as $pO_2$ and pH, which may also change during ischemia in the subdural compartment where the electrodes are located (Major et al., 2021). More suitable electrode material will hopefully enable us in the near future to record the spreading depolarization-initiated NUP in humans without these superimposed interferences (Masvidal-Codina et al., 2018; Hartings, 2019). Another limitation is that the initial spreading depolarization component of terminal depolarization does not seem to be obligatory in all circumstances; it appears that terminal depolarization may also start directly with the NUP in the form of a simultaneous depolarization under certain conditions, e.g., astrocytic pre-damage (Menyhart et al., 2021).

## THE CONTINUUM OF HEMODYNAMIC RESPONSES TO SPREADING DEPOLARIZATION

Another important continuum is the continuum of hemodynamic responses to spreading depolarization. Spreading depolarization induces tone alterations in resistance vessels, causing either predominant hyperperfusion followed by a mild oligemia (physiological hemodynamic response) in healthy tissue (Van Harreveld and Ochs, 1957; Lauritzen, 1994); or severe and prolonged initial hypoperfusion (inverse hemodynamic response = spreading ischemia) where the neurovascular unit is disturbed (Dreier et al., 1998; Dreier, 2011). Importantly, spreading depolarization can thus also be the cause of ischemia in brain tissue that was not yet ischemic at the onset of spreading depolarization (**Figure 2**). A necessary condition to diagnose spreading depolarization-induced spreading ischemia is that the negative DC shift of the associated spreading depolarization is prolonged as a result of the secondary mismatch between energy supply and demand (Dreier et al., 2002b; Dreier, 2011). Spreading ischemia is often followed by some recovery of rCBF up to marked hyperemia.

The phenomenon of spreading depolarization-induced spreading ischemia and inverse neurovascular coupling was discovered in a rat model, in which artificial cerebrospinal fluid (ACSF) with an elevated $K^+$ concentration ($[K^+]_{ACSF}$) in combination with either the nitric oxide synthase (NOS) inhibitor $N^G$-nitro-L-arginine (L-NNA) or the NO scavenger hemoglobin were topically applied to the cerebral cortex (Dreier et al., 1998, 2001, 2002b; Major et al., 2017; Sugimoto et al., 2018). Conceptually, this was a model mimicking the situation after aSAH. Similar conditions are likely responsible for spreading ischemia after arterial occlusion (Shin et al., 2006; Strong et al., 2007; Bere et al., 2014) as focal ischemia leads to a baseline elevation of the extracellular $K^+$ concentration ($[K^+]_o$) before inducing spreading depolarization (Nedergaard and Hansen, 1993; Muller and Somjen, 2000; Dreier et al., 2002a) and molecular oxygen is required for NO synthesis (Jiang et al., 2001; Uetsuka et al., 2002). Ischemia-induced baseline elevation of $[K^+]_o$ in the penumbra presumably results from activation of neuronal ATP-sensitive and G protein–dependent $Ca^{2+}$-sensitive $K^+$ channels and impaired $Na^+/K^+$-ATPase function (Erdemli et al., 1998; Muller and Somjen, 2000; Revah et al., 2016). While the normal spreading depolarization-induced spreading hyperemia is assumed to be beneficial (Oliveira-Ferreira et al., 2010), spreading depolarization-induced spreading ischemia alone – i.e., without preceding ischemia – was sufficient to lead to widespread cortical necrosis (Dreier et al., 2000). The full continuum from the normal to the inverse hemodynamic response to spreading depolarization was not only measured in animals but also in patients with aSAH (**Figure 2**), TBI and malignant hemispheric stroke (Dreier et al., 2009; Dreier, 2011; Woitzik et al., 2013; Hinzman et al., 2014). Especially in early and delayed infarcts after aSAH, measurements suggest that spreading depolarization-induced spreading ischemia plays a dominant role in infarct development (Luckl et al., 2018; Dreier et al., 2022). Mechanistically, it is interesting to note that inverse hemodynamic responses are not limited to spreading depolarization, but also occur in response to electrographic seizures (Winkler et al., 2012) or functional activation (Koide et al., 2012; Balbi et al., 2017) after aSAH, with rCBF drops under these conditions being smaller than observed in full-blown spreading depolarization-induced spreading ischemia. These forms of dysregulatory inverse neurovascular coupling must be distinguished from physiological forms of regulatory inverse neurovascular coupling. For example, salt loading in rats physiologically leads to activation of hypothalamic magnocellular vasopressin neurons along with local vasoconstriction of pial and

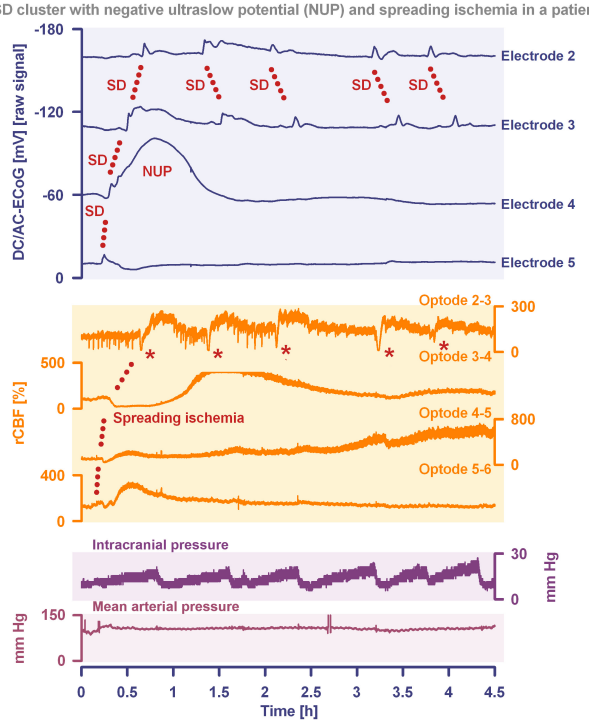


**FIGURE 2 |** Spreading depolarization inducing a spreading ischemia and a NUP. In total, this 44-year old, previously healthy woman had 174 spreading depolarizations and died due to progressive brain infarctions on day 13 (Luckl et al., 2018). The spreading depolarizations shown in the figure were recorded on day 9 after the initial hemorrhage. Traces 1–4 from top to bottom give the DC/AC-ECoG recordings (band-pass: 0–45 Hz). Spreading depolarization is observed as a negative DC shift propagating across the cortex from electrode 5 to electrode 2. At electrode 4, the spreading depolarization initiates a NUP, the electrocorticographic correlate of infarction (Luckl et al., 2018). At electrodes 2 and 3, several shorter-lasting spreading depolarizations accompany this. Traces 5–8 give regional cerebral blood flow (rCBF) recorded with four optodes between the electrodes. At the optode between electrodes 3 and 4, the spreading depolarization induced the characteristic long-lasting drop in rCBF typical of spreading ischemia. The duration of the NUP at electrode 4 correlates well with the duration of the spreading ischemia because the decrease in perfusion and energy supply limit $Na^+/K^+$-ATPase activity and prolong the neuronal depolarization (Dreier et al., 1998; Dreier, 2011; Major et al., 2017). In contrast, only short-lasting spreading depolarization-induced initial hypoperfusions followed by hyperemias are seen at optode 2–3 (compare red asterisks). Animal experiments suggested that, if sufficiently prolonged, spreading ischemia causes necrosis (Dreier et al., 2000). Accordingly, the patient developed a new scattered infarct at electrodes 4–6 between days 8 and 12. After the spreading ischemia shown in the figure, subsequent ones also involved (opto-) electrodes 4–6. Trace 9 gives the intracranial pressure recorded using an extraventricular drainage catheter and trace 10 mean arterial pressure recorded using a catheter in the radial artery. The marked fluctuations in intracranial pressure typically result from manual opening and closing of the drainage catheter. The time is given in hours (h).

supraoptic nucleus parenchymal arterioles (Roy et al., 2021). Such genuine examples of inverse neurovascular responses should not be confused with responses that only appear to be inverse, but in fact correspond to normal neurovascular coupling and occur as a remote effect of local neuronal activation. For example, unilateral stimulation and thus activation of the locus coeruleus area leads to ipsilateral inhibition of the cingulate cortex (Dillier et al., 1978). In terms of normal neurovascular coupling, there is then a decrease in local rCBF in the cingulate cortex in response to the local neuronal deactivation (de la Torre, 1976).

## ION AND TRANSMITTER CHANGES DURING SPREADING DEPOLARIZATION AND SEIZURES

It is assumed that spreading depolarization is a primarily neuronal summary process during which the transmembrane gradients of virtually all the small molecules we can measure change. That is, spreading depolarization consists of the interplay of millions of individual processes, which of course involve not only neurons but the entire neurovascular unit and microglial cells. For a few of these changes, more or less precise quantifications exist. For example, the extracellular $Na^+$ concentration ($[Na^+]_o$) drops from ∼147 to ∼60 mM and the intraneuronal $Na^+$ concentration ($[Na^+]_i$) increases from ∼10 to ∼36 mM (Kraig and Nicholson, 1978; Hansen and Zeuthen, 1981; Kager et al., 2002; Windmuller et al., 2005; Hubel and Ullah, 2016; Gerkau et al., 2017). The extracellular $Ca^{2+}$ concentration ($[Ca^{2+}]_o$) decreases from ∼1.3 mM to ∼80 μM and the intraneuronal $Ca^{2+}$ concentration ($[Ca^{2+}]_i$) increases from ∼60 nM to at least ∼25 μM (Hansen and Zeuthen, 1981; Windmuller et al., 2005; Marino et al., 2007; Dietz et al., 2008; Hubel and Ullah, 2016; Revah et al., 2016). In comparison, the changes in these concentrations during an epileptic seizure are much smaller: $[Na^+]_o$ drops from ∼150 to ∼140 mM, $[Na^+]_i$ increases from ∼10 to ∼16 mM (Lux et al., 1986; Kager et al., 2002), $[Ca^{2+}]_o$ drops from ∼1.3 to ∼0.9 mM and $[Ca^{2+}]_i$ increases from ∼60 to ∼130 nM (Wadman et al., 1985; Pisani et al., 2004; Kovacs et al., 2005; Marino et al., 2007).

In parallel with the $Na^+$ and $Ca^{2+}$ influx, there is a $K^+$ efflux from the neurons during spreading depolarization. That is, $[K^+]_o$ increases from ∼3 to ∼50 mM during spreading depolarization, whereas the intracellular $K^+$ concentration ($[K^+]_i$) decreases from ∼135 to ∼112 mM (Vyskocil et al., 1972; Kraig and Nicholson, 1978; Hansen et al., 1980; Hansen and Zeuthen, 1981; Perez-Pinzon et al., 1995; Kager et al., 2002; Windmuller et al., 2005; Hubel and Ullah, 2016). In comparison, the changes during an epileptic seizure are again much smaller: $[K^+]_o$ increases from ∼3 to ∼12 mM and $[K^+]_i$ decreases from ∼135 to ∼127 mM (Heinemann and Lux, 1977; Dreier and Heinemann, 1991; Kager et al., 2002). The situation is similar for the increase in neurotransmitters. For example, while the extracellular glutamate concentration increases from ∼2 to ∼4 μM during an epileptic seizure (Li et al., 2018), it increases up to ∼100 μM during spreading depolarization (Zhou et al., 2013).

Importantly, despite these mild but significant metabolic disturbances during a seizure and the severe metabolic disturbances during spreading depolarization, neither a seizure nor a spreading depolarization immediately kills neurons if they are of short duration and occur in tissues that are adequately supplied with oxidative substrates and not exposed to

toxins (Nedergaard and Hansen, 1988; Zachrisson et al., 2000; Besse et al., 2020). However, when they occur over a longer period of time, both seizures and spreading depolarizations can cause cellular damage. Only a few papers have directly compared the cell-damaging potency of electrographic seizures and spreading depolarizations. For example, in a study of photothrombosis in the rat, no increase in lesion volume or neuronal damage was observed in the early time window by inducing electrographic seizures with 4-aminopyridine under urethane anesthesia, whereas ketamine/xylazine anesthesia reduced the number of spontaneous spreading depolarizations and resulted in a smaller lesion volume and less neuronal damage, although 4-aminopyridine-induced electrographic seizures were concomitantly enhanced because the antiepileptic effect of ketamine is less than that of urethane (Schoknecht et al., 2021). In a recent cohort study of patients with TBI, the occurrence of spreading depolarization clusters was significantly associated with worse patient outcomes in a multivariate ordinal regression model adjusting for baseline prognostic variables (Hartings et al., 2020). In the same cohort, electrographic seizures were significantly associated with severity and number of spreading depolarizations (Foreman et al., 2022). However, in contrast to clustered spreading depolarizations, electrographic seizures detected on either ECoG or scalp electroencephalography (EEG) showed no independent association with functional outcome at 6 months after controlling for known prognostic covariates and the presence of spreading depolarizations. Thus, consistent with the much greater changes in ion gradients and neurotransmitters during spreading depolarization, these studies suggest that spreading depolarizations are fundamentally more dangerous than epileptic seizures, although, on the other hand, a single short-lasting spreading depolarization is more benign than, for example, generalized status epilepticus. A caveat, however, is that it has not been well enough studied how often spreading depolarizations occur superimposed on status epilepticus. In many status epilepticus models, spreading depolarizations typically co-occur with electrographic seizures (Koroleva and Bures, 1983; Mody et al., 1987; Hablitz and Heinemann, 1989; Avoli et al., 1991; Tamim et al., 2021).

## THE BASAL MECHANISM OF SPREADING DEPOLARIZATION

Fortunately, to understand the basal process underlying spreading depolarization, we do not need to know all the many small molecules whose transmembrane gradients change during spreading depolarization. Initially, we do not even need to know what a neuron is, but a basic knowledge of thermodynamics and electrochemistry might be helpful. For those who have not studied thermodynamics and electrochemistry in a while, there are textbooks or websites for a refresher [e.g., Map: Chemistry – The Central Science (Brown et al.) (Anon, 2021). Chapter 19: Chemical Thermodynamics and Chapter 20: Electrochemistry[2].]. With knowledge on entropy and the second law of thermodynamics, entropy changes during chemical reactions, oxidation states and redox reactions, cell potentials, Gibbs free energy, batteries, fuel cells, and electrolysis, it is possible to move on to the so called Gibbs–Donnan equilibrium. For example, the Gibbs–Donnan equilibrium is well explained in the following articles (Sarkar et al., 2010; Sperelakis, 2011). Anyone who understands what a Gibbs–Donnan equilibrium is has a basic understanding of why spreading depolarizations occur in the central nervous system (CNS) of all properly investigated insects and vertebrates under pathological conditions. In the following, we would like to briefly recapitulate the basics of this.

The physiological state of mammalian body cells is electrochemically characterized by two opposing Gibbs–Donnan effects. The first Gibbs–Donnan effect arises from the high concentration of intracellular macromolecules. These are predominantly proteins that are negatively charged both in physiological and even highly pathological pH ranges. Importantly, the cell membrane is impermeable to these macromolecules, i.e., they are trapped inside the cell. If this first Gibbs–Donnan effect is not compensated by another force, it imposes an unequal distribution of permeant charged ions such as $Na^+$, $K^+$, and $Cl^-$ ions on either side of the semipermeable cellular membrane. When an equilibrium is reached, namely the so-called Gibbs–Donnan equilibrium, (1) each bulk solution is electrically neutral on either side of the cellular membrane, (2) the product of diffusible ions on one side of the membrane is equal to the product of diffusible ions on the other side of the membrane, (3) the electrochemical gradients due to the unequal distribution of charged ions lead to a transmembrane potential difference, which can be calculated using the Nernst equation and is slightly negative on the inner side of the membrane, (4) an osmotic diffusion gradient is created attracting water into the intracellular compartment, and (5) the cells swell produced by water uptake. Although it cannot be completely ruled out that neurons can survive the complete establishment of a Gibbs–Donnan equilibrium for a very short time, we know of no experimental case in which this has been demonstrated. If, on the other hand, the cerebral cortex is freshly dead after circulatory arrest, the ion changes measured, without any exception to this rule being known to us, are consistent either with a Gibbs–Donnan equilibrium or with a state in which cell lysis has already begun as a result of cellular swelling (Hansen and Zeuthen, 1981).

Thus, in order for Gibbs–Donnan equilibrium not to occur, an opposing force is needed in body cells to balance the first Gibbs–Donnan effect. This opposing force is generated by the so-called second Gibbs–Donnan effect, for which not non-diffusible macromolecules in the intracellular space, but quasi non-diffusible $Na^+$ ions in the extracellular space are responsible (Sperelakis, 2011; Dreier et al., 2013a). These generate and maintain the osmotic countergradient for water movement. The result is a steady state characterized by isoosmolarity between intracellular and extracellular space, so that there is no net transmembrane water movement. The entrapment of $Na^+$ ions in the extracellular space is based on two mechanisms. First, the cell membrane is nearly impermeable to $Na^+$ ions under physiological conditions. Second, the ATP-powered $Na^+$ pump

[2]https://chem.libretexts.org/@go/page/21655

($Na^+/K^+$-ATPase) transports three $Na^+$ ions out of the cell in exchange for two $K^+$ ions (Skou and Esmann, 1992). This means that excess $Na^+$ ions are immediately transported back out of the cell. In summary, the two opposing Gibbs–Donnan effects, due to entrapment of non-diffusible macromolecules in the intracellular space and entrapment of quasi non-diffusible $Na^+$ ions in the extracellular space, produce the double Gibbs–Donnan steady state that characterizes the physiological state of body cells.

As long as the brain of a born human being is "healthy," the neurons are without any exception in the double Gibbs–Donnan steady state both while awake and asleep and throughout life. In any case, no exceptions to this rule have become known so far. However, excellently reproducible ion measurements and measurements of the volumes of the intracellular and extracellular compartments by many different research groups over several decades, discussed in more detail above and below, have shown that under pathological conditions two types of deflection are possible, in which the brain gray matter shifts within a few seconds from the double Gibbs–Donnan steady state toward the Gibbs–Donnan equilibrium. In both cases, the deflection initially stalls in a new metastable state without reaching the Gibbs–Donnan equilibrium. However, these two metastable states are much more unstable than the physiological double Gibbs–Donnan steady state, which in turn is less stable than the Gibbs–Donnan equilibrium. The first type of deflection is small, reaching a metastable state still close to the physiological double Gibbs–Donnan steady state, and is usually referred to as an electrographic epileptic seizure. The second type of deflection is large, close to Gibbs–Donnan equilibrium, and referred to as spreading depolarization (Dreier et al., 2013a).

A complete Gibbs–Donnan equilibrium becomes established in body cells when the $Na^+/K^+$-ATPase stops working. As already mentioned, this can happen when the pump is directly inhibited or because it lacks fuel, i.e., the necessary ATP. It is important to note that the pathological Gibbs–Donnan equilibrium does not require metabolic energy in the form of ATP for its formation; it evolves passively because its formation releases Gibbs free energy that drives the process. This is unlike the physiological double Gibbs–Donnan steady state. The physiological double Gibbs–Donnan steady state requires active ion transport by membrane pumps and the use of metabolic energy in the form of ATP to establish the large transmembrane electrochemical gradients of $Na^+$, $K^+$, $Ca^{2+}$, etc. Thus, in the physiological double Gibbs–Donnan steady state, the entropy of the system is kept artificially low by the use of ATP, and in this way electrochemical energy is stored in the system, which is then available to do work. From this electrochemical energy store, the neurons take the necessary energy to be able to send out their signals, the so-called action potentials. However, it is important to understand that although the membrane potential changes dramatically for a millisecond during an action potential, as some $Na^+$ and $K^+$ ions cross the membrane, the transmembrane concentration gradients between the bulk solutions of the intracellular and extracellular space remain virtually unchanged, implying that the cell remains in the physiological double Gibbs–Donnan steady state. This means that the energy store loses almost no energy during one action potential. Otherwise, the system would not be able to function. This should be imagined like a flashlight that can be turned on and off repeatedly without discharging the entire battery in the short term.

A characteristic of the physiological double Gibbs–Donnan steady state is a strongly negative resting membrane potential across the cell membrane. However, the membrane potential at the pathological Gibbs–Donnan equilibrium is also not zero, but is normally between 0 and −20 mV (Sperelakis, 2011). In the pathological Gibbs–Donnan equilibrium, all permeant ions are in equilibrium across the cell membrane and the equilibrium potentials for all permeant ions such as $K^+$ and $Cl^-$ are of the same magnitude and polarity, whereas this is not the case in the physiological double Gibbs–Donnan steady state. The membrane potential at the pathological Gibbs–Donnan equilibrium arises even if the cell membrane has the same permeability or conductivity for all small ions, whereas the normal resting membrane potential of the physiological double Gibbs–Donnan steady state requires different conductivities for, e.g., $Na^+$ and $K^+$ ions, namely a significantly higher conductivity for $K^+$ ions than for $Na^+$ ions. In the pathological Gibbs–Donnan equilibrium, the osmolarity of the cell increases relative to the osmolarity of the extracellular space because more $Na^+$ ions flow into the cell than $K^+$ ions flow out due to Gibbs–Donnan forces imposed by the large, negatively charged, intracellular macromolecules. In order for the bulk solutions on either side of the cell membrane to remain electrically neutral, $Cl^-$ ions must also enter the cell in addition to the $Na^+$ ions, but there are slightly less $Cl^-$ ions flowing in than $Na^+$ ions, since there are also some $K^+$ ions flowing out. In Gibbs–Donnan equilibrium, the product of the small diffusible positive and negative ions on one side of the membrane is then equal to the product of the small diffusible positive and negative ions on the other side of the membrane, even though the sum of the small diffusible positive and negative ions in the intracellular space is greater than the sum of the small diffusible positive and negative ions in the extracellular space, so that the osmolarity of the intracellular space is greater than the osmolarity of the extracellular space. Driven by the difference in osmolarity between the extracellular and intracellular space, water follows $Na^+$ and $Cl^-$ ions into the cell, resulting in what is known as cytotoxic edema (Dreier et al., 2013a, 2018a).

Neurons, unlike astrocytes, are normally relatively resistant to purely extracellular osmolarity changes because they lack regular water channels (Aitken et al., 1998; Andrew et al., 2007). On this basis, it is postulated that only membrane processes during spreading depolarization, i.e., the opening of specific channels during spreading depolarization, which are not yet clearly elucidated, allow water to follow the osmolarity gradient that builds up between the intraneuronal and extracellular space. The influx of water then leads to a marked swelling of neuronal dendrites and somas within a few seconds during spreading depolarization (Kirov et al., 2020). For example, candidate neuronal channels that could be used as water channels during spreading depolarization include membrane transporters (Steffensen et al., 2015). However, the exact mechanism is unclear, and in these considerations it is important to keep in mind

that regardless of which pore the water enters through during spreading depolarization, ATP cannot be required for it. In other words: Water transport mechanisms that require energy cannot be involved in the water influx into neurons during spreading depolarization.

There are also no satisfactory explanations yet for the abrupt non-specific increase in $Na^+/K^+$ conductance that mediates $Na^+$ influx and $K^+$ efflux during spreading depolarization (Czeh et al., 1993). Thus, the forces, namely the Gibbs–Donnan forces, that drive spreading depolarization are clear, but the exact pathways by which the large amounts of $Na^+$, $K^+$, $Ca^{2+}$, $Cl^-$, and water move across the cell membrane from one compartment to another are not.

However, since these facts are somewhat counterintuitive, they are sometimes misrepresented and it is then claimed, for example, that $K^+$ efflux and $Na^+$ influx during spreading depolarization are the same (Hellas and Andrew, 2022) or intra- and extracellular ion concentrations equilibrate during spreading depolarization. However, as previously pointed out by Somjen (2001), the reasoning error underlying such interpretations is mainly based on the failure to take into account the volume ratios and volume changes between the intracellular and extracellular space. Conversely, the conclusion that more $Na^+$ ions enter neurons than $K^+$ ions leave them during spreading depolarization (Somjen, 2001; Dreier et al., 2018a) is not based on "dogma" in "textbooks" (Hellas and Andrew, 2022) but results from quantitative measurements of $[Na^+]_o$, $[K^+]_o$, $[Cl^-]_o$ (Vyskocil et al., 1972; Kraig and Nicholson, 1978; Hansen et al., 1980; Hansen and Zeuthen, 1981; Lehmenkuhler, 1990; Perez-Pinzon et al., 1995; Somjen, 2001; Windmuller et al., 2005), $[Na^+]_i$ (Gerkau et al., 2017), and the extracellular (Vorisek and Sykova, 1997; Mazel et al., 2002; Windmuller et al., 2005) and intracellular volume changes (Takano et al., 2007; Murphy et al., 2008; Kirov et al., 2020), which have been performed and reproduced by many different research groups in different decades. Thus, $[Na^+]_o$ drops from ∼147 to ∼60 mM, that is, by ∼87 mM, but $[K^+]_o$ increases from 3 to ∼50 mM and thus by only ∼47 mM. Correspondingly, $[Cl^-]_o$ drops from ∼135 mM to at least ∼95 mM and thus by approximately 40 mM (Kraig and Nicholson, 1978; Hansen and Zeuthen, 1981; Windmuller et al., 2005). How many times more $Na^+$ ions flow from the extracellular space into the intracellular space than $K^+$ ions flow out can be estimated from the measured data. As mentioned above, it is important to consider the volume ratios and volume changes of the intracellular and extracellular space. While the percentage of extracellular space is 18–22% of the total volume under physiological conditions, it declines to 5–9% during spreading depolarization (Hansen and Olsen, 1980; Jing et al., 1994; Perez-Pinzon et al., 1995; Mazel et al., 2002; Windmuller et al., 2005). In other words, the extracellular space declines by ∼70%. If this 70% shrinkage of the extracellular space in favor of the intracellular space were due to a pure water shift and no ions crossed the cellular membranes, then $[Na^+]_o$ should increase from ∼147 to ∼490 mM and $[K^+]_o$ from ∼3 to ∼10 mM. However, $[Na^+]_o$ actually decreases from ∼147 to ∼60 mM, while $[K^+]_o$ increases from ∼3 to ∼50 mM. Assuming $[Na^+]_i$ at ∼10 mM and $[K^+]_i$ at ∼135 mM under physiological conditions (Kager et al., 2002) and taking into account the measured extracellular ion changes as well as intra- and extracellular volume changes during spreading depolarization, $[Na^+]_i$ should increase from ∼10 to ∼36 mM and $[K^+]_i$ should decrease from ∼135 to ∼112 mM during spreading depolarization. Here, most of the $[K^+]_i$ decrease results from the dilution effect due to water uptake, whereas the net loss of $K^+$ ions from the intracellular space is small. This is in stark contrast to the $[Na^+]_i$ increase, which is entirely due to the net gain in $Na^+$ ions caused by the $Na^+$ influx, while the dilution effect due to water uptake counteracts the increase in $[Na^+]_i$. From the concentration and volume changes it can then be calculated that about 11 times more $Na^+$ ions enter the intracellular space than $K^+$ ions leave during spreading depolarization. Indeed, neuronal $[Na^+]_i$ of ∼24 and ∼30 mM measured during spreading depolarization *in vivo* and *in vitro* are quite close to the estimated value (Gerkau et al., 2017). The small discrepancy between measured and estimated values should take into account that, in addition to ion shifts between the extracellular space and the cytoplasm, there are very likely also ion shifts between the cytoplasm and intracellular organelles (Hernansanz-Agustin et al., 2020). For quantitative measurements of $[Na^+]_i$ *in vivo*, it must additionally be considered that these optical measurements are made relatively superficially and the ion changes tend to be smaller there than deep in the cortex. Quantitative $[K^+]_i$ measurements do not yet exist for spreading depolarization because the available $K^+$ dyes do not have sufficient selectivity.

Overall, the extracellular ion measurements are in good agreement with the theory in textbooks of chemistry and biochemistry. Importantly, the ion measurements suggest not only that more $Na^+$ ions flow into the cells than $K^+$ ions flow out, but also that the extracellular space loses ∼80 mosmol/l in favor of the intracellular space during this process. The decrease in extracellular osmolarity and the smaller increase in intracellular osmolarity relative to the larger intracellular volume are also in good agreement with the textbook theory. Since not only the distributions of the major small ions $Na^+$, $K^+$, and $Cl^-$ across the cell membrane change during spreading depolarization, but also the concentrations of countless other molecules, and since not only neurons but also other cell types, especially astrocytes (Somjen, 2001), are involved, the complexity is certainly higher than portrayed here, but it is nevertheless not likely that the basic properties of the process change just because even more molecules and cell types are involved. Nevertheless, it would certainly be useful to develop methods to directly measure intracellular and extracellular osmolarity changes during spreading depolarization to test these conclusions.

Fortunately, then, it is not necessary to overturn the fundamentals of electrochemistry to understand spreading depolarization. In other words, during spreading depolarization the system comes very close to the pathological Gibbs–Donnan equilibrium without fully reaching it, making spreading depolarization an important metastable reference state of general interest (Kraig and Nicholson, 1978; Kager et al., 2002; Dreier et al., 2013a; Hubel and Ullah, 2016). When cells die, the pathological Gibbs–Donnan equilibrium is finally reached unless the cell membrane lyses first. $Na^+$ ions probably play a less

passive role in all these processes than has long been assumed, because there is increasing evidence that $Na^+$ ions, like $Ca^{2+}$ ions (Wolf et al., 2017), have second-messenger functions. For example, $Na^+$ ions are now thought to be directly involved in the control of mitochondrial ATP production (Hernansanz-Agustin et al., 2020; Geisberger et al., 2021).

In case the reader is now still not familiar with the principle of spreading depolarization, the authors would like to suggest a practical exercise: the reader may connect the positive terminal of her/his car battery to the negative terminal and then try to drive around with the car. With a grain of salt, the shorted car battery is a car battery in the state of spreading depolarization and the inability of the car to do any work in this situation – i.e., drive around with the battery shorted – is a car in spreading depression of activity.

In conclusion, neuronal cytotoxic edema is the morphological correlate of the near-complete neuronal battery breakdown called spreading depolarization, or conversely, spreading depolarization is the electrophysiological correlate of the initial, still reversible phase of neuronal cytotoxic edema (Van Harreveld, 1957, 1958; Hubel and Ullah, 2016; Dreier et al., 2018a; Kirov et al., 2020). Cytotoxic edema and spreading depolarization are thus different modalities of the same process (Major et al., 2020). Accordingly, the swelling of the neuronal somas and the so-called beading of the dendrites as a result of the water influx can be detected in two-photon laser scanning microscopy simultaneously with the negative shift of the DC potential (Andrew et al., 2007; Takano et al., 2007; Murphy et al., 2008; Risher et al., 2010, 2011; Steffensen et al., 2015). These facts are important for the understanding of water diffusion restrictions in the gray matter, which can be detected by magnetic resonance imaging (MRI) (Dreier and Reiffurth, 2017). Thus, the beaded morphology during spreading depolarization allows the neurons to enclose a larger volume of water within a constant surface area (Budde and Frank, 2010). In normal dendrites, water mobility is strongly constrained by the cell membrane perpendicular to the major axis, whereas water molecules diffusing along the major axis of the dendrites encounter few obstacles on the time scale of diffusion-weighted (DW) MRI. However, if water influx during spreading depolarization leads to dendritic beading – i.e., alternating between severe dendritic constrictions and balloon-like dilations – water can no longer diffuse along the major dendrite axis because water jams at the dendritic constrictions. This intracellular diffusion restriction during spreading depolarization can be imaged with DW-MRI (Busch et al., 1995, 1996; Gyngell et al., 1995; Hoehn-Berlage et al., 1995; Hossmann, 1996; Takano et al., 1996; Dreier and Reiffurth, 2017). The technology has now advanced to the point where it is experimentally possible to map the propagation path of spreading depolarization in the cortex and subcortical gray matter in high resolution and three dimensions using DW-MRI (Cain et al., 2017). The vascular neurologist who looks at DW-MRIs of her/his stroke patients should be aware that reversible diffusion restriction in the gray matter (Fiehler et al., 2004) results from spreading depolarization and persistent diffusion restriction from the transition to a NUP (**Figures 1**, **2**). However, in the case of a locally very short-lasting spreading depolarization, e.g., in the context of a normal migraine aura, the depolarized wavefront would be expected to be so narrow that it should be very difficult to detect diffusion restriction in this region with standard clinical MRI scanners.

## THE OVERARCHING THEME OF SPREADING DEPOLARIZATION

The overarching theme inherent in all spreading depolarizations comprises the near-complete breakdown of the transmembrane neuronal ion gradients that cause the water influx and neuronal swelling, the marked neuronal and astroglial depolarization, the changes in holding current and input resistance of patch-clamped neurons, intrinsic optical signal (IOS) changes, the abrupt release of neurotransmitters, including both excitatory neurotransmitters such as glutamate and inhibitory neurotransmitters such as GABA, and the fall in tissue ATP (Mies and Paschen, 1984; Somjen, 2001; Molchanova et al., 2004; Aiba and Shuttleworth, 2014; Dreier and Reiffurth, 2015). However, the changes in spontaneous neuronal activity are not part of this list because spreading depolarization may very well occur in tissues without any spontaneous activity, and the changes in spontaneous brain activity around the occurrence of spreading depolarization may exhibit large temporal and spatial variations, as explained below. The hemodynamic response to spreading depolarization is also not included in this list of common characteristics of all spreading depolarizations because spreading depolarization can also occur in brain slices that do not have an intact blood circulation, and the changes in rCBF around spreading depolarization *in vivo* can also have large temporal and spatial variations as explained above.

The Gibbs free energy released when the physiological double Gibbs–Donnan steady state transitions to the epileptic seizure state, to the state of spreading depolarization, and finally to death – that is, the Gibbs–Donnan equilibrium – can be estimated. Using simple models of neuropil, changes in cation concentrations and electric field alone resulted in a Gibbs free energy release of ∼3 J/l per tissue volume when the network entered the epileptic seizure state and of 19–22 J/l per tissue volume when it entered spreading depolarization (Dreier et al., 2013a). The subsequent transition from the spreading depolarization state to cell death resulted in an additional small free energy release of 2.5 J/l. The Gibbs free energy released is converted to heat. Based on the above estimates, tissue temperature should increase by 5 mK during spreading depolarization. This is only slightly smaller than the measured temperature increase between 5 and 30 mK in isolated bullfrog and toad retinas (Tasaki and Byrne, 1991). These estimates once again emphasize that spreading depolarization/cytotoxic edema is a thermodynamic reference state of living neurons near cell death, at which ∼90% of the Gibbs free energy contained in the ion gradients has been lost ("'free energy starving"') (Dreier and Reiffurth, 2015; Hubel and Ullah, 2016). The hypothesis that spreading depolarization is the mechanism of the neuronal cytotoxic edema is owed to Anthonie van Harreveld, who coined

it before the term cytotoxic edema even existed (Van Harreveld, 1957, 1958; Dreier et al., 2018a).

Basically, spreading depolarizations can be measured via all million-fold concentration changes of molecules in the intracellular and extracellular space that are not freely diffusible and have a non-uniform distribution across the cell membrane, as well as via many other physicochemical properties (Major et al., 2020). Thus, to detect spreading depolarizations in principle, and especially their local duration, it probably makes relatively little difference whether the DC potential, $[Na^+]_i$, $[Na^+]_o$, $[Ca^{2+}]_i$, $[Ca^{2+}]_o$, $[K^+]_i$, $[K^+]_o$, $[Cl^-]_i$, $[Cl^-]_o$, $pH_i$, $pH_o$, DW-MRI, cellular swelling, extracellular shrinkage, and so on are recorded. Whenever a new measurement method is found, it is naturally sold as better and more ingenious than the previous one. Fortunately, over time, a more realistic view develops and it is possible to move on to discussing pros and cons in a factual manner. For example, questions of interest include (1) whether the method is suitable for measuring spreading depolarizations in patients, (2) whether it is suitable for non-invasive measurement in animals and/or patients, (3) whether it allows imaging, (4) whether it has higher spatial and/or temporal resolution than previous methods, (5) whether it combines well with other recording methods and/or (6) allows more accurate quantification of individual processes nested in the overall process of spreading depolarization. In addition, it is also interesting when the new method provides new mechanistic insights, for example, regarding the mechanism underlying the large changes of membrane permeability, the mechanism of propagation, the brain activity changes, the continuum of hemodynamic responses or the edema formation. The latter not only includes the cytotoxic edema (Dreier et al., 2018a). Thus, with a delay, spreading depolarizations also induce the ionic edema (Mestre et al., 2020) and subsequently blood–brain barrier disruption and vasogenic edema (Gursoy-Ozdemir et al., 2004; Sadeghian et al., 2018).

Even though spreading depolarization primarily begins in neurons (Peters et al., 2003; Chuquet et al., 2007), a separate review can in principle be written about each cell type involved. For example, astrocytes are of paramount importance for the orderly process of spreading depolarization. To give a few examples, astrocyte-directed inactivation of connexin 43 decreased astrocytic gap junctional communication and increased tissue susceptibility to spreading depolarization and the propagation speed of spreading depolarization (Theis et al., 2003). Selective intoxication of astrocytes caused spreading depolarizations that initiated a shallow NUP as neurons began to die (Largo et al., 1996b). Glia dysfunction may accelerate neuronal death under ischemic conditions (Largo et al., 1996a; Kimelberg, 2005). Accordingly, impaired astrocyte function can abolish the typical slow spread of spreading depolarization in the ischemic zone and cause the commitment point to occur earlier (Menyhart et al., 2021).

Electrographic seizures can usually be easily distinguished from spreading depolarizations. The reader will find details on this in the following articles (Dreier et al., 2017; Revankar et al., 2017). Hybrid phenomena between spreading depolarizations and epileptic activity are further discussed below. Of note, although there are many models that lead to both epileptic seizures and spreading depolarizations (Koroleva and Bures, 1983; Mody et al., 1987; Hablitz and Heinemann, 1989; Avoli et al., 1991; Dreier et al., 2013a; Tamim et al., 2021), there are also important differences, and the type of increased excitability that leads to seizures is by no means the same as the one resulting in spreading depolarizations. For example, $GABA_A$ agonists are first-line drugs for the treatment of epileptic seizures and limit the propagation speed of spreading depolarization (Aiba et al., 2012). On the other hand, GABA is released during spreading depolarization (Molchanova et al., 2004) and may contribute to neuronal swelling through the influx of $Cl^-$ ions (Allen et al., 2004; Dreier and Reiffurth, 2015). In addition, it was recently shown that a mutation of the $Na^+$ channel NaV1.1, which in humans leads to FHM type 3, one of the Mendelian model diseases of spreading depolarization, is associated with impaired inactivation of the channel (Jansen et al., 2020). The interesting point is that this excitatory $Na^+$ channel is mainly expressed by GABAergic interneurons and the impaired inactivation should lead to increased inhibition in the network. Nevertheless, the mutation increases the propensity to spreading depolarization. In contrast, mutations leading to a loss of function instead of a gain of function of the same channel cause epilepsy syndromes such as Dravet syndrome, a pharmacoresistant developmental and epileptic encephalopathy, and genetic epilepsy with febrile seizures plus (Escayg et al., 2000; Claes et al., 2001). Another important example of divergence between epileptic excitability and excitability leading to spreading depolarization is epileptogenesis, the long-term, plastic process resulting in epilepsy. Thus, the propensity to spreading depolarization appears to decrease during epileptogenesis, although the propensity to spontaneous seizures increases (Koroleva et al., 1993; Tomkins et al., 2007; Maslarova et al., 2011).

## THERE ARE NO DISEASE-SPECIFIC SPREADING DEPOLARIZATIONS

Spreading depolarization represents the injury potential of the brain's gray matter associated with the neuronal cytotoxic edema (Major et al., 2020). Although the neural network need not tip into ruin when spreading depolarization occurs, spreading depolarization nevertheless typically occurs when the neural network tips into ruin, and second, the local duration of the spreading depolarization state indicates whether or not the neural network irreversibly perishes (Dreier et al., 2017). Of course, there are exceptions to all rules. For example, evidence has recently been found that selective ischemic death of Purkinje cells does not require the occurrence of spreading depolarization (Oliveira-Ferreira et al., 2020). Furthermore, the fact that locally long-lasting spreading depolarizations in regions of impaired metabolism lead to neuronal damage does not preclude that locally short-lasting spreading depolarizations in regions of unimpaired metabolism surrounding an emerging lesion might have beneficial adaptive properties and signaling functions (Dreier, 2011; Shuttleworth et al., 2019). There is a need

for research in both directions, as these questions are relevant to which neuroprotective interventions might be useful. In all of this, it is important to note that spreading depolarizations can occur in a plethora of clinical conditions, but there are no disease-specific spreading depolarizations, just as epileptic seizures can occur in a plethora of clinical conditions that are sometimes more and sometimes less benign, but there are no disease-specific epileptic seizures. This means, for example, that there are no specific migraine spreading depolarizations. Thus, a spreading depolarization that has migrated into the normally perfused surroundings of an ischemic zone will hardly differ there from a spreading depolarization as it occurs in the context of a migraine with aura. It is therefore advisable to detach a moment from the clinical zeal for classification and to embrace scientific abstraction. As explained above, the overarching theme is that both epileptic seizures and spreading depolarizations are network accidents that inevitably result from the way neural networks are configured. When certain neural network safety systems are overridden, the network must respond with epileptic seizures and/or spreading depolarizations because it has no other choice. Epileptic seizures and spreading depolarizations do not result from network decisions, but the network is forced to undergo these partial breakdowns of small magnitude (epileptic seizure) or massive magnitude (spreading depolarization) by the second law of thermodynamics (Dreier et al., 2013a; Hubel and Ullah, 2016). The second law of thermodynamics establishes the concept of entropy as a physical property of a thermodynamic system. During an epileptic seizure or a spreading depolarization, the entropy of the system abruptly increases, which, as explained above, is associated with the release of Gibbs free energy, which in turn is converted into heat. Thus, an epileptic seizure or a spreading depolarization proceed voluntarily (passively) and can only be terminated by the expenditure of ATP (actively), especially for the $Na^+/K^+$-ATPase. The ATPase actively lowers the entropy of the system again and in this way replenishes the electrochemical energy store of the cells.

What should not remain unmentioned in this context is the approach, which we interpret either as a little ruse or as a genuine misunderstanding, how even today it is often justified that spreading depolarizations in migraine are always harmless and have not much to do with spreading depolarizations in stroke. This consists of calling spreading depolarizations in sublethal doses spreading depression and in lethal doses anoxic depolarization. Then a spreading depression is always harmless by definition, because at the moment when the neurons unfortunately died, it was not a spreading depression but an anoxic depolarization. But if they survive, then by definition it was not an anoxic depolarization but a spreading depression. This is like writing one pharmacopeia for harmless substances and another pharmacopeia for hazardous substances and listing the same substances in both, but with different names, and justifying this by saying that, on the one hand, each of the substances in sublethal doses is not lethal and therefore harmless, and, on the other hand, each substance in lethal doses is of a different nature because it is lethal. How and when this *secundum quid et simpliciter* type of fallacy developed is difficult to trace. The fallacy dissolves when Paracelsus' concept comes into play that the dose makes the poison. His full quotation reads: "Poison is in everything, and no thing is without poison. The dosage makes it either a poison or a remedy." In the context of the summary process of spreading depolarization, which is ultimately a concert of thousands or millions of more or less parallel processes, it might even be worthwhile to think more deeply about the whole meaning of the quote, including the part about the potential healing effects of possible poisons, as already discussed above (Dreier, 2011; Shuttleworth et al., 2019). Moreover, it should be added that the term dose in the context of spreading depolarization means the cumulative dose of the potentially noxious changes, such as the 500–1,000-fold increase in $[Ca^{2+}]_i$ (Dietz et al., 2008, 2009; Revah et al., 2016), as a function of exposure time, i.e., as a function of the local duration of spreading depolarization (Dreier et al., 2017). As a rule of thumb, one locally long-lasting spreading depolarization is more dangerous than 100 locally short-lasting spreading depolarizations (**Figures 1**, **2**). In this context, it should also be briefly mentioned that a spreading depolarization is certainly not a homogeneous process, but has different phases, such as a wave front and a sustained phase, which often has a saddle-shaped or even more complex forms (Somjen, 2001). The changing mechanisms of these phases may well be important for the toxicity of a given spreading depolarization (Herreras and Somjen, 1993; Aiba and Shuttleworth, 2012; Reinhart and Shuttleworth, 2018; Mei et al., 2020).

Unfortunately, when the intermediate range of the spreading-depolarization continuum was increasingly encountered in rodent MCAO experiments since the early 1980s, the rigid separation between anoxic depolarization and spreading depression was not immediately abolished. Instead, a third type of wave was postulated, which was termed peri-infarct depolarization. However, we believe that this term also conveys a misleading concept, because when the first spreading depolarizations occur during MCAO, no infarct is yet present and, accordingly, these spreading depolarizations cannot be called peri-infarct depolarizations. In this context, it is important that the pathologist defines an infarct and an ischemic stroke, respectively, by the ischemic necrosis of neurons and not by decreases in cerebral perfusion, tissue partial pressure of oxygen ($p_{ti}O_2$), tissue glucose or tissue ATP, or by an initially reversible state of depolarized neurons. That we have used the terms "spreading depression," "peri-infarct depolarization," and "anoxic depolarization" in this twisted manner in the past, when knowledge was less, is hopefully forgivable (Dreier et al., 1998) and should not diminish the value of the earlier publications that used this nomenclature, but to continue to use this twisted nomenclature today is problematic because it cements a concept that is ultimately misleading. A continuum (cf. **Figures 1**, **2**) should not be cut into rigid parts to pretend that they are unrelated. By analogy, light waves, for example, also differ greatly in their properties as a function of wavelength and yet can only be interpreted and quantified if it is understood that they are part of the light wave continuum. What makes all this particularly difficult is the fact that the term 'spreading depression' is still needed for what it really denotes, namely the spreading depression of spontaneous activity caused by

spreading depolarization. So the point is not to stop using the term spreading depression, but to use it correctly. In the last section, we will explain how spreading depolarization and spreading depression differ from each other.

## THE ROLE OF THE $Na^+/K^+$-ATPase IN SPREADING DEPOLARIZATION

Sufficient activity of the $Na^+/K^+$ pump protects against spreading depolarization because, as explained above, the pump is responsible for maintaining the second Gibbs–Donnan effect by trapping $Na^+$ ions in the extracellular space, which counteracts the first Gibbs–Donnan effect due to the high concentration of negatively charged intracellular macromolecules. For the same reason, tissue recovery from spreading depolarization is not possible, if $Na^+/K^+$ pump activity is insufficient. All three α isoforms of the $Na^+/K^+$ pump presumably antagonize the spreading depolarization process. Their roles, however, vary, as they differ in their cellular and subcellular localizations, kinetic properties and affinities to $Na^+$, $K^+$ and ATP (O'Brien et al., 1994). Thus, the housekeeping $\alpha_1$ isoform is found on all vertebrate cells, is very sensitive to both $K^+$ and $Na^+$, has the greatest turnover and shows an intermediate dependence on the membrane potential. Accordingly, this isoform works at optimum rates under physiological conditions but seems to respond less well to demands (Crambert et al., 2000; Reiffurth et al., 2020). By contrast, the $\alpha_2$ isoform, which is located on glial cells but not on neurons in the adult brain, is ideally suited to oppose acute rises in $[K^+]_o$ because of its low affinity to $K^+$. This low affinity permits the enzyme to rapidly adapt its turnover over a wide range of $[K^+]_o$ (Grisar et al., 1980; Walz and Hertz, 1982). In addition, $\alpha_2$ activity rises in response to the membrane depolarizing effect of increasing $[K^+]_o$ (Crambert et al., 2000; Horisberger and Kharoubi-Hess, 2002), which applies in particular when the $\alpha_2$ isoform is linked with the $\beta_2$ subunit (Stoica et al., 2017). Accordingly, the $K^+$ threshold for spreading depolarization was exclusively lower in $\alpha_2$ isoform-deficient mice in contrast to $\alpha_1$ or $\alpha_3$ isoform-deficient mice (Reiffurth et al., 2020) and mutations in the ATP1A2 gene, encoding the $\alpha_2$ isoform, cause FHM type 2, a rare Mendelian model disease of spreading depolarization (De Fusco et al., 2003; Jurkat-Rott et al., 2004; Dreier et al., 2005; Leo et al., 2011; Unekawa et al., 2018). In contrast to the $\alpha_2$ isoform, the $\alpha_3$ isoform is found on neurons. This isoform is characterized by a low $Na^+$ affinity which allows it to respond particularly well to the marked rise in $[Na^+]_i$ during spreading depolarization, suggesting its involvement in the neuronal recovery from spreading depolarization (Crambert et al., 2000). However, application of ouabain at 100 μM in interface slices of rodents should fully block the $\alpha_2/\alpha_3$ portion of the $Na^+/K^+$ pump. Yet, ouabain at 100 μM induces a prolonged but largely reversible spreading depolarization (Balestrino et al., 1999). This means that high intraneuronal $Na^+$-induced activation (Skou and Esmann, 1992) of the less ouabain-sensitive $\alpha_1$ isoform alone is still sufficient to largely reestablish the ion gradients and repolarize the neurons during spreading depolarization. In contrast, complete blockade of all three isoforms by a very high dose of ouabain leads to terminal spreading depolarization, that is, the Gibbs–Donnan equilibrium and death of the cells.

An interesting detail is that prolonged exposure to slightly elevated $[K^+]_o$ levels appears to decrease the activity of certain $Na^+/K^+$-ATPases, which may explain a decrease in the $K^+$ threshold for spreading depolarization with increasing duration of exposure to slightly elevated $[K^+]_o$. Thus, Major et al. (2017) measured a selective decline in $\alpha_2/\alpha_3$ $Na^+/K^+$-ATPase activity only 30 min after exposure to elevated $[K^+]_o$ below the $K^+$ threshold of spreading depolarization. Importantly, the *ex vivo* enzyme assay was performed under optimal biochemical conditions, suggesting that the prior prolonged exposure to elevated $[K^+]_o$ *in vivo* must have caused a persistent disturbance of the pump, which was still detectable *ex vivo*. A similar decline in activity was also previously observed in cultured astrocytes within 10 min of $[K^+]_o$ elevation to a relatively high concentration of 30 mM (Hajek et al., 1996). Overall, the experimental data currently indicate that this suppression of $\alpha_2/\alpha_3$ enzyme activity by prolonged $[K^+]_o$ elevation results from modifications of specific active sites. This could trap the enzyme in an inactive phosphorylated state (Mishra and Delivoria-Papadopoulos, 1999).

Apart from this detail, it has been found that all $Na^+/K^+$-ATPases are strongly activated over the entire range of $[K^+]_o$ and $[Na^+]_i$ levels reached during spreading depolarization (Skou and Esmann, 1992; Crambert et al., 2000; Horisberger and Kharoubi-Hess, 2002; Larsen et al., 2014). In other words, the activability of $Na^+/K^+$-ATPases by $[K^+]_o$ and $[Na^+]_i$ is not abolished as a result of the abrupt maximal increases of $[K^+]_o$ and $[Na^+]_i$, because otherwise spreading depolarization would always be irreversible. Together with the fact that ouabain at high concentrations that inhibit all three α isoforms prevents recovery from spreading depolarization, all the known properties of the $Na^+/K^+$-ATPases (Skou and Esmann, 1992; Crambert et al., 2000; Horisberger and Kharoubi-Hess, 2002; Larsen et al., 2014) strongly support the notion that their increased activation is a necessary mechanism for recovery from spreading depolarization.

The question remains as to what structure underlies the non-specific $Na^+/K^+$ conductance that initially drives spreading depolarization (Czeh et al., 1993) and whereby this increase in permeability of the cell membrane disappears again, rather than that $Na^+/K^+$-ATPases are additionally required to terminate spreading depolarization. While we do not rule it out, we do not consider it very likely that the structure underlying the non-specific $Na^+/K^+$ conductance is the same as that responsible for recovery from spreading depolarization. That is, we do not consider it likely that the conversion of one or more $Na^+/K^+$-ATPases into channels drives spreading depolarization (Robertson et al., 2020), because it would then be difficult to explain why spreading depolarization is in principle a reversible phenomenon. Also, this hypothesis would hardly be suitable to explain why spreading depolarization with the characteristic abrupt depolarization, the abrupt near-complete breakdown of the ion gradients and the recovery occurring at the earliest after several tens of seconds has so far only been detected in the CNS, since $Na^+/K^+$-ATPases are also present in all other

tissues. The $\alpha_1$ isoform prevails in all vertebrate cells, but the $\alpha_2$ and $\alpha_3$ isoforms also exist not only in the CNS (Blanco, 2005). Although the search for the non-specific $Na^+/K^+$ channels in neuronal membranes that drive spreading depolarization has been unsuccessful to date, it remains the most likely hypothesis that such channels exist (Makarova et al., 2007; Dreier et al., 2013a), that they are relatively specific to neurons, and that they are structures that are different in nature from those required to restore ion homeostasis after the onset of spreading depolarization. The caveat is added, however, that it has not yet been sufficiently investigated whether spreading depolarization is indeed so specific to the gray matter of the brain or whether similar phenomena may also occur in other tissues of the body. A first step might be to characterize the exact time course of depolarization and breakdown of ion gradients during intoxication with ascending concentrations of the $Na^+/K^+$-ATPase inhibitor ouabain using ion-sensitive microelectrodes in comparative studies between brain and other organs. Flooding of brain gray matter with increasing concentrations of ouabain results in a continuum of initially reversible, single and clustered spreading depolarizations with progressively broadened negative DC shifts starting from an elevated level of baseline $[K^+]_o$ and returning to that elevated baseline (Balestrino et al., 1999; Major et al., 2017). Eventually, a terminal spreading depolarization occurs (Jarvis et al., 2001). Overall, the changes are very similar to those produced by ischemia of various severities. Alternatively, focal ischemia could also be directly investigated in comparative studies between brain and other organs.

In such experiments it is important to understand that the postulated principal difference between neurons and other body cells is not that the other body cells do not also swell when the $Na^+/K^+$-ATPase inhibitor ouabain is administered or ischemia is induced, but that other body cells swell very slowly over many hours. For example, erythrocytes do not swell in response to ouabain in the form of sudden events as neurons in the brain gray matter do in the form of spreading depolarizations (Kowluru et al., 1989). The fundamental difference is that the $Na^+$ permeability of erythrocytes remains extremely low when ouabain is administered, so that the evolution from the physiological double Gibbs–Donnan steady state to Gibbs–Donnan equilibrium is very slow. On the other hand, if $Na^+$ permeability is increased artificially by toxins such as palytoxin while $Na^+/K^+$-ATPase is inhibited, the swelling process and lysis of erythrocytes can be accelerated significantly (Volpe et al., 2014).

## BRAIN ACTIVITY CHANGES IN THE CONTEXT OF SPREADING DEPOLARIZATION

A fair question is then how all this translates into changes of neural function. The simplest way to observe neural function is to measure changes in spontaneous activity. Spontaneous brain activity results from the firing of cortical neurons. The firing of upstream neurons causes postsynaptic potentials in downstream neurons. These postsynaptic potentials are associated with rapid extracellular field potential changes. Synchronous activity from thousands or millions of neurons with similar spatial orientation produces fast extracellular field potential changes that are electrocorticographically recorded as brain electrical activity. As is well known, the minor breakdown, namely the epileptic seizure, involves an increase in firing rate and increased synchronization in the network, and the major breakdown, the spreading depolarization, results in loss of function, that is, silencing of spontaneous activity (Leão, 1944b). This spreading depolarization-induced spreading depression of spontaneous activity is observed as a rapidly evolving reduction in the amplitudes of spontaneous activity in the alternating current (AC) frequency band of the ECoG above 0.5 Hz and spreads along with spreading depolarization between neighboring recording sites (**Figure 1**). This migratory extinction of spontaneous activity was discovered by Leão (1944b) and termed spreading depression of spontaneous activity before he demonstrated the underlying process in 1947, i.e., the large negative DC shift. Leão (1947) interpreted the latter as an expression of neuronal depolarization. He based this interpretation on the similarity between the DC shift he recorded in the cerebral cortex and the asphyxia-induced DC shift recorded in the spinal cord by Van Harreveld and Hawes (1946), who previously interpreted this negative DC shift as reflecting neuronal depolarization. It is assumed that spreading depolarization initiates spreading depression because the sustained depolarization exceeds the inactivation threshold for the action potential generating channels (Kager et al., 2002). In practice, however, the observed patterns often deviate from expectations and sometimes depression begins, for example, only when the negative DC shift is already in regression, or it does not occur at all. If depression occurs, it usually lasts significantly longer than the negative DC shift, suggesting that it is maintained by other mechanisms than the depolarization block such as intracellular zinc or $Ca^{2+}$ and/or extracellular adenosine accumulation (Lindquist and Shuttleworth, 2012; Carter et al., 2013; Sawant-Pokam et al., 2017).

Already Leão (1944b, 1947) discovered additional patterns of spontaneous activity changes that can co-occur with the large negative DC shift of spreading depolarization such as non-spreading depression of activity or epileptic field potentials that replace the spreading depression of activity. The first signs of non-spreading depression start within seconds of anoxia, focal or global circulatory arrest with an arousal reaction of fast, irregular low-voltage activity (Dreier and Reiffurth, 2015). Synchronous gamma oscillations then occur within the first 30 s which are global and highly coherent with a striking increase in anterior-posterior-directed connectivity (Borjigin et al., 2013). Isoelectricity is usually reached within 30–40 s, well before the neuronal ATP pool is depleted (**Figure 1**) (Hochachka et al., 1996). As opposed to spreading depolarization-induced spreading depression, non-spreading depression develops simultaneously in the whole area exposed to severe ischemia. Also of particular importance is that non-spreading depression is associated with neuronal hyperpolarization in contrast to the depolarization block that initiates spreading depression (Tanaka et al., 1997; Muller and Somjen, 2000). It is still unclear how

hypoxic neurons and astrocytes are able to sense the drop in $p_{ti}O_2$ but several mechanisms have been proposed that may mediate non-spreading depression. These include: (i) changes in vesicular transmitter release (Katchman and Hershkowitz, 1993b; Fleidervish et al., 2001; Revah et al., 2016), (ii) activation of ATP-sensitive or G protein–dependent $Ca^{2+}$-sensitive $K^+$ channels (Erdemli et al., 1998; Muller and Somjen, 2000), (iii) release of adenosine (Fowler, 1989; Katchman and Hershkowitz, 1993a; Khazipov et al., 1993, 1995; Dzhala et al., 1999; Canals et al., 2008), (iv) acidosis (Mutch and Hansen, 1984; Taylor et al., 1996), and (v) breakdown of gamma oscillations ("interneuron energy hypothesis") (Kann et al., 2014). In animals, non-spreading depression of activity is typically measured in the center of ischemia after MCAO or during anoxia or global circulatory arrest (Leão, 1947; Mayevsky and Chance, 1975; Luckl et al., 2018) (**Figure 1**). In humans, it has only been clearly demonstrated so far in the dying process during cardio circulatory arrest (Dreier et al., 2018b). Non-spreading depression of activity usually significantly precedes the first spreading depolarization in the center of ischemia. The median latency between cessation of spontaneous activity and onset of spreading depolarization was 65 s in the center of ischemia after MCAO in rats (Luckl et al., 2018) and 76 s in the dying process in humans during cardio circulatory arrest (Dreier et al., 2018b). Non-spreading depression is thought to lead to the sudden and simultaneous neurological deficits in various modalities, such as language, motor, sensory, or visual functions, that are typical of transient ischemic attacks and most types of ischemic strokes (Dreier and Reiffurth, 2015).

However, simultaneous depressions of spontaneous activity at different recording sites may precede spreading depolarization not only in the context of ischemia. For example, they can typically be detected even at some distance from a KCl droplet application to trigger spreading depolarization *in vivo*, even if no local increase in $[K^+]_o$ precedes the spreading depolarization at the affected recording site (**Figure 3**). The underlying mechanism of this type of simultaneous depression, however, is unknown.

Another curiosity, described as early as 1944 (Leão, 1944b) and 1953 (van Harreveld and Stamm, 1953), is that the silencing of brain activity induced by spreading depolarization changed as a result of minimal electrical stimulations. Finally, epileptic field potentials were recorded during the period that had originally seen spreading depression of activity. Van Harreveld and Stamm called this phenomenon spreading convulsion. It is characterized by epileptic field potentials superimposed on the negative DC potential. Most often these occur on the final shoulder of the negative DC potential. Spreading convulsions have been observed, e.g., in organotypic cultures (Kunkler and Kraig, 1998) but also in human brain slices and in patients (Dreier et al., 2012). Based on a discussion with our colleagues Jeff Noebels, Jed Hartings, and Bill Shuttleworth, it is probably more appropriate to use the term spreading depolarization with epileptiform activity (SDEA) instead of spreading convulsion to refer to the phenomenon, since it is not a behavioral phenomenon but an electrographic phenomenon.

A special case of such SDEA occurs when the electrographic seizures overlie a terminal spreading depolarization, i.e., a spreading depolarization-initiated NUP, rather than a short-lasting spreading depolarization. Examples are given in **Figure 4** after MCAO in the rat and in **Figures 5**, **6** in

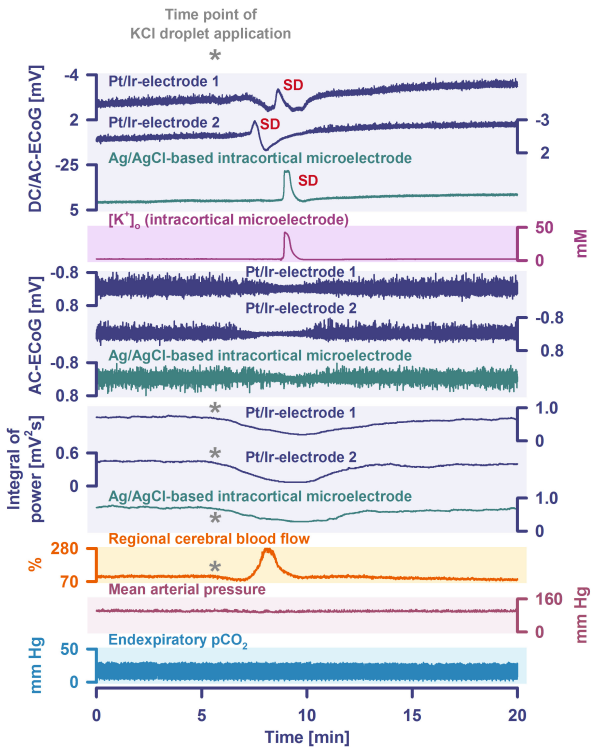


**FIGURE 3 |** Spreading depolarization remotely triggered by a droplet of KCl (2 M) in a naïve rat *in vivo* is shown. Traces 1–3: the full-band ECoG signal [DC/AC-ECoG] contains information on both the negative DC shift that identifies spreading depolarization (Dreier, 2011) and the activity changes. Note the differences in amplitude and shape of the DC shift between the gold standard recording technique in animals, the intracortical glass-microelectrode, and the platinum/iridium (Pt/Ir) electrodes on the brain surface, gold standard in humans (Dreier et al., 2017; Major et al., 2021). Also note the spread of the spreading depolarization in rostral (Pt/Ir-electrode 2)-caudal (Pt/Ir-electrode 1) direction. Trace 4: the hallmark of spreading depolarization is the near-complete breakdown of the transcellular ion concentration gradients. Here, the large spreading depolarization-associated increase in $[K^+]_o$ is seen. Traces 5–7: the spontaneous activity is assessed in the AC-ECoG, i.e., the higher frequency band between 0.5 and 45 Hz. Traces 8–10 display the integral of power of the spontaneous activity (Dreier et al., 2006, 2017). The integral of the power of the AC-ECoG is based on a method of computing time integrals over a sliding window according to a time decay function. This mathematical procedure provides a smoothed curve easing visual assessment of changes in AC-ECoG power. The method has become standard to score depression durations accompanying spreading depolarization. Spreading depolarization shows a depressive effect on spontaneous activity (=spreading depression). However, other events can also cause depression of activity. For example, we observed here a simultaneous depression of spontaneous activity at all electrodes immediately after the rostral KCl application (cf. asterisks). A subsequent, additional spreading depolarization-induced depression is observed at the caudal Pt/Ir electrode. Trace 11: a shallow initial hypoperfusion accompanied the KCl-triggered simultaneous depression of spontaneous activity that preceded the spreading depolarization-induced hyperemia. Trace 12 shows the mean arterial pressure (measured via femoral artery catheter). Trace 13 shows the end-expiratory $pCO_2$.

aSAH patients. Such patterns can probably be explained by portions of the network jumping from the near-complete sustained depolarization of spreading depolarization to the less pronounced sustained depolarization of electrographic seizures. In animal experiments, this pattern was associated with particularly large infarcts (Luckl et al., 2018). However, this was most likely related to the fact that the associated NUPs were particularly pronounced.

On the basis of all these observations, although spreading depression is an excellent term for the spreading depression of activity, it is misleading and tantamount to semantic paraphasia to use the term spreading depression as a generic term for the underlying process of spreading depolarization. This is especially true as it has been widely reproduced that spreading depolarization can also occur in tissues without any spontaneous neuronal activity such as in normoxic and normoglycemic brain slices (Dreier et al., 2001). In such tissues we would then have to speak of 'spreading depression in absence of spreading depression,' if the term 'spreading depression' is used once as a generic term instead of the term 'spreading depolarization' and on the other hand denotes the spreading depression of spontaneous activity, which is clearly absurd. Instead, the COSBID group has recommended to use the term spreading depolarization as the generic term for the underlying process (Dreier et al., 2017). However, this should in no way prevent us from using the term spreading depression for the spreading depression of activity, i.e., where this term is scientifically correct. For example, spreading depolarization-induced spreading depression of activity in **Figure 1** is more pronounced the farther the electrode is from the center of ischemia because the farther the electrode is from the center of ischemia, the less pronounced (or even absent) the non-spreading depression of activity. Furthermore, whereas the dying process in cardio circulatory arrest usually leads first to non-spreading depression and then to spreading depolarization, the development of brain death during continued circulation in the intensive care unit is most commonly initiated by spreading depolarization and induced spreading depression (Dreier et al., 2018b, 2019, 2022; Carlson et al., 2019).

A particular problem in migraine research is that quite a few migraine researchers are convinced that all spreading depolarizations of interest to the migraine researcher induce spreading depression, which is thought to entail the patient percept of the migraine aura (Leão and Morison, 1945), and spreading depolarizations, once accompanied by other spontaneous activity changes, no longer have anything to do with migraine and therefore are not relevant to the migraine researcher. However, this is at odds with the thin data available. Indeed, there is only a single case report in the world literature to date in which spreading depolarization-induced spreading depression was electrocorticographically recorded while the patient had symptoms of a migraine aura, i.e., the patient reported the sequential series of neurological deficits typical of migraine aura (Major et al., 2020). She even had two migraine auras in succession, during each of which spreading depolarization-induced spreading depression was recorded. However, the patient had subdural electrodes implanted only because she had suffered aSAH a few days earlier, and she had no previous history of migraine with aura or without aura. Apart from one more study investigating magnetoencephalographic fields from patients during spontaneous and induced migraine aura (Bowyer et al., 2001), the other evidence supporting that migraine aura is caused by spreading depolarization is all indirect and based on the similarity of recorded rCBF or blood oxygen level-dependent (BOLD) changes during migraine aura with the normal hemodynamic response to spreading depolarization in animal studies (Olesen et al., 1981; Lauritzen et al., 1983; Hadjikhani et al., 2001). However, not only is the evidence from these studies indirect, but the studies using the planar intracarotid $^{133}$Xenon method and single-photon emission computed tomography (SPECT) in patients undergoing migraine auras were additionally problematic as the migraine auras recorded in these studies cannot be referred to as normal migraine auras. Very likely, not only spreading depressions but also non-spreading depressions of spontaneous activity may have occurred in the context of spreading depolarizations in these studies, because it is assumed that the large number of recorded migraine auras in these studies resulted from the procedure of catheterizing and injecting the carotid artery, which provoked visual migraine aura in more than 50% of the patients (Lassen and Friberg, 1991). It is now widely assumed that the mechanism leading to these auras was cerebral microemboli causing brief ischemic episodes, because such microemboli are potent triggers of spreading depolarizations in animals (Nozari et al., 2010; Dreier and Reiffurth, 2015). That is, these studies were essentially a proof of Leão's original hypothesis that the basal neural network processes during migraine aura and during disturbances of the cerebral circulation are "*of the same nature*."

Although most spreading depolarizations that occur in association with migraine aura are unlikely to be primarily vascular in origin, the alert neurologist working in a stroke unit or as a consultant in a cardiology department where there is a high volume of interventions such as cardiac catheterization and atrial ablation will see single cases of migraine aura associated with minor, often pinpoint stroke every year if the patients are carefully interviewed and MRIs are performed (Olesen et al., 1993; Klingebiel et al., 2008; Dreier and Reiffurth, 2015; Waters et al., 2018; Altamura et al., 2021). Also, to understand why relatively small strokes can sometimes be accompanied by transient global neurological deficits (Dreier et al., 2006) or why transient focal symptoms can sometimes occur whose representational fields are not in the ischemic zone proper (Klingebiel et al., 2008), it is useful to have an understanding of the spreading-depolarization continuum, because spreading depolarizations are precisely not only local but can spread over large areas of cortex and subcortical gray matter (James et al., 1999; Cain et al., 2017; Kaufmann et al., 2017; Milakara et al., 2017). For basic researchers, the erroneous use of the term 'spreading depression' for the phenomenon of 'spreading depolarization' is particularly problematic because, often believing that the changes in spontaneous activity are irrelevant, they use inadequate filter settings for the ECoG, i.e., record only the DC potential, and all valuable information from the experiments contained in the changes in spontaneous activity

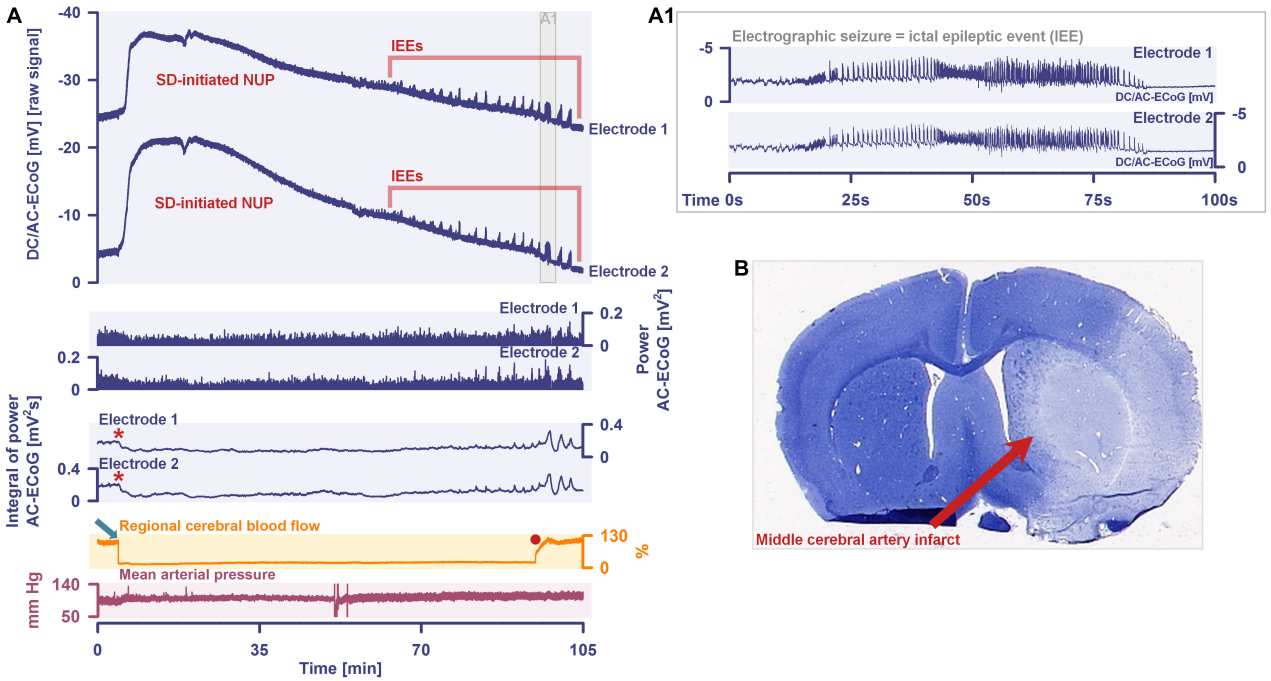


**FIGURE 4 | (A)** Spreading depolarization-initiated NUP with superimposed ictal epileptic events (IEEs) after middle cerebral artery occlusion (MCAO) in a rat (Luckl et al., 2018). Traces 1 and 2 show the full-band ECoG signal [DC/AC-ECoG] which contains both the negative DC shifts that identify spreading depolarizations and the changes in spontaneous brain activity. Traces 3 and 4 only show the spontaneous activity in the higher frequency band (AC-ECoG, bandpass: 0.5–45 Hz). Traces 5 and 6 display the integral of the power of the AC-ECoG which provides a smoothed curve easing visual assessment of changes in AC-ECoG power. Trace 8: regional cerebral blood flow (rCBF) recorded with laser-Doppler flowmetry. Trace 9: mean arterial pressure measured via femoral artery catheter. MCAO leads to a sharp decrease in rCBF (dark green arrow in trace 7). Shortly after MCAO, non-spreading depression of activity occurs and is best observable in the integral of the power (red asterisks at traces 5 and 6). The drop in rCBF triggers a spreading depolarization that propagates from electrode 2–1 and initiates a NUP (traces 1 and 2). Electrographic seizures, also known as IEE, occur superimposed on the NUP. They continue and even intensify after the reperfusion (red dot at trace 7). **(A1)** Displays one of the IEEs at higher temporal resolution. **(B)** The animal was sacrificed 72 h later. The infarct in both basal ganglia and cortex is macroscopically identified as a pale area using hematoxylin staining.

is lost. This is especially relevant when the experiments are used to correlate electrophysiology and behavior.

## DISCUSSION

Spreading depolarization is one of the most important pathophysiological processes of the CNS, with far-reaching implications for neurology, and there, not only for migraine with aura, but also for the most diverse forms of acute injury of the cerebrum and most likely also of the cerebellum, brainstem and spinal cord, and even for paroxysmal movement disorders (Lu et al., 2021). Spreading depolarization is among the most basic pathological processes in the nervous system that appeared in phylogenesis even before the development of a proper blood circulation (Spong et al., 2017). The reason why spreading depolarization must occur in insects and vertebrates under certain conditions is derived from the fundamental structure of their neural networks and, in particular, from the second law of thermodynamics. In this context, the role of certain neurotransmitters in the nervous systems of different species (Robertson et al., 2020), such as the role of glutamate, may be fundamentally different without altering the basic property of spreading depolarization, which is that the state of the neural network shifts abruptly toward the pathological Gibbs–Donnan equilibrium, but without reaching it completely unless the neurons eventually die.

For individuals suffering from migraine with aura, all this means that they should minimize their vascular risk factors, even though their absolute risk of stroke is low. On the one hand, patients with typical migraine with aura should be reassured that the constellations under which spreading depolarizations occur in migraine with aura are almost always benign, and they should not be subjected to inappropriate and potentially dangerous investigations and treatments. On the other hand, if the migraine aura occurs in an unusual constellation, the treating physician should be alert and perform further diagnostic workup, as it may conceal a stroke (Olesen et al., 1993; Klingebiel et al., 2008; Waters et al., 2018). It is also particularly important to understand that migraine is not a prerequisite for the occurrence of spreading depolarizations, and very many spreading depolarizations do not manifest clinically as migraine auras. Any stroke that affects the gray matter is presumably associated with spreading depolarizations, and almost all of us will end up with a terminal spreading depolarization regardless of whether or not we had migraine auras during our lifetime

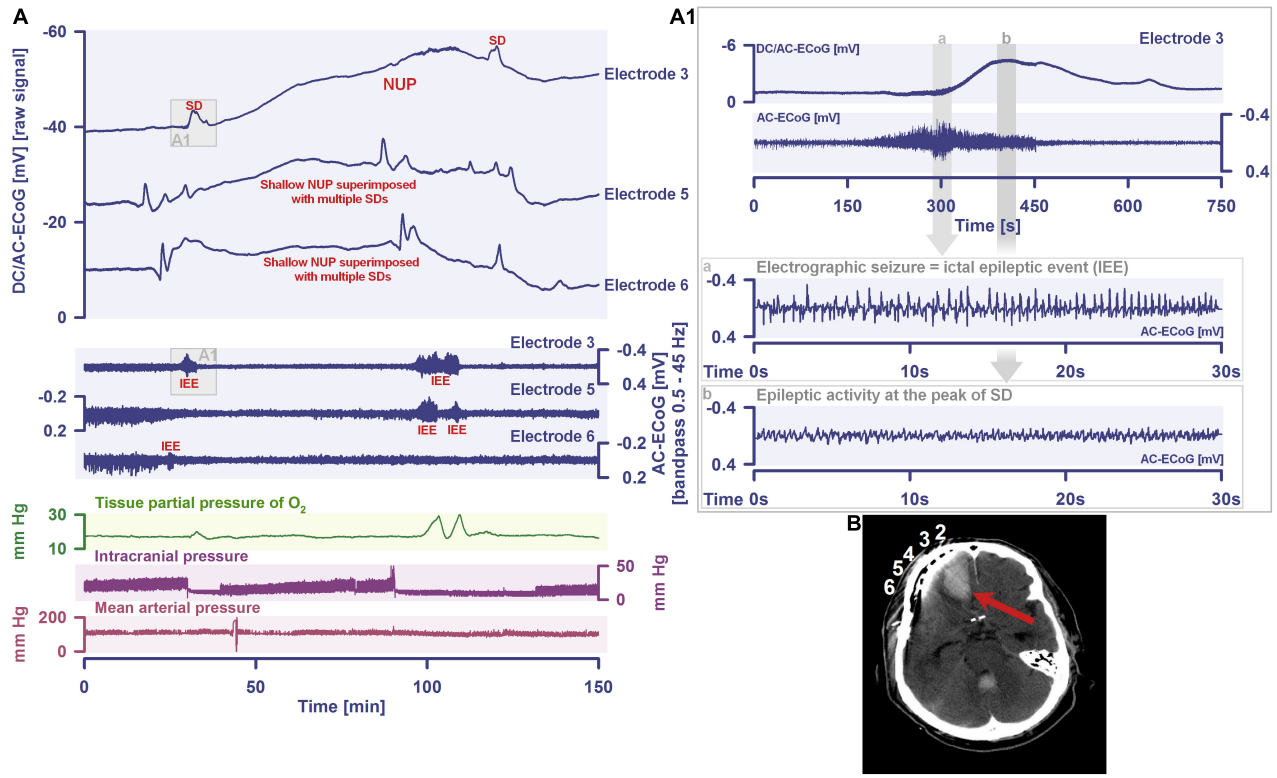


**FIGURE 5 | (A)** Spreading depolarization-initiated NUP superimposed with further SDs and IEEs recorded after aneurysmal subarachnoid hemorrhage (aSAH) in a 71-year old man (Dreier et al., 2012; Winkler et al., 2012). The NUP occurred on day 10 after the initial hemorrhage. Traces 1–3 from top to bottom give the DC/AC-ECoG recordings (band-pass: 0–45 Hz). The SD-initiated NUP and the later superimposed SDs are observed as negative DC shifts (negative upward). Traces 4–6 not only show the depressive effect of the SDs on the spontaneous brain activity but also the superimposed IEEs (AC-ECoG, band-pass: 0.5–45 Hz). Note that the first IEE at electrode 3 (trace 4) is temporally associated with the onset of an SD [shown at higher temporal resolution in the insert **(A1)**]. Since the IEE is at least partially superimposed on the negative DC shift, it is a spreading convulsion according to the old nomenclature (van Harreveld and Stamm, 1953) or a spreading depolarization with epileptiform activity (SDEA) according to the new nomenclature. Trace 7 shows the tissue partial pressure of oxygen ($p_{ti}O_2$) measured with an intraparenchymal sensor. Trace 8 gives the intracranial pressure (ICP) measured with an extraventricular drainage (EVD) catheter. Trace 9 shows the mean arterial pressure (MAP) measured with a radial artery catheter. The IEEs are associated with hyperoxic responses (the oxygen sensor was located in the cortex between electrodes 3 and 4). **(B)** Post-operative computed tomography (CT) scan showing an intracerebral hematoma (red arrow) in the right frontal lobe of the patient and electrodes 2–6 of the subdural recording strip.

(Dreier et al., 2018b, 2019, 2022; Carlson et al., 2019). Exceptions are of course conceivable, starting with the fact that one can also die from the immediate impact of a bomb.

It may be added that the fact that spreading depolarization does not occur in highly artificial systems such as cell cultures is not an argument against a thorough investigation of this process; on the contrary, it is another argument in favor of it. Indeed, there are a number of prominent examples where the results of cell culture experiments may be consistent in themselves, but the experiments do not examine the *in vivo* state of the animal or patient that they purport to examine. For example, as explained above, spreading depolarization secondarily leads to a massive increase in the concentrations of many different neurotransmitters, including glutamate (Van Harreveld and Fifkova, 1970; Fabricius et al., 1993; Molchanova et al., 2004; Enger et al., 2015). Indeed, spreading depolarization is the only process in the brain that causes a considerable increase in glutamate in the extracellular space. In non-ischemic tissue, glutamate increased up to 100 μM during spreading depolarization (Zhou et al., 2013). Accordingly, in ischemia *in vivo*, no glutamate increase is directly measurable before the onset of spreading depolarization, but the directly measurable glutamate increase follows the ischemia-induced spreading depolarization (Hinzman et al., 2015). Although the glutamate increase due to spreading depolarization does not occur in isolation but is accompanied by massive concentration changes of innumerable other factors, a pure glutamate application of 100 μM to primary cell culture is often presented as a proxy for ischemia (Randall and Thayer, 1992; Keelan et al., 1999; Vergun et al., 1999; Rueda et al., 2016). A blind spot in all these models is not only that the glutamate increase is studied in isolation from the many other changes, but also that molecular oxygen, which is, after all, absent during ischemia, is required not only for ATP production but also for numerous other cellular processes. To give but two examples: (1) Molecular oxygen is required for NO synthesis (Jiang et al., 2001; Uetsuka et al., 2002). So, how will an increase in extracellular glutamate cause increased NO production during ischemia (Keelan et al., 1999)

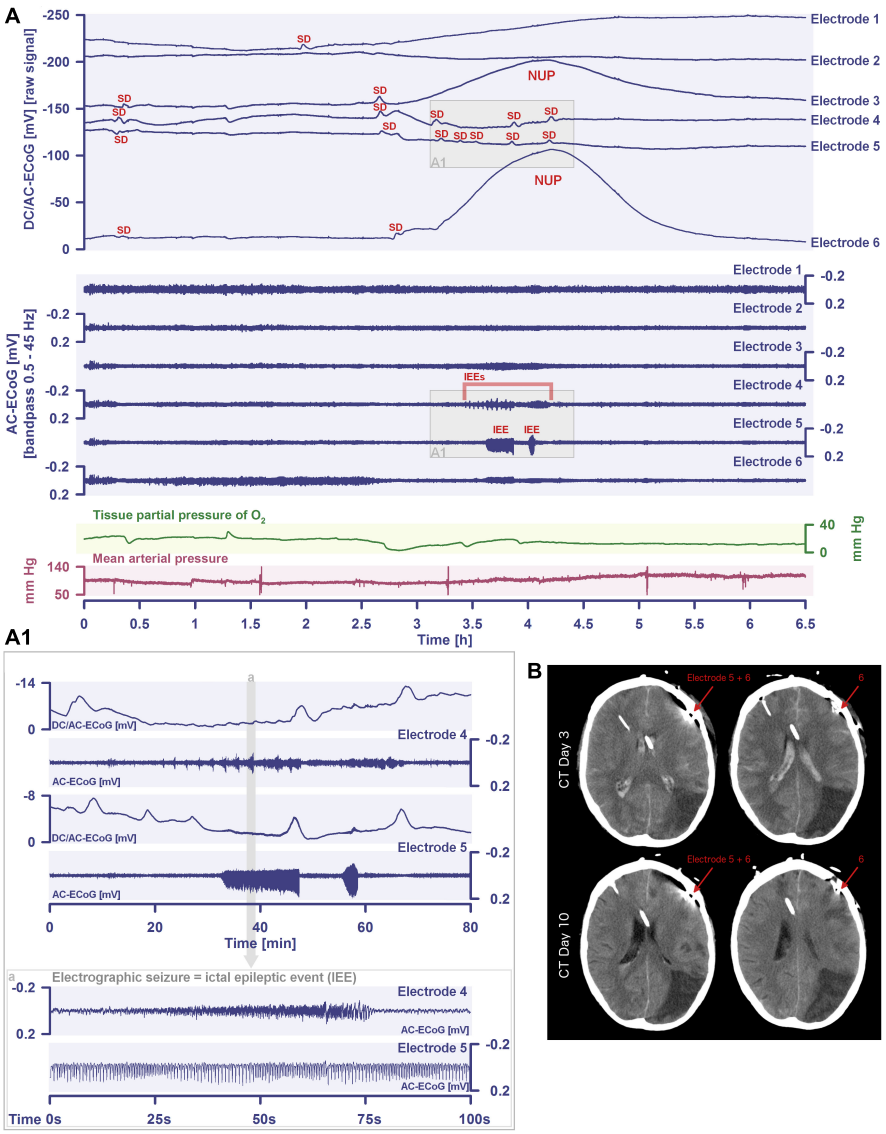


**FIGURE 6 | (A)** A cluster of SDs initiating a NUP is shown that occurred in a 57-year old man after aneurysmal subarachnoid hemorrhage. The cluster was recorded with a 6-contact subdural strip for ECoG on day 7 after the initial hemorrhage. Traces 1–6 from top to bottom give the DC/AC-ECoG recordings (band-pass: 0–45 Hz). Spreading depolarizations and spreading depolarization-initiated NUP are observed as negative DC shifts (negative upward). Traces 8–12 show persistent depression of the spontaneous activity after the first spreading depolarization at electrodes 3–5 as assessed in the high frequency band (AC-ECoG, band-pass: 0.5–45 Hz). This depression is interrupted by IEEs best seen at electrodes 4 and 5 [traces 10 and 11; shown at higher temporal resolution in the insert **(A1)**]. Trace 13: tissue partial pressure of oxygen ($p_{ti}O_2$) measured with an intraparenchymal sensor. Trace 14: mean arterial pressure measured with a radial artery catheter. **(B)** Compared with computed tomography (CT) at day 3 after the initial hemorrhage, CT at day 10 shows new hypodensities typical of scattered delayed ischemic infarction in the cortex near the subdural electrodes, matching the spreading depolarization-induced NUP at electrode 6 on day 7. Accurate assessment is somewhat limited by the typical hyperdense streak artifacts around the electrodes.

when the normal NO synthesis is blocked by lack of molecular oxygen? How is it then that numerous review articles and neuroscience textbooks convey the message that ischemic cell injury is a consequence of excitotoxic increase in NO levels as a result of glutamate release (Belov Kirdajova et al., 2020)? Some NO production via endothelial NOS by reduction of nitrite may occur under anoxia (Gautier et al., 2006). However, this pathway is temporally limited because it depends on nitrite reserves, and it is questionable whether it is sufficient to maintain even the basal NO level. If anything, administration of an NO donor to the patient in acute ischemic stroke appears to have a beneficial effect if treatment is started within 6 h of the onset of ischemia (Woodhouse et al., 2015). (2) Another example is that the production of reactive oxygen species (ROS) also requires molecular oxygen (Dirnagl et al., 1995; Dreier et al., 1998; Peters et al., 1998). Thus, glutamate is a potent stimulus of ROS production in cell culture (Kubota et al., 2010), but the spreading depolarization-induced glutamate increase

under ischemic conditions *in vivo* cannot cause an increase in ROS production because ROS production is blocked by lack of molecular oxygen (Dirnagl et al., 1995; Dreier et al., 1998; Peters et al., 1998). In fact, an increase in ROS production only occurs in the context of ischemia *in vivo*, if the tissue is fortunate enough to be reperfused and glutamate is taken up again into the cells from the extracellular space. That is, ROS production in response to an ischemic event *in vivo* increases to the pathological range only when (i) tissue is reperfused, (ii) neurons recover from the ischemia-induced spreading depolarization and (iii) extracellular glutamate concentration decreases again, which is the opposite of what is observed in cell culture upon glutamate application (Dirnagl et al., 1995; Dreier et al., 1998; Peters et al., 1998). Numerous studies on thrombolysis and mechanical recanalization of ischemic stroke patients have now shown that reperfusion does not lead to additional damage, but is currently the only chance for ischemic brain tissue to survive (Prabhakaran et al., 2015). Cell culture models are often touted as an effective substitute for animal experiments in order to reduce the number of animal experiments, and considerable political, economic and social pressure is built up, e.g., through poster campaigns in public transport, prizes and other initiatives, to achieve this goal. However, the above examples show how easily artifacts from cell culture experiments can corrupt scientific concepts, which is then reflected in countless review articles and textbook chapters, although the lack of validity of the concepts is easily revealed once they are tested *in vivo* (Dreier et al., 1998; Peters et al., 1998; Uetsuka et al., 2002), where, unlike in cell cultures, intracellular space is large and extracellular space is small, the full context of cell–cell, cell–circulation, and organ–organ interactions is preserved, spreading depolarizations occur, and neurons die from severe oxygen-glucose deprivation within minutes rather than within hours (Wappler et al., 2013). Cell culture experiments are of high scientific value for the study of intracellular signaling cascades only when used as a complement to, rather than as a replacement of, *in vivo* experiments, because *in vivo* experiments are indispensable for providing guidance and testing hypotheses derived from cell culture experiments, which are inevitably subject to myriad biases due to the artifact-laden circumstances.

## CONCLUSION

Spreading depolarization is a metastable universal reference state for acute CNS pathology. All relevant mechanisms in the context of acute ischemic or traumatic CNS injury, whether parenchymal, vascular, or immunologic, should be studied in relation to this reference state in order to correctly place them in the overall context. The fact that spreading depolarization can be harmless on the one hand and lead to neuronal death and even brain death on the other, that it is a huge electrochemical wave that is nevertheless difficult to detect in scalp EEG, that it can be triggered experimentally so easily and in a nicely stereotyped manner and yet is one of the most complex phenomena of the CNS with a highly complex pharmacology, explains at least in part why neuroscientists and neurologists have not struggled as hard with any other phenomenon for decades as they have with spreading depolarization.

## AUTHOR CONTRIBUTIONS

CL and JD contributed substantially to the conception and design of the work and drafting and revising the manuscript for important intellectual content. JL, VH, CR, SM, NH, and JW drafted parts of the manuscript. All authors approved the final version to be published and agreed to be accountable for all aspects of the work.

## FUNDING

This work was supported by grants from the: DFG Deutsche Forschungsgemeinschaft (German Research Council) (DFG DR 323/5-1) to JW and JD, DFG DR 323/10-1 to JD and BMBF Bundesministerium für Bildung und Forschung (Era-Net Neuron EBio2, with funds from BMBF 01EW2004) to JD. We acknowledge support from the German Research Foundation (DFG) and the Open Access Publication Fund of Charité – Universitätsmedizin Berlin.

## REFERENCES

Aiba, I., Carlson, A. P., Sheline, C. T., and Shuttleworth, C. W. (2012). Synaptic release and extracellular actions of Zn2+ limit propagation of spreading depression and related events in vitro and in vivo. *J. Neurophysiol.* 107, 1032–1041. doi: 10.1152/jn.00453.2011

Aiba, I., and Shuttleworth, C. W. (2012). Sustained NMDA receptor activation by spreading depolarizations can initiate excitotoxic injury in metabolically compromised neurons. *J. Physiol.* 590(Pt 22), 5877–5893. doi: 10.1113/jphysiol.2012.234476

Aiba, I., and Shuttleworth, C. W. (2014). Characterization of inhibitory GABA-A receptor activation during spreading depolarization in brain slice. *PLoS One* 9:e110849. doi: 10.1371/journal.pone.0110849

Aitken, P. G., Borgdorff, A. J., Juta, A. J., Kiehart, D. P., Somjen, G. G., and Wadman, W. J. (1998). Volume changes induced by osmotic stress in freshly isolated rat hippocampal neurons. *Pflugers Arch.* 436, 991–998. doi: 10.1007/s004240050734

Allen, N. J., Rossi, D. J., and Attwell, D. (2004). Sequential release of GABA by exocytosis and reversed uptake leads to neuronal swelling in simulated ischemia of hippocampal slices. *J. Neurosci.* 24, 3837–3849. doi: 10.1523/JNEUROSCI.5539-03.2004

Altamura, C., Cascio Rizzo, A., Viticchi, G., Maggio, P., Costa, C. M., Brunelli, N., et al. (2021). Shorter visual aura characterizes young and middle-aged stroke patients with migraine with aura. *J. Neurol.* 2021:10671. doi: 10.1007/s00415-021-10671-x

Andrew, R. D., Labron, M. W., Boehnke, S. E., Carnduff, L., and Kirov, S. A. (2007). Physiological evidence that pyramidal neurons lack functional water channels. *Cereb. Cortex* 17, 787–802. doi: 10.1093/cercor/bhk032

Anon, (2021). *Map: Chemistry — The Central Science (Brown et al.)*. Available online at: https://chem.libretexts.org/@go/page/21655 (accessed February 1, 2022).

Avoli, M., Drapeau, C., Louvel, J., Pumain, R., Olivier, A., and Villemure, J. G. (1991). Epileptiform activity induced by low extracellular magnesium in the human cortex maintained in vitro. *Ann. Neurol.* 30, 589–596. doi: 10.1002/ana.410300412

Ayad, M., Verity, M. A., and Rubinstein, E. H. (1994). Lidocaine delays cortical ischemic depolarization: relationship to electrophysiologic recovery

and neuropathology. *J. Neurosurg. Anesthesiol.* 6, 98–110. doi: 10.1097/00008506-199404000-00005

Balbi, M., Koide, M., Wellman, G. C., and Plesnila, N. (2017). Inversion of neurovascular coupling after subarachnoid hemorrhage in vivo. *J. Cereb. Blood Flow Metab.* 37, 3625–3634. doi: 10.1177/0271678X16686595

Balestrino, M., Young, J., and Aitken, P. (1999). Block of (Na+,K+)ATPase with ouabain induces spreading depression-like depolarization in hippocampal slices. *Brain Res.* 838, 37–44. doi: 10.1016/s0006-8993(99)01674-1

Belov Kirdajova, D., Kriska, J., Tureckova, J., and Anderova, M. (2020). Ischemia-Triggered glutamate excitotoxicity from the perspective of glial cells. *Front. Cell Neurosci.* 14:51. doi: 10.3389/fncel.2020.00051

Bere, Z., Obrenovitch, T. P., Bari, F., and Farkas, E. (2014). Ischemia-induced depolarizations and associated hemodynamic responses in incomplete global forebrain ischemia in rats. *Neuroscience* 260, 217–226. doi: 10.1016/j.neuroscience.2013.12.032

Besse, M., Belz, M., Folsche, T., Vogelgsang, J., Methfessel, I., Steinacker, P., et al. (2020). Serum neurofilament light chain (NFL) remains unchanged during electroconvulsive therapy. *World J. Biol. Psychiatry* 21, 148–154. doi: 10.1080/15622975.2019.1702717

Bignami, A., and Palladini, G. (1966). Experimentally produced cerebral status spongiosus and continuous pseudorhythmic electroencephalographic discharges with a membrane-ATPase inhibitor in the rat. *Nature* 209, 413–414. doi: 10.1038/209413a0

Blanco, G. (2005). Na,K-ATPase subunit heterogeneity as a mechanism for tissue-specific ion regulation. *Semin Nephrol.* 25, 292–303. doi: 10.1016/j.semnephrol.2005.03.004

Blau, J. (2004). Harold G Wolff: the man and his migraine. *Cephalalgia* 24, 215–222. doi: 10.1111/j.1468-2982.2003.00642.x

Blau, J. N. (1992). Migraine: theories of pathogenesis. *Lancet* 339, 1202–1207. doi: 10.1016/0140-6736(92)91140-4

Borjigin, J., Lee, U., Liu, T., Pal, D., Huff, S., Klarr, D., et al. (2013). Surge of neurophysiological coherence and connectivity in the dying brain. *Proc. Natl. Acad. Sci. USA* 110, 14432–14437. doi: 10.1073/pnas.1308285110

Bosche, B., Graf, R., Ernestus, R. I., Dohmen, C., Reithmeier, T., Brinker, G., et al. (2010). Recurrent spreading depolarizations after subarachnoid hemorrhage decreases oxygen availability in human cerebral cortex. *Ann. Neurol.* 67, 607–617. doi: 10.1002/ana.21943

Bowyer, S. M., Aurora, K. S., Moran, J. E., Tepley, N., and Welch, K. M. (2001). Magnetoencephalographic fields from patients with spontaneous and induced migraine aura. *Ann. Neurol.* 50, 582–587. doi: 10.1002/ana.1293

Brennan, K. C., Bates, E. A., Shapiro, R. E., Zyuzin, J., Hallows, W. C., Huang, Y., et al. (2013). Casein kinase idelta mutations in familial migraine and advanced sleep phase. *Sci. Transl. Med.* 56, 181–111. doi: 10.1126/scitranslmed.3005784

Budde, M. D., and Frank, J. A. (2010). Neurite beading is sufficient to decrease the apparent diffusion coefficient after ischemic stroke. *Proc. Natl. Acad. Sci. U S A* 107, 14472–14477. doi: 10.1073/pnas.1004841107

Busch, E., Gyngell, M. L., Eis, M., Hoehn-Berlage, M., and Hossmann, K. A. (1996). Potassium-induced cortical spreading depressions during focal cerebral ischemia in rats: contribution to lesion growth assessed by diffusion-weighted NMR and biochemical imaging. *J. Cereb. Blood Flow Metab.* 16, 1090–1099. doi: 10.1097/00004647-199611000-00002

Busch, E., Hoehn-Berlage, M., Eis, M., Gyngell, M. L., and Hossmann, K. A. (1995). Simultaneous recording of EEG, DC potential and diffusion-weighted NMR imaging during potassium induced cortical spreading depression in rats. *NMR Biomed.* 8, 59–64. doi: 10.1002/nbm.1940080203

Cain, S. M., Bohnet, B., LeDue, J., Yung, A. C., Garcia, E., Tyson, J. R., et al. (2017). In vivo imaging reveals that pregabalin inhibits cortical spreading depression and propagation to subcortical brain structures. *Proc. Natl. Acad. Sci. USA* 114, 2401–2406. doi: 10.1073/pnas.1614447114

Canals, S., Larrosa, B., Pintor, J., Mena, M. A., and Herreras, O. (2008). Metabolic challenge to glia activates an adenosine-mediated safety mechanism that promotes neuronal survival by delaying the onset of spreading depression waves. *J. Cereb. Blood Flow Metab.* 28, 1835–1844. doi: 10.1038/jcbfm.2008.71

Carlson, A. P., Shuttleworth, C. W., Major, S., Lemale, C. L., Dreier, J. P., and Hartings, J. A. (2019). Terminal spreading depolarizations causing electrocortical silencing prior to clinical brain death: case report. *J. Neurosurg.* 131, 1773–1779. doi: 10.3171/2018.7.JNS181478

Carter, R. E., Seidel, J. L., Lindquist, B. E., Sheline, C. T., and Shuttleworth, C. W. (2013). Intracellular Zn2+ accumulation enhances suppression of synaptic activity following spreading depolarization. *J. Neurochem.* 125, 673–684. doi: 10.1111/jnc.12237

Charles, A. C., and Baca, S. M. (2013). Cortical spreading depression and migraine. *Nat. Rev. Neurol.* 9, 637–644. doi: 10.1038/nrneurol.2013.192

Charriaut-Marlangue, C., Margaill, I., Represa, A., Popovici, T., Plotkine, M., and Ben-Ari, Y. (1996). Apoptosis and necrosis after reversible focal ischemia: an in situ DNA fragmentation analysis. *J. Cereb. Blood Flow Metab.* 16, 186–194. doi: 10.1097/00004647-199603000-00002

Chuquet, J., Hollender, L., and Nimchinsky, E. A. (2007). High-resolution in vivo imaging of the neurovascular unit during spreading depression. *J. Neurosci.* 27, 4036–4044. doi: 10.1523/jneurosci.0721-07.2007

Claes, L., Del-Favero, J., Ceulemans, B., Lagae, L., Van Broeckhoven, C., and De Jonghe, P. (2001). De novo mutations in the sodium-channel gene SCN1A cause severe myoclonic epilepsy of infancy. *Am. J. Hum. Genet.* 68, 1327–1332. doi: 10.1086/320609

Cornog, J. L., Gonatas, N. K., and Feierman, J. R. (1967). Effects of intracerebral injection of ouabain on the fine structure of rat cerebral cortex. *Am. J. Pathol.* 51, 573–590.

Crambert, G., Hasler, U., Beggah, A. T., Yu, C., Modyanov, N. N., Horisberger, J. D., et al. (2000). Transport and pharmacological properties of nine different human Na, K-ATPase isozymes. *J. Biol. Chem.* 275, 1976–1986. doi: 10.1074/jbc.275.3.1976

Czeh, G., Aitken, P. G., and Somjen, G. G. (1993). Membrane currents in CA1 pyramidal cells during spreading depression (SD) and SD-like hypoxic depolarization. *Brain Res.* 632, 195–208. doi: 10.1016/0006-8993(93)91154-k

De Fusco, M., Marconi, R., Silvestri, L., Atorino, L., Rampoldi, L., Morgante, L., et al. (2003). Haploinsufficiency of ATP1A2 encoding the Na+/K+ pump alpha2 subunit associated with familial hemiplegic migraine type 2. *Nat. Genet.* 33, 192–196. doi: 10.1038/ng1081

de la Torre, J. C. (1976). Evidence for central innervation of intracerebral blood vessels: local cerebral blood flow measurements and histofluorescence analysis by the sucrose-phosphate-glyoxylic acid (SPG) method. *Neuroscience* 1, 455–457. doi: 10.1016/0306-4522(76)90096-8

del Zoppo, G. J., Sharp, F. R., Heiss, W. D., and Albers, G. W. (2011). Heterogeneity in the penumbra. *J. Cereb. Blood Flow Metab.* 31, 1836–1851. doi: 10.1038/jcbfm.2011.93

Dichgans, M., Freilinger, T., Eckstein, G., Babini, E., Lorenz-Depiereux, B., Biskup, S., et al. (2005). Mutation in the neuronal voltage-gated sodium channel SCN1A in familial hemiplegic migraine. *Lancet* 366, 371–377. doi: 10.1016/S0140-6736(05)66786-4

Dietz, R. M., Weiss, J. H., and Shuttleworth, C. W. (2008). Zn2+ influx is critical for some forms of spreading depression in brain slices. *J. Neurosci.* 28, 8014–8024. doi: 10.1523/JNEUROSCI.0765-08.2008

Dietz, R. M., Weiss, J. H., and Shuttleworth, C. W. (2009). Contributions of Ca2+ and Zn2+ to spreading depression-like events and neuronal injury. *J. Neurochem.* 109(Suppl. 1), 145–152. doi: 10.1111/j.1471-4159.2009.05853.x

Dijkhuizen, R. M., Beekwilder, J. P., van der Worp, H. B., Berkelbach van der Sprenkel, J. W., Tulleken, K. A., and Nicolay, K. (1999). Correlation between tissue depolarizations and damage in focal ischemic rat brain. *Brain Res.* 840, 194–205. doi: 10.1016/s0006-8993(99)01769-2

Dillier, N., Laszlo, J., Muller, B., Koella, W. P., and Olpe, H. R. (1978). Activation of an inhibitory noradrenergic pathway projecting from the locus coeruleus to the cingulate cortex of the rat. *Brain Res.* 154, 61–68. doi: 10.1016/0006-8993(78)91051-x

Dirnagl, U., Lindauer, U., Them, A., Schreiber, S., Pfister, H. W., Koedel, U., et al. (1995). Global cerebral ischemia in the rat: online monitoring of oxygen free radical production using chemiluminescence in vivo. *J. Cereb. Blood Flow. Metab.* 15, 929–940. doi: 10.1038/jcbfm.1995.118

Dohmen, C., Sakowitz, O. W., Fabricius, M., Bosche, B., Reithmeier, T., Ernestus, R. I., et al. (2008). Spreading depolarizations occur in human ischemic stroke with high incidence. *Ann. Neurol.* 63, 720–728. doi: 10.1002/ana.21390

Dreier, J. P. (2011). The role of spreading depression, spreading depolarization and spreading ischemia in neurological disease. *Nat. Med.* 17, 439–447. doi: 10.1038/nm.2333

Dreier, J. P., Ebert, N., Priller, J., Megow, D., Lindauer, U., Klee, R., et al. (2000). Products of hemolysis in the subarachnoid space inducing spreading ischemia in the cortex and focal necrosis in rats: a model for delayed ischemic neurological deficits after subarachnoid hemorrhage? *J. Neurosurg.* 93, 658–666. doi: 10.3171/jns.2000.93.4.0658

Dreier, J. P., Fabricius, M., Ayata, C., Sakowitz, O. W., William Shuttleworth, C., Dohmen, C., et al. (2017). Recording, analysis, and interpretation of spreading depolarizations in neurointensive care: Review and recommendations of the COSBID research group. *J. Cereb. Blood Flow Metab.* 37, 1595–1625. doi: 10.1177/0271678x16654496

Dreier, J. P., and Heinemann, U. (1991). Regional and time dependent variations of low Mg2+ induced epileptiform activity in rat temporal cortex slices. *Exp. Brain Res.* 87, 581–596. doi: 10.1007/BF00227083

Dreier, J. P., Jurkat-Rott, K., Petzold, G. C., Tomkins, O., Klingebiel, R., Kopp, U. A., et al. (2005). Opening of the blood-brain barrier preceding cortical edema in a severe attack of FHM type II. *Neurology* 64, 2145–2147. doi: 10.1212/01.WNL.0000176298.63840.99

Dreier, J. P., Kleeberg, J., Alam, M., Major, S., Kohl-Bareis, M., Petzold, G. C., et al. (2007). Endothelin-1-induced spreading depression in rats is associated with a microarea of selective neuronal necrosis. *Exp. Biol. Med.* 232, 204–213.

Dreier, J. P., Kleeberg, J., Petzold, G., Priller, J., Windmuller, O., Orzechowski, H. D., et al. (2002a). Endothelin-1 potently induces Leao's cortical spreading depression in vivo in the rat: a model for an endothelial trigger of migrainous aura? *Brain* 125(Pt 1), 102–112. doi: 10.1093/brain/awf007

Dreier, J. P., Windmuller, O., Petzold, G., Lindauer, U., Einhaupl, K. M., and Dirnagl, U. (2002b). "Ischemia caused by inverse coupling between neuronal activation and cerebral blood flow in rats," in *Brain activation and CBF control*, eds M. Tomita, I. Kanno, and E. Hamel (Amsterdam: Elsevier), 487–492. doi: 10.1016/s0531-5131(02)00235-2

Dreier, J. P., Korner, K., Ebert, N., Gorner, A., Rubin, I., Back, T., et al. (1998). Nitric oxide scavenging by hemoglobin or nitric oxide synthase inhibition by N-nitro-L-arginine induces cortical spreading ischemia when K+ is increased in the subarachnoid space. *J. Cereb. Blood Flow Metab.* 18, 978–990. doi: 10.1097/00004647-199809000-00007

Dreier, J. P., Victorov, I. V., Petzold, G. C., Major, S., Windmuller, O., Fernandez-Klett, F., et al. (2013b). Electrochemical failure of the brain cortex is more deleterious when it is accompanied by low Perfusion. *Stroke* 44, 490–496. doi: 10.1161/STROKEAHA.112.660589

Dreier, J. P., Isele, T., Reiffurth, C., Offenhauser, N., Kirov, S. A., Dahlem, M. A., et al. (2013a). Is spreading depolarization characterized by an abrupt, massive release of gibbs free energy from the human brain cortex? *Neuroscientist* 19, 25–42. doi: 10.1177/1073858412453340

Dreier, J. P., Lemale, C. L., Kola, V., Friedman, A., and Schoknecht, K. (2018a). Spreading depolarization is not an epiphenomenon but the principal mechanism of the cytotoxic edema in various gray matter structures of the brain during stroke. *Neuropharmacology* 134(Pt B), 189–207. doi: 10.1016/j.neuropharm.2017.09.027

Dreier, J. P., Major, S., Foreman, B., Winkler, M. K. L., Kang, E. J., Milakara, D., et al. (2018b). Terminal spreading depolarization and electrical silence in death of human cerebral cortex. *Ann. Neurol.* 83, 295–310. doi: 10.1002/ana.25147

Dreier, J. P., Major, S., Lemale, C. L., Kola, V., Reiffurth, C., Schoknecht, K., et al. (2019). Correlates of Spreading Depolarization, Spreading Depression, and Negative Ultraslow Potential in Epidural Versus Subdural Electrocorticography. *Front. Neurosci.* 13:373. doi: 10.3389/fnins.2019.00373

Dreier, J. P., Major, S., Manning, A., Woitzik, J., Drenckhahn, C., Steinbrink, J., et al. (2009). Cortical spreading ischaemia is a novel process involved in ischaemic damage in patients with aneurysmal subarachnoid haemorrhage. *Brain* 132(Pt 7), 1866–1881. doi: 10.1093/brain/awp102

Dreier, J. P., Major, S., Pannek, H. W., Woitzik, J., Scheel, M., Wiesenthal, D., et al. (2012). Spreading convulsions, spreading depolarization and epileptogenesis in human cerebral cortex. *Brain* 135(Pt 1), 259–275. doi: 10.1093/brain/awr303

Dreier, J. P., Petzold, G., Tille, K., Lindauer, U., Arnold, G., Heinemann, U., et al. (2001). Ischaemia triggered by spreading neuronal activation is inhibited by vasodilators in rats. *J. Physiol.* 531(Pt 2), 515–526. doi: 10.1111/j.1469-7793.2001.0515i.x

Dreier, J. P., and Reiffurth, C. (2015). The Stroke-Migraine Depolarization Continuum. *Neuron* 86, 902–922. doi: 10.1016/j.neuron.2015.04.004

Dreier, J. P., and Reiffurth, C. (2017). Exploitation of the spreading depolarization-induced cytotoxic edema for high-resolution, 3D mapping of its heterogeneous propagation paths. *Proc. Natl. Acad. Sci. U S A* 114, 2112–2114. doi: 10.1073/pnas.1700760114

Dreier, J. P., Winkler, M. K. L., Major, S., Horst, V., Lublinsky, S., Kola, V., et al. (2022). Spreading depolarisations in ischaemia after subarachnoid haemorrhage, a diagnostic phase III study. *Brain*, in press.

Dreier, J. P., Woitzik, J., Fabricius, M., Bhatia, R., Major, S., Drenckhahn, C., et al. (2006). Delayed ischaemic neurological deficits after subarachnoid haemorrhage are associated with clusters of spreading depolarizations. *Brain* 129(Pt 12), 3224–3237. doi: 10.1093/brain/awl297

Drenckhahn, C., Winkler, M. K., Major, S., Scheel, M., Kang, E. J., Pinczolits, A., et al. (2012). Correlates of spreading depolarization in human scalp electroencephalography. *Brain* 135(Pt 3), 853–868. doi: 10.1093/brain/aws010

Ducros, A. (2012). Reversible cerebral vasoconstriction syndrome. *Lancet Neurol.* 11, 906–917. doi: 10.1016/S1474-4422(12)70135-7

Ducros, A., Denier, C., Joutel, A., Cecillon, M., Lescoat, C., Vahedi, K., et al. (2001). The clinical spectrum of familial hemiplegic migraine associated with mutations in a neuronal calcium channel. *N. Engl. J. Med.* 345, 17–24. doi: 10.1056/NEJM200107053450103

Dzhala, V., Desfreres, L., Melyan, Z., Ben-Ari, Y., and Khazipov, R. (1999). Epileptogenic action of caffeine during anoxia in the neonatal rat hippocampus. *Ann. Neurol.* 46, 95–102.

Enger, R., Tang, W., Vindedal, G. F., Jensen, V., Johannes Helm, P., Sprengel, R., et al. (2015). Dynamics of Ionic Shifts in Cortical Spreading Depression. *Cereb Cortex* 25, 4469–4476. doi: 10.1093/cercor/bhv054

Erdemli, G., Xu, Y. Z., and Krnjevic, K. (1998). Potassium conductance causing hyperpolarization of CA1 hippocampal neurons during hypoxia. *J. Neurophysiol.* 80, 2378–2390. doi: 10.1152/jn.1998.80.5.2378

Escayg, A., MacDonald, B. T., Meisler, M. H., Baulac, S., Huberfeld, G., An-Gourfinkel, I., et al. (2000). Mutations of SCN1A, encoding a neuronal sodium channel, in two families with GEFS+2. *Nat. Genet.* 24, 343–345. doi: 10.1038/74159

Etminan, M., Takkouche, B., Isorna, F. C., and Samii, A. (2005). Risk of ischaemic stroke in people with migraine: systematic review and meta-analysis of observational studies. *BMJ* 330:63. doi: 10.1136/bmj.38302.504063.8F

Fabricius, M., Fuhr, S., Bhatia, R., Boutelle, M., Hashemi, P., Strong, A. J., et al. (2006). Cortical spreading depression and peri-infarct depolarization in acutely injured human cerebral cortex. *Brain* 129(Pt 3), 778–790. doi: 10.1093/brain/awh716

Fabricius, M., Fuhr, S., Willumsen, L., Dreier, J. P., Bhatia, R., Boutelle, M. G., et al. (2008). Association of seizures with cortical spreading depression and peri-infarct depolarisations in the acutely injured human brain. *Clin. Neurophysiol.* 119, 1973–1984. doi: 10.1016/j.clinph.2008.05.025

Fabricius, M., Jensen, L. H., and Lauritzen, M. (1993). Microdialysis of interstitial amino acids during spreading depression and anoxic depolarization in rat neocortex. *Brain Res.* 612, 61–69. doi: 10.1016/0006-8993(93)91644-8

Fiehler, J., Knudsen, K., Kucinski, T., Kidwell, C. S., Alger, J. R., Thomalla, G., et al. (2004). Predictors of apparent diffusion coefficient normalization in stroke patients. *Stroke* 35, 514–519. doi: 10.1161/01.STR.0000114873.28023.C2

Fleidervish, I. A., Gebhardt, C., Astman, N., Gutnick, M. J., and Heinemann, U. (2001). Enhanced spontaneous transmitter release is the earliest consequence of neocortical hypoxia that can explain the disruption of normal circuit function. *J. Neurosci.* 21, 4600–4608. doi: 10.1523/JNEUROSCI.21-13-04600.2001

Foreman, B., Lee, H., Okonkwo, D. O., Strong, A. J., Pahl, C., Shutter, L. A., et al. (2022). The relationship between seizures and spreading depolarizations in patients with severe traumatic brain injury. *Neurocrit Care*, in press. doi: 10.1007/s12028-020-01107-x

Fowler, J. C. (1989). Adenosine antagonists delay hypoxia-induced depression of neuronal activity in hippocampal brain slice. *Brain Res.* 490, 378–384. doi: 10.1016/0006-8993(89)90258-8

Gautier, C., van Faassen, E., Mikula, I., Martasek, P., and Slama-Schwok, A. (2006). Endothelial nitric oxide synthase reduces nitrite anions to NO under anoxia. *Biochem. Biophys. Res. Commun.* 341, 816–821. doi: 10.1016/j.bbrc.s2006.01.031

Geisberger, S., Bartolomaeus, H., Neubert, P., Willebrand, R., Zasada, C., Bartolomaeus, T., et al. (2021). Salt Transiently Inhibits Mitochondrial

Energetics in Mononuclear Phagocytes. *Circulation* 144, 144–158. doi: 10.1161/CIRCULATIONAHA.120.052788

Gerkau, N. J., Rakers, C., Petzold, G. C., and Rose, C. R. (2017). Differential effects of energy deprivation on intracellular sodium homeostasis in neurons and astrocytes. *J. Neurosci. Res.* 95, 2275–2285. doi: 10.1002/jnr.23995

Gill, R., Andine, P., Hillered, L., Persson, L., and Hagberg, H. (1992). The effect of MK-801 on cortical spreading depression in the penumbral zone following focal ischaemia in the rat. *J. Cereb. Blood Flow Metab.* 12, 371–379. doi: 10.1038/jcbfm.1992.54

Ginsberg, M. D. (2008). Neuroprotection for ischemic stroke: past, present and future. *Neuropharmacology* 55, 363–389. doi: 10.1016/j.neuropharm.2007.12.007

Grisar, T., Franck, G., and Schoffeniels, E. (1980). Glial control of neuronal excitability in mammals: II. Enzymatic evidence : Two molecular forms of the (Na(+),K(+))-ATPase in brain. *Neurochem. Int.* 2C, 311–320. doi: 10.1016/0197-0186(80)90038-8

Gursoy-Ozdemir, Y., Qiu, J., Matsuoka, N., Bolay, H., Bermpohl, D., Jin, H., et al. (2004). Cortical spreading depression activates and upregulates MMP-9. *J. Clin. Invest.* 113, 1447–1455. doi: 10.1172/JCI21227

Gyngell, M. L., Busch, E., Schmitz, B., Kohno, K., Back, T., Hoehn-Berlage, M., et al. (1995). Evolution of acute focal cerebral ischaemia in rats observed by localized 1H MRS, diffusion-weighted MRI, and electrophysiological monitoring. *NMR Biomed.* 8, 206–214. doi: 10.1002/nbm.1940080505

Hablitz, J. J., and Heinemann, U. (1989). Alterations in the microenvironment during spreading depression associated with epileptiform activity in the immature neocortex. *Brain Res. Dev. Brain Res.* 46, 243–252. doi: 10.1016/0165-3806(89)90288-5

Hadjikhani, N., Sanchez Del Rio, M., Wu, O., Schwartz, D., Bakker, D., Fischl, B., et al. (2001). Mechanisms of migraine aura revealed by functional MRI in human visual cortex. *Proc. Natl. Acad. Sci. U S A* 98, 4687–4692. 071582498 doi: 10.1073/pnas.071582498

Hajek, I., Subbarao, K. V., and Hertz, L. (1996). Acute and chronic effects of potassium and noradrenaline on Na+, K+-ATPase activity in cultured mouse neurons and astrocytes. *Neurochem. Int.* 28, 335–342. doi: 10.1016/0197-0186(95)00081-x

Hansen, A. J., and Olsen, C. E. (1980). Brain extracellular space during spreading depression and ischemia. *Acta Physiol. Scand.* 108, 355–365. doi: 10.1111/j.1748-1716.1980.tb06544.x

Hansen, A. J., Quistorff, B., and Gjedde, A. (1980). Relationship between local changes in cortical blood flow and extracellular K+ during spreading depression. *Acta Physiol. Scand.* 109, 1–6. doi: 10.1111/j.1748-1716.1980.tb06557.x

Hansen, A. J., and Zeuthen, T. (1981). Extracellular ion concentrations during spreading depression and ischemia in the rat brain cortex. *Acta Physiol. Scand.* 113, 437–445. doi: 10.1111/j.1748-1716.1981.tb06920.x

Hartings, J. A. (2019). How slow can you go? *Nat. Mater.* 18, 194–196. doi: 10.1038/s41563-018-0272-5

Hartings, J. A., Andaluz, N., Bullock, M. R., Hinzman, J. M., Mathern, B., Pahl, C., et al. (2020). Prognostic Value of Spreading Depolarizations in Patients With Severe Traumatic Brain Injury. *JAMA Neurol.* 77, 489–499. doi: 10.1001/jamaneurol.2019.4476

Hartings, J. A., Watanabe, T., Bullock, M. R., Okonkwo, D. O., Fabricius, M., Woitzik, J., et al. (2011b). Spreading depolarizations have prolonged direct current shifts and are associated with poor outcome in brain trauma. *Brain* 134, 1529–1540. doi: 10.1093/brain/awr048

Hartings, J. A., Bullock, M. R., Okonkwo, D. O., Murray, L. S., Murray, G. D., Fabricius, M., et al. (2011a). Spreading depolarisations and outcome after traumatic brain injury: a prospective observational study. *Lancet Neurol.* 10, 1058–1064. doi: 10.1016/S1474-4422(11)70243-5

Hartings, J. A., York, J., Carroll, C. P., Hinzman, J. M., Mahoney, E., Krueger, B., et al. (2017b). Subarachnoid blood acutely induces spreading depolarizations and early cortical infarction. *Brain* 140, 2673–2690. doi: 10.1093/brain/awx214

Hartings, J. A., Shuttleworth, C. W., Kirov, S. A., Ayata, C., Hinzman, J. M., Foreman, B., et al. (2017a). The continuum of spreading depolarizations in acute cortical lesion development: Examining Leao's legacy. *J. Cereb. Blood Flow Metab.* 37, 1571–1594. doi: 10.1177/0271678x16654495

Heinemann, U., and Lux, H. D. (1977). Ceiling of stimulus induced rises in extracellular potassium concentration in the cerebral cortex of cat. *Brain Res.* 120, 231–249. doi: 10.1016/0006-8993(77)90903-9

Heiss, W. D., and Rosner, G. (1983). Functional recovery of cortical neurons as related to degree and duration of ischemia. *Ann. Neurol.* 14, 294–301. doi: 10.1002/ana.410140307

Helbok, R., Schiefecker, A. J., Friberg, C., Beer, R., Kofler, M., Rhomberg, P., et al. (2017). Spreading depolarizations in patients with spontaneous intracerebral hemorrhage: Association with perihematomal edema progression. *J. Cereb. Blood Flow Metab.* 37, 1871–1882. doi: 10.1177/0271678X16651269

Hellas, J. A., and Andrew, R. D. (2022). Neuronal swelling: a non-osmotic consequence of spreading depolarization. *Neurocrit. Care* 35(Suppl. 2), 112–134. doi: 10.1007/s12028-021-01326-w

Hernansanz-Agustin, P., Choya-Foces, C., Carregal-Romero, S., Ramos, E., Oliva, T., Villa-Pina, T., et al. (2020). Na(+) controls hypoxic signalling by the mitochondrial respiratory chain. *Nature* 586, 287–291. doi: 10.1038/s41586-020-2551-y

Herreras, O., and Makarova, J. (2020). Mechanisms of the negative potential associated with Leao's spreading depolarization: A history of brain electrogenesis. *J. Cereb. Blood Flow Metab.* 2020:271678X20935998. doi: 10.1177/0271678X20935998

Herreras, O., and Somjen, G. G. (1993). Analysis of potential shifts associated with recurrent spreading depression and prolonged unstable spreading depression induced by microdialysis of elevated K+ in hippocampus of anesthetized rats. *Brain Res.* 610, 283–294. doi: 10.1016/0006-8993(93)91412-l

Hinzman, J. M., Andaluz, N., Shutter, L. A., Okonkwo, D. O., Pahl, C., Strong, A. J., et al. (2014). Inverse neurovascular coupling to cortical spreading depolarizations in severe brain trauma. *Brain* 137(Pt 11), 2960–2972. doi: 10.1093/brain/awu241

Hinzman, J. M., DiNapoli, V. A., Mahoney, E. J., Gerhardt, G. A., and Hartings, J. A. (2015). Spreading depolarizations mediate excitotoxicity in the development of acute cortical lesions. *Exp. Neurol.* 267, 243–253. doi: 10.1016/j.expneurol.2015.03.014

Hochachka, P. W., Buck, L. T., Doll, C. J., and Land, S. C. (1996). Unifying theory of hypoxia tolerance: molecular/metabolic defense and rescue mechanisms for surviving oxygen lack. *Proc. Natl. Acad. Sci. U S A* 93, 9493–9498. doi: 10.1073/pnas.93.18.9493

Hoehn-Berlage, M., Norris, D. G., Kohno, K., Mies, G., Leibfritz, D., and Hossmann, K. A. (1995). Evolution of regional changes in apparent diffusion coefficient during focal ischemia of rat brain: the relationship of quantitative diffusion NMR imaging to reduction in cerebral blood flow and metabolic disturbances. *J. Cereb. Blood Flow Metab.* 15, 1002–1011. doi: 10.1038/jcbfm.1995.126

Horisberger, J. D., and Kharoubi-Hess, S. (2002). Functional differences between alpha subunit isoforms of the rat Na,K-ATPase expressed in Xenopus oocytes. *J. Physiol.* 539(Pt 3), 669–680. doi: 10.1113/jphysiol.2001.013201

Hossmann, K. A. (1996). Periinfarct depolarizations. *Cerebrovasc. Brain Metab. Rev.* 8, 195–208.

Hougaard, A., Younis, S., Iljazi, A., Haanes, K. A., Lindberg, U., Vestergaard, M. B., et al. (2020a). Cerebrovascular effects of endothelin-1 investigated using high-resolution magnetic resonance imaging in healthy volunteers. *J. Cereb. Blood Flow Metab.* 40, 1685–1694. doi: 10.1177/0271678X19874295

Hougaard, A., Younis, S., Iljazi, A., Sugimoto, K., Ayata, C., and Ashina, M. (2020b). Intravenous Endothelin-1 Infusion Does Not Induce Aura or Headache in Migraine Patients With Aura. *Headache* 60, 724–734. doi: 10.1111/head.13753

Hu, X., Zhou, Y., Zhao, H., and Peng, C. (2017). Migraine and the risk of stroke: an updated meta-analysis of prospective cohort studies. *Neurol. Sci.* 38, 33–40. doi: 10.1007/s10072-016-2746-z

Hubel, N., and Ullah, G. (2016). Anions Govern Cell Volume: A Case Study of Relative Astrocytic and Neuronal Swelling in Spreading Depolarization. *PLoS One* 11:e0147060. doi: 10.1371/journal.pone.0147060

James, M. F., Smith, M. I., Bockhorst, K. H., Hall, L. D., Houston, G. C., Papadakis, N. G., et al. (1999). Cortical spreading depression in the gyrencephalic feline brain studied by magnetic resonance imaging. *J. Physiol.* 519(Pt 2), 415–425. doi: 10.1111/j.1469-7793.1999.0415m.x

Jansen, N. A., Dehghani, A., Linssen, M. M. L., Breukel, C., Tolner, E. A., and van den Maagdenberg, A. (2020). First FHM3 mouse model shows spontaneous

cortical spreading depolarizations. *Ann. Clin. Transl. Neurol.* 7, 132–138. doi: 10.1002/acn3.50971

Jarvis, C. R., Anderson, T. R., and Andrew, R. D. (2001). Anoxic depolarization mediates acute damage independent of glutamate in neocortical brain slices. *Cereb Cortex* 11, 249–259. doi: 10.1093/cercor/11.3.249

Jiang, H. B., Yoneyama, H., Furukawa, A., Hamamoto, T., Takahara, J., and Ichikawa, Y. (2001). Effect of isosorbide dinitrate on nitric oxide synthase under hypoxia. *Pharmacology* 62, 10–16. doi: 10.1159/000056066

Jing, J., Aitken, P. G., and Somjen, G. G. (1994). Interstitial volume changes during spreading depression (SD) and SD-like hypoxic depolarization in hippocampal tissue slices. *J. Neurophysiol.* 71, 2548–2551. doi: 10.1152/jn.1994.71.6.2548

Jurkat-Rott, K., Freilinger, T., Dreier, J. P., Herzog, J., Gobel, H., Petzold, G. C., et al. (2004). Variability of familial hemiplegic migraine with novel A1A2 Na+/K+-ATPase variants. *Neurology* 62, 1857–1861. doi: 10.1212/01.wnl.0000127310.11526.fd

Kager, H., Wadman, W. J., and Somjen, G. G. (2002). Conditions for the triggering of spreading depression studied with computer simulations. *J. Neurophysiol.* 88, 2700–2712. doi: 10.1152/jn.00237.2002

Kann, O., Papageorgiou, I. E., and Draguhn, A. (2014). Highly energized inhibitory interneurons are a central element for information processing in cortical networks. *J. Cereb. Blood Flow Metab.* 34, 1270–1282. doi: 10.1038/jcbfm.2014.104

Katchman, A. N., and Hershkowitz, N. (1993b). Early anoxia-induced vesicular glutamate release results from mobilization of calcium from intracellular stores. *J. Neurophysiol.* 70, 1–7. doi: 10.1152/jn.1993.70.1.1

Katchman, A. N., and Hershkowitz, N. (1993a). Adenosine antagonists prevent hypoxia-induced depression of excitatory but not inhibitory synaptic currents. *Neurosci. Lett.* 159, 123–126. doi: 10.1016/0304-3940(93)90814-2

Kaufmann, D., Theriot, J. J., Zyuzin, J., Service, C. A., Chang, J. C., Tang, Y. T., et al. (2017). Heterogeneous incidence and propagation of spreading depolarizations. *J. Cereb. Blood Flow Metab.* 37, 1748–1762. doi: 10.1177/0271678X16659496

Keelan, J., Vergun, O., and Duchen, M. R. (1999). Excitotoxic mitochondrial depolarisation requires both calcium and nitric oxide in rat hippocampal neurons. *J. Physiol.* 520(Pt 3), 797–813. doi: 10.1111/j.1469-7793.1999.00797.x

Khazipov, R., Bregestovski, P., and Ben-Ari, Y. (1993). Hippocampal inhibitory interneurons are functionally disconnected from excitatory inputs by anoxia. *J. Neurophysiol.* 70, 2251–2259. doi: 10.1152/jn.1993.70.6.2251

Khazipov, R., Congar, P., and Ben-Ari, Y. (1995). Hippocampal CA1 lacunosum-moleculare interneurons: comparison of effects of anoxia on excitatory and inhibitory postsynaptic currents. *J. Neurophysiol.* 74, 2138–2149. doi: 10.1152/jn.1995.74.5.2138

Kimelberg, H. K. (2005). Astrocytic swelling in cerebral ischemia as a possible cause of injury and target for therapy. *Glia* 50, 389–397. doi: 10.1002/glia.20174

Kirov, S. A., Fomitcheva, I. V., and Sword, J. (2020). Rapid Neuronal Ultrastructure Disruption and Recovery during Spreading Depolarization-Induced Cytotoxic Edema. *Cereb Cortex* 30, 5517–5531. doi: 10.1093/cercor/bhaa134

Kleeberg, J., Petzold, G. C., Major, S., Dirnagl, U., and Dreier, J. P. (2004). ET-1 induces cortical spreading depression via activation of the ETA receptor/phospholipase C pathway in vivo. *Am. J. Physiol. Heart Circ. Physiol.* 286, H1339–H1346. doi: 10.1152/ajpheart.00227.2003

Klingebiel, R., Friedman, A., Shelef, I., and Dreier, J. P. (2008). Clearance of a status aurae migraenalis in response to thrombendarterectomy in a patient with high grade internal carotid artery stenosis. *J. Neurol. Neurosurg. Psychiatry* 79, 89–90. doi: 10.1136/jnnp.2007.119230

Kobari, M., Fukuuchi, Y., Tomita, M., Tanahashi, N., Konno, S., and Takeda, H. (1994a). Cerebral vasodilatory effect of high-dose, intravascular endothelin-1: inhibition by NG-monomethyl-L-arginine. *J. Auton. Nerv. Syst.* 49(Suppl.), S111–S115. doi: 10.1016/0165-1838(94)90097-3

Kobari, M., Fukuuchi, Y., Tomita, M., Tanahashi, N., Konno, S., and Takeda, H. (1994b). Constriction/dilatation of the cerebral microvessels by intravascular endothelin-1 in cats. *J. Cereb. Blood Flow Metab.* 14, 64–69. doi: 10.1038/jcbfm.1994.10

Koide, M., Bonev, A. D., Nelson, M. T., and Wellman, G. C. (2012). Inversion of neurovascular coupling by subarachnoid blood depends on large-conductance Ca2+-activated K+ (BK) channels. *Proc. Natl. Acad. Sci. U S A* 109, E1387–E1395. doi: 10.1073/pnas.1121359109

Koroleva, V. I., and Bures, J. (1983). Cortical penicillin focus as a generator of repetitive spike-triggered waves of spreading depression in rats. *Exp. Brain Res.* 51, 291–297. doi: 10.1007/BF00237205

Koroleva, V. I., and Bures, J. (1996). The use of spreading depression waves for acute and long-term monitoring of the penumbra zone of focal ischemic damage in rats. *Proc. Natl. Acad. Sci. U S A* 93, 3710–3714. doi: 10.1073/pnas.93.8.3710

Koroleva, V. I., Vinogradova, L. V., and Bures, J. (1993). Reduced incidence of cortical spreading depression in the course of pentylenetetrazol kindling in rats. *Brain Res.* 608, 107–114. doi: 10.1016/0006-8993(93)90780-q

Kovacs, R., Kardos, J., Heinemann, U., and Kann, O. (2005). Mitochondrial calcium ion and membrane potential transients follow the pattern of epileptiform discharges in hippocampal slice cultures. *J. Neurosci.* 25, 4260–4269. doi: 10.1523/JNEUROSCI.4000-04.2005

Kowluru, R., Bitensky, M. W., Kowluru, A., Dembo, M., Keaton, P. A., and Buican, T. (1989). Reversible sodium pump defect and swelling in the diabetic rat erythrocyte: effects on filterability and implications for microangiopathy. *Proc. Natl. Acad. Sci. U S A* 86, 3327–3331. doi: 10.1073/pnas.86.9.3327

Kraig, R. P., and Nicholson, C. (1978). Extracellular ionic variations during spreading depression. *Neuroscience* 3, 1045–1059. doi: 10.1016/0306-4522(78)90122-7

Kubota, C., Torii, S., Hou, N., Saito, N., Yoshimoto, Y., Imai, H., et al. (2010). Constitutive reactive oxygen species generation from autophagosome/lysosome in neuronal oxidative toxicity. *J. Biol. Chem.* 285, 667–674. doi: 10.1074/jbc.M109.053058

Kunkler, P. E., Hulse, R. E., and Kraig, R. P. (2004). Multiplexed cytokine protein expression profiles from spreading depression in hippocampal organotypic cultures. *J. Cereb. Blood Flow Metab.* 24, 829–839. doi: 10.1097/01.WCB.0000126566.34753.30

Kunkler, P. E., and Kraig, R. P. (1998). Calcium waves precede electrophysiological changes of spreading depression in hippocampal organ cultures. *J. Neurosci.* 18, 3416–3425. doi: 10.1523/JNEUROSCI.18-09-03416.1998

Largo, C., Cuevas, P., Somjen, G. G., Martin, del Rio, R., and Herreras, O. (1996b). The effect of depressing glial function in rat brain in situ on ion homeostasis, synaptic transmission, and neuron survival. *J. Neurosci.* 16, 1219–1229. doi: 10.1523/JNEUROSCI.16-03-01219.1996

Largo, C., Cuevas, P., and Herreras, O. (1996a). Is glia disfunction the initial cause of neuronal death in ischemic penumbra? *Neurol. Res.* 18, 445–448. doi: 10.1080/01616412.1996.11740449

Larsen, B. R., Assentoft, M., Cotrina, M. L., Hua, S. Z., Nedergaard, M., Kaila, K., et al. (2014). Contributions of the Na(+)/K(+)-ATPase, NKCC1, and Kir4.1 to hippocampal K(+) clearance and volume responses. *Glia* 62, 608–622. doi: 10.1002/glia.22629

Lassen, N. A., and Friberg, L. (1991). "Cerebral blood flow measured by xenon 133 using the intraarterial injection method or inhalation combined with SPECT in migraine research," in *Migraine and other headaches. The vascular mechanisms*, ed. J. Olesen (New York, NY: Raven Press), 5–13.

Lauritzen, M. (1994). Pathophysiology of the migraine aura. The spreading depression theory. *Brain* 117(Pt 1), 199–210.

Lauritzen, M., Skyhoj Olsen, T., Lassen, N. A., and Paulson, O. B. (1983). Changes in regional cerebral blood flow during the course of classic migraine attacks. *Ann. Neurol.* 13, 633–641. doi: 10.1002/ana.410130609

Leão, A. A. P. (1944a). Pial circulation and spreading depression of activity in the cerebral cortex. *J. Neurophysiol.* 7, 391–396.

Leão, A. A. P. (1944b). Spreading depression of activity in the cerebral cortex. *J. Neurophysiol.* 7, 359–390.

Leão, A. A. P. (1947). Further observations on the spreading depression of activity in the cerebral cortex. *J. Neurophysiol.* 10, 409–414. doi: 10.1152/jn.1947.10.6.409

Leão, A. A. P., and Morison, R. S. (1945). Propagation of spreading cortical depression. *J. Neurophysiol.* 8, 33–45.

Lees, G. J., and Leong, W. (1996). Interactions between excitotoxins and the Na+/K+-ATPase inhibitor ouabain in causing neuronal lesions in the rat hippocampus. *Brain Res.* 714, 145–155. doi: 10.1016/0006-8993(95)01518-3

Lehmenkuhler, A. (1990). [Spreading depression–cortical reactions: disorders of the extracellular microenvironment]. *EEG EMG Z Elektroenzephalogr. Elektromyogr. Verwandte Geb.* 21, 1–6. doi: 10.1007/978-1-4614-7320-6_507-5

Leo, L., Gherardini, L., Barone, V., De Fusco, M., Pietrobon, D., Pizzorusso, T., et al. (2011). Increased susceptibility to cortical spreading depression in the mouse model of familial hemiplegic migraine type 2. *PLoS Genet.* 7:e1002129. doi: 10.1371/journal.pgen.1002129

Li, Z., Song, Y., Xiao, G., Gao, F., Xu, S., Wang, M., et al. (2018). Bio-electrochemical microelectrode arrays for glutamate and electrophysiology detection in hippocampus of temporal lobe epileptic rats. *Analytical. Biochem.* 550, 123–131. doi: 10.1016/j.ab.2018.04.023

Liman, T. G., Bachelier-Walenta, K., Neeb, L., Rosinski, J., Reuter, U., Bohm, M., et al. (2015). Circulating endothelial microparticles in female migraineurs with aura. *Cephalalgia* 35, 88–94. doi: 10.1177/0333102414529671

Lindquist, B. E., and Shuttleworth, C. W. (2012). Adenosine receptor activation is responsible for prolonged depression of synaptic transmission after spreading depolarization in brain slices. *Neuroscience* 223, 365–376. doi: 10.1016/j.neuroscience.2012.07.053

Lu, B., Lou, S. S., Xu, R. S., Kong, D. L., Wu, R. J., Zhang, J., et al. (2021). Cerebellar spreading depolarization mediates paroxysmal movement disorder. *Cell Rep.* 36:109743. doi: 10.1016/j.celrep.2021.109743

Luckl, J., Lemale, C. L., Kola, V., Horst, V., Khojasteh, U., Oliveira-Ferreira, A. I., et al. (2018). The negative ultraslow potential, electrophysiological correlate of infarction in the human cortex. *Brain* 141, 1734–1752. doi: 10.1093/brain/awy102

Lux, H. D., Heinemann, U., and Dietzel, I. (1986). Ionic changes and alterations in the size of the extracellular space during epileptic activity. *Adv. Neurol.* 44, 619–639.

Mahmoud, A. N., Mentias, A., Elgendy, A. Y., Qazi, A., Barakat, A. F., Saad, M., et al. (2018). Migraine and the risk of cardiovascular and cerebrovascular events: a meta-analysis of 16 cohort studies including 1 152 407 subjects. *BMJ Open* 8:e020498. doi: 10.1136/bmjopen-2017-020498

Major, S., Gajovic-Eichelmann, N., Woitzik, J., and Dreier, J. P. (2021). Oxygen-Induced and pH-Induced Direct Current Artifacts on Invasive Platinum/Iridium Electrodes for Electrocorticography. *Neurocrit. Care* 2021:2. doi: 10.1007/s12028-021-01358-2

Major, S., Huo, S., Lemale, C. L., Siebert, E., Milakara, D., Woitzik, J., et al. (2020). Direct electrophysiological evidence that spreading depolarization-induced spreading depression is the pathophysiological correlate of the migraine aura and a review of the spreading depolarization continuum of acute neuronal mass injury. *Geroscience* 42, 57–80. doi: 10.1007/s11357-019-00142-7

Major, S., Petzold, G. C., Reiffurth, C., Windmuller, O., Foddis, M., Lindauer, U., et al. (2017). A role of the sodium pump in spreading ischemia in rats. *J. Cereb. Blood Flow Metab.* 37, 1687–1705. doi: 10.1177/0271678x16639059

Makarova, J., Ibarz, J. M., Canals, S., and Herreras, O. (2007). A steady-state model of spreading depression predicts the importance of an unknown conductance in specific dendritic domains. *Biophys. J.* 92, 4216–4232. doi: 10.1529/biophysj.106.090332

Marino, S., Marani, L., Nazzaro, C., Beani, L., and Siniscalchi, A. (2007). Mechanisms of sodium azide-induced changes in intracellular calcium concentration in rat primary cortical neurons. *Neurotoxicology* 28, 622–629. doi: 10.1016/j.neuro.2007.01.005

Maslarova, A., Alam, M., Reiffurth, C., Lapilover, E., Gorji, A., and Dreier, J. P. (2011). Chronically epileptic human and rat neocortex display a similar resistance against spreading depolarization in vitro. *Stroke* 42, 2917–2922. doi: 10.1161/strokeaha.111.621581

Masvidal-Codina, E., Illa, X., Dasilvas, M., Calia, A. B., Dragojevic, T., Vidal-Rosas, E. E., et al. (2018). High-resolution mapping of infraslow cortical brain activity enabled by graphene microtransistors. *Nat. Mater.* 2018:4. doi: 10.1038/s41563-018-0249-4

Mayevsky, A., and Chance, B. (1975). Metabolic responses of the awake cerebral cortex to anoxia hypoxia spreading depression and epileptiform activity. *Brain Res.* 98, 149–165. doi: 10.1016/0006-8993(75)90515-6

Mazel, T., Richter, F., Vargova, L., and Sykova, E. (2002). Changes in extracellular space volume and geometry induced by cortical spreading depression in immature and adult rats. *Physiol. Res.* 51(Suppl. 1), S85–S93.

Mei, Y. Y., Lee, M. H., Cheng, T. C., Hsiao, I. H., Wu, D. C., and Zhou, N. (2020). NMDA receptors sustain but do not initiate neuronal depolarization in spreading depolarization. *Neurobiol. Dis.* 145:105071. doi: 10.1016/j.nbd.2020.105071

Memezawa, H., Smith, M. L., and Siesjo, B. K. (1992). Penumbral tissues salvaged by reperfusion following middle cerebral artery occlusion in rats. *Stroke* 23, 552–559. doi: 10.1161/01.str.23.4.552

Menyhart, A., Frank, R., Farkas, A. E., Sule, Z., Varga, V. E., Nyul-Toth, A., et al. (2021). Malignant astrocyte swelling and impaired glutamate clearance drive the expansion of injurious spreading depolarization foci. *J. Cereb. Blood Flow Metab.* 2021:271678X211040056. doi: 10.1177/0271678X211040056

Mestre, H., Du, T., Sweeney, A. M., Liu, G., Samson, A. J., Peng, W., et al. (2020). Cerebrospinal fluid influx drives acute ischemic tissue swelling. *Science* 367:6483. doi: 10.1126/science.aax7171

Mies, G., Iijima, T., and Hossmann, K. A. (1993). Correlation between peri-infarct DC shifts and ischaemic neuronal damage in rat. *Neuroreport* 4, 709–711. doi: 10.1097/00001756-199306000-00027

Mies, G., and Paschen, W. (1984). Regional changes of blood flow, glucose, and ATP content determined on brain sections during a single passage of spreading depression in rat brain cortex. *Exp. Neurol.* 84, 249–258. doi: 10.1016/0014-4886(84)90222-x

Milakara, D., Grozea, C., Dahlem, M., Major, S., Winkler, M. K. L., Luckl, J., et al. (2017). Simulation of spreading depolarization trajectories in cerebral cortex: Correlation of velocity and susceptibility in patients with aneurysmal subarachnoid hemorrhage. *Neuroimage Clin.* 16, 524–538. doi: 10.1016/j.nicl.2017.09.005

Mishra, O. P., and Delivoria-Papadopoulos, M. (1999). Cellular mechanisms of hypoxic injury in the developing brain. *Brain Res. Bull.* 48, 233–238. doi: 10.1016/s0361-9230(98)00170-1

Mody, I., Lambert, J. D., and Heinemann, U. (1987). Low extracellular magnesium induces epileptiform activity and spreading depression in rat hippocampal slices. *J. Neurophysiol.* 57, 869–888. doi: 10.1152/jn.1987.57.3.869

Mohammad, L. M., Abbas, M., Shuttleworth, C. W., Ahmadian, R., Bhat, A., Hill, D. A., et al. (2020). Spreading depolarization may represent a novel mechanism for delayed fluctuating neurological deficit after chronic subdural hematoma evacuation. *J. Neurosurg.* 2020, 1–9. doi: 10.3171/2020.1.JNS192914

Molchanova, S., Koobi, P., Oja, S. S., and Saransaari, P. (2004). Interstitial concentrations of amino acids in the rat striatum during global forebrain ischemia and potassium-evoked spreading depression. *Neurochem. Res.* 29, 1519–1527. doi: 10.1023/b:nere.0000029564.98905.5c

Muller, M., and Somjen, G. G. (2000). Na(+) and K(+) concentrations, extra- and intracellular voltages, and the effect of TTX in hypoxic rat hippocampal slices. *J. Neurophysiol.* 83, 735–745. doi: 10.1152/jn.2000.83.2.735

Murphy, T. H., Li, P., Betts, K., and Liu, R. (2008). Two-photon imaging of stroke onset in vivo reveals that NMDA-receptor independent ischemic depolarization is the major cause of rapid reversible damage to dendrites and spines. *J. Neurosci.* 28, 1756–1772. doi: 10.1523/JNEUROSCI.5128-07.2008

Mutch, W. A., and Hansen, A. J. (1984). Extracellular pH changes during spreading depression and cerebral ischemia: mechanisms of brain pH regulation. *J. Cereb. Blood Flow Metab.* 4, 17–27. doi: 10.1038/jcbfm.1984.3

Nallet, H., MacKenzie, E. T., and Roussel, S. (1999). The nature of penumbral depolarizations following focal cerebral ischemia in the rat. *Brain Res.* 842, 148–158. doi: 10.1016/s0006-8993(99)01859-4

Nedergaard, M., and Hansen, A. J. (1988). Spreading depression is not associated with neuronal injury in the normal brain. *Brain Res.* 449, 395–398. doi: 10.1016/0006-8993(88)91062-1

Nedergaard, M., and Hansen, A. J. (1993). Characterization of cortical depolarizations evoked in focal cerebral ischemia. *J. Cereb. Blood Flow Metab.* 13, 568–574. doi: 10.1038/jcbfm.1993.74

Nozari, A., Dilekoz, E., Sukhotinsky, I., Stein, T., Eikermann-Haerter, K., Liu, C., et al. (2010). Microemboli may link spreading depression, migraine aura, and patent foramen ovale. *Ann. Neurol.* 67, 221–229. doi: 10.1002/ana.21871

O'Brien, W. J., Lingrel, J. B., and Wallick, E. T. (1994). Ouabain binding kinetics of the rat alpha two and alpha three isoforms of the sodium-potassium adenosine triphosphate. *Arch. Biochem. Biophys.* 310, 32–39. doi: 10.1006/abbi.1994.1136

Oie, L. R., Kurth, T., Gulati, S., and Dodick, D. W. (2020). Migraine and risk of stroke. *J. Neurol. Neurosurg. Psychiatry* 91, 593–604. doi: 10.1136/jnnp-2018-318254

Olesen, J., Friberg, L., Olsen, T. S., Andersen, A. R., Lassen, N. A., Hansen, P. E., et al. (1993). Ischaemia-induced (symptomatic) migraine attacks may be more frequent than migraine-induced ischaemic insults. *Brain* 116(Pt 1), 187–202. doi: 10.1093/brain/116.1.187

Olesen, J., Larsen, B., and Lauritzen, M. (1981). Focal hyperemia followed by spreading oligemia and impaired activation of rCBF in classic migraine. *Ann. Neurol.* 9, 344–352. doi: 10.1002/ana.410090406

Oliveira-Ferreira, A. I., Major, S., Przesdzing, I., Kang, E. J., and Dreier, J. P. (2020). Spreading depolarizations in the rat endothelin-1 model of focal cerebellar ischemia. *J. Cereb. Blood Flow Metab.* 40, 1274–1289. doi: 10.1177/0271678X19861604

Oliveira-Ferreira, A. I., Milakara, D., Alam, M., Jorks, D., Major, S., Hartings, J. A., et al. (2010). Experimental and preliminary clinical evidence of an ischemic zone with prolonged negative DC shifts surrounded by a normally perfused tissue belt with persistent electrocorticographic depression. *J. Cereb. Blood Flow Metab.* 30, 1504–1519. doi: 10.1038/jcbfm.2010.40

Paolucci, M., Altamura, C., and Vernieri, F. (2021). The Role of Endothelial Dysfunction in the Pathophysiology and Cerebrovascular Effects of Migraine: A Narrative Review. *J. Clin. Neurol.* 17, 164–175. doi: 10.3988/jcn.2021.17.2.164

Parker, P. D., Suryavanshi, P., Melone, M., Sawant-Pokam, P. A., Reinhart, K. M., Kaufmann, D., et al. (2021). Non-canonical glutamate signaling in a genetic model of migraine with aura. *Neuron*. 61:e618. doi: 10.1016/j.neuron.2020.11.018

Perez-Pinzon, M. A., Tao, L., and Nicholson, C. (1995). Extracellular potassium, volume fraction, and tortuosity in rat hippocampal CA1, CA3, and cortical slices during ischemia. *J. Neurophysiol.* 74, 565–573. doi: 10.1152/jn.1995.74.2.565

Peters, O., Back, T., Lindauer, U., Busch, C., Megow, D., Dreier, J., et al. (1998). Increased formation of reactive oxygen species after permanent and reversible middle cerebral artery occlusion in the rat. *J. Cereb. Blood Flow Metab.* 18, 196–205. doi: 10.1097/00004647-199802000-00011

Peters, O., Schipke, C. G., Hashimoto, Y., and Kettenmann, H. (2003). Different mechanisms promote astrocyte Ca2+ waves and spreading depression in the mouse neocortex. *J. Neurosci.* 23, 9888–9896. doi: 10.1523/JNEUROSCI.23-30-09888.2003

Pietrobon, D., and Moskowitz, M. A. (2014). Chaos and commotion in the wake of cortical spreading depression and spreading depolarizations. *Nat. Rev. Neurosci.* 15, 379–393. doi: 10.1038/nrn3770

Pignataro, G., Simon, R. P., and Boison, D. (2007). Transgenic overexpression of adenosine kinase aggravates cell death in ischemia. *J. Cereb. Blood Flow Metab.* 27, 1–5. doi: 10.1038/sj.jcbfm.9600334

Pisani, A., Bonsi, P., Martella, G., De Persis, C., Costa, C., Pisani, F., et al. (2004). Intracellular calcium increase in epileptiform activity: modulation by levetiracetam and lamotrigine. *Epilepsia* 45, 719–728. doi: 10.1111/j.0013-9580.2004.02204.x

Planck, M. (1968). *Scientific autobiography, and other papers*. Westport: Greenwood Press.

Pomper, J. K., Haack, S., Petzold, G. C., Buchheim, K., Gabriel, S., Hoffmann, U., et al. (2006). Repetitive spreading depression-like events result in cell damage in juvenile hippocampal slice cultures maintained in normoxia. *J. Neurophysiol.* 95, 355–368. doi: 10.1152/jn.00186.2005

Prabhakaran, S., Ruff, I., and Bernstein, R. A. (2015). Acute stroke intervention: a systematic review. *JAMA* 313, 1451–1462. doi: 10.1001/jama.2015.3058

Pulsinelli, W. A. (1985). Selective neuronal vulnerability: morphological and molecular characteristics. *Prog. Brain Res.* 63, 29–37. doi: 10.1016/S0079-6123(08)61973-1

Randall, R. D., and Thayer, S. A. (1992). Glutamate-induced calcium transient triggers delayed calcium overload and neurotoxicity in rat hippocampal neurons. *J. Neurosci.* 12, 1882–1895. doi: 10.1523/JNEUROSCI.12-05-01882.1992

Reiffurth, C., Alam, M., Zahedi-Khorasani, M., Major, S., and Dreier, J. P. (2020). Na(+)/K(+)-ATPase alpha isoform deficiency results in distinct spreading depolarization phenotypes. *J. Cereb. Blood Flow Metab.* 40, 622–638. doi: 10.1177/0271678X19833757

Reinhart, K. M., and Shuttleworth, C. W. (2018). Ketamine reduces deleterious consequences of spreading depolarizations. *Exp. Neurol.* 305, 121–128. doi: 10.1016/j.expneurol.2018.04.007

Revah, O., Lasser-Katz, E., Fleidervish, I. A., and Gutnick, M. J. (2016). The earliest neuronal responses to hypoxia in the neocortical circuit are glutamate-dependent. *Neurobiol. Dis.* 95, 158–167. doi: 10.1016/j.nbd.2016.07.019

Revankar, G. S., Winkler, M. K. L., Major, S., Schoknecht, K., Heinemann, U., Woitzik, J., et al. (2017). "Spreading depolarizations and seizures in clinical subdural electrocorticographic recordings," in *Seizures in Critical Care. A Guide to Diagnosis and Therapeutics*, eds P. N. Varelas and J. Claassen (New York, NY: Springer), 77–90.

Risher, W. C., Ard, D., Yuan, J., and Kirov, S. A. (2010). Recurrent spontaneous spreading depolarizations facilitate acute dendritic injury in the ischemic penumbra. *J. Neurosci.* 30, 9859–9868. doi: 10.1523/jneurosci.1917-10.2010

Risher, W. C., Lee, M. R., Fomitcheva, I. V., Hess, D. C., and Kirov, S. A. (2011). Dibucaine mitigates spreading depolarization in human neocortical slices and prevents acute dendritic injury in the ischemic rodent neocortex. *PLoS One* 6:e22351. doi: 10.1371/journal.pone.0022351

Robertson, R. M., Dawson-Scully, K. D., and Andrew, R. D. (2020). Neural shutdown under stress: an evolutionary perspective on spreading depolarization. *J. Neurophysiol.* 123, 885–895. doi: 10.1152/jn.00724.2019

Roy, R. K., Althammer, F., Seymour, A. J., Du, W., Biancardi, V. C., Hamm, J. P., et al. (2021). Inverse neurovascular coupling contributes to positive feedback excitation of vasopressin neurons during a systemic homeostatic challenge. *Cell Rep.* 37:109925. doi: 10.1016/j.celrep.2021.109925

Rueda, C. B., Llorente-Folch, I., Traba, J., Amigo, I., Gonzalez-Sanchez, P., Contreras, L., et al. (2016). Glutamate excitotoxicity and Ca2+-regulation of respiration: Role of the Ca2+ activated mitochondrial transporters (CaMCs). *Biochim. Biophys. Acta* 1857, 1158–1166. doi: 10.1016/j.bbabio.2016.04.003

Sadeghian, H., Lacoste, B., Qin, T., Toussay, X., Rosa, R., Oka, F., et al. (2018). Spreading depolarizations trigger caveolin-1-dependent endothelial transcytosis. *Ann. Neurol.* 84, 409–423. doi: 10.1002/ana.25298

Sarkar, S., SenGupta, A. K., and Prakash, P. (2010). The Donnan membrane principle: opportunities for sustainable engineered processes and materials. *Environ. Sci. Technol.* 44, 1161–1166. doi: 10.1021/es9024029

Sawant-Pokam, P. M., Suryavanshi, P., Mendez, J. M., Dudek, F. E., and Brennan, K. C. (2017). Mechanisms of Neuronal Silencing After Cortical Spreading Depression. *Cereb. Cortex* 27, 1311–1325. doi: 10.1093/cercor/bhv328

Schoknecht, K., Kikhia, M., Lemale, C. L., Liotta, A., Lublinsky, S., Mueller, S., et al. (2021). The role of spreading depolarizations and electrographic seizures in early injury progression of the rat photothrombosis stroke model. *J. Cereb. Blood Flow Metab.* 41, 413–430. doi: 10.1177/0271678X20915801

Schumm, L., Lemale, C. L., Major, S., Hecht, N., Nieminen-Kelha, M., Zdunczyk, A., et al. (2021). Physiological variables in association with spreading depolarizations in the late phase of ischemic stroke. *J. Cereb. Blood Flow Metab.* 2021:271678X211039628. doi: 10.1177/0271678X211039628

Schurks, M., Rist, P. M., Bigal, M. E., Buring, J. E., Lipton, R. B., and Kurth, T. (2009). Migraine and cardiovascular disease: systematic review and meta-analysis. *BMJ* 339:b3914. doi: 10.1136/bmj.b3914

Shen, Q., Ren, H., Cheng, H., Fisher, M., and Duong, T. Q. (2005). Functional, perfusion and diffusion MRI of acute focal ischemic brain injury. *J. Cereb. Blood Flow Metab.* 25, 1265–1279. doi: 10.1038/sj.jcbfm.9600132

Shin, H. K., Dunn, A. K., Jones, P. B., Boas, D. A., Moskowitz, M. A., and Ayata, C. (2006). Vasoconstrictive neurovascular coupling during focal ischemic depolarizations. *J. Cereb. Blood Flow Metab.* 26, 1018–1030. doi: 10.1038/sj.jcbfm.9600252

Shuttleworth, C. W., Andrew, R. D., Akbari, Y., Ayata, C., Balu, R., Brennan, K. C., et al. (2019). Which Spreading Depolarizations Are Deleterious To Brain Tissue? *Neurocrit. Care* 2019:7. doi: 10.1007/s12028-019-00776-7

Skou, J. C., and Esmann, M. (1992). The Na,K-ATPase. *J. Bioenerg. Biomembr.* 24, 249–261.

Smith, S. E., Chen, X., Brier, L. M., Bumstead, J. R., Rensing, N. R., Ringel, A. E., et al. (2020). Astrocyte deletion of alpha2-Na/K ATPase triggers episodic motor paralysis in mice via a metabolic pathway. *Nat. Commun.* 11:6164. doi: 10.1038/s41467-020-19915-2

Somjen, G. G. (2001). Mechanisms of spreading depression and hypoxic spreading depression-like depolarization. *Physiol. Rev.* 81, 1065–1096. doi: 10.1152/physrev.2001.81.3.1065

Somjen, G. G. (2004a). *Ions in the brain*. New York, NY: Oxford University Press.

Somjen, G. G. (2004b). "Irreversible hypoxic (ischemic) neuron injury," in *Ions in the brain*, ed. G. G. Somjen (New York, NY: Oxford University Press), 338–372.

Spector, J. T., Kahn, S. R., Jones, M. R., Jayakumar, M., Dalal, D., and Nazarian, S. (2010). Migraine headache and ischemic stroke risk: an updated meta-analysis. *Am. J. Med.* 123, 612–624. doi: 10.1016/j.amjmed.2009.12.021

Sperelakis, N. (2011). "Gibbs-Donnan Equilibrium Potentials," in *Cell Physiology Source Book*, 4 Edn, ed. N. Sperelakis (Cambridge, MA: Academic Press), 147–151.

Spong, K. E., Dreier, J. P., and Robertson, R. M. (2017). A new direction for spreading depolarization: Investigation in the fly brain. *Channels* 11, 97–98. doi: 10.1080/19336950.2016.1239898

Steen, P. A., Michenfelder, J. D., and Milde, J. H. (1979). Incomplete versus complete cerebral ischemia: improved outcome with a minimal blood flow. *Ann. Neurol.* 6, 389–398. doi: 10.1002/ana.410060503

Steffensen, A. B., Sword, J., Croom, D., Kirov, S. A., and MacAulay, N. (2015). Chloride Cotransporters as a Molecular Mechanism underlying Spreading Depolarization-Induced Dendritic Beading. *J. Neurosci.* 35, 12172–12187. doi: 10.1523/JNEUROSCI.0400-15.2015

Stoica, A., Larsen, B. R., Assentoft, M., Holm, R., Holt, L. M., Vilhardt, F., et al. (2017). The alpha2beta2 isoform combination dominates the astrocytic Na(+) /K(+) -ATPase activity and is rendered nonfunctional by the alpha2.G301R familial hemiplegic migraine type 2-associated mutation. *Glia* 65, 1777–1793. doi: 10.1002/glia.23194

Strong, A. J., Anderson, P. J., Watts, H. R., Virley, D. J., Lloyd, A., Irving, E. A., et al. (2007). Peri-infarct depolarizations lead to loss of perfusion in ischaemic gyrencephalic cerebral cortex. *Brain* 130(Pt 4), 995–1008. doi: 10.1093/brain/awl392

Strong, A. J., Fabricius, M., Boutelle, M. G., Hibbins, S. J., Hopwood, S. E., Jones, R., et al. (2002). Spreading and synchronous depressions of cortical activity in acutely injured human brain. *Stroke* 33, 2738–2743. doi: 10.1161/01.str.0000043073.69602.09

Sueiras, M., Thonon, V., Santamarina, E., Sanchez-Guerrero, A., Poca, M. A., Quintana, M., et al. (2021). Cortical Spreading Depression Phenomena Are Frequent in Ischemic and Traumatic Penumbra: A Prospective Study in Patients With Traumatic Brain Injury and Large Hemispheric Ischemic Stroke. *J. Clin. Neurophysiol.* 38, 47–55. doi: 10.1097/WNP.0000000000000648

Sugimoto, K., Nomura, S., Shirao, S., Inoue, T., Ishihara, H., Kawano, R., et al. (2018). Cilostazol decreases duration of spreading depolarization and spreading ischemia after aneurysmal subarachnoid hemorrhage. *Ann. Neurol.* 84, 873–885. doi: 10.1002/ana.25361

Takano, K., Latour, L. L., Formato, J. E., Carano, R. A., Helmer, K. G., Hasegawa, Y., et al. (1996). The role of spreading depression in focal ischemia evaluated by diffusion mapping. *Ann. Neurol.* 39, 308–318. doi: 10.1002/ana.410390307

Takano, T., Tian, G. F., Peng, W., Lou, N., Lovatt, D., Hansen, A. J., et al. (2007). Cortical spreading depression causes and coincides with tissue hypoxia. *Nat. Neurosci.* 10, 754–762. doi: 10.1038/nn1902

Tamim, I., Chung, D. Y., de Morais, A. L., Loonen, I. C. M., Qin, T., Misra, A., et al. (2021). Spreading depression as an innate antiseizure mechanism. *Nat. Commun.* 12:2206. doi: 10.1038/s41467-021-22464-x

Tanaka, E., Yamamoto, S., Kudo, Y., Mihara, S., and Higashi, H. (1997). Mechanisms underlying the rapid depolarization produced by deprivation of oxygen and glucose in rat hippocampal CA1 neurons in vitro. *J. Neurophysiol.* 78, 891–902. doi: 10.1152/jn.1997.78.2.891

Tang, D., Kang, R., Berghe, T. V., Vandenabeele, P., and Kroemer, G. (2019). The molecular machinery of regulated cell death. *Cell Res.* 29, 347–364. doi: 10.1038/s41422-019-0164-5

Tasaki, I., and Byrne, P. M. (1991). Demonstration of heat production associated with spreading depression in the amphibian retina. *Biochem. Biophys. Res. Commun.* 174, 293–297. doi: 10.1016/0006-291x(91)90519-d

Taylor, D. L., Obrenovitch, T. P., and Symon, L. (1996). Changes in extracellular acid-base homeostasis in cerebral ischemia. *Neurochem. Res.* 21, 1013–1021. doi: 10.1007/BF02532411

Theis, M., Jauch, R., Zhuo, L., Speidel, D., Wallraff, A., Doring, B., et al. (2003). Accelerated hippocampal spreading depression and enhanced locomotory activity in mice with astrocyte-directed inactivation of connexin43. *J. Neurosci.* 23, 766–776. doi: 10.1523/JNEUROSCI.23-03-00766.2003

Tomkins, O., Friedman, O., Ivens, S., Reiffurth, C., Major, S., Dreier, J. P., et al. (2007). Blood-brain barrier disruption results in delayed functional and structural alterations in the rat neocortex. *Neurobiol. Dis.* 25, 367–377. doi: 10.1016/j.nbd.2006.10.006

Uetsuka, S., Fujisawa, H., Yasuda, H., Shima, H., and Suzuki, M. (2002). Severe cerebral blood flow reduction inhibits nitric oxide synthesis. *J. Neurotrauma* 19, 1105–1116. doi: 10.1089/089771502760342009

Unekawa, M., Ikeda, K., Tomita, Y., Kawakami, K., and Suzuki, N. (2018). Enhanced susceptibility to cortical spreading depression in two types of Na(+),K(+)-ATPase alpha2 subunit-deficient mice as a model of familial hemiplegic migraine 2. *Cephalalgia* 38, 1515–1524. doi: 10.1177/0333102417738249

Vahedi, K., Denier, C., Ducros, A., Bousson, V., Levy, C., Chabriat, H., et al. (2000). CACNA1A gene de novo mutation causing hemiplegic migraine, coma, and cerebellar atrophy. *Neurology* 55, 1040–1042. doi: 10.1212/wnl.55.7.1040

van den Maagdenberg, A. M., Pietrobon, D., Pizzorusso, T., Kaja, S., Broos, L. A., Cesetti, T., et al. (2004). A Cacna1a knockin migraine mouse model with increased susceptibility to cortical spreading depression. *Neuron* 41, 701–710. doi: 10.1016/s0896-6273(04)00085-6

Van Harreveld, A. (1957). Changes in volume of cortical neuronal elements during asphyxiation. *Am. J. Physiol.* 191, 233–242. doi: 10.1152/ajplegacy.1957.191.2.233

Van Harreveld, A. (1958). Changes in the diameter of apical dendrites during spreading depression. *Am. J. Physiol.* 192, 457–463. doi: 10.1152/ajplegacy.1958.192.3.457

Van Harreveld, A., and Fifkova, E. (1970). Glutamate release from the retina during spreading depression. *J. Neurobiol.* 2, 13–29. doi: 10.1002/neu.480020103

Van Harreveld, A., and Hawes, R. C. (1946). Asphyxial depolarisation in the spinal cord. *Am. J. Physiol.* 147, 669–684. doi: 10.1152/ajplegacy.1946.147.4.669

Van Harreveld, A., and Ochs, S. (1957). Electrical and vascular concomitants of spreading depression. *Am. J. Physiol.* 189, 159–166. doi: 10.1152/ajplegacy.1957.189.1.159

van Harreveld, A., and Stamm, J. S. (1953). Spreading cortical convulsions and depressions. *J. Neurophysiol.* 16, 352–366. doi: 10.1152/jn.1953.16.4.352

Vergun, O., Keelan, J., Khodorov, B. I., and Duchen, M. R. (1999). Glutamate-induced mitochondrial depolarisation and perturbation of calcium homeostasis in cultured rat hippocampal neurones. *J. Physiol.* 519(Pt 2), 451–466. doi: 10.1111/j.1469-7793.1999.0451m.x

Volpe, G., Cozzi, L., Migliorelli, D., Croci, L., and Palleschi, G. (2014). Development of a haemolytic-enzymatic assay with mediated amperometric detection for palytoxin analysis: application to mussels. *Anal. Bioanal. Chem.* 406, 2399–2410. doi: 10.1007/s00216-014-7630-1

Vorisek, I., and Sykova, E. (1997). Ischemia-induced changes in the extracellular space diffusion parameters, K+, and pH in the developing rat cortex and corpus callosum. *J. Cereb. Blood Flow Metab.* 17, 191–203. doi: 10.1097/00004647-199702000-00009

Vyskocil, F., Kritz, N., and Bures, J. (1972). Potassium-selective microelectrodes used for measuring the extracellular brain potassium during spreading depression and anoxic depolarization in rats. *Brain Res.* 39, 255–259. doi: 10.1016/0006-8993(72)90802-5

Wadman, W. J., Heinemann, U., Konnerth, A., and Neuhaus, S. (1985). Hippocampal slices of kindled rats reveal calcium involvement in epileptogenesis. *Exp. Brain Res.* 57, 404–407. doi: 10.1007/BF00236547

Walz, W., and Hertz, L. (1982). Ouabain-sensitive and ouabain-resistant net uptake of potassium into astrocytes and neurons in primary cultures. *J. Neurochem.* 39, 70–77. doi: 10.1111/j.1471-4159.1982.tb04702.x

Wappler, E. A., Institoris, A., Dutta, S., Katakam, P. V., and Busija, D. W. (2013). Mitochondrial dynamics associated with oxygen-glucose deprivation in rat primary neuronal cultures. *PLoS One* 8:e63206. doi: 10.1371/journal.pone.0063206

Waters, M. J., Cheong, E., Jannes, J., and Kleinig, T. (2018). Ischaemic stroke may symptomatically manifest as migraine aura. *J. Clin. Neurosci.* 55, 62–64. doi: 10.1016/j.jocn.2018.07.017

Windmuller, O., Lindauer, U., Foddis, M., Einhaupl, K. M., Dirnagl, U., Heinemann, U., et al. (2005). Ion changes in spreading ischaemia induce rat middle cerebral artery constriction in the absence of NO. *Brain* 128(Pt 9), 2042–2051. doi: 10.1093/brain/awh545

Winkler, M. K., Chassidim, Y., Lublinsky, S., Revankar, G. S., Major, S., Kang, E. J., et al. (2012). Impaired neurovascular coupling to ictal epileptic activity and spreading depolarization in a patient with subarachnoid hemorrhage: possible link to blood-brain barrier dysfunction. *Epilepsia* 53(Suppl. 6), 22–30. doi: 10.1111/j.1528-1167.2012.03699.x

Woitzik, J., Hecht, N., Pinczolits, A., Sandow, N., Major, S., Winkler, M. K., et al. (2013). Propagation of cortical spreading depolarization in the human cortex after malignant stroke. *Neurology* 80, 1095–1102. doi: 10.1212/WNL.0b013e3182886932

Wolf, S. G., Mutsafi, Y., Dadosh, T., Ilani, T., Lansky, Z., Horowitz, B., et al. (2017). 3D visualization of mitochondrial solid-phase calcium stores in whole cells. *Elife* 6:29929. doi: 10.7554/eLife.29929

Woodhouse, L., Scutt, P., Krishnan, K., Berge, E., Gommans, J., Ntaios, G., et al. (2015). Effect of Hyperacute Administration (Within 6 Hours) of Transdermal Glyceryl Trinitrate, a Nitric Oxide Donor, on Outcome After Stroke: Subgroup Analysis of the Efficacy of Nitric Oxide in Stroke (ENOS) Trial. *Stroke* 46, 3194–3201. doi: 10.1161/STROKEAHA.115.009647

Zachrisson, O. C., Balldin, J., Ekman, R., Naesh, O., Rosengren, L., Agren, H., et al. (2000). No evident neuronal damage after electroconvulsive therapy. *Psychiatry Res.* 96, 157–165. doi: 10.1016/s0165-1781(00)00202-x

Zhou, N., Rungta, R. L., Malik, A., Han, H., Wu, D. C., and MacVicar, B. A. (2013). Regenerative glutamate release by presynaptic NMDA receptors contributes to spreading depression. *J. Cereb. Blood Flow Metab.* 33, 1582–1594. doi: 10.1038/jcbfm.2013.113

**Conflict of Interest:** The authors declare that the research was conducted in the absence of any commercial or financial relationships that could be construed as a potential conflict of interest.

The reviewer OH declared a past co-authorship with the authors JD, CR to the handling editor.

frontiers | Frontiers in Cellular Neuroscience

ERRATUM
published: 26 April 2022
doi: 10.3389/fncel.2022.917669

# Erratum: Migraine Aura, Transient Ischemic Attacks, Stroke, and Dying of the Brain Share the Same Key Pathophysiological Process in Neurons Driven by Gibbs–Donnan Forces, Namely Spreading Depolarization

*Frontiers Production Office**

*Frontiers Media SA, Lausanne, Switzerland*

**Keywords: migraine aura, traumatic brain injury, circulatory arrest, subarachnoid hemorrhage, spreading depolarization, spreading depression, brain death, brain ischemia**

OPEN ACCESS

***Approved by:***
*Frontiers Editorial Office, Frontiers Media SA, Switzerland*

***Correspondence:**
*Frontiers Production Office*
*production.office@frontiersin.org*

***Specialty section:***
*This article was submitted to Cellular Neurophysiology, a section of the journal Frontiers in Cellular Neuroscience*

***Received:*** *11 April 2022*
***Accepted:*** *11 April 2022*
***Published:*** *26 April 2022*

***Citation:***
*Frontiers Production Office (2022) Erratum: Migraine Aura, Transient Ischemic Attacks, Stroke, and Dying of the Brain Share the Same Key Pathophysiological Process in Neurons Driven by Gibbs–Donnan Forces, Namely Spreading Depolarization. Front. Cell. Neurosci. 16:917669. doi: 10.3389/fncel.2022.917669*

**An Erratum on**

**Migraine Aura, Transient Ischemic Attacks, Stroke, and Dying of the Brain Share the Same Key Pathophysiological Process in Neurons Driven by Gibbs–Donnan Forces, Namely Spreading Depolarization**

*by Lemale, C. L., Lückl, J., Horst, V., Reiffurth, C., Major, S., Hecht, N., Woitzik, J., and Dreier, J. P. (2022). Front. Cell. Neurosci. 16:837650. doi: 10.3389/fncel.2022.837650*

Due to a publisher error, the below statement was not included:

The reviewer OH declared a past co-authorship with the authors JD, CR to the handling editor.

The publisher apologizes for this mistake. The original version of this article has been updated.

frontiers | Frontiers in Cellular Neuroscience

TYPE Original Research
PUBLISHED 09 September 2022
DOI 10.3389/fncel.2022.868291



OPEN ACCESS

EDITED BY
Jukka Jolkkonen,
University of Eastern Finland, Finland

REVIEWED BY
Murali Vijayan,
Texas Tech University Health Sciences Center, United States
Qi Yuan,
Memorial University of Newfoundland, Canada

*CORRESPONDENCE
Hong Zheng
hzheng@zzu.edu.cn
Ying He
heying39@163.com

†These authors have contributed equally to this work and share first authorship

SPECIALTY SECTION
This article was submitted to Cellular Neuropathology, a section of the journal Frontiers in Cellular Neuroscience

RECEIVED 02 February 2022
ACCEPTED 20 June 2022
PUBLISHED 09 September 2022

CITATION
Liu Y, Shang G, Zhang X, Liu F, Zhang C, Li Z, Jia J, Xu Y, Zhang Z, Yang S, Zhou B, Luan Y, Huang Y, Peng Y, Han T, He Y and Zheng H (2022) *CAMTA1* gene affects the ischemia-reperfusion injury by regulating *CCND1*. *Front. Cell. Neurosci.* 16:868291. doi: 10.3389/fncel.2022.868291



# *CAMTA1* gene affects the ischemia-reperfusion injury by regulating *CCND1*

Yang Liu[1†], Guohui Shang[1†], Xuran Zhang[2], Fuyong Liu[3], Chi Zhang[1], Zhihao Li[1], Jing Jia[1], Yan Xu[1], Zhaojing Zhang[1], Shangdong Yang[1], Baixue Zhou[1], Yingying Luan[1], Yanyang Huang[1], Yue Peng[1], Tianyi Han[1], Ying He[1*] and Hong Zheng[1*]

[1]Department of Medical Genetics and Cell Biology, School of Basic Medical Sciences, Zhengzhou University, Zhengzhou, China, [2]Department of Clinical Laboratory, The First Affiliated Hospital of Henan University of CM, Henan University of CM, Zhengzhou, China, [3]Department of Pathogenic Biology and Immunology, School of Life Sciences, Sanquan College of Xinxiang Medical University, Xinxiang, China

Epigenetic modulations lead to changes in gene expression, including DNA methylation, histone modifications, and noncoding RNAs. In recent years, epigenetic modifications have been related to the pathogenesis of different types of cancer, cardiovascular disease, and other diseases. Emerging evidence indicates that DNA methylation could be associated with ischemic stroke (IS) and plays a role in pathological progression, but the underlying mechanism has not yet been fully understood. In this study, we used human methylation 850K BeadChip to analyze the differences in gene methylation status in the peripheral blood samples from two groups (3 IS patients vs. 3 healthy controls). According to their bioinformatics profiling, we found 278 genes with significantly different methylation levels. Seven genes with the most significant methylation modifications were validated in two expanded groups (100 IS patients vs. 100 healthy controls). The *CAMTA1* gene had significantly different methylation changes in patients compared to the controls. To understand the CAMTA1 function in stroke, we generated *CAMTA1* knockout in SH-SY5Y cells. RNA seq results in *CAMTA1* knockout cells revealed the pathways and gene set enrichments involved in cellular proliferation and cell cycle. Furthermore, a series of experiments demonstrated that in the oxygen-glucose deprivation/re-oxygenation (OGD/R) model system, the expression of cyclin D1, an essential regulator of cell cycle progression, was increased in SH-SY5Y *CAMTA1* KO cells. Increasing evidence demonstrated that ischemic stress could inappropriately raise cyclin D1 levels in mature neurons. However, the molecular signals leading to an increased cyclin D1 level are unclear. Our findings demonstrate for the first time that the *CAMTA1* gene could regulate cyclin D1 expression and implicate their role in strokes.

KEYWORDS

**ischemic stroke, DNA methylation modification, *CAMTA1*, *CCND1*, cell cycle**

## Introduction

A stroke is an acute cerebrovascular incident. It affects the arteries leading to and within the brain, preventing oxygen and nutrients. About 80% of strokes are caused by ischemic compared to 20% hemorrhagic. It is one of the leading causes of death and disability worldwide. Currently, the stroke burden remains high, with 5.5 million deaths in 2016 based on the Global Burden of Disease report (Fogh et al., 2016). Besides, the stroke burden has also increased in young people aged 18–49 (GBD 2016 Stroke Collaborators, 2019). That implies massive public health issues and needs scaled-up prevention strategies. Therefore, a complete understanding of the pathogenesis of ischemic stroke (IS) is required.

Although substantial evidence has pointed to numerous environmental and genetic risk factors associated with IS (Giralt-Steinhauer et al., 2014; Feigin et al., 2017; GBD 2016 Stroke Collaborators, 2019; Singer et al., 2019), additional mechanisms remain clarified. Over the past years, with the improvement of research in the epigenetic field, multiple studies have revealed the epigenetic modifications involved in the pathogenesis of the cardiovascular disease (Traylor et al., 2012; Singer et al., 2019). One of the most understood epigenetic modifications, DNA methylation, usually occurs on the CpG site by adding one or more methyl groups to a cytosine. It affects gene transcription and expression without changing DNA sequences (Morgado-Pascual et al., 2018). Abnormal DNA methylation patterns have been investigated in IS pathogenesis (Feinberg, 2007; Udali et al., 2013). The global level of DNA methylation increased in the rat model of IS (Deng et al., 2019). Recently, more studies demonstrated that gene-specific methylation could also be involved in IS. For example, the hypermethylation in the cystathionine-beta-synthase promoter (Stanzione et al., 2020) and the AHCY gene encoding the S-adenosine homocysteine hydrolase (Dock et al., 2015) have been identified to increase ischemic stroke risk. People with hypomethylation in Long Interspersed Nucleotide Element-1 (LINE-1) may also have a higher risk of IS (Wang et al., 2019). Additionally, the higher methylation of cyclin-dependent kinase inhibitor 2B (CDKN2B) may affect arterial calcification in IS patients (Zhao et al., 2020). Despite these results, the new gene-specific methylation and its mechanisms remain unexplored.

Additionally, dysregulation of cell cycle machinery is also implicated in strokes. Empirical evidence suggests that inappropriately activated complex cyclin D1/cyclin-dependent kinases (Cdk) under ischemic stress conditions were responsible for the dysregulated cell cycle. The cyclin D1 levels were increased by the oxygen-glucose deprivation (Cai et al., 2009; Baccarelli et al., 2010b; Zhou et al., 2016). In addition, an increase in cyclin D1 immunoreactivity has also been detected in human stroke brains (Katchanov et al., 2001). However, the molecular signals leading to an increased cyclin D1 level have not been clarified.

In this study, we conducted a genome-wide analysis extracted from the peripheral blood to identify differentially methylated genes in IS patients using Illumina Infinium Methylation EPIC Bead Chip (850K chip) and Methyl Target (target regional methylation level sequencing). *CAMTA1* gene was the most highly methylated in patients compared to the controls. It encodes synthetic Calmodulin Binding Transcription Activator 1 (CAMTA1), which could inhibit the proliferation of various tumor cells, including breast cancer, colon cancer, pheochromocytoma, etc. Current research on the CAMTA1 protein has focused on its role in the pathogenesis of Epithelioid hemangioendothelioma (EHE), a malignant tumor of vascular endothelial cell origin. The primary mechanism of its pathogenesis is multiple translocations in the chromosome 1p36.3 and 3q25 regions, which happens to be the location of the *CAMTA1* gene. Long-term studies have found that *WWTR1-CAMTA1* gene fusion occurs in 90% of EHE cases. Under the transcriptional control of the WWTR1 promoter, this fusion gene activates the abnormally high expression of the *CAMTA1* gene, encoding a specific fusion transcription factor that plays a crucial role in the EHE pathogenesis. Few studies have reported that the *CAMTA1* gene was also associated with neurodegenerative diseases. Fogh et al. have shown that the *CAMTA1* gene affects the survival of patients with sporadic amyotrophic lateral sclerosis (ALS) (Fogh et al., 2016). Studies have shown that *CAMTA1* KO mice could develop ataxia, Purkinje fibrosis, and other characteristics (Long et al., 2014). However, the involvement of CAMTA1 in stroke has not been reported. Our results show that CAMTA1 knockout could attenuate oxygen-glucose deprivation/re-oxygenation (OGD/R)-induced apoptosis and block more cells at the S phase. Moreover, the *CCND1* mRNA and its coding protein: cyclin D1, were increased by decreased CAMTA1 levels. Our findings demonstrate that the *CAMTA1* gene affects the ischemia-reperfusion injury by regulating cyclin D1 proteins.

## Materials and methods

### Study population

The study was conducted on three healthy people and three acute cerebral infarction patients with magnetic resonance imaging scans performed in the Department of Neurology, the First Affiliated Hospital of the Henan University of Chinese Medicine, from May 2017 to September 2017. Two men and one woman with an average age of 57.3 years were in the IS group. Likewise, in the healthy control group, there are two men and

one woman with an average age of 58.7 years. The validation of the population included 100 IS patients (60 men and 40 women), with an average age ranging between 58.34 and 72.1 years. The control group included 100 control groups (including 52 men and 48 women), with an average age ranging between 51.3 and 74.8 years.

Inclusion criteria: (1) The diagnosis of ischemic stroke conformed to the guideline for the diagnosis and treatment of acute ischemic stroke in China in 2010 and was confirmed by head MRI scans. (2) The course of the stroke was <1 week. (3) Over 18 years of age. Exclusion criteria: (1) Patients accompanied by unconsciousness, aphasia, or severe cognitive impairment could not cooperate with the examination. (2) Patients with psychosis or other psychiatric conditions such as anxiety, depression, and suicidal behavior. (3) Patients with other severe systemic diseases, including infection, cardiac and pulmonary failure, or hepatic and renal dysfunction. (4) Patients failed to perform MRI scans for various reasons. The Ethics Committee approved the study protocol of the First Affiliated Hospital of the Henan University of Chinese Medicine. All participants signed a written consent form.

Expanding clinical validation of population: peripheral blood samples were obtained from IS patients and stored at −80°C freezer. The inclusion criteria and exclusion criteria, as detailed above, were followed.

## Extraction of proteins

For mononuclear cell pellets, 100 μL of cell lysate buffer was added to the centrifuge tube (RIPA lysate is mixed well with PMSF in a 100:1 ratio) and readied for use. It was pipetted repeatedly until it was mixed well and the lysate was then transferred to a new 1.5 ml EP tube. It was incubated on ice for 30 min, during which time it was vortexed every 10 min to allow the cells to be fully lysed. The mixture was centrifuged at 12,000 rpm for 15 min at 4°C and the supernatant was transferred into a new 1.5 ml EP tube to obtain the total soluble protein from the mononuclear cells for subsequent experiments and stored at −80°C.

## DNA methylation

Peripheral blood samples from the six subjects were collected and used for the 850K DNA methylation analysis. The DNA microarray results were validated using the remaining samples.

After the frozen blood samples were thawed, the DNA from human whole blood cells was extracted with a Tiangen kit (Beijing, China, Catalog Number: DP319). DNA concentration and purity were quantified in a NanoDrop 2000 system (NanoDrop, Wilmington, DE). The DNA concentration must be higher than 50 ng/μl.

Whole DNA methylation (3 IS vs. 3 healthy controls) was assessed with the Infinium Human Methylation 850 BeadChip Kit (Illumina, Inc., San Diego, CA, United States), covering the human genome's 853,307 cytosine positions. Data preprocessing and analyses were conducted in the statistical programming environment R v3.1.2 with RnBeads v0.99. Normalization and background correction was applied to the methylation data with manufacture-recommended algorithms and implemented in the methylome package. Methylation levels were averaged for the replicates for each biopsy after normalization. We calculated the difference in methylation β-value between the two groups or the mean of the pairwise difference for paired samples. False discovery rates (FDR) were calculated using an improved Benjamini-Hochberg procedure to correct *p*-values for multiple hypothesis testing, and the methylation changes in CpG sites/regions with FDR < 0.05 were considered statistically significant. Ingenuity Pathway Analysis (IPA) was used to identify functional interactions of genes differentially methylated between groups. Average methylation signals on the CpG sites within each CpG site and/or promoter region were hierarchically clustered with Pearson dissimilarity and average linkage as clustering parameters.

## Screening of differential genes

Difference setting criteria: The absolute value of the Diff Score value between the case group and the control group sample was >13, and the Absolute value of Delta Beta was >0. 17, that is, the differential methylation gene.

Diff score = 10*sgn(13ref-13cond)4logl0(p)

For a *P*-value of 0.05, Diff Score = 4–13

For a *P*-value of 0.01. Diff Score = 4–20

For a *P*-value of 0.001. Diff Score = 4–30.

The Ddta Beta value was calculated as the difference between the case group and the control group and Avg Beta was the degree of methylation difference between the case group and the control group at each site.

## Verifying candidate genes by methyl target region methylation sequencing

The methylation level of the promoter region of the *CAMTA1* gene in 100 IS cases vs. 100 healthy control samples was detected by methyl target region methylation sequencing. MethylTarget™ assays (targeted bisulfite sequencing) developed by Genesky Biotech (Shanghai, China) were carried out as previously described. Briefly, CpG sites adjacent to the promoter region of the *CAMTA1* gene were analyzed, and based on

these CpG sites, four CpG regions from CpG sites in *CAMTA1* were sequenced (the relative distance from the transcriptional start site, amplification primers, and product size of these CpG regions are described in Tables 2, 3). Genomic DNA was converted with bisulfite, and PCR was performed to amplify the targeted DNA sequences. The products were sequenced by an Illumina MiSeq benchtop sequencer (Illumina, CA, United States).

The total RNA was extracted using the Tiangen reagent (Beijing, China, Catalog Number: DP424). Using a QuantiTect Reverse Transcription kit (Vazyme, Wuhan, China, Catalog Number: R333-01), 2 μg of each RNA was reverse transcribed into cDNA. Expression levels of the genes were analyzed using a QuantiTect SYBR Green PCR kit (Vazyme, Nanjing, China, Catalog Number: Q221-01). The primer sequences are listed below:

Forward primer: gattatggtttgtttttaggatgagag
Reverse primer: aacccrattcaaactcrttcc.

## Western blot

Cells were lysed with RIPA lysis buffer and completed with protease inhibitor (Solarbio, Beijing, China, Catalog Number: R0020). Lysates were centrifuged at 4°C, 12,000 × g for 10 min, supernatants collected, and protein concentrations assessed using a BCA protein assay kit (Solarbio, Beijing, China, Catalog Number: PC0020). Equal amounts of protein were placed on 10% SDS-PAGE gels and blotted onto polyvinylidene difluoride membranes (Millipore, Hercules, CA, USA Catalog Number: IPVH00010). Membranes were blocked with 5% nonfat milk for 2 h at room temperature and then probed with CAMTA1(Abcam; Cambridge, UK, Catalog Number: ab251843), and cyclin D1 (ProteinTech, Wuhan, Hubei, China, Catalog Number: 60186-1-Ig) antibodies at 4°C overnight. The blots were then incubated with HRP conjugated secondary antibody. GAPDH and β-actin were used as an endogenous protein control. ECL substrates were used to visualize signals (ProteinTech, Wuhan, Hubei, China, Catalog Number: 60004-1-Ig).

## Bioinformatic analysis

For 850K chip and RNA seq omics results, we performed GO function annotation analysis based on the GO database (http://geneontology.org/page/go-database), and KEGG pathway annotation analysis based on the KEGG database (http://www.kegg.jp/kegg/ko.html).

## Cell culture and generation of *CAMTA1* knockout cell lines

Human neuroblastoma cell lines (SH-SY5Y) were maintained in Dulbecco's minimum essential medium (DMEM/F12, Seven biotech, Shanghai, China, Catalog Number: SC103-01) with 10% fetal bovine serum (FBS, ExCell Bio, Shanghai, China, Catalog Number: FSS500) and 1% penicillin/streptomycin (Gbico, MA, USA, Catalog 30-2220). All cells were cultured in an incubator with 5% $CO_2$ at 37°C. Lipofectamine 3000 (Invitrogen, Shanghai, China, Catalog Number: L3000150) was used for miRNA transfection. Cells were assayed 48 h after transfection.

Knockout cell lines were generated using the CRISPR/Cas9 system. Cells were transfected with a px330 vector (Addgene, MA, USA, Catalog Number: 42230) encoding a gRNA for the gene of interest and a vector encoding a gRNA for the homo sapiens *CAMTA1* gene (5′-ggtatgtcgggaacctctcc-3′). Resistant clones were expanded after adding blasticidin selection (4 μg/ml).

To generate knockout HEK293T and SH-SY5Y cells, they were transfected with pLentiCRISPRv2 vector (Addgene, MA, USA, Catalog Number: 52961) encoding gRNAs targeting non-overlapping regions of the *CAMTA1* gene. Following puromycin selection (2 μg/ml, for 2 days), single cell clones were expanded, and gene disruptions were validated by sequencing.

The gRNA sequence CCGGGTCCTCCTCCGTAGTG was used to generate the SH-SY5Y *CAMTA1* knockout clone.

## siRNA transfection

*CCND*1 siRNA and non-sense siRNA (random siRNA) were purchased from Hanbio (Shanghai, China). The efficiency of transfection was evaluated using real-time RT-PCR. The sequences of *CCND1* and scrambled siRNAs are as follows: Target Sequence: CCACAGATGTGAAGTTCATTT, scrambled siRNA: CCGAAGTTACTATGAACAA. Transient transfection with siRNA was performed using Lipofectamine RNAiMAX reagent (Invitrogen), and siRNA was reverse transfected into cells according to the supplied protocol.

## Cell counting kit-8 assay and oxygen glucose deprivation/reoxygenation model

We applied cell counting kit-8 (Topscience, Shanghai, China, Catalog Number: TP1197) to assess cell proliferation. The cells were seeded on the 96-well plate with a density of 1,000 cells/well, 10 μL 5 mg/mL CCK-8 reagent was added to the well at 0, 24, 48, and 72 h. The culture was terminated 1 h after

CCK- 8 regent adding, and the optical density OD value of each well was detected by a microplate reader (Tecan, Mannedorf, Switzerland) at 450 nm. The experiments were repeated in triplicate for each group.

OGD/R is the most common cell model in the study of ischemic stroke: $5 \times 10^5$ cells were seeded in a 35 mm culture dish, and 2 ml of complete DMEM/F12 medium was added and placed in a regular cell incubator for a whole night. Further, $5 \times 10^5$ cells were seeded in a 35 mm culture dish, 2 ml of complete DMEM medium was added and placed in a standard cell incubator for 4 h. Then cells were replaced with serum-free, dual-antibiotics and low-sugar DMEM medium (DMEM, sbjbio, Nanjing, China, Catalog Number: BC-M-038), and the cells were placed in an anaerobic incubator (HENGZI-HYQX-II, Shanghai, China) without $O_2$ at 37°C for 4 h. (This step was to complete hypoglycemia and hypoxia and we checked cell viability at the corresponding time point).

The cells were taken out and replaced with a high-sugar complete medium and placed back into the regular cell incubator for several hours. (Reperfusion was completed in this step and cell viability was checked after 4 h).

## Colony formation assay

The cells were seeded on the 6-well plates with a density of 10,000 cells/well in triplicate in 3 ml of medium containing 10% FBS and allowed to grow for 3 days. The culture medium was replaced every day. After incubation, the medium was removed. The colonies were fixed with 4% paraformaldehyde for 15 min and then stained with hematoxylin for 15 min. The stained cells were rinsed three times with tap water to remove the excess dye. Each dish was then washed and dried. The colonies with a diameter larger than 0.6 mm were counted.

## Cell cycle assay

The cell cycle progression was assessed *via* a Cell Cycle Analysis kit (Beyotime, Shanghai, China, Beyotime, Shanghai, China, Catalog Number: C1052) in compliance with the manufacturer's instruction book. Then, cell proportion was measured at each phase through a flow cytometer (BD Biosciences, San Diego, CA, United States).

## TUNEL assay

According to the manufacturer's protocol, apoptotic DNA fragmentation was examined using the One Step TUNEL Apoptosis Assay kit (Beyotime Institute of Biotechnology, Haimen, China, Catalog Number: C1089). Briefly, cells were seeded into 24-well plates, respectively. Then, cells were fixed in 4% paraformaldehyde for 30 min at 4°C, permeabilized in 0.1% Triton X-100 for 2 min on ice, followed by the TUNEL assay for 1 h at 37°C. Cy3 (Cyanine 3)-labeled TUNEL-positive cells were imaged under a fluorescence microscope.

## Luciferase reporter gene

HEK293T *CAMTA1* KO cells ($6 \times 10^5$ cells/well) were cultured in 96-well plates and co-transfected with the control vector, *CAMTA1* overexpression vector, and the Renilla plasmid using Lipofectamine 3000 (Invitrogen, USA). The concentration of CAMTA1 overexpression vector is gradient-increasing from 0 to 100 ng. The procedure is performed according to the protocol of the kit (Catalog Number: MA0520-1). Firefly luciferase values were normalized to Renilla luciferase values, and the resulting ratios were used to express luciferase activities.

## Statistical analysis

We used SPSS 21.0 to perform statistical analysis. The distribution of variables was tested with the Kolmogorov Smirnov normal distribution test. Student's *t*-test or nonparametric test compared means of designated comparison groups.

# Results

## Characteristics of the patients included in the microarray analysis and validation

The population in Microarray: Total DNAs from the peripheral blood samples of three patients and three controls were extracted for the genomic DNA methylation assay. Table 1 presents the clinical characteristics of these six people (3 IS patients vs. 3 healthy controls). Compared to the control group, there were significant increases in TC, TG, and LDL levels and significant decreases in HDL levels in the IS group ($P < 0.01$), and no other significant differences were observed between these two groups.

The population of validation: Total DNA from the peripheral blood samples of 100 patients and 100 controls was extracted for the blood genomic DNA methylation assay. Table 2 lists the clinical characteristics of these 200 people (100 IS patients and 100 controls). TC, TG, LDL, and HDL levels were significantly different between these two groups. More details of these two groups can be seen in Supplementary Tables 1, 2.

TABLE 1 Characteristics of the patients included in the microarray analysis.

| Types | IS ($n = 3$) | Con ($n = 3$) | $t/\chi^2$-value | *P*-value |
|---|---|---|---|---|
| Gender (male/female) | 2/1 | 2/1 | - | - |
| Age (years) | 60.3 ± 9.5 | 65.6 ± 7.2 | −0.986 | 0.38 |
| Weight (kg) | 62.5 ± 7.3 | 68.6 ± 8.0 | 0.976 | 0.385 |
| MAP (mmHg) | 95.1 ± 13.7 | 102.3 ± 15.2 | 0.609 | 0.575 |
| BMI (kg/m$^2$) | 22.1 ± 4.3 | 24.9 ± 3.6 | 4.877 | 0.008 |
| Total cholesterol (mmol/L) | 7.55 ± 0.64 | 5.21 ± 0.53 | 0.929 | 0.405 |
| Blood sugar (mmol/L) | 6.930 ± 2.58 | 6.383 ± 2.89 | 0.245 | 0.819 |
| Triglyceride (mmol/L) | 3.581 ± 0.791 | 2.128 ± 0.169 | 3.111 | 0.036 |
| HDL (mmol/L) | 0.903 ± 0.252 | 1.422 ± 0.194 | 2.827 | 0.048 |
| LDL (mmol/L) | 3.834 ± 0.960 | 2.101 ± 0.683 | 2.938 | 0.042 |
| HbA1c (%) | 6.58 ± 1.74 | 6.13 ± 1.95 | 0.298 | 0.780 |

MAP, mean artery pressure; BMI, body mass index; LDL, low density lipoprotein; HDL, high density lipoprotein.

TABLE 2 Characteristics of the patients of the verification population.

| Types | ($n = 100$) | ($n = 100$) | $t/\chi^2$-value | *P*-value |
|---|---|---|---|---|
| Gender (male/female) | 55/45 | 58/42 | 0.183 | 0.669 |
| Age (years) | 61.3 ± 8.5 | 67.4 ± 7.8 | 0.083 | 0.934 |
| Weight (kg) | 69.5 ± 7.6 | 67.6 ± 8.5 | 1.82 | 0.07 |
| MAP (mmHg) | 102.3 ± 16.6 | 96.3 ± 12.8 | 2.858 | 0.005 |
| BMI (kg/m$^2$) | 23.3 ± 4.6 | 22.6 ± 4.3 | 1.112 | 0.268 |
| Total cholesterol (mmol/L) | 4.73 ± 0.55 | 5.50 ± 1.51 | 4.791 | 0.000 |
| Blood sugar (mmol/L) | 6.59 ± 2.58 | 6.17 ± 2.36 | 1.201 | 0.231 |
| Triglyceride (mmol/L) | 2.881 ± 0.531 | 3.958 ± 0.459 | 15.334 | 0.000 |
| Albumin (g/L) | 40.63 ± 4.73 | 39.38 ± 5.53 | 1.718 | 0.087 |
| HDL (mmol/L) | 1.243 ± 0.252 | 0.979 ± 0.194 | 8.301 | 0.000 |
| LDL (mmol/L) | 2.689 ± 0.570 | 3.156 ± 0.669 | 5.313 | 0.000 |

MAP, mean artery pressure; BMI, body mass index; LDL, low density lipoprotein; HDL, high density lipoprotein.

## Global changes in blood genomic methylation patterns in IS

We used Genome Studio V2018 software to report the β-values of 853,307 DNA methylation sites for the samples from the controls ($n = 3$) and the IS patients ($n = 3$) (Figure 1A). Statistical analysis revealed that 622 sites showed a difference in the degree of methylation; 502 sites were hypermethylated, and 120 sites were hypomethylated, with a ratio of 4:12. Manhattan map shows the distribution of methylation sites on chromosomes (Figure 1B).

Most hypomethylated sites were located on chromosomes 2, 5, 6, and 7, the most hypermethylated sites were on chromosomes 1, 2, and 6, and the most overall differentially methylated sites were located on chromosomes 1 and 6. The distribution of CpG sites in different regions of genes is shown in Supplementary Figures 2A,B.

Next, we carried out an analysis according to the functional domains of DNA. Two hundred and fifty-one sites (50%) situated within 1,500 bp upstream of the transcription start site (TSS 1500) among the hypermethylated sites, followed by 100 sites situated within 200 bp upstream of the transcription start site (TSS 200). Ninety-five sites (19%) were located at the gene bodies. In addition, the smallest percentage (0.02%) was in the 3′UTR for hypermethylated loci, while mostly hypomethylated loci had the smallest percentage in the first exon, 5′UTR and 3′UTR (0.04%) (Figure 1C).

Among the hypomethylated sites, 120 sites were located at gene bodies (50.0%), followed by 40 sites situated within 1,500 bp upstream of TSS (19.4%) and 40 sites at noncoding intergenic domains (19.4%) (Figure 1D).

When comparing the IS group to the control group, we observed that most of the hypermethylated loci (42.59%) were found in CpG sites, while most of the hypomethylated loci were in the open sea (70.57%) (Figure 1E). The smallest percentage (4.33%) of hypomethylated loci was in sites, compared to the smallest percentage of hypermethylated sites (3.06%) found on shores (Figure 1F). The distribution of DMCs according to the island regions of the hypomethylation and hypomethylation is shown in Supplementary Figures 1A,B.

## Bioinformatics analysis of differentially methylated genes of whole blood from IS patients

The differentially methylated sites were analyzed concerning known functional genes with the DAVID bioinformatics database. Among the 622 differentially methylated sites, the top 19 genes with the greatest extent of hypermethylation were *ABCA1, ADAMTSL5, COLgA2, ERCC5, TGFB1, ABCG1, ATP10A, CYP2E1, HOX4A, PCDHB7, ARL4C, SULF2, KLF11, ADARB2, GDFl5, CDHJ5, CAMTA1, SMG6*, and *RNFl44b* (Supplementary Figure 3). After analyzing the methylation detection data of the target region, especially the methylation level of the differential site, the methylation levels of the 19 candidate genes in different CpG sites are described in Table 3. *ABCA1, ADARB2, ATPI0A, CAMTA1, CDHI5, COL942,* and *TGFB1* have differences in the overall methylation level of CpG sites between the IS group and the healthy control group, and they are statistically significant (at the same time satisfying the triple test, that is, *T*-test *P*-value $< 0.05$, *U*-test *P*-value $< 0.05$ and logistic regression analysis *P*-value $< 0.05$). Among the above seven genes (marketed * in Table 3), the CpG site in the *CAMTA1* promoter region was hypermethylated in the IS case group. The CpG site of the promoter region of six genes, *ABCA1, ADARB2, ATPI0A,*

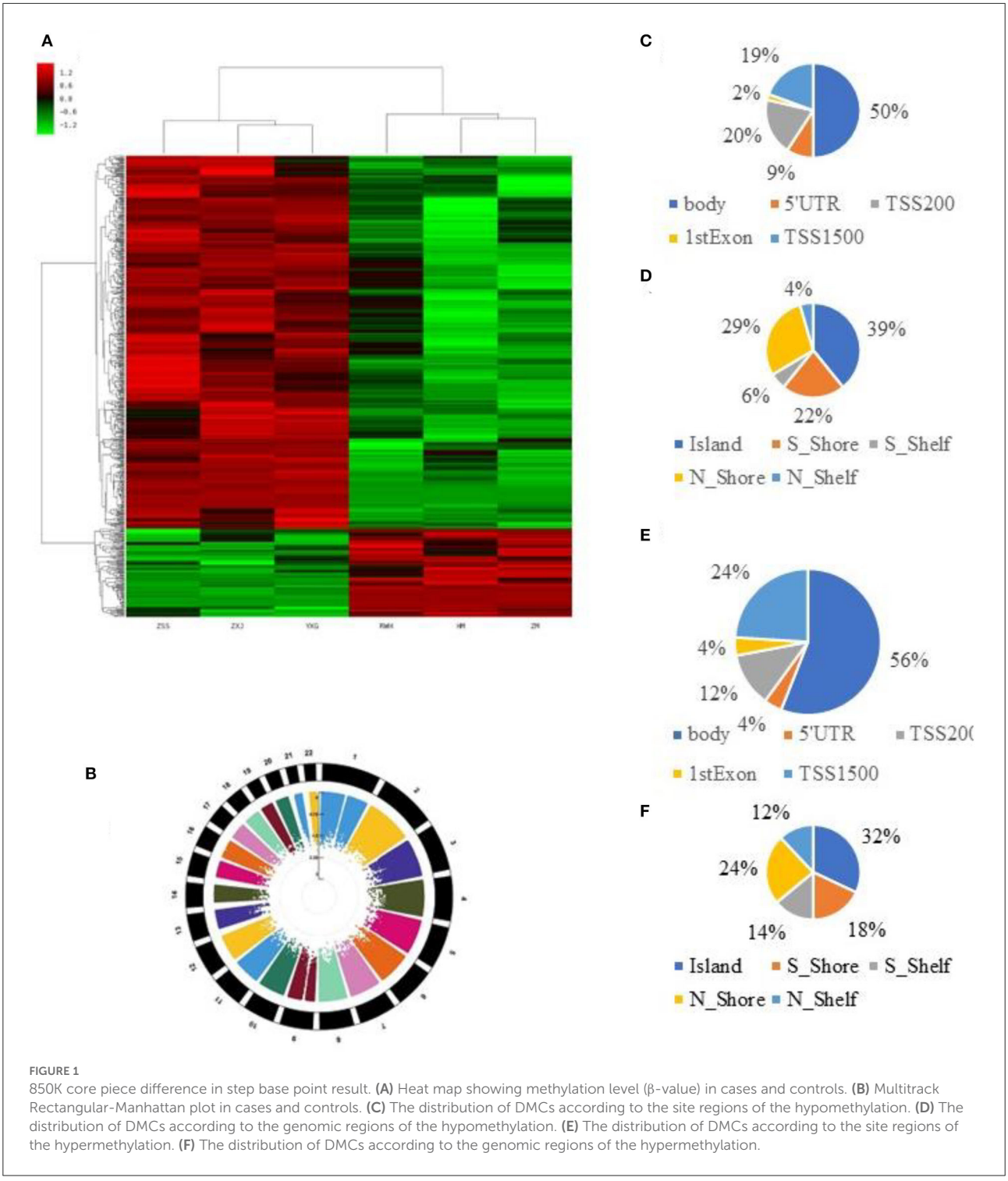


FIGURE 1
850K core piece difference in step base point result. **(A)** Heat map showing methylation level (β-value) in cases and controls. **(B)** Multitrack Rectangular-Manhattan plot in cases and controls. **(C)** The distribution of DMCs according to the site regions of the hypomethylation. **(D)** The distribution of DMCs according to the genomic regions of the hypomethylation. **(E)** The distribution of DMCs according to the site regions of the hypermethylation. **(F)** The distribution of DMCs according to the genomic regions of the hypermethylation.

*CDHI5*, *COL942*, and *TGFβ1*, was hypomethylated in the IS case group.

We undertook the gene ontology and pathway analysis of 502 differentially methylated sites to categorize them according to their biological functions and pathways. As Figures 2A,B show, the KEGG pathway analysis affiliated them with numerous pathways. The highest number of genes participated in Cell Adhesion Molecules (CAMs) (142 genes, $P = 0.0021$). Morphine addiction and the Hippo signaling pathway were involved in 92 ($P = 0.028$) and 154 ($P =$

TABLE 3 Genes with significant differences in CpG site methylation levels.

| Genes | *P*-value (*T*-test) | *R*-value (*U*-test) | *R*-value (logistic) | OR (L95-U95) (logistic) | Methyl diff |
|---|---|---|---|---|---|
| *ABCA1_1* | 0.1168 | 0.0876 | 0.1237 | 0.1100 (0.0066–1.8294) | −0.00121 |
| *ABCA1_2** | 0.0050* | 0.0032* | 0.0102* | 0.1234 (0.0246–0.6191) | −0.00425 |
| *ABCG1_1* | 0.3874 | 0.3107 | 0.3769 | 1.2366 (0.7720–1.9806) | 0.0045 |
| *ABCG1_2* | 0.7507 | 0.4457 | 0.7444 | 13221 (0.2467–7.0848) | 0.00037 |
| *4DAMTSL5J* | 0.0725 | 0.0682 | 0.0825 | 1.9938 (0.9149–4.3449) | 0.00586 |
| *ADA/fTSL5_2* | 0.1073 | 0.0391 | 0.1183 | 5.6142 (0.644148–0.9353) | 0.00165 |
| *ADARB_1** | 0.0161* | 0.0328* | 0.0299* | 0.0982 (0.0121–0.7982) | −0.00316 |
| *ADARB2_2* | 0.1428 | 0.0696 | 0.1456 | 0.4684 (0.686–1.3011) | −0.00301 |
| *ARL4C_1* | 0.7746 | 0.7473 | 0.7679 | 1.8657 (0.0296–117.429) | 0.00013 |
| *ARI,4C_2* | 0.1067 | 0.0732 | 0.1160 | 3.6092 (0.728247–0.8893) | 0.00221 |
| *ATPIOA_1** | 0.0264* | 0.0045* | 0.0415* | 0.0612 (0.0042–0.8992) | −0.00234 |
| *CAKfTAl1_1** | 0.0286* | 0.0348 | 0.Q387* | 247764.8000 (1.9042–32 238134221.0000) | 0.00042 |
| *CAMTAI_2* | 0.4899 | 0.2708 | 0.4799 | 0.0512 2 (0.0000–195.381) | −0.00017 |
| *CAMTAI_3* | 0.6222 | 0.8309 | 0.6109 | 0.4530 (0.0214–9.5705) | −0.00037 |
| *CAMTA1_4* | 0.7710 | 0.8287 | 0.7638 | 0.9715 (0.8043–1.1734) | −0.0033 |
| *CDH15_1** | 0.0408 | 0.0102 | 0.045 P | 0.8533 (0.7257–1.0035) | −0.03357 |
| *COL9A21** | 0.0151* | 0.0589 | 0.0253* | 0.0046 (0.0000–0.5159) | −0.00125 |
| *COL9A2_2* | *0.5745* | 0.8063 | 0.5655 | 0.8485 (0.4844–1.4861) | −0.00201 |
| *CYP2E1_1* | 0.1898 | 0.1760 | 0.1859 | 0.9616 (0.9074–1.0190) | −0.04958 |
| *CYP2E1_2* | 0.4219 | 0.4773 | 0.4116 | 0.9807 (0.9360–1.0275) | −0.03444 |
| *ERCC5_1* | 0.9926 | 0.3862 | 0.9925 | 0.9914 (0.1607–6.1143) | −0.0000098 |
| *ERCC5_2* | 0.4109 | 0.5268 | 0.4012 | 5.0355 (0.1155–219.515) | 0.00043 |
| *GDF15_1* | 0.5398 | 0.4304 | 0.5298 | 1.0709 (0.8649–1.3259) | 0.00572 |
| *H0XA4_1* | 0.1381 | 0.1258 | 0.1570 | 1.0787 (0.9713–1.1980) | 0.07174 |
| *HOXA4_2* | 0.0606 | 0.0927 | 0.0679 | 7.0837 (0.8654–57.9837) | 0.00192 |
| *KLFU_1* | 0.7047 | 0.6891 | 0.7038 | 1.0456 (0.8308–13160) | 0.00333 |
| *KLFU_2* | 0.4291 | 0.6146 | 0.4208 | 0.9219 (0.7563–1.1238) | −0.00810 |
| *KLFU_1* | 0.0952 | 0.1989 | 0.1045 | 1.0586 (0.9882–1.1340) | 0.05322 |
| *PCDHB7_1* | 3,606 | 0.3862 | 0.3534 | 0.9594 (0.8789–1.0472) | −0.02123 |
| *PCDHB7_1* | 0.3076 | 0.4006 | 0.2946 | 0.9154 (0.7758–1.0800) | −0.01267 |
| *RNF14-4B_1* | 0.0551 | 0.0451 | 0.0744 | 0.0263 (0.0005–1.4318) | −0.00119 |
| *SMG6_1* | 0.8594 | 0.7864 | 0.8550 | 0.5022 (0.0003–812.876) | −0.000047 |
| *SULF2_1* | 0.8628 | 0.8264 | 0.8586 | 0.8899 (0.2465–3.2125) | −0.00027 |
| *SULF2_2* | 0.1106 | 0.0980 | 0.1169 | 0.5068 (0.2167–1.1854) | −0.00406 |
| *SULF2_1* | 0.3171 | 0.0927 | 3,169 | 0.6329 (0.2583–1.5505) | −0.00238 |
| *TGFβ1** | 0.00/2* | 0.0006* | 0.0052* | 0.5052 (031270–0.863) | −0.01798 |

"OR(L95-U95) (Logistic)" means the OR value of the regression regression and 95% confidence interval: "MethylDif" means the degree of difference in methylation between the two groups-the average degree of methylation in the case group-the control group Average degree of methylation.

0.042) genes, respectively. The genes hypermethylated CpG mapped were involved in the Hippo signaling pathway (154 genes, $P = 0.014$), Dorso-ventral axis formation (27 genes, $P = 0.028$), and Arrhythmogenic Right Ventricular Cardiomyopathy (ARVC) (74 genes, $P = 0.032$). The hypomethylated genes were implicated in CAMs (142 genes, $P = 0.0008$), Allograft rejection (37 genes, $P = 0.005$), and Graft-vs.-host disease (41 genes, $P = 0.007$) (Figures 4D,E; Supplementary Tables 4, 5).

The GO pathway analysis results are presented in Supplementary Tables 6–8. GO enrichment analysis in the categories of cellular component (CC) revealed that 10 GO terms from CC were significantly enriched in patients (Figure 2D). The top three terms are listed as follows: (1) early endosome membrane; (2) MHC class I protein complex; (3) cell junction. Furthermore, homophilic cell adhesion *via* plasma membrane adhesion molecules, cell adhesion, and phospholipid translocation were the top three pathways in biological processing systems (BP pathways). The differentially methylated genes were arranged into 10 groups based on their molecular function (e.g., biochemical cascade) like calcium ion binding, phospholipid-translocating ATPase activity, and collagen binding.

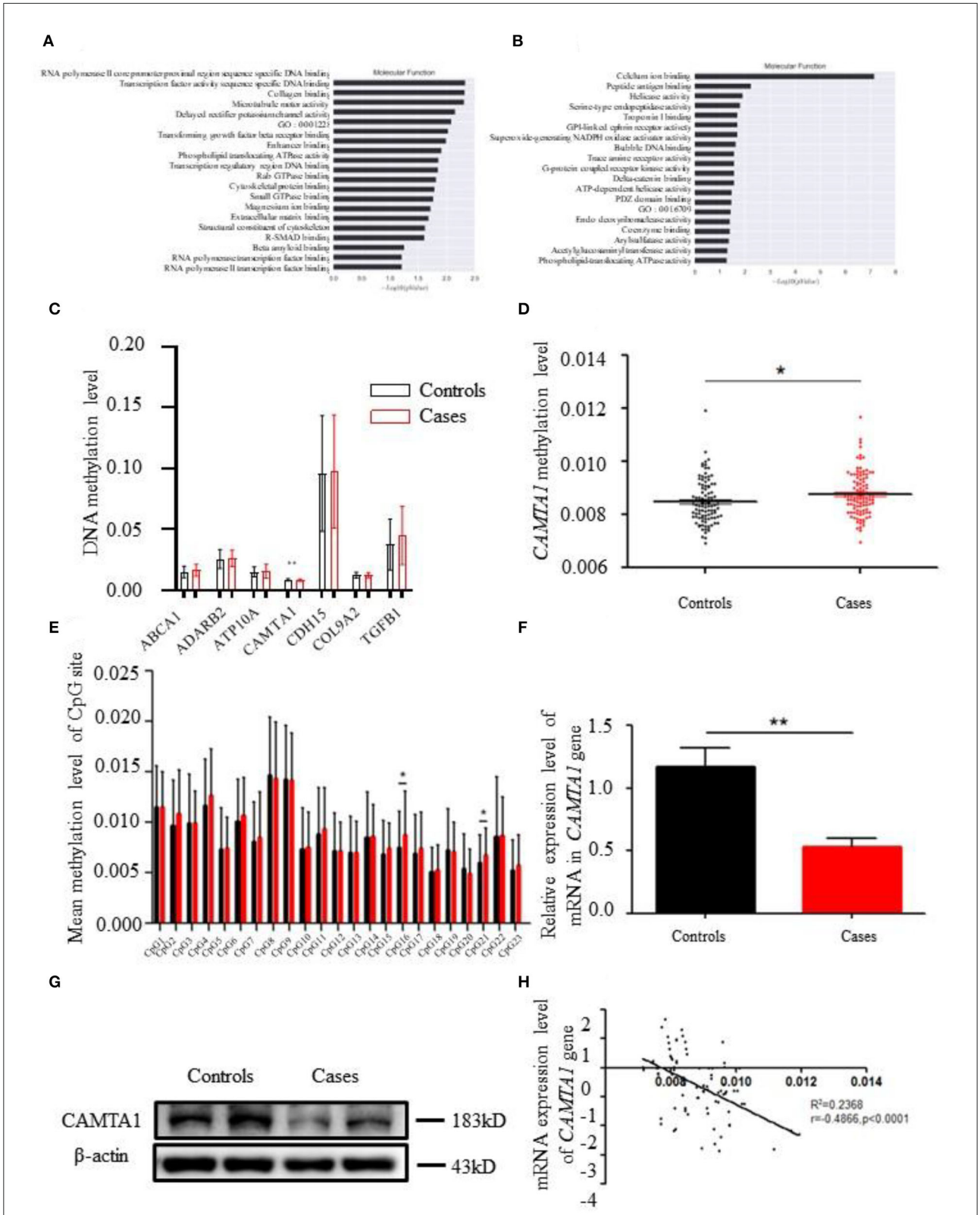


FIGURE 2
The bioinformatics results of 850K methylation microarray. **(A,B)** KEGG analysis results of different genes in cases and controls. **(C)** Comparison of DNA methylation differences of seven genes. **(D)** Methylation levels of *CAMTA1* gene in cases and controls (*$P < 0.05$). **(E)** Comparison of the average methylation levels of 23 CpG sites in the *CAMTA1* gene promoter region between two groups (*$P < 0.05$). **(F)** *CAMTA1* mRNA expression in the expanded population (**$P < 0.01$). **(G)** CAMTA1 protein expression in patients and healthy people. **(H)** Correlation between *CAMTA1* gene expression level and methylation level.

10.3389/fncel.2022.868291

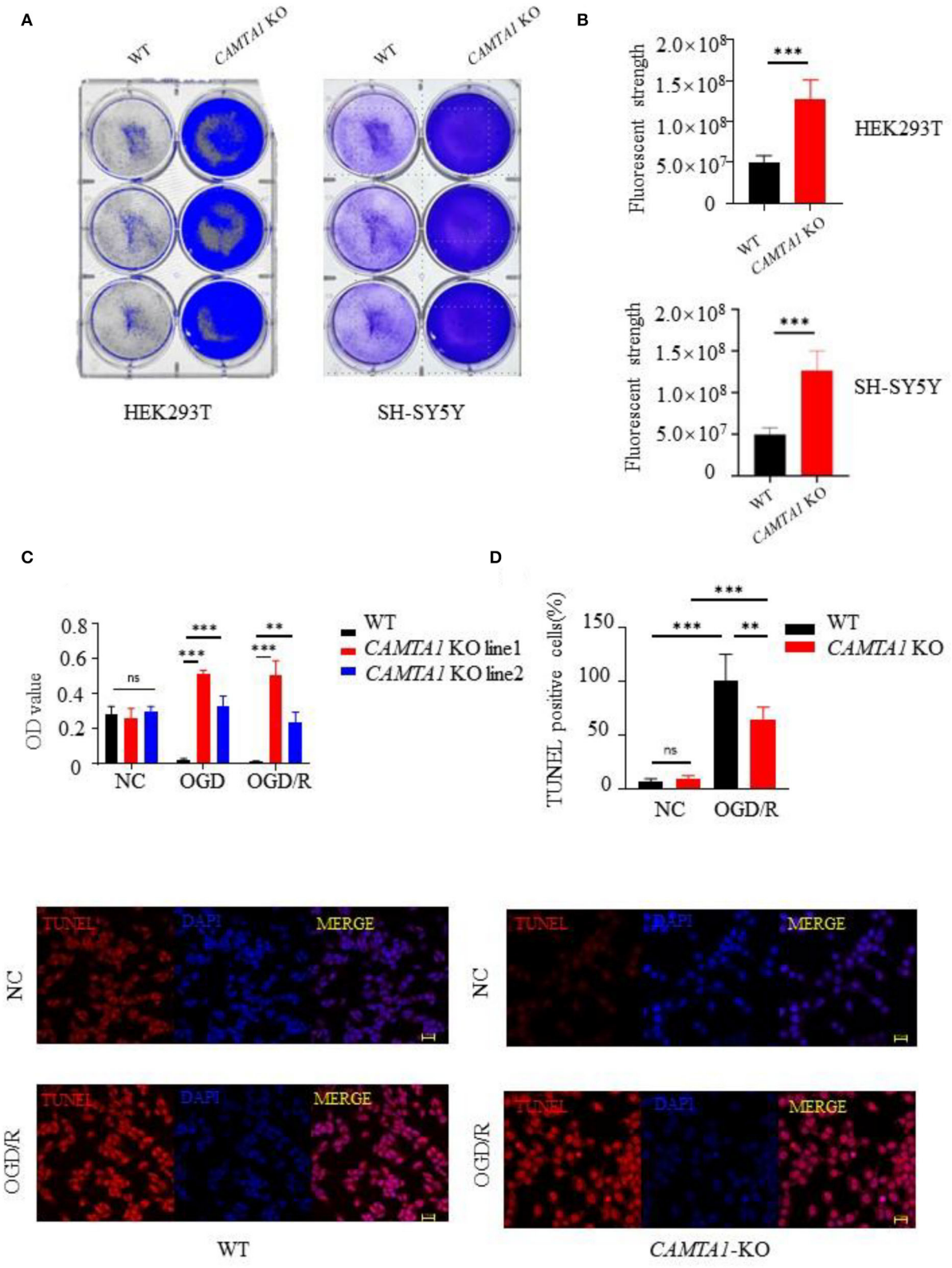


FIGURE 3
*CAMTA1* KO influences cell proliferation. **(A,B)** Gentian Violet staining shows differences in cell proliferation in HEK293T and SH-SY5Y cell lines (**$P < 0.01$, ***$P < 0.001$). **(C)** Relative viabilities of HEK293T and SH-SY5Y cells after incubation with OGD/R treatments (**$P < 0.01$). **(D)** Cell apoptosis was detected by TUNEL staining (*$P < 0.05$, **$P < 0.01$, ***$P < 0.001$). ns stand for not statistically different.

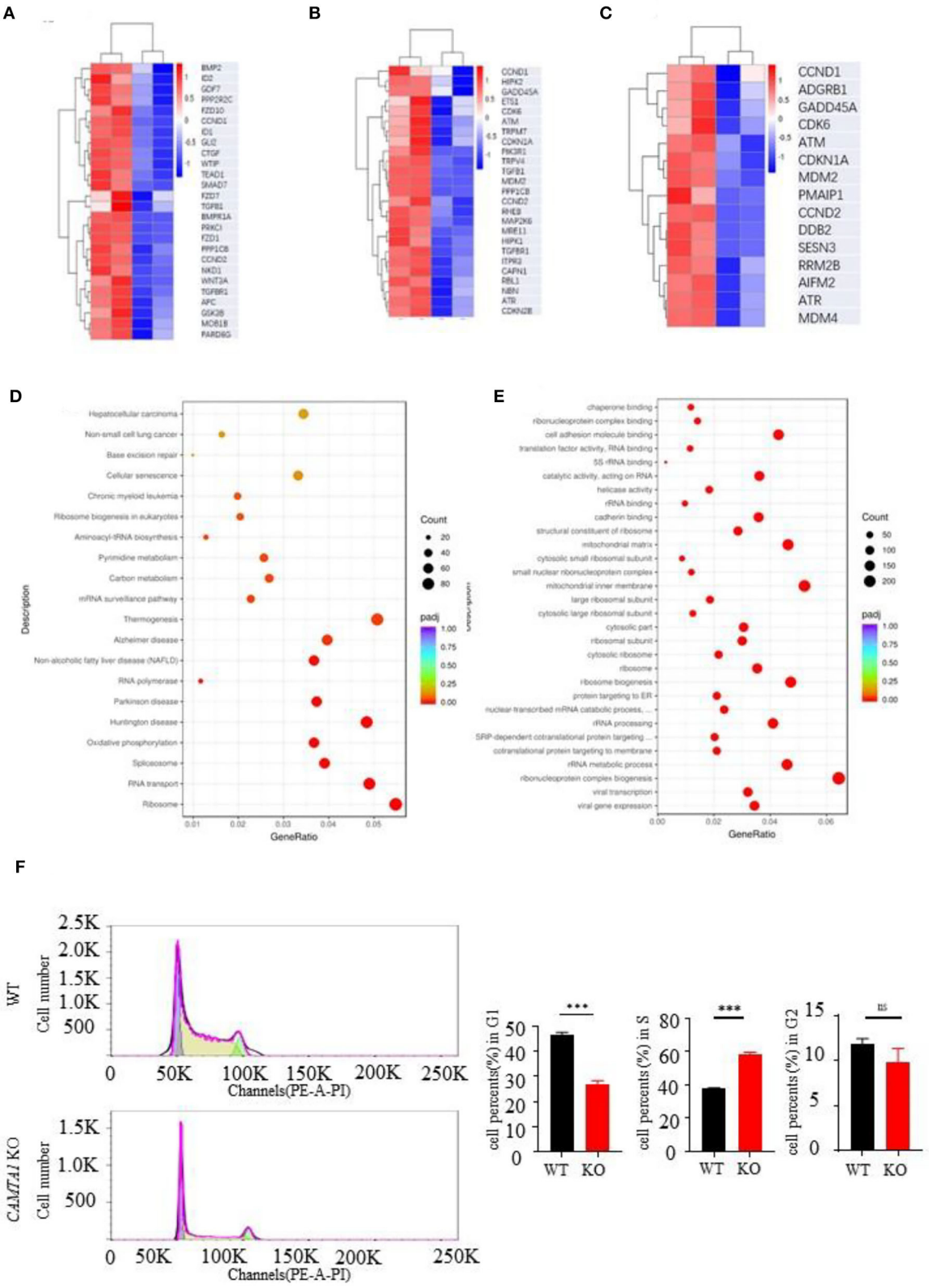


FIGURE 4
RNA seq results of *CAMTA1* KO SH-SY5Y cell lines and WT cell lines. **(A–C)** Heatmap of P53 relative genes, senescence genes, and Hippo pathways of the RNA seq in *CAMTA1* KO SH-SY5Y cell lines. **(D)** Bubble plot shows the significant GO pathways involved by the *CAMTA1* KO SH-SY5Y cell lines. **(E)** Bubble plot shows the significant KEGG pathways involved by the *CAMTA1* KO SH-SY5Y cell lines. **(F)** Flow cytometry histograms of actively dividing and quiescent cells. The percent of cells in each cell cycle phase is shown above the peaks (**$P < 0.01$, ***$P < 0.001$). ns stand for not statistically different.

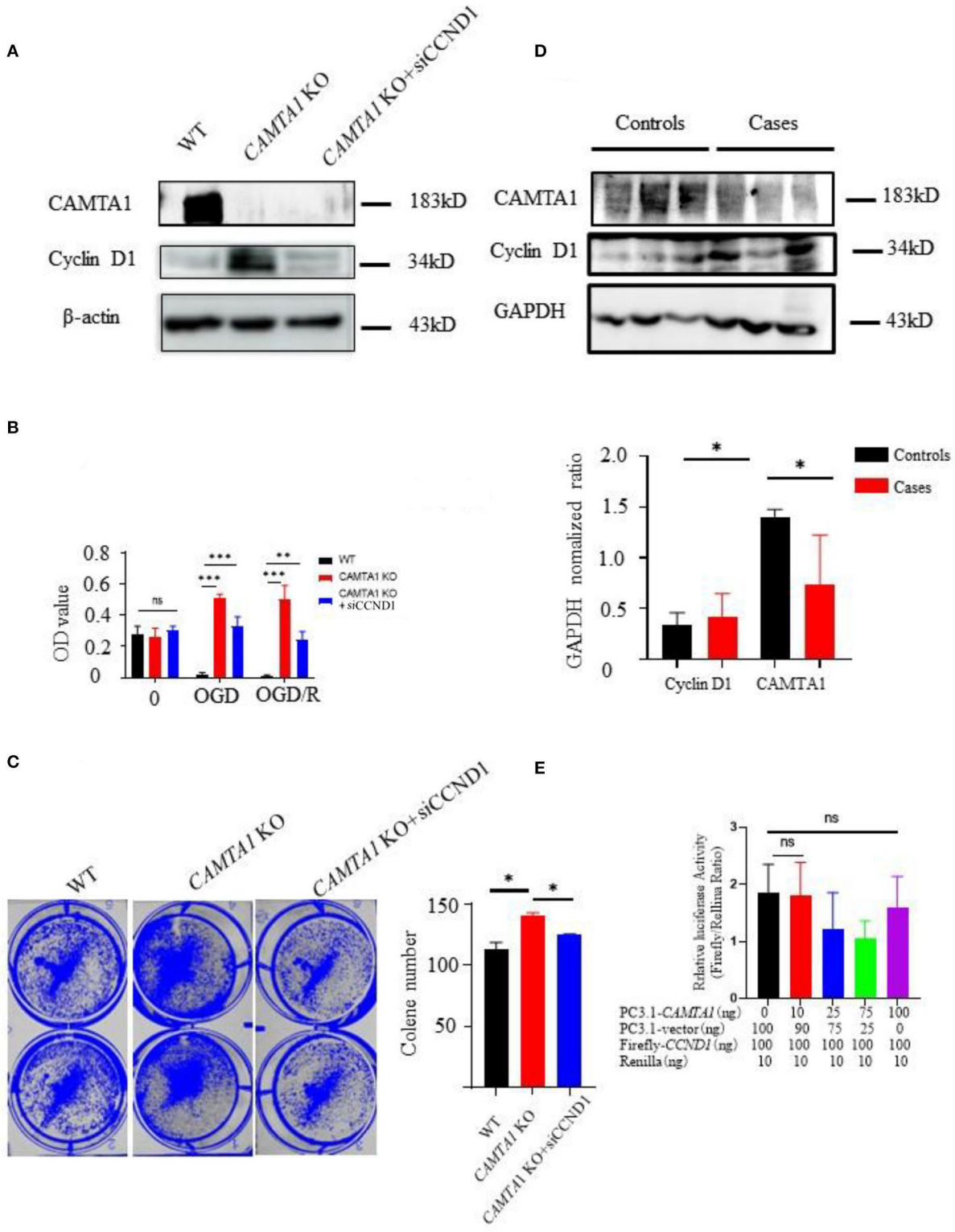


FIGURE 5
The downregulation of *CAMTA1* could promote cyclin D1 expression. **(A)** CAMTA1 and cyclin D1 expressions in different SH-SY5Y cell lines. **(B)** Relative cell viabilities in different SH-SY5Y cell lines after incubation with OGD/R treatments (**$P < 0.01$). **(C)** Gentian Violet staining shows differences in cell proliferation after the treatment in different SH-SY5Y cell lines (**$P < 0.01$, ***$P < 0.001$). **(D)** CAMTA1 and cyclin D1 expressions in IS patients. **(E)** In HEK293T KO cell, the effect of CAMTA1 on *CCND1* transcriptional activity was evaluated using a luciferase reporter assay. (Statistical analysis of 3–6 independent experiments under each condition is shown in the column chart, and the error bar indicates ± 1 SD. *$p < 0.05$). ns stand for not statistically different.

## Validation of the differentially methylated CpG Loci in *CAMTA1*

After analyzing the methylation detection data of the target region, especially the methylation level of the differential site, the methylation levels of the 19 candidate genes in different CpG sites were validated. *ABCA1, ADARB1, ATP10A, CAMTA1, CDH15, COL9A2,* and *TGFβ1* were the top seven genes having significantly different methylation levels (Figure 2C). The *CAMTA1* gene presents the most different hypermethylation levels between the two groups (Figure 2D).

Next, we explored the most common methylation sites of *CAMTA1*, located on Chr1. We screened out a CpG site in the promoter region of the *CAMTA1* gene through website prediction. The sequence of this region is as follows, with a total of 23 CpG sites, marked in red:
GACTCATGGTTGCCTGTCCCAGGATGAGGCCGCCGGC
CGAAAGCAGAGAAGCGCCAGCCCCGGCCGCCCGGGT
GGAGCGCTGGGCAGCCGAGTTTCCCACCCTCCTCAA
TCCGGAGAGTCCGCGCGGGGCTTTTCCTAATAAATA
GCCAGGCACCCGCTGCCCTCGCGCTGCGTACGGAGC
ACGTGCCCCCCGGGAGGTGGGCGCCCGCCAGGTGCC
CGAACGAGCCTAGGAACCGGGTCGGGAACGAGCCTAG
GAACCGGGTC.

We compared mean methylation levels at 23 CpG sites in the promoter region of the *CAMTA1* gene in the control and case groups. In the *CAMTA1* display, 16 CpG and 21 CpG sites showed a significant difference ($P < 0.05$; Figure 2E). We found elevated methylation levels in the promoter region of the *CAMTA1* gene in ischemic stroke patients, at the same time with decreased *CAMTA1* mRNA expression (Figure 2F). As a consequence, its protein level was also reduced in IS patients (Figure 2G). To validate the correlation of DNA methylation with gene expression, we analyzed the Pearson correlation between the degree of methylation in the promoter region of the *CAMTA1* gene and its corresponding *CAMTA1* mRNA expression level ($P < 0.0001$; Figure 2H).

## *CAMTA1* knockout accelerated cell proliferation and inhibited apoptosis

To investigate the CAMTA1 function implicated in stroke, we did knockout *CAMTA1* gene in HEK 293T and SH-SY5Y cell lines by Crisper/Cas9 (Supplementary Figure 1D). The qPCR results showed that the mRNA of *CAMTA1* had decreased successfully (Supplementary Figure 1E). The HEK 293T cells are a well-established tool. Moreover, the SH-SY5Y cell line was selected because it has a higher expression of *CAMTA1* mRNA compared to other neural cells (Supplementary Figure 1C). The staining of cells with crystal violet dye showed that the number of staining cells significantly increased in both *CAMTA1*-KO cells (Figures 3A,B) due to the accelerated cell proliferation (Figure 3C). Furthermore, the TUNEL assay demonstrated that decreased *CAMTA1* protected cells from oxygen-glucose deprivation/reperfusion (OGD/R) injury, and the TUNEL positive cells decreased in *CAMTA1*-KO cells compared after OGD/R (Figure 3D). Taken together, these results indicate that decreased *CAMTA1* levels could influence OGD/R injury.

## The transcriptomic study found that *CCND1* was upregulated in SH-SY5Y *CAMTA1*-KO cell line

Next, we used the RNA-seq approach to analyze the transcriptomes of two cell lines :SH-SY5Y and HEK293T. The genes having different expression levels in two cell lines are shown in Supplementary Table 9. We performed GO term and KEGG pathway enrichment analysis to analyze this signature further. From the KEGG enrichment results, it listed the top six KEGG pathways of the hypermethylated genes: focal adhesion (31 genes, $P = 0.0076$), Hippo signaling pathway (26 genes, $P = 0.0076$), cellular senescence (25 genes, $P = 0.0121$), p53 signaling pathway (15 genes, $P = 0.0202$), chronic myeloid leukemia (15 genes, $P = 0.0308$) and ECM-receptor interaction (14 genes, $P = 0.0446$). The pathways of hypomethylated genes are Ribosome (94 genes, $P = 0.0076$), Huntington's disease (81 genes, $P < 0.0001$), Parkinson's disease (63 genes, $P < 0.0001$), Oxidative phosphorylation (60 genes, $P < 0.0001$), RNA transport (63 genes, $P < 0.0001$), and Spliceosome (53 genes, $P < 0.0001$).

The GO analysis results are shown in the Supplementary materials. We expected to find some pathways to explain the excessive proliferation of the *CAMTA1* KO cells. The heat map of the genes involved in the Hippo signaling pathway, cellular senescence pathways, and p53 signaling pathway is presented in Figures 4A–C. The heat map of the whole genes is shown in Figures 4D,E. These results revealed that the *CCND1* gene was upregulated and implicated in all these pathways. Interestingly, the cell cycle analysis by flow cytometry (Figure 4F) demonstrated that more SH-SY5Y *CAMTA1*-KO cells entered the S phase. As we know, the *CCND1* gene codes cyclin D1 is an important cell cycle regulator that controls the transition from G1 to the S phase. Meanwhile, many studies in mouse models and different neural cell lines demonstrated that cyclin D1 level was increased under ischemic stress conditions. Therefore, we suppose that CAMTA1 could regulate cyclin D1, and through this intermediate CAMTA1 could play a role in stroke.

## CAMTA1 may regulate cyclin D1 to control the cell cycle

Next, the new cell line was generated in SH-SY5Y *CAMTA1* KO cells with si*CCND1* (Figure 5A). The result of the CCK-8 assay demonstrated that decreased expression of the cyclin D1 reduced cell viabilities compared to SH-SY5Y *CAMTA1* KO cells (Figure 5B). The crystal violet staining was consistent with the cell viability data (Figure 5C). The results illustrated that cyclin D1 regulates cell proliferation induced by decreased CAMTA1. We also checked the cyclin D1 expression in IS patients (Figure 5D). Their expression is markedly elevated in patients having lower CAMTA1 levels. The results suggested that CAMTA1 controlled the cell cycle by regulating cyclin D1 expression in IS. As CAMTA1 is a transcription activator, a dual luciferase reporter assay was generated to investigate whether CAMTA1 directly regulates cyclin D1 expression. In HEK293T cells, the Firefly/Renilla ratio was not significantly changed with different expressions of CAMTA1, compared to without CAMTA1 (Figure 5E; Supplementary Figure 2F). It demonstrated that CAMTA1 could not directly affect the *CCND1* promoter region. There may be an intermediary between them.

# Discussion

Emerging evidence indicates that DNA methylation plays a role in the pathogenesis of IS. In this context, we analyzed the genome methylation levels from the peripheral blood samples of IS patients and healthy controls using an 850K Bead Chip. Out of the 622 CpG sites showing differential methylation, 80.4% (502 sites) exhibited hypermethylation, and 19.6% (122 sites) indicated hypomethylation, which suggests sufficient differences in the DNA methylation between patients and controls. These different sites were traced to 278 genes. According to our GO analysis and KEGG pathway analysis, they are mainly involved in the following pathways and functions: adhesion of cell membrane, adhesion molecules to homophilic cells, cell adhesion, phospholipid transport, neurogenesis regulation, calcium ion binding, collagen-binding, and sugar metabolism. All these pathways and functions have been previously reported to be related to the ischemic stroke (Love, 2003; Wen et al., 2005; Zündorf and Reiser, 2011; Zhao et al., 2020).

A disadvantage of our experience is the sample size ($n = 3$); we verified the top 19 differentially methylated genes: *ABCA1, ADAMTSL5, COL9A2, ERCC5, TGFBI, ABCG1, ATP104, CYP2EI, HOX44, PCDHB7, ARL4C, KLFI1, SULF2, ADARB2, GDFI5, CDHI5, CAMTAI, SMG6*, and *RNF144b*. Several DNA methylation modifications in the pathogenesis of IS have been investigated in the past few years. For example, the study in the middle cerebral artery occlusion (MCAO) in a rat model showed DNA methylation level of Na-K-Cl cotransporter 1 (NKCC1) was decreased (Lagarde et al., 2015). Hu et al. found the hypermethylation of thrombospondin 1 (THBS1), an angiostatic factor implicated in platelet aggregation, in an *in vitro* model of stroke. IS patients presented high plasma homocysteine levels associated with DNA hypermethylation of the thrombomodulin (TM) (Stanzione et al., 2020). Hypermethylation of cyclin-dependent kinase inhibitor 2B (CDKN2B), a gene involved in the pathogenesis of calcification, was also demonstrated to relate to calcification of the arteries in patients with IS (Unzeta et al., 2021). Baccarelli et al. suggested that the association between the hypomethylation of long interspersed nucleotide elements (LINE-1) and vascular cell adhesion protein 1 (VCAM-1) expression could be an early event in the etiology of cerebrovascular diseases, including IS (Lee et al., 2010). All these 19 genes have never been reported in the IS field. Although they could be new candidate genes related to the occurrence and development of stroke, we cannot rule out the possibility that this is just one bias from our experiment. Even though blood is commonly used in epigenomic studies, its heterogeneous nature leads to interpretation difficulties. For future research on defining their specific role in IS, we could verify their differential methylation levels from a selected single cell type, for example, lymphocytes.

We took CAMTA1 as the first candidate to be explored because its methylation markedly differs between patients and controls. Recently, Shen et al. also identified methylation modification of the *CAMTA1* gene in more than 400 IS patients (Shen et al., 2019). Furthermore, our MetylTarget analysis found that the methylation levels of CpG16 and CpG21 at the two sites in the IS group were significantly higher than those in the healthy control. It suggests that the hypermethylation of the *CAMTA1* gene promoter might relate to ischemic stroke.

*CAMTA1* gene was identified in 2003 as a candidate for tumor suppressor in neuroblastoma (Henrich et al., 2006). The following year, Nakatani et al. investigated the relationship between *CAMTA1* expression and cell cycle progression in N-type neuroblastoma SK-N-SH cells. They suggested that CAMTA1 could play a role in cell cycle regulation. Many studies examined its functions in various tumor cells, including breast cancer, colon cancer, pheochromocytoma, neuroblastoma, and glioma. The results showed that CAMTA1 could regulate tumor proliferation as an antitumor gene (Katoh and Katoh, 2003; Kim et al., 2006; Baccarelli et al., 2010a; Juhlin et al., 2015; Lu et al., 2018). Genetic studies of the WWTR1 (a protein known as TAZ)-CAMTA1 were well established in epithelioid hemangioendothelioma (EHE), a malignant vascular cancer. This discovery led *WWTR1-CAMTA1* fusions to become useful diagnostic markers for EHE (He et al., 2021). The mechanistic basis of the oncogenic functions of the TAZ-CAMTA1(TC) fusion protein has been distinctly defined. The fusion of CAMTA1 drove the constitutive nuclear localization to TAZ, and they escaped from the Hippo pathway regulation, rendering it constitutively active (Asgharzadeh et al., 2012).

Consequently, cells expressing TC oncoprotein display a TAZ-like transcriptional program that causes resistance to oncogenic transformation (Phurailatpam et al., 2015). More recently, He et al. demonstrated that CAMTA1 could regulate proliferation and the cell cycle in glioma by inhibiting AKT phosphorylation (He et al., 2021). Nevertheless, the function of CAMTA1 in neurological diseases is largely unknown. Just a few studies reported that the CAMTA1 gene had been associated with neonatal neuroblastoma, ataxia (Phurailatpam et al., 2015), and sporadic amyotrophic lateral sclerosis (Liang et al., 2020).

Our research focused on studying the function of CAMTA1 in strokes. The results showed that knockout of the *CAMTA1* gene in SH-SY5Y cells increased the proliferation and reduced the apoptosis after oxygen-glucose deprivation/reoxygenation, and more cells entered the S phase. The results revealed that the cell cycle was dysregulated in CAMTA1 KO cells. Our findings were consistent with the previous studies on tumor cells. CAMTA1 also plays an essential role in cell cycle regulation in strokes. We examined the changes of the mRNA and protein expression under CAMTA1 deletion to clarify its mechanisms in strokes. The *CCND1* mRNA and its protein cyclin D1 expression were significantly increased in *CAMTA1* KO cells. The functions of cyclin D1 are known for regulating the cell cycle's progression through the G1 to S phase (Fu et al., 2004). Increasing evidence demonstrates that dysregulation of cell cycle machinery is implicated in strokes. Significantly, many studies reported that cyclin D1 levels are increased in models of cerebral ischemia (Cai et al., 2009; Baccarelli et al., 2010b; Zhou et al., 2016). Our data suggest CAMTA1 could implicate IS through increasing cyclin D1. As we know, cyclin D1 could be regulated by different signal pathways, like the Hippo pathway, Jak/Stat pathway, etc. Our results established for the first time the link between CAMTA1 and cyclin D1. However, the dual-luciferase assay showed that there might not be a direct link between them. It is supposed that CAMTA1 could affect one intermediary protein that induces the cyclin D1 expression. *CCND1* gene is a downstream transcriptional target of the Hippo pathway, which was affected in SH-SY5Y CAMTA1 KO cells. One possibility is that a specific protein implicated in the Hippo signaling pathways could be regulated by CAMTA1. One limitation in our work is that we used SH-SY5Y cells, which is broadly studied for elucidating molecular mechanism in IS pathogenesis field. It's a neuroblastoma cell line, and we should explore the effect of CAMTA1 in a mouse model. CAMTA1 is principally expressed in the brain. For future study, we could decrease the expression of CAMTA1 in mouse brain and then study its effect under ischemic stress conditions.

In conclusion, (1) our study helped identify new candidate genes for the pathogenesis of IS. We found 19 genes with significant DNA methylation modifications in IS patients. All of them are involved in the pathways related to stroke. However, the sample size is our limitation. In future studies, this result should be validated using a large-scale sample size and selecting a single cell type (to avoid the bias due to the heterogeneous compositions from blood samples), and then define their specific functions in strokes. (2) Out of 19 genes, we concentrated on studying the role of CAMTA1 in Stroke because of its most different DNA methylation levels between healthy people and IS patients. Cell experiences demonstrated that CAMTA1 could affect cell proliferation and cell cycle in normal conditions or in the OGD/R model. (3) Moreover, decreased CAMTA1 could raise cyclin D1 levels. Our results showed for the first time that CAMTA1 plays a role in strokes by regulating cyclin D1, which increased under ischemic stress conditions. However, the mechanism by which CAMTA1 regulates cyclin D1 is presently unclear. As our result shows, there is no direct link between them; identifying their intermediary using a different neuron cell line and in vivo models could form part of future studies.

## Data availability statement

The datasets presented in this study can be found in online repositories. The names of the repository/repositories and accession number(s) can be found below: https://www.ncbi.nlm.nih.gov/geo/ GSE197080, GSE197081, and GSE205687.

## Ethics statement

The studies involving human participants were reviewed and approved by the Institutional Ethics Board of The First Affiliated Hospital of the Henan University of Chinese Medicine. The patients/participants provided their written informed consent to participate in this study.

## Author contributions

HZ and YHe designed the experiments. YLi and GS carried out most of the experiments. JJ, XZ, and FL analyzed the experimental results. CZ and YLi wrote the manuscript. ZL, YX, ZZ, SY, BZ, YLu, YHu, YP, and TH participated in the discussion of this project. All authors contributed to the article and approved the submitted version.

## Funding

This study was supported by the National Natural Science Foundation of China (Nos. U2004114 and 81571154).

## Conflict of interest

The authors declare that the research was conducted in the absence of any commercial or financial relationships that could be construed as a potential conflict of interest.

## Publisher's note

All claims expressed in this article are solely those of the authors and do not necessarily represent those of their affiliated organizations, or those of the publisher, the editors and the reviewers. Any product that may be evaluated in this article, or claim that may be made by its manufacturer, is not guaranteed or endorsed by the publisher.

## Supplementary material

The Supplementary Material for this article can be found online at: https://www.frontiersin.org/articles/10.3389/fncel.2022.868291/full#supplementary-material

## References


Asgharzadeh, S., Salo, J. A., Ji, L., Oberthuer, A., Fischer, M., Berthold, F., et al. (2012). Clinical significance of tumor-associated inflammatory cells in metastatic neuroblastoma. *J. Clin. Oncol.* 30, 3525–3532. doi: 10.1200/JCO.2011.40.9169

Baccarelli, A., Tarantini, L., Wright, R. O., Bollati, V., Litonjua, A. A., Zanobetti, A., et al. (2010a). Repetitive element DNA methylation and circulating endothelial and inflammation markers in the VA normative aging study. *Epigenetics*. 5, 222–228. doi: 10.4161/epi.5.3.11377

Baccarelli, A., Wright, R., Bollati, V., Litonjua, A., Zanobetti, A., Tarantini, L., et al. (2010b). Ischemic heart disease and stroke in relation to blood DNA methylation. *Epidemiology*. 21, 819–828. doi: 10.1097/EDE.0b013e3181f20457

Cai, K., Di, Q., Shi, J., and Zhang, Y. (2009). Dynamic changes of cell cycle elements in the ischemic brain after bone marrow stromal cells transplantation in rats. *Neurosci. Lett.* 467, 15–19. doi: 10.1016/j.neulet.2009.09.052

Deng, G. X., Xu, N., Huang, Q., Tan, J. Y., Zhang, Z., Li, X. F., et al. (2019). Association between promoter DNA methylation and gene expression in the pathogenesis of ischemic stroke. *Aging*. 11, 7663–7677. doi: 10.18632/aging.102278

Dock, H., Theodorsson, A., and Theodorsson, E. D. N. A. (2015). Methylation inhibitor zebularine confers stroke protection in ischemic rats. *Transl. Stroke Res.* 6, 296–300. doi: 10.1007/s12975-015-0397-7

Feigin, V. L., Norrving, B., and Mensah, G. A. (2017). Global burden of stroke. *Circ. Res.* 120, 439–448. doi: 10.1161/CIRCRESAHA.116.308413

Feinberg, A. P. (2007). Phenotypic plasticity and the epigenetics of human disease. *Nature*. 447, 433–440. doi: 10.1038/nature05919

Fogh, I., Lin, K., Tiloca, C., Rooney, J., Gellera, C., Diekstra, F. P., et al. (2016). Association of a locus in the CAMTA1 gene with survival in patients with sporadic amyotrophic lateral sclerosis. *JAMA Neurol.* 73, 812–820. doi: 10.1001/jamaneurol,.2016.1114

Fu, M., Wang, C., Li, Z., Sakamaki, T., and Pestell, R. G. (2004). Minireview: cyclin D1: normal and abnormal functions. *Endocrinology*. 145, 5439–5447. doi: 10.1210/en.2004-0959

GBD 2016 Stroke Collaborators (2019). Global, regional, and national burden of stroke, 1990-2016: a systematic analysis for the Global Burden of Disease Study. *Lancet Neurol.* 18, 439–458. doi: 10.1016/S1474-4422(19)30034-1

Giralt-Steinhauer, E., Jiménez-Conde, J., Soriano Tárraga, C., Mola, M., Rodríguez-Campello, A., Cuadrado-Godia, E., et al. (2014). Exploring the genetic basis of stroke. Spanish stroke genetics consortium. Neurologia. 29, 560–566. doi: 10.1016/j.nrleng.2013.04.004

He, Z., Yang, C., He, Y., Gong, B., Yin, C., Feng, J., et al. (2021). CAMTA1, a novel antitumor gene, regulates proliferation and the cell cycle in glioma by inhibiting AKT phosphorylation. *Cell. Signal.* 79, 109882. doi: 10.1016/j.cellsig.2020.109882

Henrich, K., Fischer, M., Mertens, D., Benner, A., Wiedemeyer, R., Brors, B., et al. (2006). Reduced expression of CAMTA1 correlates with adverse outcome in neuroblastoma patients. *J. Clin. Cancer*. 12, 131–1388. doi: 10.1158/1078-0432.Ccr-05-1431

Juhlin, C. C., Stenman, A., Haglund, F., Clark, V. E., Brown, T. C., Baranoski, J., et al. (2015). Whole-exome sequencing defines the mutational landscape of pheochromocytoma and identifies KMT2D as a recurrently mutated gene. *Genes Chromos. Cancer*. 54, 542–554. doi: 10.1002/gcc.22267

Katchanov, J., Harms, C., Gertz, K., Hauck, L., Waeber, C., Hirt, L., et al. (2001). Mild cerebral ischemia induces loss of cyclin-dependent kinase inhibitors and activation of cell cycle machinery before delayed neuronal cell death. *J. Neurosci.* 21, 5045–5053. doi: 10.1523/JNEUROSCI.21-14-05045.2001

Katoh, M., and Katoh, M. (2003). Identification and characterization of FLJ10737 and CAMTA1 genes on the commonly deleted region of neuroblastoma at human chromosome 1p36.31-p36.23. *Int. J. Oncol.* 23, 1219–1224. doi: 10.3892/ijo.23.4.1219

Kim, M. Y., Yim, S. H., Kwon, M. S., Kim, T. M., Shin, S. H., Kang, H. M., et al. (2006). Recurrent genomic alterations with impact on survival in colorectal cancer identified by genome-wide array comparative genomic hybridization. *Gastroenterology*. 131, 1913–1924. doi: 10.1053/j.gastro.2006.10.021

Lagarde, M., Hachem, M., Bernoud-Hubac, N., Picq, M., Véricel, E., Guichardant, M., et al. (2015). Biological properties of a DHA-containing structured phospholipid (AceDoPC) to target the brain. *Prostaglandins Leukot Essent Fatty Acids*. 92, 63–65. doi: 10.1016/j.plefa.2014.01.005

Lee, H. A., Hong, S. H., Kim, J. W., and Jang, I. S. (2010). Possible involvement of DNA methylation in NKCC1 gene expression during postnatal development and in response to ischemia. *J. Neurochem.* 114, 520–529. doi: 10.1111/j.1471-4159.2010.06772.x

Liang, Y., Rong, X., Luo, Y., Li, P., Han, Q., Wei, L., et al. (2020). Corrigendum to "A novel long non-coding RNA LINC00355 promotes proliferation of lung adenocarcinoma cells by down-regulating miR-195 and up-regulating the expression of CCNE1." *Cell Signal.* 66, 109462. doi: 10.1016/j.cellsig.2019.109462

Long, C., Grueter, C. E., Song, K., Qin, S., Qi, X., Kong, Y. M., et al. (2014). Ataxia and Purkinje cell degeneration in mice lacking the CAMTA1 transcription factor. *Proc. Natl. Acad. Sci. U. S. A.* 111, 11521–11526. doi: 10.1073/pnas.1411251111

Love, S. (2003). Neuronal expression of cell cycle-related proteins after brain ischaemia in man. *Neurosci. Lett.* 353, 29–32. doi: 10.1016/j.neulet.2003.09.004

Lu, P., Gu, Y., Li, L., Wang, F., Yang, X., Yang, Y., et al. (2018). Long noncoding RNA CAMTA1 promotes proliferation and mobility of the human breast cancer cell line MDA-MB-231 *via* targeting miR-20b. *Oncol. Res.* 26, 625–635. doi: 10.3727/096504017X14953948675395

Morgado-Pascual, J. L., Marchant, V., Rodrigues-Diez, R., Dolade, N., Suarez-Alvarez, B., Kerr, B., et al. (2018). Epigenetic modification mechanisms involved in inflammation and fibrosis in renal pathology. *Mediators Inflamm.* 2018, 2931049. doi: 10.1155/2018/2931049

Phurailatpam, R., Agarwal, P., Paul, S. N., and Sv, J. (2015). In regard to the paper: patient performance-based plan parameter optimization for prostate cancer in tomotherapy [Cao YJ, Lee S, Chang KH, Shim JB, Kim KH, Park YJ, Kim CY]. *Med Dosim.* 40, 285–289. doi: 10.1016/j.meddos.2015.03.005

Shen, Y., Peng, C., Bai, Q., Ding, Y., Yi, X., Du, H., et al. (2019). Epigenome-wide association study indicates hypomethylation of MTRNR2L8 in large-artery atherosclerosis stroke. *Stroke* 50, 1330–1338. doi: 10.1161/STROKEAHA.118.023436

Singer, J., Gustafson, D., Cummings, C., Egelko, A., Mlabasati, J., Conigliaro, A., et al. (2019). Independent ischemic stroke risk factors in older Americans: a systematic review. *Aging*. 11, 3392–3407. doi: 10.18632/aging.101987

Stanzione, R., Cotugno, M., Bianchi, F., Marchitti, S., Forte, M., Volpe, M., et al. (2020). Pathogenesis of ischemic stroke: role of epigenetic mechanisms. *Genes*. 11, 1101189. doi: 10.3390/genes11010089

Traylor, M., Farrall, M., Holliday, E. G., Sudlow, C., Hopewell, J. C., Cheng, Y. C., et al. (2012). Genetic risk factors for ischaemic stroke and its subtypes (the METASTROKE collaboration): a meta-analysis of genome-wide association studies. *Lancet Neurol*. 11, 951–962. doi: 10.1016/S1474-4422(12)70234-X

Udali, S., Guarini, P., Moruzzi, S., Choi, S. W., and Friso, S. (2013). Cardiovascular epigenetics: from DNA methylation to microRNAs. *Mol Aspects Med*. 34, 883–901. doi: 10.1016/j.mam.2012.08.001

Unzeta, M., Hernàndez-Guillamon, M., Sun, P., and Solé, M. (2021). SSAO/VAP-1 in cerebrovascular disorders: a potential therapeutic target for stroke and Alzheimer's disease. *Int. J. Mol. Sci*. 22, 365. doi: 10.3390/ijms22073365

Wang, C., Xu, G., Wen, Q., Peng, X., Chen, H., Zhang, J., et al. (2019). CBS promoter hypermethylation increases the risk of hypertension and stroke. *Clinics*. 74, e630. doi: 10.6061/clinics/2019/e630

Wen, Y., Yang, S., Liu, R., and Simpkins, J. W. (2005). Cell-cycle regulators are involved in transient cerebral ischemia induced neuronal apoptosis in female rats. *FEBS Lett*. 579, 4591–4599. doi: 10.1016/j.febslet.2005.07.028

Zhao, L., Chen, X., Zhou, S., Lin, Z., Yu, X., Huang, Y. D. N. A., et al. (2020). methylation of AHCY may increase the risk of ischemic stroke. *Bosn. J. Basic Med. Sci*. 20, 471–476. doi: 10.17305/bjbms.2020.4535

Zhou, S., Zhang, Y., Wang, L., Zhang, Z., Cai, B., Liu, K., et al. (2016). CDKN2B methylation is associated with carotid artery calcification in ischemic stroke patients. *J. Transl. Med*. 14, 333. doi: 10.1186/s12967-016-1093-4

Zündorf, G., and Reiser, G. (2011). Calcium dysregulation and homeostasis of neural calcium in the molecular mechanisms of neurodegenerative diseases provide multiple targets for neuroprotection. *Antioxid. Redox Signal*. 14, 1275–1288. doi: 10.1089/ars.2010.3359

frontiers | Frontiers in Pharmacology

TYPE Original Research
PUBLISHED 24 November 2022
DOI 10.3389/fphar.2022.940260



OPEN ACCESS

EDITED BY
Arn MJM Van Den Maagdenberg,
Leiden University Medical Center (LUMC), Netherlands

REVIEWED BY
Sizhe Zhu,
Huazhong University of Sciences and Technology, China
Francisca Pérez-Severiano,
Instituto Nacional de Neurología y Neurocirugía MVS y, Mexico

*CORRESPONDENCE
Hongjie Xi,
xihongjie1973@163.com

SPECIALTY SECTION
This article was submitted to Neuropharmacology, a section of the journal Frontiers in Pharmacology

RECEIVED 10 May 2022
ACCEPTED 04 November 2022
PUBLISHED 24 November 2022

CITATION
Liu C, Li Z and Xi H (2022), Bioinformatics analysis and *in vivo* validation of ferroptosis-related genes in ischemic stroke.
*Front. Pharmacol.* 13:940260.
doi: 10.3389/fphar.2022.940260



# Bioinformatics analysis and *in vivo* validation of ferroptosis-related genes in ischemic stroke

Chang Liu[1,2,3], Zhixi Li[1,2,3] and Hongjie Xi[1,3]*

[1]Heilongjiang Province Key Laboratory of Research on Anesthesiology and Critical Care Medicine, Harbin, China, [2]The Key Laboratory of Myocardial Ischemia Organization, Chinese Ministry of Education, Harbin, China, [3]Department of Anesthesiology, The Second Affiliated Hospital of Harbin Medical University, Harbin, China

Ischemic stroke (IS) is a neurological condition associated with high mortality and disability rates. Although the molecular mechanisms underlying IS remain unclear, ferroptosis was shown to play an important role in its pathogenesis. Hence, we applied bioinformatics analysis to identify ferroptosis-related therapeutic targets in IS. IS-related microarray data from the GSE61616 dataset were downloaded from the Gene Expression Omnibus (GEO) database and intersected with the FerrDb database. In total, 33 differentially expressed genes (DEGs) were obtained and subjected to functional enrichment and protein–protein interaction (PPI) network analyses. Four candidate genes enriched in the HIF-1 signaling pathway (*HMOX1*, *STAT3*, *CYBB*, and *TLR4*) were selected based on the hierarchical clustering of the PPI dataset. We also downloaded the IR-related GSE35338 dataset and GSE58294 dataset from the GEO database to verify the expression levels of these four genes. ROC monofactor analysis demonstrated a good performance of *HMOX1*, *STAT3*, *CYBB*, and *TLR4* in the diagnosis of ischemic stroke. Transcriptional levels of the above four genes, and translational level of GPX4, the central regulator of ferroptosis, were verified in a mouse model of middle cerebral artery occlusion (MCAO)-induced IS by qRT-PCR and western blotting. Considering the regulation of the HIF-1 signaling pathway, dexmedetomidine was applied to the MCAO mice. We found that expression of these four genes and GPX4 in MCAO mice were significantly reduced, while dexmedetomidine reversed these changes. In addition, dexmedetomidine significantly reduced MCAO-induced cell death, improved neurobehavioral deficits, and reduced the serum and brain levels of inflammatory factors (TNF-α and IL-6) and oxidative stress mediators (MDA and GSSG). Further, we constructed an mRNA-miRNA-lncRNA network based on the four candidate genes and predicted possible transcription factors. In conclusion, we identified four ferroptosis-related candidate genes in IS and proposed, for the first time, a possible mechanism for dexmedetomidine-mediated inhibition of ferroptosis during IS. These findings may help design novel therapeutic strategies for the treatment of IS.

KEYWORDS

**ischemic stroke, ferroptosis, HIF-1 signaling pathway, dexmedetomidine, microarray, oxidative stress, inflammatory response**

## Introduction

As the third leading cause of death and the first leading cause of disability, stroke is a major public health concern worldwide (Tao et al., 2020). Ischemic stroke (IS) results from cerebral hypoperfusion and occupies roughly 85% of stroke cases (Liu et al., 2020). Although endovascular-reperfusion therapy can improve outcomes in some patients, the prognosis of IS still poor due to the narrow therapeutic window, potential hemorrhagic risk, and subsequent reperfusion injury (Jahan et al., 2019; Liao et al., 2020).

Multiple intricate biological processes have been implicated in IS-related neuronal death. These include oxidative stress, neuroinflammation, excitotoxicity, and various forms of regulated cell death (Zhang et al., 2019; Han et al., 2020; Liao et al., 2020; Liu et al., 2020). Among the latter, ferroptosis constitutes a form of programmed necrosis that shows unique features, namely iron dependency and accumulation of reactive oxygen species (ROS) (Gao et al., 2016). Since its identification, ferroptosis has been reported in several neurological disorders, including cerebral ischemia/reperfusion injury (CIRI) and neurodegenerative diseases (Yan et al., 2021). Researchers reported that disturbance in the levels of trace elements, including iron, combined with a reduction in antioxidant activity, associated with the etiology of CIRI (Fang et al., 2013). Supporting evidence for this association was provided by the fact that specific interventions could reverse the increased level of lipid peroxide and the reduction of ferroptosis marker glutathione peroxidase 4 (Guan et al., 2019). However, the specific molecular mechanism underlying ferroptosis in IS poorly understood.

Dexmedetomidine (DEX), an α2 receptor antagonist, has been shown to significantly reduce both the inflammatory response and oxidative stress in diseases caused by ischemia-reperfusion injury, potentially via the HIF-1 signaling pathway (Shi et al., 2021). However, studies investigating the specific mechanisms by which DEX attenuates ferritin formation during CIRI are still lacking.

In the present study, we used publicly available gene expression datasets and bioinformatics analysis to identify critical genes and possible mechanisms related to ferroptosis in IS. By analyzing GEO microarray expression profiles from control and IS rat brains and intersecting these data with the FerrDB database, we identified and conducted functional enrichment analyses on ferroptosis-related differentially expressed genes (DEGs). After validation of the expression and diagnostic efficacy of these four genes in different datasets, the effect of DEX on ferroptosis and these four genes in the HIF-1 signaling pathway during IS was assessed in a mouse model of IS induced by middle cerebral artery occlusion (MCAO). Finally, we constructed an mRNA-miRNA-lncRNA interaction network based on main ferroptosis-related candidate genes and predicted transcription factors (TFs) potentially involved in their regulation. This research provides a starting point for further studies into the molecular mechanisms of IS and may lead to novel intervention strategies targeting neuronal ferroptosis in stroke patients.

## Materials and methods

### Microarray data

We downloaded transcriptome data from IS-related microarrays (coded as GSE61616, GSE35338, and GSE58294) from the Gene Expression Omnibus (GEO) database (https://www.ncbi.nlm.nih.gov/geo/). The GSE61616 dataset was analyzed using Affymetrix Rat 230 2.0 Array, in which we used data expression profile in the infarcted hemispheres at 7 days after Sham operation and MCAO surgery ($n$ = 5 per group). We used data from the GSE35338 and GSE58294 for validation. GSE35338 dataset was sourced from male mouse brain tissue after MCAO surgery ($n$ = 5) and Sham operation ($n$ = 4). GSE58294 dataset contains blood samples from 23 control patients and 69 stroke patients.

### Differential gene expression analysis

We accessed GEO2R (https://www.ncbi.nlm.nih.gov/geo/geo2r/) to compare gene expression data from MCAO-treated and control mice in the GSE61616 dataset, with padj<0.05 and |logFC|>1 as the threshold. The results were presented in the form of a volcano plot and a heatmap. Next, we downloaded 259 genetic regulators of ferroptosis from the FerrDb database (http://www.zhounan.org/ferrdb/index.html), including drivers, suppressors, and markers. Finally, these ferroptosis-related genes were intersected with the DEGs obtained from the analysis of the GSE61616 dataset to identify ferroptosis-related DEGs.

### Functional enrichment analysis

The clusterProfiler package, the org. Hs.eg.db package, and the GOplot package of R software were used to perform Gene ontology (GO) and Kyoto Encyclopedia of Genes and Genomes (KEGG) analysis on ferroptosis-related DEGs using ($p$ < 0.05).

### Protein-protein interaction network analysis

We uploaded ferroptosis-related DEGs to the STRING database (http://www/string-db.org/) for PPI network prediction (interaction score >0.4). Nine genes in cluster one were identified by importing analysis results from the STRING

database into Cytoscape v.3.7.2, and the Molecular Complex Detection (MCODE) plugin was then used to perform clustering analysis for the ferroptosis-related DEGs (Degree Cutoff = 2, Node Score Cutoff = 0.2, K-Core = 2, and Max. Depth = 100).

## Diagnostic value of ferroptosis-related biomarkers in ischemic stroke

ROC monofactor analysis was performed in the GSE58294 dataset to evaluate the diagnostic value of ferroptosis-related biomarkers in ischemic stroke. Application of the pROC package, ggplot2 for statistical analysis and visualization of ROC monofactor analysis.

## Animals and experimental procedures

C57BL/6 mice (8–10 weeks old, male, weighing 22–25 g) were purchased from Beijing Weitong Lihua Experimental Animal Technology Co. Animals were kept in a specific pathogen-free and environmentally controlled room with free access to standard laboratory food and water and a 12-h light and dark cycle. To mimic IS, a mouse model of middle cerebral artery occlusion/reperfusion (MCAO/R) was established as described previously (Longa et al., 1989). Briefly, mice were anesthetized with isoflurane (5% for induction and 1.5%–2.5% for maintenance). A 6–0 silicone rubber-coated nylon monofilament (Doccol Corporation) was inserted from an incision of the left external carotid artery, then the monofilament was guided into the internal carotid artery through the bifurcation and advanced about 11 mm to occlude the MCA for 120 min. The filament was withdrawn after 120 min to allow reperfusion after re-anesthesia. Sham-operated mice went through the same procedure except for embolization. We dissolved DEX with saline to a concentration of 5 μg/ml. Each mouse was injected intraperitoneally twice with DEX (50 μg/kg) dissolved in saline immediately after reperfusion and 120 min after reperfusion (Li et al., 2020). After 24 h of reperfusion, the Zea Longa scoring method was used to score the MCAO/R model. Mice scoring 2 or three were considered to suffer from IS. The scoring criteria were as follows: 0 (normal or no neurological deficit perceivable), 1 (inability to fully stretch the front paw on the paralyzed lateral), 2 (mice turned in circles towards the paralyzed side), 3 (slouching towards the paralyzed side), and 4 (loss of consciousness without automatic walking).

The animals were divided into three groups: SHAM, MCAO, and MCAO + DEX. The animal study was reviewed and approved by the Animal Care and Use Committee of the Second Affiliated Hospital of Harbin Medical University (Approval No. SYDW 2021–086). All invasive operations were performed after adequate anesthesia in strict compliance with the National Institutes of Health and the Guiding Principles for the Protection and Use of Laboratory Animals.

## Infarct volume measurement

After 24 h of reperfusion, mice were decapitated under deep isoflurane anesthesia. Brains were quickly removed and snap-frozen for 10 min, cut into thin slices of approximately 1 mm along the coronal plane, stained with 2% 2,3,5-triphenyltetrazolium chloride (TTC), incubated at 37°C for 15 min with turning to ensure even staining, fixed in 4% paraformaldehyde overnight, and photographed. Infarct areas were measured using Image-Pro Plus software (Version 6.0, Media Cybernetics, Bethesda, MD, United States). Infarct volume (compensated for brain edema) was calculated as:

$$(Contralateral\ hemisphere\ area - ipsilateral\ hemisphere\ without\ infarct) / contralateral\ hemisphere\ area$$

## TdT-mediated dUTP nick end labeling

The TUNEL method was performed to visualize the 3′-OH ends of DNA fragments in dead cells for paraffin-embedded brain slides according to the manufacturer's protocol (Roche, Germany). The results are quantified as (TUNEL-positive cells)/(total cells) ×100%.

## Neurobehavioral analysis

Neurobehavioral analysis was performed in a double-blinded manner after MCAO. Sensorimotor deficits were assessed by the rotarod test, the corner test, and the adhesive removal test, performed at 1 day, 3 days, 5 days, 7 days, and 14 days after MCAO. Rotarod test was carried out as described previously after 3 days of adaptation training (Wang et al., 2014; Xu et al., 2020). Briefly, mice were placed on a rotating drum with speed from 4 to 40 rpm during a 5-min period. Each mouse was tested three times per day, with an intermission of at least 15 min between tests. Latency to fall off the rotating rod was recorded. Data were expressed as mean values from the three trials. The adhesive removal test was performed according to previous literature (Bouet et al., 2009; Qu et al., 2021). The test was carried out with 2 × 3 mm tape. Adhesive tapes were applied to the ipsilateral or contralateral forepaw of the mouse to evaluate the sensory and motor function of mice. Time is recorded when the mouse perceives the sticker attached to the foot and removes it as time-to-contact and time-to-remove. The amount of time-to-contact and time-to-remove for the mouse was measured up to 120 s. The

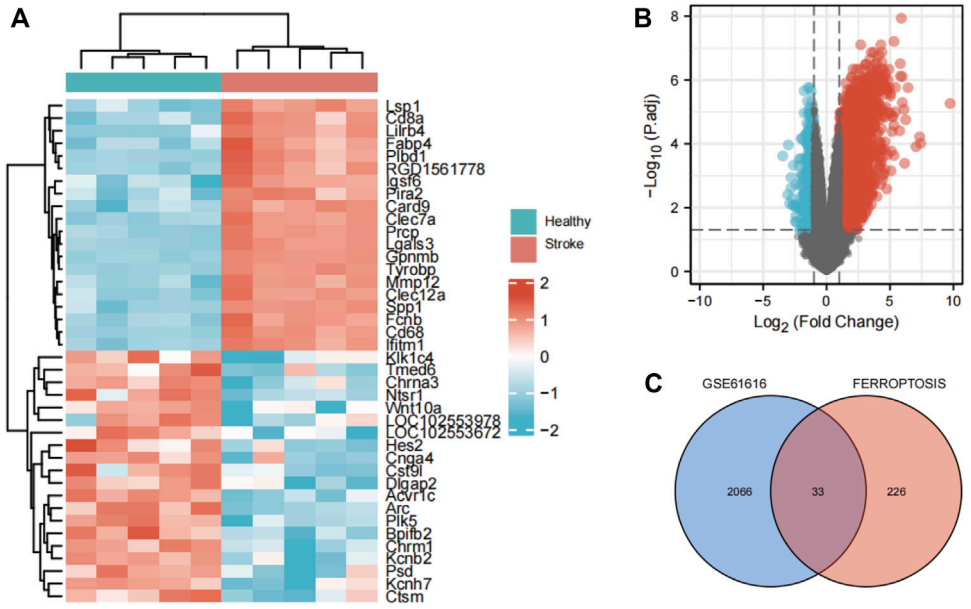


FIGURE 1
Identification of ferroptosis-related DEGs in IS. **(A)** Heatmap of DEGs between the MCAO cohort and the sham cohort in the GSE1 dataset. **(B)** Volcano plots of DEGs. **(C)** Venn diagram of DEGs from the two datasets.

corner test is a widely used functional assessment for unilateral sensorimotor cortical damage (Yu et al., 2019). Two cardboard plates (30 cm × 20 cm) were attached at a 30° angle in a home cage. Each mouse was placed between the two plates and allowed to move freely to the corner. The number of times the mice turned to the left in 10 trials were recorded. Only mice without a preference for turning left and right in the pre-training were included. Normal mice make about equal left and right turns in their exploratory turning behavior. After the ischemic and reperfusion insult to the sensorimotor cortex, mice showed biased turns consistent with the side of their brain damage.

## Enzyme linked immunosorbent assay

Mice were sacrificed after 24 h of reperfusion, and blood samples collected by cardiac puncture were stored at −80°C before analysis. Serum levels of TNF-α and IL-6 were determined by commercial ELISA kits (Mouse TNF-α and IL-6 ELISA Kit, Jingkang, China), following the manufacturer's instructions.

## Detection of MDA levels

Lipid peroxidation in the ischemic penumbra area was assessed using an MDA assay kit (S0131, Beyotime Institute of Biotechnology, China), in accordance with the manufacturer's instructions. Absorbance measurements were made at 532 nm.

## GSSG content detection

Oxidized glutathione disulfide (GSSG) levels were measured in tissue homogenates obtained from the penumbra area using a GSSG detection kit (S0053, Beyotime Institute of Biotechnology). Absorbance measurements were made at 412 nm.

## Western blotting

Protein was extracted from the penumbra area of mice with RIPA lysis buffer. Primary antibodies against GPX4 (Abcam, ab125066), HIF1A (CST, #36169), and β-actin (ABclonal, AC026) were used. After washing, incubate the membranes with an anti-rabbit secondary antibody (Abcam, ab6721).

## Extraction of RNA and qRT-PCR

We used trizol reagent to extract RNA from ischemic penumbra brain tissue. cDNA was then synthesized with the First Strand cDNA Synthesis Kit (Code No. FSK-101, Toyobo, Osaka, Japan) on a thermal cycler (BIO-RAD S1000).

TABLE 1 Ferroptosis-related differentially expressed genes.

| Gene symbol | Name | logFC | adj.P.Val | Id |
|---|---|---|---|---|
| RGS4 | Regulator of G protein signaling 4 | −1.53 | 3.15E-02 | 1368505_at |
| GLS2 | Glutaminase 2 | −1.26 | 1.47E-02 | 1370375_at |
| FBXW7 | F-box and WD repeat domain containing 7 | −1.05 | 8.85E-03 | 1379332_at |
| VLDLR | Very low density lipoprotein receptor | −1.02 | 9.90E-05 | 1392924_at |
| DUSP1 | Dual specificity phosphatase 1 | −1.01 | 9.08E-03 | 1368146_at |
| SAT1 | Spermidine/spermine N1-acetyltransferase 1 | 1.03 | 1.09E-04 | 1371774_at |
| *STAT3* | Signal transducer and activator of transcription 3 | 1.13 | 5.53E-04 | 1370224_at |
| FANCD2 | FA complementation group D2 | 1.25 | 4.53E-05 | 1378240_at |
| HERPUD1 | Homocysteine inducible ER protein with ubiquitin like domain 1 | 1.32 | 6.45E-03 | 1367741_at |
| RIPK1 | Receptor interacting serine/threonine kinase 1 | 1.34 | 8.90E-05 | 1371529_at |
| BID | BH3 interacting domain death agonist | 1.42 | 1.48E-04 | 1377759_at |
| GDF15 | Growth differentiation factor 15 | 1.45 | 1.20E-02 | 1370153_at |
| IL6 | Interleukin 6 | 1.46 | 9.28E-03 | 1369191_at |
| LPCAT3 | Lysophosphatidylcholine acyltransferase 3 | 1.52 | 7.59E-05 | 1376813_at |
| ANO6 | Anoctamin 6 | 1.60 | 1.35E-03 | 1372624_at |
| HIC1 | HIC ZBTB transcriptional repressor 1 | 1.72 | 3.68E-04 | 1381942_at |
| LAMP2 | Lysosomal associated membrane protein 2 | 1.76 | 1.20E-05 | 1370010_at |
| NFE2L2 | Nuclear factor, erythroid 2 like 2 | 1.86 | 2.67E-06 | 1367826_at |
| TXNIP | Thioredoxin interacting protein | 1.96 | 1.57E-03 | 1371131_a_at |
| SLC1A5 | Solute carrier family 1 member 5 | 2.04 | 1.25E-05 | 1371040_at |
| CD44 | CD44 molecule (Indian blood group) | 2.15 | 1.13E-05 | 1368921_a_at |
| AURKA | Aurora kinase A | 2.21 | 2.65E-05 | 1376039_at |
| ATF3 | Activating transcription factor 3 | 2.30 | 1.16E-03 | 1369268_at |
| CDKN2A | Cyclin dependent kinase inhibitor 2 A | 2.40 | 1.37E-03 | 1369194_a_at |
| GCH1 | GTP cyclohydrolase 1 | 2.42 | 1.31E-04 | 1387221_at |
| PLIN2 | Perilipin 2 | 2.52 | 7.28E-05 | 1382680_at |
| TGFBR1 | Transforming growth factor beta receptor 1 | 2.88 | 8.21E-07 | 1376636_at |
| *TLR4* | Toll like receptor 4 | 2.94 | 1.08E-05 | 1387982_at |
| HSPB1 | Heat shock protein family B (small) member 1 | 3.05 | 2.61E-05 | 1367577_at |
| ALOX12 | Arachidonate 12-lipoxygenase, 12 S type | 3.09 | 1.49E-02 | 1380636_at |
| *HMOX1* | Heme oxygenase 1 | 3.32 | 1.12E-05 | 1370080_at |
| CAPG | Capping actin protein, gelsolin like | 4.41 | 7.50E-06 | 1388460_at |
| *CYBB* | Cytochrome b-245 beta chain | 4.88 | 1.08E-05 | 1379344_at |

Quantitative RT-PCR (qRT-PCR) was performed using AceQ Universal SYBR qPCR Master Mix (Vazyme, Nanjing, China). Target genes' mRNA levels were normalized to endogenous GAPDH expression and quantified by the 2-△△ct method. Primer sequences were as follows:

Gapdh-F: 5′-AGGTCGGTGTGAACGGATTTG.
Gapdh-R: 5′-TGTAGACCATGTAGTTGAGGTCA;
*HMOX1*-F: 5′-GCCCCACCAAGTTCAAACAG.
*HMOX1*-R: 5′-GCTCCTCAAACAGCTCAATGT;
*STAT3*-F: 5′-TGGGCTAAATTCTGCAAAGAAAAC.
*STAT3*-R: 5′-GGCTTTGTGCTTAGGATGGC;
*CYBB*-F: 5′-TGGAAACCCTCCTATGACTTGG.
*CYBB*-R: 5′-AAACCGAACCAACCTCTCACAAA;
*TLR4*-F: 5′-GCTTGAATCCCTGCATAGAGGTAG.
*TLR4*-R: 5′-TGTCATCAGGGACTTTGCTGAG.
TNFα-F: 5′- GTAGCCCACGTCGTAGCAAA.
TNFα-R: 5′- ACAAGGTACAACCCATCGGC.
Il6-F: 5′- CGTGGAAATGAGAAAAGAGTTGTGC.
Il6-R: 5′- GGTACTCCAGAAGACCAGAGGA.

## Construction of an mrna-mirna-lncrna interaction network

We used a combination of five databases (miRDB, miRmap, miRWalk, RNA22, and TargetScan) to predict miRNAs with potential regulatory activity on the candidate genes. LncRNA prediction of selected miRNA was performed *via* starBase v2.0 (https://starbase.

sysu.edu.cn/) with the following screening criteria: mammalian, human h19 genome, strict stringency (≥5) of CLIP-Data, with or without degradome data. We then created a competing endogenous RNAs (ceRNA) regulatory network for DEGs using Cytoscape.

## Transcription factor prediction

After retrieving high-confidence and experimentally validated gene-TF pairs *via* the NetworkAnalyst platform and JASPAR database, Cytoscape software was used to create a TF-based regulatory network of candidate ferroptosis-related genes.

## Statistical analyses

Statistical analyses were done using SPSS 25.0 (IBM, Armonk, NY, United States), Prism 6.01 (GraphPad, San Diego, CA, United States), and R. Data were displayed as mean ± SD. The Student's t-test was used for comparison between two groups. One-way ANOVA was employed for comparison between multiple groups, and the post hoc multiple comparisons least significant difference and Student–Newman–Keuls model were selected for analyses, $p < 0.05$ was considered significant.

# Results

## Identification of ferroptosis-related DEGs after IS

Using defined criteria, we identified 2099 DEGs between control and IS samples in the GSE61616 dataset. Heatmaps of all these DEGs showed excellent discrimination between IS and control samples and volcano plots of the top 20 genes that were highly expressed and the top 20 genes that were lowly expressed in the MCAO group compared to the SHAM group (Figure Figure1 A, B). We also acquired a dataset that included 259 genes from the Ferroptosis Database (FerrDb). Venn diagram analysis of these two gene sets identified 33 ferroptosis-related DEGs (Figure 1C), including 28 up-regulated and five down-regulated genes (Table 1).

## GO and KEGG analysis of ferroptosis-related DEGs

The R package clusterProfiler was used to conduct GO and KEGG pathway enrichment analysis of the 33 ferroptosis-related DEGs. On GO analysis, for the biological process (BP), cell component (CC), and molecular function (MF) categories, these DEGs were mainly enriched in 'cellular response to oxidative stress,' 'receptor complex,' and 'cytokine receptor binding,' respectively (Figure 2). On KEGG pathways analysis, the ferroptosis-related DEGs were mainly enriched in 'ferroptosis', followed by 'HIF-1 signaling pathway' (Figure 3). This finding supports the notion that HIF-1 signaling is intrinsically linked to the occurrence of ferroptosis in IS.

## PPI analysis of ferroptosis-related DEGs

Next, we accessed the STRING database and constructed, a PPI network for the 33 ferroptosis-related DEGs using Cytoscape software. This network included 33 nodes and 64 edges (Figure 4A). MCODE was used to explore the most significant cluster (cluster one; containing nine genes). The nine genes in cluster one were then incorporated into the PPI network map (Figure 4B).

## Functional enrichment analysis of cluster one

Based on GO and KEGG analysis, we found that four out of the nine genes in cluster1 (*HMOX1*, *STAT3*, *CYBB*, and *TLR4*) were enriched in the HIF-1 signaling pathway. These genes were then selected as candidate genes for further analysis (Figure 5).

## Verification of the expression of the four candidate genes in IS

Next, we validated the expression levels of the four candidate ferroptosis-related genes by assessing their expression in two different IS-related datasets (GSE35338 and GSE58294; Figures 6A,B). The expression levels of all four genes were significantly upregulated in samples from the IS group compared to those of the sham-operated group. These results, which were consistent with those obtained from the GSE61616 dataset, further suggest the importance of these four ferroptosis-related genes in IS.

## The diagnostic value of four candidate genes in IS

ROC univariate analysis was performed in the GSE58294 dataset to assess the diagnostic value of four candidate genes for IS. As a result, the accuracy of *HMOX1*, *STAT3*, *CYBB*, and *TLR4* in diagnosing IS in the GSE58294 dataset was 0.820, 0.841, 0.911, and 0.895, respectively (Figure 6C).

## DEX alleviated cerebral ischemic/reperfusion injury in a mouse model of IS

We next investigated the effect of dexmedetomidine (DEX), a highly selective alpha-2 adrenoceptor agonist with anti-ferroptosis

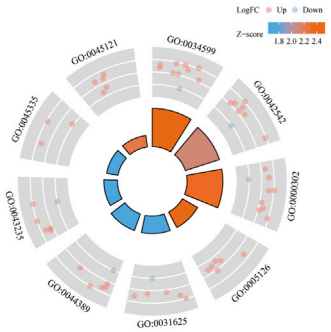


| Ontology | ID | description | Gene ID |
|---|---|---|---|
| BP | GO:0034599 | cellular response to oxidative stress | Fbxw7, Fancd2, Ripk1, Il6, Nfe2l2, Cdkn2a, Gch1, Tlr4, Hspb1, Hmox1 |
| BP | GO:0042542 | response to hydrogen peroxide | Dusp1, Ripk1, Il6, Nfe2l2, Txnip, Cdkn2a, Hspb1, Hmox1 |
| BP | GO:0000302 | response to reactive oxygen species | Dusp1, Ripk1, Il6, Nfe2l2, Txnip, Cdkn2a, Gch1, Hspb1, Hmox1 |
| CC | GO:0043235 | receptor complex | Vldlr, Ripk1, Il6, Cd44, Tgfbr1, Tlr4 |
| CC | GO:0045335 | phagocytic vesicle | Lamp2, Capg, Cybb |
| CC | GO:0045121 | membrane raft | Ripk1, Lamp2, Tgfbr1, Tlr4, Hmox1 |
| MF | GO:0005126 | cytokine receptor binding | Stat3, Ripk1, Gdf15, Il6, Cd44, Tgfbr1 |
| MF | GO:0031625 | ubiquitin protein ligase binding | Fbxw7, Ripk1, Bid, Txnip, Aurka, Tgfbr1 |
| MF | GO:0044389 | ubiquitin-like protein ligase binding | Fbxw7, Ripk1, Bid,T xnip, Aurka, Tgfbr1 |

FIGURE 2
Gene ontology enrichment analysis of ferroptosis-related DEGs.

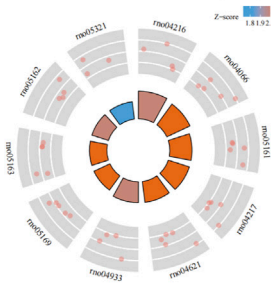


| Ontolog | ID | description | Gene ID |
|---|---|---|---|
| KEGG | rno04216 | Ferroptosis | Sat1, Lpcat3, Hmox1, Cybb |
| KEGG | rno04066 | HIF-1 signaling pathway | Stat3, Il6, Tlr4, Hmox1, Cybb |
| KEGG | rno05161 | Hepatitis B | Stat3, Bid, Il6, Tgfbr1, Tlr4 |
| KEGG | rno04217 | Necroptosis | Stat3, Ripk1, Bid, Tlr4, Cybb |
| KEGG | rno04621 | NOD-like receptor signaling pathway | Ripk1, Il6, Txnip, Tlr4, Cybb |
| KEGG | rno04933 | AGE-RAGE signaling pathway in diabetic complications | Stat3, Il6, Tgfbr1, Cybb |
| KEGG | rno05169 | Epstein-Barr virus infection | Stat3, Ripk1, Bid, Il6, Cd44 |
| KEGG | rno05163 | Human cytomegalovirus infection | Stat3, Ripk1, Bid, Il6, Cdkn2a |
| KEGG | rno05162 | Measles | Stat3, Bid, Il6, Tlr4 |
| KEGG | rno05321 | Inflammatory bowel disease | Stat3, Il6, Tlr4 |

FIGURE 3
Kyoto Encyclopedia of Genes and Genomes pathway analysis of ferroptosis-related DEGs.

action, in a mouse model of MCAO-induced IS. After 24 h of reperfusion, we determined infarct size by staining brain sections with TTC. As shown in Figure 7A, infarct size was significantly attenuated by DEX administration. In addition, neurological deficits in the MCAO + DEX group were significantly milder than those in the MCAO group (Figure 7B). To further assess the sensorimotor function of the mice, we applied the rotarod test, the corner test, and the adhesive removal test. IS induced severe sensorimotor impairment in mice, which was manifested as decreased latency to fall off the rotating rod (Figure 7C), increased number of left turns in the corner test (Figure 7D), and a prolonged time to contact and remove the tape in the adhesive removal test (Figure 7E). Interestingly, DEX showed a protective effect on sensorimotor dysfunction by increasing the right limb use and correcting for the turning bias in 5, 7 and 14 days after MCAO. However, no turn bias was observed in the acute phase of IS (1 and 3 days after MCAO). To assess whether the beneficial effects of DEX on IS are related to the inhibition of inflammatory processes, we quantified through ELISA serum and brain levels of pro-inflammatory cytokines. A prominent reduction in TNF-α and IL-6 levels in the brain was noted in the MCAO + DEX group compared with the MCAO group (Figure 7F). And there is a mild decrease in serum levels of TNF-α and IL-6 in the MCAO + DEX group compared with the MCAO group (Figure 7G). These findings are thus consistent with previous evidence indicating that dexmedetomidine alleviates IS severity in rodent models of CIRI.

## DEX alleviated ferroptosis and regulated candidate genes

Western blotting analysis of brain tissue revealed markedly higher levels of GPX4 in DEX-treated mice compared to the untreated MCAO mice (Figure 8A). We next analyzed the impact of DEX on oxidative stress, a primary trigger of ferroptosis, by

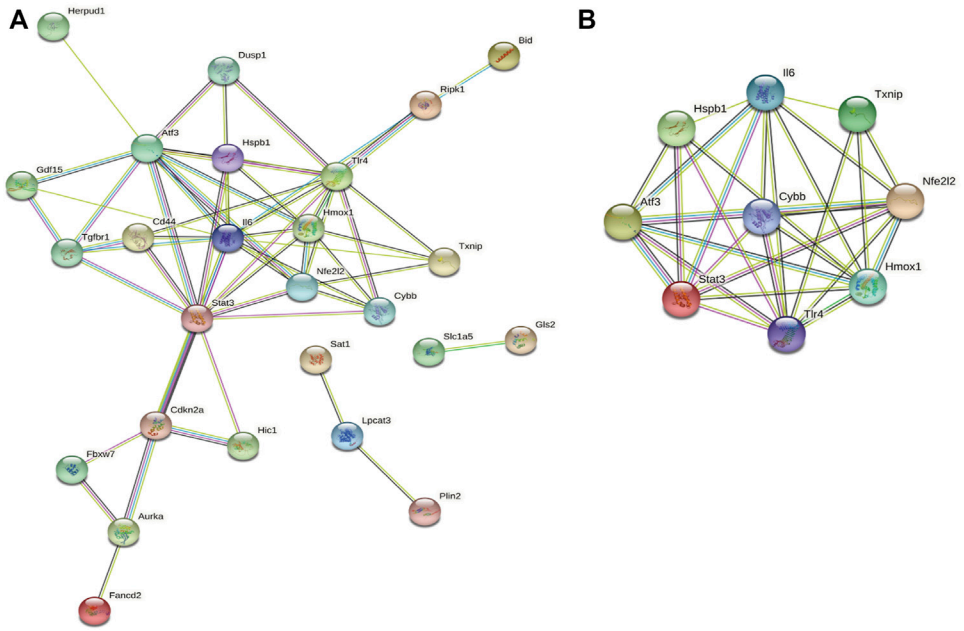


FIGURE 4
PPI analysis of ferroptosis-related DEGs. **(A)** PPI network of ferroptosis-related DEGs. **(B)** Gene clustering based on the MCODE algorithm.

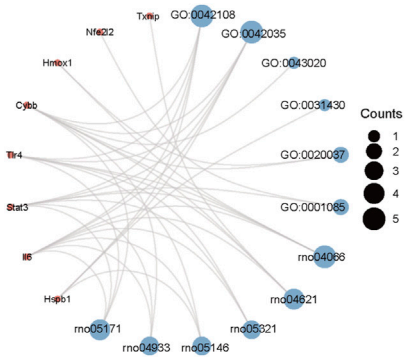


| Ontology | ID | description | Gene ID |
|---|---|---|---|
| BP | GO:0042108 | positive regulation of cytokine biosynthetic process | Hspb1, Il6, Stat3, Tlr4, Cybb |
| BP | GO:0042035 | regulation of cytokine biosynthetic process | Hspb1, Il6, Stat3, Tlr4, Cybb |
| CC | GO:0043020 | NADPH oxidase complex | Cybb |
| CC | GO:0031430 | M band | Hspb1 |
| MF | GO:0020037 | heme binding | Hmox1, Cybb |
| MF | GO:0001085 | RNA polymerase II transcription factor binding | Stat3, Nfe2l2 |
| KEGG | rno04066 | HIF−1 signaling pathway | Hmox1, Stat3, Tlr4, Cybb |
| KEGG | rno04621 | NOD−like receptor signaling pathway | Il6, Tlr4, Cybb, Txnip |
| KEGG | rno05321 | Inflammatory bowel disease | Il6, Stat3, Tlr4 |
| KEGG | rno05146 | Amoebiasis | Hspb1, Il6, Tlr4 |
| KEGG | rno04933 | AGE-RAGE signaling pathway in diabetic complications | Il6, Stat3, Cybb |
| KEGG | rno05171 | Coronavirus disease - COVID-19 | Il6, Stat3, Tlr4, Cybb |

FIGURE 5
Functional enrichment analysis of genes in cluster 1.

measuring the contents of MDA and GSSG in the penumbra region of the infarcted tissue. Results showed a significant reduction in both MDA and GSSG levels following administration of DEX (Figures 8B,C). Because ferroptosis has TUNEL positivity as described previously (Ueta et al., 2012), we used TUNEL staining *in vivo* as a potential marker of ferroptosis and observed that TUNEL-positive cells increased in the brain of MCAO mice. However, the proportion of TUNEL-positive cells in the MCAO + DEX group was lower (Figure 8D). Using Western blotting analysis and qRT-PCR analysis, we verified whether DEX treatment influenced the expression of HIF1α and the four ferroptosis-related candidate genes selected through our bioinformatics analysis. Results showed that after IS induction, brain *HMOX1*, *STAT3*, *CYBB*, and *TLR4* mRNA levels were dramatically decreased in DEX-treated mice (Figure 8E). Protein expression levels of HIF1α in brain tissue were elevated after MCAO and had higher expression in the DEX group (Figure 8F). These findings provide robust evidence that DEX inhibits CIRI-induced ferroptosis by blunting HIF-1 signaling through regulation of *HMOX1*, *STAT3*, *CYBB*, and *TLR4* expression.

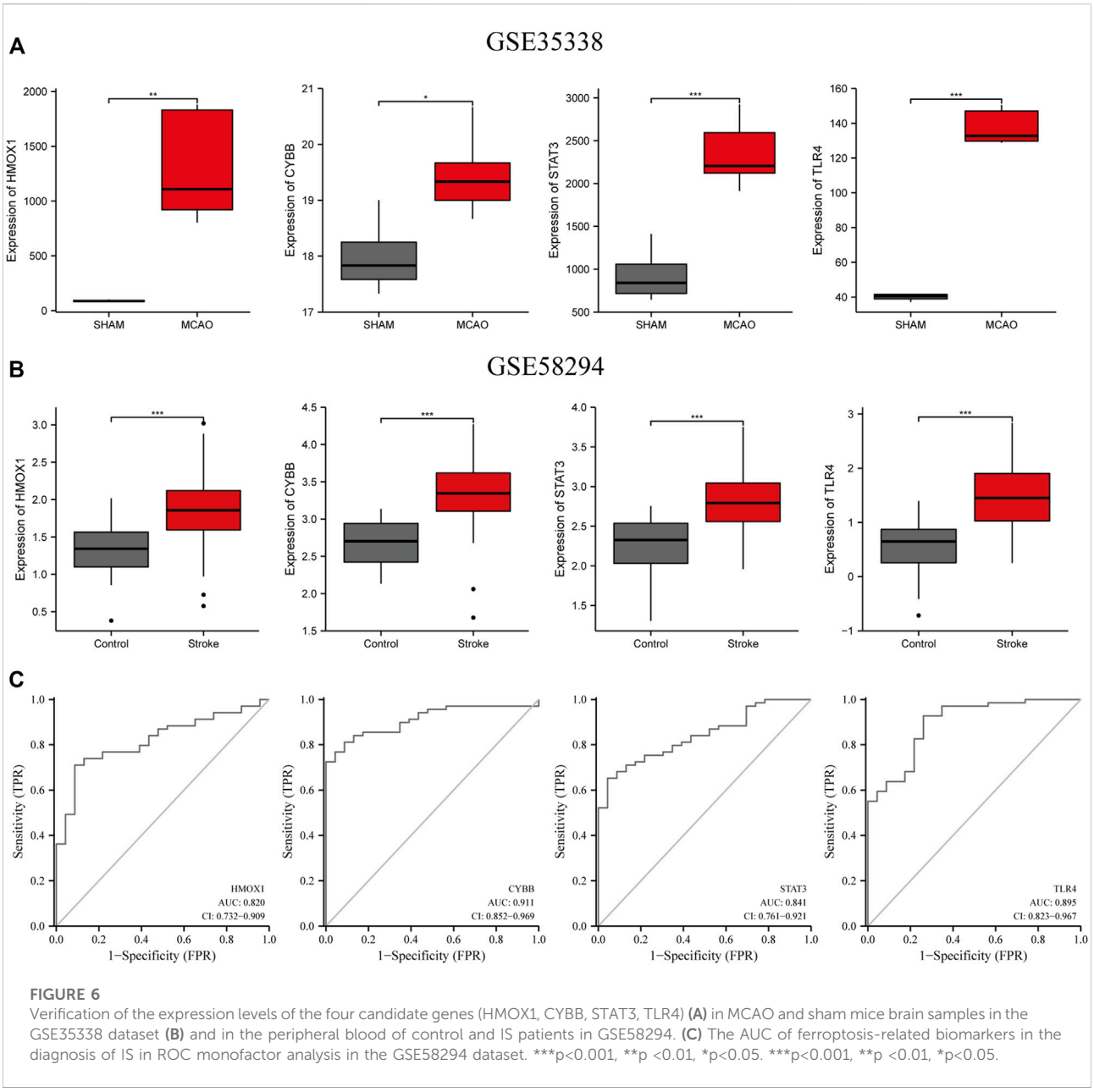


FIGURE 6
Verification of the expression levels of the four candidate genes (HMOX1, CYBB, STAT3, TLR4) **(A)** in MCAO and sham mice brain samples in the GSE35338 dataset **(B)** and in the peripheral blood of control and IS patients in GSE58294. **(C)** The AUC of ferroptosis-related biomarkers in the diagnosis of IS in ROC monofactor analysis in the GSE58294 dataset. ***p<0.001, **p <0.01, *p<0.05. ***p<0.001, **p <0.01, *p<0.05.

## Construction of a mRNA -miRNA-lncRNA interaction network

Next, we consulted the miRDB, miRmap, miRWalk, RNA22, and TargetScan databases to identify potential regulatory miRNAs for the *HMOX1*, *STAT3*, *CYBB*, and *TLR4* transcripts. Among a total of 22 miRNAs retrieved, hsa-miR-106a-5p and hsa-miR-106b-5p ranked first, while hsa-miR-1299 was found to bind to more than one mRNA. Subsequently, for the 22 miRNAs predicted, analysis on the starBase platform identified 18 potentially interacting lncRNAs. Based on the above analysis, a ferroptosis-related mRNA-miRNA-lncRNA interaction network is presented in Figure 9A.

## Identification of TFs potentially influencing the expression of ferroptosis-related genes in IS

Using data from NetworkAnalyst, we finally created an interaction network with 32 connections featuring the four candidate genes and 24 TFs predicted to regulate their expression (Figure 9B). Among the predicted TFs, NR3C1,

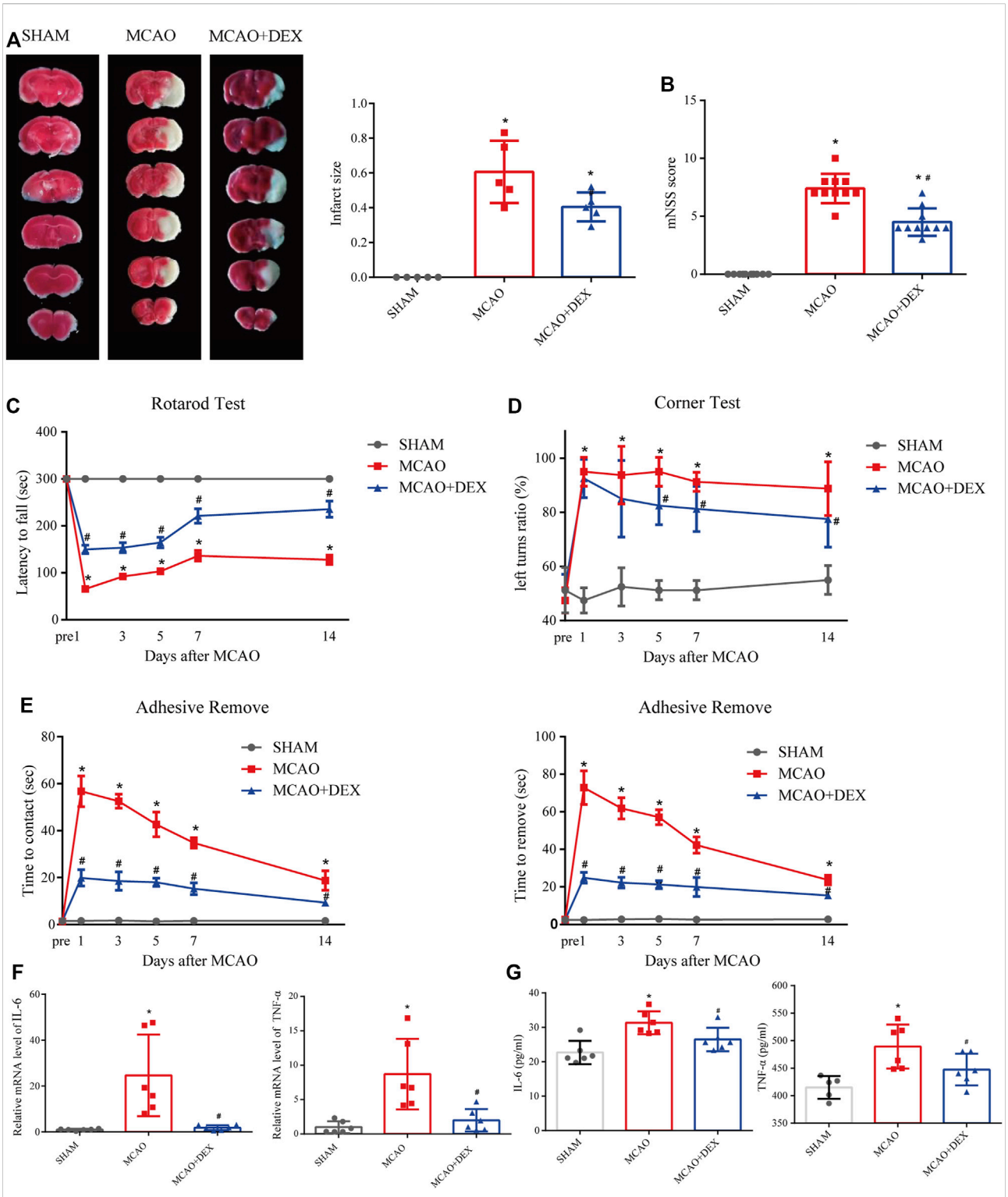


FIGURE 7
**(A)** Representative TTC staining in comparable sections from the three mice groups and quantification of infarct volume ($n$ = 5). **(B)** Modified neurological severity (mNSS) scores for mice in the three experimental groups ($n$ = 10). On different days after ischemic stroke, **(C)** the time for the mice to contact or remove the sticker was recorded, **(D)** the latency to fall off the rotating rod, and **(E)** the turning bias in the corner test. $n$ = 8 per group. **(F)** Brain levels of IL-6 **(E)** and TNF-α. $n$ = 6 per group **(G)** Serum levels of IL-6 ($n$ = 6) and TNF-α ($n$ = 5 for SHAM group, and $n$ = 6 for MCAO and MCAO + DEX group). Data are presented as the mean ± SD. *p<0.05 vs. SHAM group, #p<0.05 vs. MCAO group.

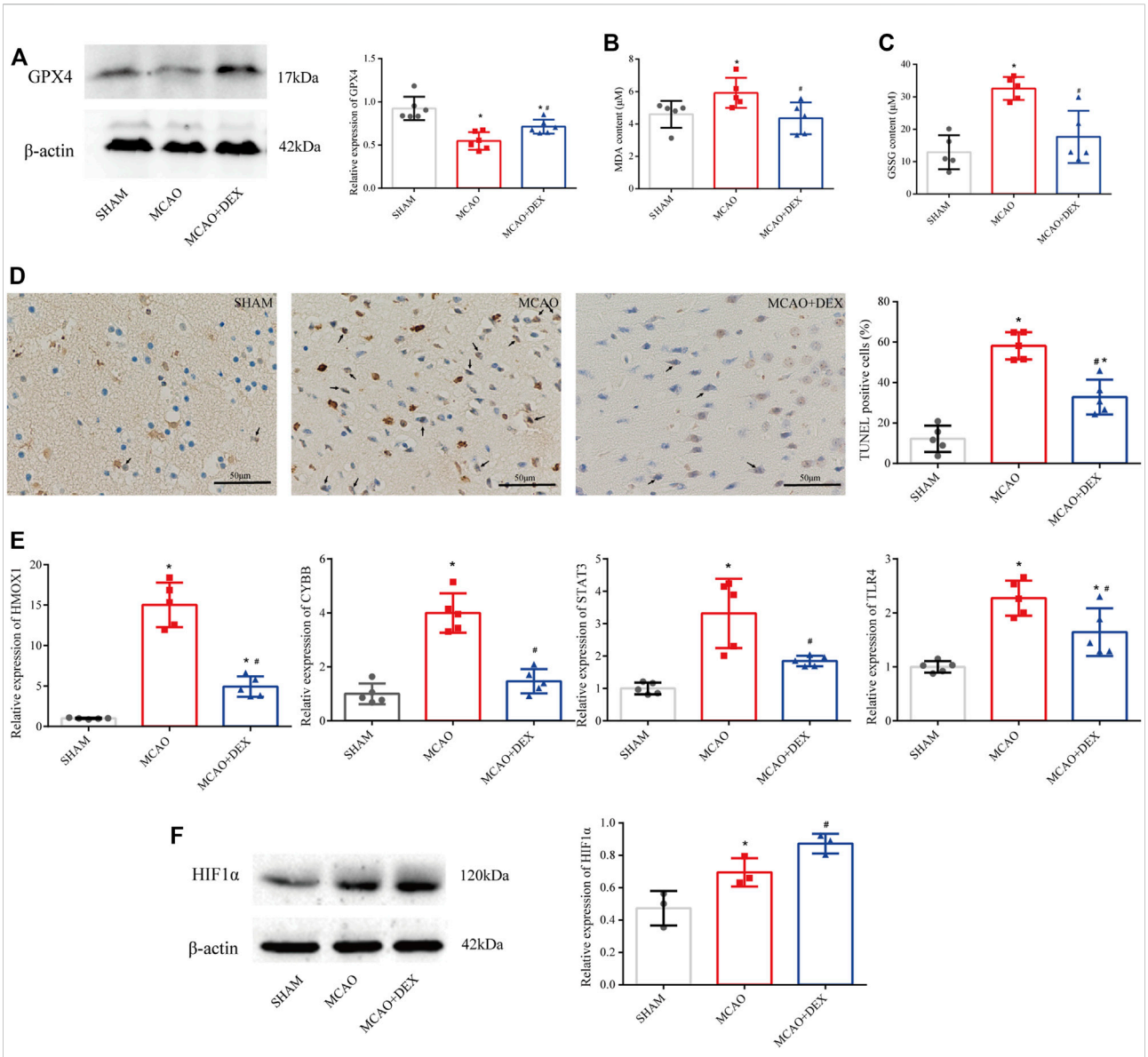


FIGURE 8
**(A)** Western blotting analysis of GPX4 in the penumbra area ($n$ = 6 per group). **(B)** MDA levels in brain tissues ($n$ = 5 per group). **(C)** GSSG levels in brain tissues ($n$ = 6 per group). **(D)** TUNEL staining in SHAM, MCAO and DEX + MCAO mice (Scale bars = 50 μm) and quantification of the number of TUNEL+ cells ($n$ = 3). **(E)** Relative mRNA levels of HMOX1, CYBB, STAT3, and TLR4 in mice brain by qRT-PCR ($n$ = 5). **(F)** Western blotting analysis of HIF1α in the penumbra area ($n$ = 3). Data are presented as the mean ± SD. *p<0.05 vs. SHAM group, #p<0.05 vs. MCAO group.

FOXC1, SREBF1, YY1, and NF1C were shown to regulate more than one candidate gene, thus suggesting a high level of interaction within the ferroptosis-related gene-TF network.

## Discussion

Ferroptosis has been widely studied in neoplastic disease, and its role in neuronal cell death is becoming well established (Lu et al., 2017; Datta et al., 2020). Previous research showed that ferroptosis aggravates the outcome of CIRI; hence, its inhibition may represent a novel therapeutic direction (Tuo et al., 2017). However, the molecular events and signaling pathways associated with ferroptosis induction in IS have not been thoroughly investigated.

The HIF-1 signaling pathway is activated under hypoxic conditions and acts as a master regulator of multiple pathological processes in IS by modulating glucose metabolism, angiogenesis, erythropoiesis, and cell survival (Pan et al., 2021). A rapid and transient increase in the

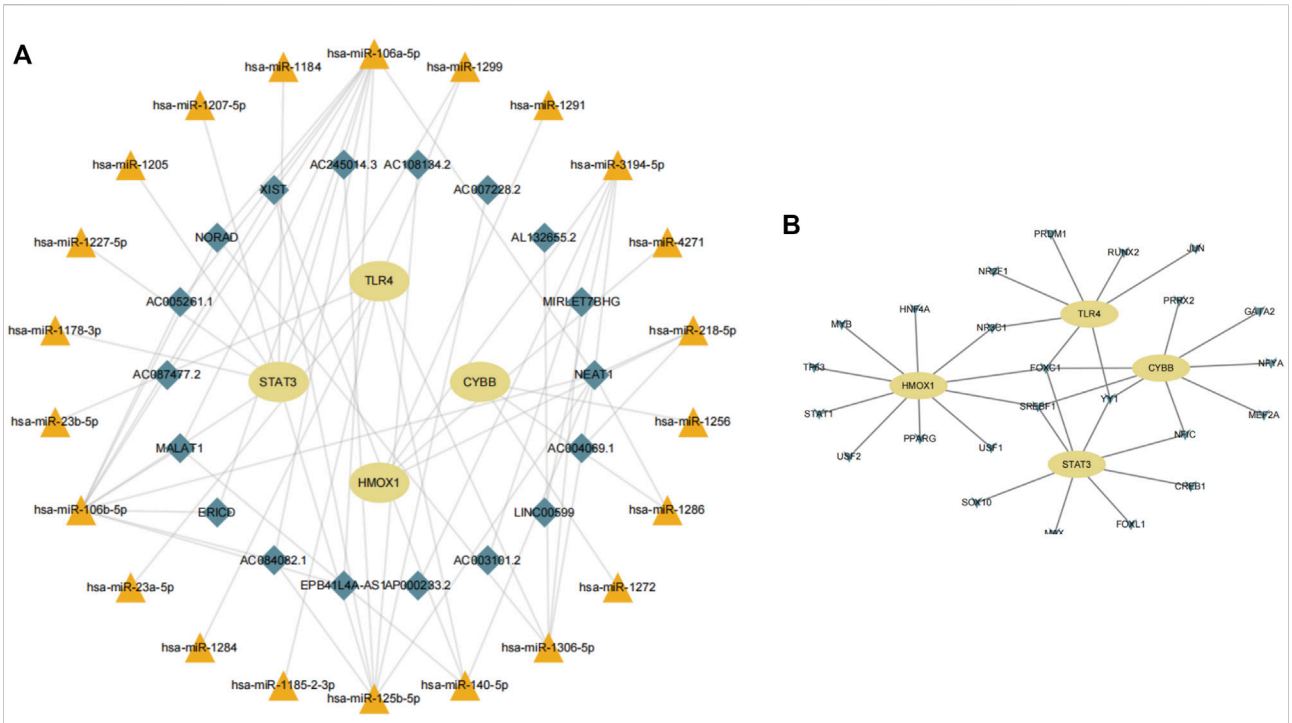


FIGURE 9
**(A)** Construction of a gene-miRNA-lncRNA interaction network. **(B)** Identification of potential TFs.

activation of the HIF-1 signaling pathway in brain endothelial cells is responsible for blood-brain barrier disruption, especially during severe and sustained hypoxia (Yeh et al., 2007; Yan et al., 2011). A previous study confirmed that activation of the HIF-1 signaling pathway is closely related to ferroptosis (Li et al., 2020). Therefore, HIF-1 signaling activation may play a crucial role in ferroptosis induction during IS.

In the present study, we identified four essential ferroptosis-related genes involved in the pathogenesis of IS and predicted, for these candidate genes, a regulatory non-coding RNA network as well as several putative TFs. By intersecting the GSE61616 and FerrDb dataset, we identified 33 ferroptosis-related DEGs, including 28 upregulated and five downregulated genes. Functional enrichment analysis of these DEGs showed that they were mainly clustered in the HIF-1 signaling pathway. Then, nine hub genes, *Il6*, *TXNIP*, *NFE212*, *HMOX1*, *TLR4*, *STAT3*, *ATF3*, *HSPB1*, and *CYBB*, were identified by PPI and MCODE analysis in cluster 1. Notably, four of the nine hub genes (*HMOX1*, *TLR4*, *STAT3*, and *CYBB*) were also enriched in the HIF-1 signaling pathway, a finding that suggested their central involvement in ferroptosis-mediated neuronal death in CIRI.

*HMOX1* encodes heme oxygenase 1, an enzyme involved in the catabolism of cellular heme induced by various pro-oxidant and inflammatory stimuli. Animal studies indicated that HO-1 expression in the brain is induced by stroke and plays, *via* activation of Nrf2, a protective role by exerting antioxidant, antiapoptotic, anti-inflammatory, and vasorelaxant effects (Bereczki et al., 2018). Studies have demonstrated that HO-1 expression in brain tissue is significantly increased within 24 h after IS, which is consistent with the results of our bioinformatics analysis and returns to baseline levels after several months. In our mouse model of IS, we verified that the mRNA level of *HMOX1* in the penumbra region was significantly increased compared to non-infarcted brain tissue from sham-operated mice. In addition, we found that GPX4 protein levels were downregulated in affected brain tissue from mice with MCAO-induced IS. Recent research on cognitive impairment after CIRI concluded that HO-1 levels were negatively correlated with the extent of ferroptosis 14 days after reperfusion (Fu et al., 2022). Interestingly, our animal experiments showed that DEX treatment rescued GPX4 expression in MCAO mice. Although this may be related to the fact that in this study DEX treatment mildly decreased HMOX-1 mRNA expression, the specific mechanisms need to be confirmed by further experiments.

*STAT3* belongs to the signal transducer and activator of the transcription family of proteins. Interestingly, *STAT3* activation during stroke was shown to exert pro-inflammatory and anti-inflammatory effects on different cell types and stages (Qi and Yang, 2014). Upregulation of *STAT3* in microglia was shown to exacerbate CIRI by promoting the expression of various pro-inflammatory factors, including TNF-α and IL-6 (Hu et al., 2017; Bousoik and Montazeri Aliabadi, 2018). In the present work, the

upregulation of *STAT3* mRNA observed in the ischemic penumbra area of MCAO mice was consistent with the results of the aforementioned study, and *STAT3* levels in peripheral blood also have considerable diagnostic efficacy for acute ischemic stroke (AIS). Of note, recent studies indicated that *STAT3* expression critically regulates ferroptosis in various diseases, including acute lung injury and lymphoma (Qiang et al., 2020; Schmitt et al., 2021). However, the impact of *STAT3* signaling on IS-related ferroptosis remains unexplored. Thus, although further confirmatory experiments are warranted, the present findings suggest that *STAT3* might be an important therapeutic target to inhibit ferroptosis in IS.

The *CYBB* gene encodes the cytochrome b-245 beta chain, also known as NADPH oxidase 2 (NOX2). This enzyme is one of the major ROS-producing isoforms in IS and is closely associated with poor outcomes. Consistent with the results of our study, *CYBB* was found to be significantly upregulated in brain tissue from mice with experimental IS(Li et al., 2014). In addition, in our previous study, we observed that silencing of *CYBB* in microglia notably reduced neuronal apoptosis in a co-culture system (Zeng et al., 2018). These findings are thus consistent with evidence indicating that *CYBB* is an important ferroptosis driver and hence a promising therapeutic target to reduce ferroptosis during stroke.

The *TLR4* gene encodes a member of the Toll-like receptor (TLR) family of proteins, which show increased expression during stroke through multiple pathways (Caso et al., 2007). Recent studies have identified the possible involvement of *TLR4* in post-stroke neuroinflammation, specifically in neutrophil differentiation and CNS infiltration, thus highlighting the regulation of *TLR4* at the peripheral level in stroke (García-Culebras et al., 2019). The present study reported the upregulation of *TLR4* expression in peripheral blood of ischemic stroke patients from the GEO database and verified that in brain tissue of MCAO mice, which is consistent with the results of previous studies. As a ferroptosis driver, its role in hypoxic-ischemic brain damage-induced ferroptosis and brain homeostasis has been validated by Zhu's study (Zhu et al., 2021). As expected, in the present study, GPX4 levels were negatively correlated with *TLR4* mRNA levels in brain tissue from MCAO mice. Hence, we speculate that *TLR4* may aggravate CIRI by promoting ferroptosis and oxidative stress. However, further research is needed to elucidate the mechanisms by which *TLR4* triggers ferroptosis in IS.

The results of our bioinformatics analysis were corroborated in a mouse model of MCAO-induced IS. In addition, we evaluated the effect of DEX, a sedative agent with analgesic and anti-ferroptosis actions, on both IS severity and the expression of the above four ferroptosis-related genes (Gao et al., 2019; Ross and Siegel, 2021; She et al., 2021). In line with previous findings, qRT-PCR assays showed *HMOX1*, *CYBB*, *STAT3*, and *TLR4* were significantly upregulated after IS induction. In our MCAO model, DEX reversed this effect. Recent studies have found that DEX exerts a protective effect by modulating the HIF-1 signaling pathway, improving mitochondrial function, and inhibiting ferroptosis in endothelial cells (She et al., 2021). However, whether DEX attenuates ferroptosis in IS and whether this effect is associated with inhibition of HIF-1 signaling has not been so far determined. Our study demonstrated that DEX significantly reduced oxidative stress in the brain and reduced circulating levels of pro-inflammatory cytokines in MCAO mice. Furthermore, DEX also reversed the downregulation of GPX4, a key negative regulator of ferroptosis, and the upregulation of ferroptosis-related gene expression induced by IS. Therefore, these findings suggest plausible mechanisms by which DEX therapy may reduce ferroptosis-mediated neuronal death in stroke.

To further investigate the factors that may affect the expression of our candidate genes, we identified TFs that may bind to their promoter regions. In addition, based on the four candidate genes, an mRNA-miRNA-lncRNA network was constructed. Of the 22 miRNAs obtained by targeting the four candidate genes, hsa-miR-1299 was found to bind to more than one mRNA. Studies on hsa-miR-1299 unmasked its inhibitory role on tumor cell proliferation (Zhang et al., 2020) but have not addressed its potential role in IS. However, the top-ranking predicted miRNAs were hsa-miR-106a-5p and hsa-miR-106b-5p. miR-106 is associated with microglial activation and neuroinflammatory diseases (Liu et al., 2021). Given the complexity of its regulatory network, miR-106 may represent an essential target for the regulation of stroke. LncRNAs represent promising targets for the diagnosis and treatment of various diseases. These non-coding RNAs have diverse functions and can interact with and regulate the expression of various endogenous molecules, including miRNAs(Bao et al., 2021; Bridges et al., 2021). In the present study, nine out of the 22 retrieved miRNAs were known targets of lncRNAs. Of these, NEAT1 may regulate up to eight miRNAs. Based on the neuroprotective role of NEAT1 (Ni et al., 2020; Zhou et al., 2022) we propose that NEAT1 may regulate, via a ceRNA network, the expression of ferroptosis-related genes in IS through mutual interactions with multiple miRNAs among the 24 TFs identified, FOXC1, SREBF1, and YY1 were found to target three of the four candidate genes. The upregulation of FOXC1 has been shown to alleviate neuroinflammation in mice with ischemic brain injury (He et al., 2021). Interestingly, YY1-induced upregulation of NEAT1 led to inflammatory damage following oxygen-glucose deprivation and reperfusion injury in microglia (Chen et al., 2019; Han and Zhou, 2019), thus contradicting the widely recognized neuroprotective role of NEAT. Whether this effect is or is not cell-type specific requires further investigation.

## Conclusion

We identified four candidate ferroptosis-related genes, *HMOX1*, *CYBB*, *STAT3*, and *TLR4*, which may be involved in

neuronal ferroptosis in CIRI. In addition, we showed that DEX treatment reduced infarct volume, improved sensorimotor function, and downregulated the expression of ferroptosis-related genes in mice with MCAO-induced IS. These genes may thus serve as new therapeutic targets to prevent or attenuate ferroptosis and thus improve prognosis in stroke patients. In addition, we predicted through bioinformatics analyses a set of miRNAs, lncRNAs, and TFs that may regulate the above candidate genes. The results of this study may broaden our understanding of IS and provide new concepts for its treatment. However, there are some limitations in the present work. Due to the disease characteristics, we could not apply gene expression data from human brain tissue for analysis, nor were we able to collect enough brain tissue from AIS patients to validate our findings. Furthermore, we did not perform experimental validation of the predicted miRNAs, lncRNAs, and TFs, therefore, further verification is required.

## Data availability statement

The datasets analyzed for this study can be found in the GEO database (www.ncbi.nlm.nih.gov/geo/). The accession numbers can be found in the article.

## Ethics statement

The animal study was reviewed and approved by the Animal Care and Use Committee of the Second Affiliated Hospital of Harbin Medical University.

## Author contributions

CL designed the study, performed experiments, analyzed data, and wrote the manuscript. ZL performed experiments and analyzed data. HX approved the implementation of the study, refined this study, reviewed the manuscript, and was responsible for financial support.

## Acknowledgments

We would like to thank all members for their kind comments.

## Conflict of interest

The authors declare that the research was conducted in the absence of any commercial or financial relationships that could be construed as a potential conflict of interest.

## Publisher's note

All claims expressed in this article are solely those of the authors and do not necessarily represent those of their affiliated organizations, or those of the publisher, the editors and the reviewers. Any product that may be evaluated in this article, or claim that may be made by its manufacturer, is not guaranteed or endorsed by the publisher.

## References

Bao, W. W., Shi, Y. L., Ma, Y., Qu, X. H., Pang, G. M., and Yang, L. (2021). MiR-590-5p regulates cell proliferation, apoptosis, migration and invasion in oral squamous cell carcinoma by targeting RECK. *Histol. Histopathol.* 36 (3), 355–365. doi:10.14670/hh-18-306

Bereczki, D., Jr., Balla, J., and Bereczki, D. (2018). Heme oxygenase-1: Clinical relevance in ischemic stroke. *Curr. Pharm. Des.* 24 (20), 2229–2235. doi:10.2174/1381612824666180717101104

Bouet, V., Boulouard, M., Toutain, J., Divoux, D., Bernaudin, M., Schumann-Bard, P., et al. (2009). The adhesive removal test: A sensitive method to assess sensorimotor deficits in mice. *Nat. Protoc.* 4 (10), 1560–1564. doi:10.1038/nprot.2009.125

Bousoik, E., and Montazeri Aliabadi, H. (2018). Do we know jack" about jak? A closer look at JAK/STAT signaling pathway. *Front. Oncol.* 8, 287. doi:10.3389/fonc.2018.00287

Bridges, M. C., Daulagala, A. C., and Kourtidis, A. (2021). LNCcation: lncRNA localization and function. *J. Cell Biol.* 220 (2), e202009045. doi:10.1083/jcb.202009045

Caso, J. R., Pradillo, J. M., Hurtado, O., Lorenzo, P., Moro, M. A., and Lizasoain, I. (2007). Toll-like receptor 4 is involved in brain damage and inflammation after experimental stroke. *Circulation* 115 (12), 1599–1608. doi:10.1161/circulationaha.106.603431

Chen, F., Chen, J., Yang, L., Liu, J., Zhang, X., Zhang, Y., et al. (2019). Extracellular vesicle-packaged HIF-1α-stabilizing lncRNA from tumour-associated macrophages regulates aerobic glycolysis of breast cancer cells. *Nat. Cell Biol.* 21 (4), 498–510. doi:10.1038/s41556-019-0299-0

Datta, A., Sarmah, D., Mounica, L., Kaur, H., Kesharwani, R., Verma, G., et al. (2020). Cell death pathways in ischemic stroke and targeted pharmacotherapy. *Transl. Stroke Res.* 11 (6), 1185–1202. doi:10.1007/s12975-020-00806-z

Fang, K. M., Cheng, F. C., Huang, Y. L., Chung, S. Y., Jian, Z. Y., and Lin, M. C. (2013). Trace element, antioxidant activity, and lipid peroxidation levels in brain cortex of gerbils after cerebral ischemic injury. *Biol. Trace Elem. Res.* 152 (1), 66–74. doi:10.1007/s12011-012-9596-1

Fu, C., Wu, Y., Liu, S., Luo, C., Lu, Y., Liu, M., et al. (2022). Rehmannioside A improves cognitive impairment and alleviates ferroptosis via activating PI3K/AKT/Nrf2 and SLC7A11/GPX4 signaling pathway after ischemia. *J. Ethnopharmacol.* 289, 115021. doi:10.1016/j.jep.2022.115021

Gao, M., Monian, P., Pan, Q., Zhang, W., Xiang, J., and Jiang, X. (2016). Ferroptosis is an autophagic cell death process. *Cell Res.* 26 (9), 1021–1032. doi:10.1038/cr.2016.95

Gao, Y., Yin, H., Zhang, Y., Dong, Y., Yang, F., Wu, X., et al. (2019). Dexmedetomidine protects hippocampal neurons against hypoxia/reoxygenation-induced apoptosis through activation HIF-1α/p53 signaling. *Life Sci.* 232, 116611. doi:10.1016/j.lfs.2019.116611

García-Culebras, A., Durán-Laforet, V., Peña-Martínez, C., Moraga, A., Ballesteros, I., Cuartero, M. I., et al. (2019). Role of *TLR4* (Toll-Like receptor 4) in N1/N2 neutrophil programming after stroke. *Stroke* 50 (10), 2922–2932. doi:10.1161/strokeaha.119.025085

Guan, X., Li, X., Yang, X., Yan, J., Shi, P., Ba, L., et al. (2019). The neuroprotective effects of carvacrol on ischemia/reperfusion-induced hippocampal neuronal impairment by ferroptosis mitigation. *Life Sci.* 235, 116795. doi:10.1016/j.lfs.2019.116795

Han, B., Jiang, W., Liu, H., Wang, J., Zheng, K., Cui, P., et al. (2020). Upregulation of neuronal PGC-1α ameliorates cognitive impairment induced by chronic cerebral hypoperfusion. *Theranostics* 10 (6), 2832–2848. doi:10.7150/thno.37119

Han, D., and Zhou, Y. (2019). YY1-induced upregulation of lncRNA NEAT1 contributes to OGD/R injury-induced inflammatory response in cerebral microglial cells via Wnt/β-catenin signaling pathway. *Vitro Cell. Dev. Biol. Anim.* 55 (7), 501–511. doi:10.1007/s11626-019-00375-y

He, T., Shang, J., Gao, C., Guan, X., Chen, Y., Zhu, L., et al. (2021). A novel SIRT6 activator ameliorates neuroinflammation and ischemic brain injury via EZH2/FOXC1 axis. *Acta Pharm. Sin. B* 11 (3), 708–726. doi:10.1016/j.apsb.2020.11.002

Hu, G. Q., Du, X., Li, Y. J., Gao, X. Q., Chen, B. Q., and Yu, L. (2017). Inhibition of cerebral ischemia/reperfusion injury-induced apoptosis: Nicotiflorin and JAK2/*STAT3* pathway. *Neural Regen. Res.* 12 (1), 96–102. doi:10.4103/1673-5374.198992

Jahan, R., Saver, J. L., Schwamm, L. H., Fonarow, G. C., Liang, L., Matsouaka, R. A., et al. (2019). Association between time to treatment with endovascular reperfusion therapy and outcomes in patients with acute ischemic stroke treated in clinical practice. *Jama* 322 (3), 252–263. doi:10.1001/jama.2019.8286

Li, H., Wang, Y., Feng, D., Liu, Y., Xu, M., Gao, A., et al. (2014). Alterations in the time course of expression of the nox family in the brain in a rat experimental cerebral ischemia and reperfusion model: Effects of melatonin. *J. Pineal Res.* 57 (1), 110–119. doi:10.1111/jpi.12148

Li, Y., Cao, Y., Xiao, J., Shang, J., Tan, Q., Ping, F., et al. (2020). Inhibitor of apoptosis-stimulating protein of p53 inhibits ferroptosis and alleviates intestinal ischemia/reperfusion-induced acute lung injury. *Cell Death Differ.* 27 (9), 2635–2650. doi:10.1038/s41418-020-0528-x

Liao, Y., Cheng, J., Kong, X., Li, S., Li, X., Zhang, M., et al. (2020). HDAC3 inhibition ameliorates ischemia/reperfusion-induced brain injury by regulating the microglial cGAS-STING pathway. *Theranostics* 10 (21), 9644–9662. doi:10.7150/thno.47651

Liu, J., Ai, P., Sun, Y., Yang, X., Li, C., Liu, Y., et al. (2021). Propofol inhibits microglial activation via miR-106b/pi3k/akt Axis. *Front. Cell. Neurosci.* 15, 768364. doi:10.3389/fncel.2021.768364

Liu, J., Guo, Z. N., Yan, X. L., Huang, S., Ren, J. X., Luo, Y., et al. (2020). Crosstalk between autophagy and ferroptosis and its putative role in ischemic stroke. *Front. Cell. Neurosci.* 14, 577403. doi:10.3389/fncel.2020.577403

Longa, E. Z., Weinstein, P. R., Carlson, S., and Cummins, R. (1989). Reversible middle cerebral artery occlusion without craniectomy in rats. *Stroke* 20 (1), 84–91. doi:10.1161/01.str.20.1.84

Lu, B., Chen, X. B., Ying, M. D., He, Q. J., Cao, J., and Yang, B. (2017). The role of ferroptosis in cancer development and treatment response. *Front. Pharmacol.* 8, 992. doi:10.3389/fphar.2017.00992

Ni, X., Su, Q., Xia, W., Zhang, Y., Jia, K., Su, Z., et al. (2020). Knockdown lncRNA NEAT1 regulates the activation of microglia and reduces AKT signaling and neuronal apoptosis after cerebral ischemic reperfusion. *Sci. Rep.* 10 (1), 19658. doi:10.1038/s41598-020-71411-1

Pan, Z., Ma, G., Kong, L., and Du, G. (2021). Hypoxia-inducible factor-1: Regulatory mechanisms and drug development in stroke. *Pharmacol. Res.* 170, 105742. doi:10.1016/j.phrs.2021.105742

Qi, Q. R., and Yang, Z. M. (2014). Regulation and function of signal transducer and activator of transcription 3. *World J. Biol. Chem.* 5 (2), 231–239. doi:10.4331/wjbc.v5.i2.231

Qiang, Z., Dong, H., Xia, Y., Chai, D., Hu, R., and Jiang, H. (2020). Nrf2 and *STAT3* alleviates ferroptosis-mediated IIR-ALI by regulating SLC7A11. *Oxid. Med. Cell. Longev.* 2020, 5146982. doi:10.1155/2020/5146982

Qu, M., Zhao, J., Zhao, Y., Sun, J., Liu, L., Wei, L., et al. (2021). Vascular protection and regenerative effects of intranasal DL-3-N-butylphthalide treatment after ischaemic stroke in mice. *Stroke Vasc. Neurol.* 6 (1), 74–79. doi:10.1136/svn-2020-000364

Ross, D., and Siegel, D. (2021). The diverse functionality of NQO1 and its roles in redox control. *Redox Biol.* 41, 101950. doi:10.1016/j.redox.2021.101950

Schmitt, A., Xu, W., Bucher, P., Grimm, M., Konantz, M., Horn, H., et al. (2021). Dimethyl fumarate induces ferroptosis and impairs NF-κB/*STAT3* signaling in DLBCL. *Blood* 138 (10), 871–884. doi:10.1182/blood.2020009404

She, H., Hu, Y., Zhou, Y., Tan, L., Zhu, Y., Ma, C., et al. (2021). Protective effects of dexmedetomidine on sepsis-induced vascular leakage by alleviating ferroptosis via regulating metabolic reprogramming. *J. Inflamm. Res.* 14, 6765–6782. doi:10.2147/jir.S340420

Shi, J., Yu, T., Song, K., Du, S., He, S., Hu, X., et al. (2021). Dexmedetomidine ameliorates endotoxin-induced acute lung injury *in vivo* and *in vitro* by preserving mitochondrial dynamic equilibrium through the HIF-1a/HO-1 signaling pathway. *Redox Biol.* 41, 101954. doi:10.1016/j.redox.2021.101954

Tao, T., Liu, M., Chen, M., Luo, Y., Wang, C., Xu, T., et al. (2020). Natural medicine in neuroprotection for ischemic stroke: Challenges and prospective. *Pharmacol. Ther.* 216, 107695. doi:10.1016/j.pharmthera.2020.107695

Tuo, Q. Z., Lei, P., Jackman, K. A., Li, X. L., Xiong, H., Li, X. L., et al. (2017). Tau-mediated iron export prevents ferroptotic damage after ischemic stroke. *Mol. Psychiatry* 22 (11), 1520–1530. doi:10.1038/mp.2017.171

Ueta, T., Inoue, T., Furukawa, T., Tamaki, Y., Nakagawa, Y., Imai, H., et al. (2012). Glutathione peroxidase 4 is required for maturation of photoreceptor cells. *J. Biol. Chem.* 287 (10), 7675–7682. doi:10.1074/jbc.M111.335174

Wang, J., Shi, Y., Zhang, L., Zhang, F., Hu, X., Zhang, W., et al. (2014). Omega-3 polyunsaturated fatty acids enhance cerebral angiogenesis and provide long-term protection after stroke. *Neurobiol. Dis.* 68, 91–103. doi:10.1016/j.nbd.2014.04.014

Xu, J., Chen, Z., Yu, F., Liu, H., Ma, C., Xie, D., et al. (2020). IL-4/STAT6 signaling facilitates innate hematoma resolution and neurological recovery after hemorrhagic stroke in mice. *Proc. Natl. Acad. Sci. U. S. A.* 117 (51), 32679–32690. doi:10.1073/pnas.2018497117

Yan, H. F., Zou, T., Tuo, Q. Z., Xu, S., Li, H., Belaidi, A. A., et al. (2021). Ferroptosis: Mechanisms and links with diseases. *Signal Transduct. Target. Ther.* 6 (1), 49. doi:10.1038/s41392-020-00428-9

Yan, J., Zhou, B., Taheri, S., and Shi, H. (2011). Differential effects of HIF-1 inhibition by YC-1 on the overall outcome and blood-brain barrier damage in a rat model of ischemic stroke. *PLoS One* 6 (11), e27798. doi:10.1371/journal.pone.0027798

Yeh, W. L., Lu, D. Y., Lin, C. J., Liou, H. C., and Fu, W. M. (2007). Inhibition of hypoxia-induced increase of blood-brain barrier permeability by YC-1 through the antagonism of HIF-1alpha accumulation and VEGF expression. *Mol. Pharmacol.* 72 (2), 440–449. doi:10.1124/mol.107.036418

Yu, S. P., Tung, J. K., Wei, Z. Z., Chen, D., Berglund, K., Zhong, W., et al. (2019). Optochemogenetic stimulation of transplanted iPS-NPCs enhances neuronal repair and functional recovery after ischemic stroke. *J. Neurosci.* 39 (33), 6571–6594. doi:10.1523/jneurosci.2010-18.2019

Zeng, X., Ren, H., Zhu, Y., Zhang, R., Xue, X., Tao, T., et al. (2018). Gp91phox (NOX2) in activated microglia exacerbates neuronal damage induced by oxygen glucose deprivation and hyperglycemia in an *in vitro* model. *Cell. Physiol. biochem.* 50 (2), 783–797. doi:10.1159/000494243

Zhang, K., Tu, M., Gao, W., Cai, X., Song, F., Chen, Z., et al. (2019). Hollow prussian blue nanozymes drive neuroprotection against ischemic stroke via attenuating oxidative stress, counteracting inflammation, and suppressing cell apoptosis. *Nano Lett.* 19 (5), 2812–2823. doi:10.1021/acs.nanolett.8b04729

Zhang, L., Bu, Z., Shen, J., Shang, L., Chen, Y., and Wang, Y. (2020). A novel circular RNA (hsa_circ_0000370) increases cell viability and inhibits apoptosis of FLT3-ITD-positive acute myeloid leukemia cells by regulating miR-1299 and S100A7A. *Biomed. Pharmacother.* 122, 109619. doi:10.1016/j.biopha.2019.109619

Zhou, Z. W., Ren, X., Zheng, L. J., Li, A. P., and Zhou, W. S. (2022). LncRNA NEAT1 ameliorate ischemic stroke via promoting Mfn2 expression through binding to Nova and activates Sirt3. *Metab. Brain Dis.* 37 (3), 653–664. doi:10.1007/s11011-021-00895-1

Zhu, K., Zhu, X., Sun, S., Yang, W., Liu, S., Tang, Z., et al. (2021). Inhibition of *TLR4* prevents hippocampal hypoxic-ischemic injury by regulating ferroptosis in neonatal rats. *Exp. Neurol.* 345, 113828. doi:10.1016/j.expneurol.2021.113828

frontiers | Frontiers in Cellular Neuroscience

TYPE Original Research
PUBLISHED 09 March 2023
DOI 10.3389/fncel.2023.1106268



OPEN ACCESS

EDITED BY
Yevgeny Berdichevsky,
Lehigh University, United States

REVIEWED BY
Helen E. Scharfman,
Nathan Kline Institute for Psychiatric Research, United States
Michel J.A.M. van Putten,
University of Twente, Netherlands

*CORRESPONDENCE
Roustem Khazipov
✉ roustem.khazipov@inserm.fr

†These authors have contributed equally to this work

SPECIALTY SECTION
This article was submitted to Cellular Neuropathology, a section of the journal Frontiers in Cellular Neuroscience

RECEIVED 23 November 2022
ACCEPTED 16 February 2023
PUBLISHED 09 March 2023

CITATION
Gainutdinov A, Juzekaeva E, Mukhtarov M and Khazipov R (2023) Anoxic spreading depolarization in the neonatal rat cortex *in vitro*.
Front. Cell. Neurosci. 17:1106268.
doi: 10.3389/fncel.2023.1106268



# Anoxic spreading depolarization in the neonatal rat cortex *in vitro*

Azat Gainutdinov[1,2†], Elvira Juzekaeva[1†], Marat Mukhtarov[1] and Roustem Khazipov[1,2*]

[1]Laboratory of Neurobiology, Institute of Fundamental Medicine and Biology, Kazan Federal University, Kazan, Russia, [2]INMED—INSERM, Aix-Marseille University, Marseille, France

Anoxic spreading depolarization (aSD) is a hallmark of ischemic injury in the cerebral cortex. In adults, aSD is associated with rapid and nearly complete neuronal depolarization and loss of neuronal functions. While ischemia also evokes aSD in the immature cortex, developmental aspects of neuronal behavior during aSD remain largely unknown. Here, using oxygen-glucose deprivation (OGD) ischemia model in slices of the postnatal rat somatosensory cortex, we found that immature neurons displayed much more complex behaviors: they initially moderately depolarized during aSD, then transiently repolarised (for up to tens of minutes), and only then passed to terminal depolarization. The ability to fire action potentials was maintained in neurons mildly depolarized during aSD without reaching the level of depolarization block, and these functions were regained in the majority of immature neurons during post-aSD transient repolarization. The amplitude of depolarization and the probability of depolarization block during aSD increased, whereas transient post-SD repolarization levels and duration, and associated recovery in neuronal firing decreased with age. By the end of the first postnatal month, aSD acquired an adult-like phenotype, where depolarization during aSD merged with terminal depolarization and the phase of transient recovery was lost. Thus, changes in neuronal function during aSD undergo remarkable developmental changes that may contribute to lower susceptibility of the immature neurons to ischemia.

KEYWORDS

**patch-clamp, membrane potential, ischemia, somatosensory cortex, spreading depolarization, neonate, development**

## Introduction

Anoxic Spreading Depolarization (aSD) is a hallmark of ischemic brain injury (Andrew et al., 2022). aSD develops within several minutes after metabolic deprivation and manifests as a wave of collective and nearly complete neuronal depolarization, and depression of electrical activity largely due to depolarization block of action potentials (APs; Somjen, 2001; Dreier and Reiffurth, 2015). aSD is associated with the large negative shift of the extracellular field potential and an increase in tissue light transmittance caused by cytotoxic cell edema (Rader and Lanthorn, 1989; Aitken et al., 1998; Dzhala et al., 2000; Joshi and Andrew, 2001; Juzekaeva et al., 2017, 2018, 2020; Toyoda et al., 2021; Vinokurova et al., 2022). aSD is a highly energy consuming event which aggravates metabolic deficits and initiates intracellular cascades leading to cell death (Somjen, 2001; Strong et al., 2002; Hartings et al., 2003, 2017; Dreier, 2011; Dreier et al., 2013, 2022; Dreier and Reiffurth, 2015). In the OGD model of brain ischemia using submerged brain slices, which simulates the condition of severe global brain ischemia, cortical neurons typically undergo terminal SD to zero mV without recovery (Rader and Lanthorn, 1989; Tanaka et al., 1997; Toyoda et al., 2021; Andrew et al., 2022).

While an immature brain is more tolerant to metabolic deprivation, ischemic/hypoxic brain damage remains a major problem in peri- and neonatology (Saugstad, 2011; Douglas-Escobar and Weiss, 2015). As in adults, aSD occurs during metabolic deprivation in the neonatal cortex and heralds neuronal death. However, in neonates, aSD occurs at much longer delays (up to tens of minutes in the neonatal neocortex and ∼1 h in the fetal hippocampus at term) from the onset of hypoxia/OGD than in the adults consistent with higher tolerance of the immature brain to metabolic deprivation (Cherubini et al., 1989; Luhmann and Kral, 1997; Dzhala et al., 2000, 2001; Tyzio et al., 2006), and with lower proneness of the neonatal cortex to SD in general (Bures, 1957; Schade, 1959; Richter et al., 1998; Hertelendy et al., 2019; Andrew et al., 2022). However, aSD in the neocortex during the neonatal period [P0–10 in rodents, which corresponds to a period from mid-gestation to term in human fetus (Khazipov and Luhmann, 2006; Clancy et al., 2007; Colonnese et al., 2010; Colonnese and Khazipov, 2012; Luhmann and Khazipov, 2018; Khazipov and Milh, 2018)] at the cellular level remains largely unexplored. Here, we addressed this question using whole-cell recordings from L4 neurons in slices of the somatosensory whisker-related barrel cortex from 3 to 31 days old rats in the OGD model. We chose this area because it is highly sensitive to ischemia and prone to SD (Lin et al., 1990; Bogdanov et al., 2016; Kaufmann et al., 2017; Juzekaeva et al., 2017, 2020). Our main finding is that neonatal neurons only moderately depolarize during aSD, then transiently repolarise, and only then pass to terminal depolarization. The ability to fire action potentials persists in neurons showing mild depolarization during aSD without reaching the level of depolarization block, and these functions are regained in the majority of immature neurons during post-aSD transient repolarization phase. Thus, immature neurons display protracted in time and complex aSD phenotype with a phase of transient recovery. We suggest that these developmentally unique features of aSD contribute to higher tolerance of the immature brain to ischemia.

# Materials and methods

## Brain slices

Wistar rats (3–31 days old) of either sex were used. Animals were decapitated under isoflurane anesthesia (5%), the brain was rapidly removed and placed in ice-cold (2–5°C) oxygenated (95% $O_2$–5% $CO_2$) artificial cerebrospinal fluid (ACSF) of the following composition (in mM): NaCl 126, KCl 3.5, $CaCl_2$ 2, $MgCl_2$ 1.3, $NaHCO_3$ 25, $NaH_2PO_4$ 1.2, and glucose 20 (pH 7.4). Four hundred μm thick thalamocortical slices were cut using a PELCO easiSlicer$^{TM}$ vibratome (Ted Pella, Inc., Redding, CA, USA). A total of $n$ = 58 slices obtained from 43 rats were used (1 slice/rat: $n$ = 29 rats; 2 slices/rat: $n$ = 13 rats; 3 slices/rat: $n$ = 1 rat). Data from all slices were pooled for analysis; n indicates the number of slices. Slices containing the barrel cortex were selected by anatomical coordinates (Khazipov et al., 2015) and the presence of barrel structures in L4. Slices were first kept in ACSF for 30 min at 32°C and then at room temperature (20–22°C) for at least 1 h before use. For recordings, slices were placed into a submerged chamber and superfused with oxygenated ACSF at 30–32°C at a flow rate of 10 ml/min. Oxygen/glucose deprivation (OGD) was induced by superfusion with ACSF in which $N_2$ replaced $O_2$ and sucrose replaced glucose at equimolar concentration.

## Electrophysiological recordings

For electrophysiological recordings, slices were placed in the recording chamber under an upright microscope BX51WI (Olympus, Tokyo, Japan) equipped with a dry 4×/0.10 Plan N objective and a water immersed 40×/0.80 LUMPlanFL N objective. L4 neurons were identified at 40× magnification using infrared-differential interference contrast (IR-DIC) microscopy. Visual patch-clamp recordings were performed using a MultiClamp 700B (Axon Instruments, Union City, CA, USA) amplifier as described previously (Juzekaeva et al., 2018). Patch electrodes were made from borosilicate glass capillaries (BF150-86-10, Sutter Instrument, Novato, CA, USA) and had a resistance of 4–7 MΩ. The pipette (intracellular) solution contained (in mM) 131 potassium gluconate, 4 KCl, 10 HEPES, 10 phosphocreatine, 4 MgATP, and 0.3 $Na_2GTP$ (adjusted to pH 7.3 with KOH). 200-ms suprathreshold depolarizing current pulses were applied every 10 s to examine the ability of neurons to fire APs and monitor the membrane resistance ($R_m$). Extracellular DC recordings of the local field potentials (LFP) were performed in the barrel cortex using glass pipette electrodes pulled from borosilicate glass capillaries (BF150-86-10, Sutter Instrument, Novato, CA, USA) with resistances of 2–3 MΩ when filled with ACSF. LFP recordings were performed in voltage-clamp DC mode, then currents were inverted and voltage calibrated using 5 mV steps. Extracellular and patch-clamp recordings were digitized at 32 kHz with a Digidata 1440A interface card (Axon Instruments) and analyzed offline using MATLAB (MathWorks, Natick, MA, USA) routines. Optical intrinsic signal (OIS) recordings were performed at 4× magnification. The boundaries of layer 4 were discerned by barrel-shaped structures at 4× magnification and high cell density in layer 4 at 40× magnification. The slice was illuminated by a halogen lamp with a 775 nm bandpass filter. Images were acquired using a QIClick-R-F-M-12 CCD camera (QImaging, Surrey, BC, Canada) at 696 × 520 or 1,392 × 1,040 pixel resolution at 1 frame/2.5 s acquisition rate.

## Data analysis

Experimental data were processed using MATLAB environment (MathWorks, USA). Matlab's Signal Processing Toolbox functions were used for peak detection procedures. Patch-clamp $E_m$ recordings were down-sampled to 1 Hz and filtered using a median filter within sliding 30 s window with 1 s time step to eliminate responses to depolarizing current steps. aSD was detected as a wave of $E_m$ depolarization occurring in association with characteristic negative LFP shifts and OIS signals (Juzekaeva et al., 2020). The time corresponding to the peak depolarization during aSD was defined as aSD time. aSD amplitude was defined as a difference between $E_m$ at the aSD peak and the

baseline $E_m$ values between -3 and -1 min time interval before the aSD peak. The term of transient recovery (TR) was applied for a phase of transient $E_m$ repolarization between aSD and terminal depolarization (TD). TR duration was defined as a time period between aSD peak (TR onset = time of aSD peak) and transition to TD was determined at the peak of the first $E_m$ derivative ($dE_m/dt$, dt = 1 min). The peak of $E_m$ repolarization during TR was taken as the TR time reference point. Action potentials (AP) in response to suprathreshold current steps were detected from raw signals using *peak detection* function as events with the peak prominence of >3 mV and 5 ms minimum inter-peak interval. Two neurons at P25 with the electrophysiological phenotype of fast spiking interneurons showed no differences in response to OGD and were pooled with other neurons in the P25–31 age group. DC LFP signals were down-sampled to 1 kHz and low-pass filtered using 1 s sliding window. OIS was calculated using the first-frame subtraction approach: OIS (t) = (I (t) − I0)/I0, where I (t)—pixel intensity at the moment t, I0—time-averaged pixel intensity in the preconditioned control period (1 min). The resulting frames were filtered with a 2 × 2 Gaussian filter. Regions of interest (ROIs) were selected as square areas near the recording site. OIS traces were calculated as the average OIS signal in the selected ROIs.

## Statistical analysis

Statistical analysis was performed using the MATLAB Statistics toolbox. Pooled data are presented as median, 25th (Q1), and 75th (Q3) percentiles in boxplots or shaded areas. A two-sided Wilcoxon rank sum test was performed to assess the difference between groups. For testing binomial data and proportions we used Two Sample Z-Test for Proportions. Correlations were calculated as Spearman's correlation coefficient with the exact *p*-value. The level of significance was kept at $p < 0.05$.

# Results

In the present study, we explored the dynamics of the resting membrane potential ($E_m$) and neuronal firing during OGD in slices of the barrel cortex of rats aged from P3 to P31 using whole-cell current-clamp recordings of L4 neurons and concomitant extracellular recordings of LFP, and optical intrinsic signals (OIS) imaging. Perfusion with OGD-solution evoked aSD in all neurons at all ages. However, aSD amplitude and aSD delay after OGD onset, and post-aSD $E_m$ dynamics were variable and age-dependent (**Figure 1**). $E_m$ dynamics aligned against aSD peak (marked by red dots) and sorted by the aSD amplitude in neurons from newborn (P3–8) and juvenile (P16–31) rats are shown in **Figures 1A,B**, respectively. Overall, in the newborn animals, aSD was smaller in amplitude, and was typically followed by a remarkable phase of transient recovery (TR) of $E_m$ before a passage to terminal plateau depolarization (TD) near 0 mV. The level and duration of TR were more pronounced in the cases with low-amplitude aSDs, where TR could last for up to 15 min. Only a few neurons with large-amplitude aSD showed "adult-like" aSD phenotype of permanent depolarization without TR in the newborn animals. In contrast, neurons in juvenile rats typically displayed large amplitude aSDs without TR, or, less frequently, with a short and small TR (**Figure 1B**). At the group level, aSD delay from the OGD onset shortened (**Figure 1C**), whereas aSD amplitude increased (**Figure 1D**) with the animals' age. Thus, aSD in the immature neurons is smaller in amplitude and displays a unique intermediate phase of TR before a passage to TD.

We further explored changes in neuronal firing by injecting suprathreshold depolarizing current steps. Exemplary whole-cell recordings from L4 neurons in P4 and P30 rats are presented in **Figure 2**. P4 neuron displayed small-amplitude aSD associated with a mild transient drop in membrane resistance ($R_m$) followed by 10 min-long TR with a regain in $R_m$ values (**Figures 2A,C**). TR was followed by nearly complete depolarization during TD. Action potentials (APs) could be reliably evoked by depolarizing current in this neuron not only through the pre-aSD period, but also during aSD and TR phase (*nota bene*: no depolarization block in this case!), and were lost only after a passage to TD (**Figure 2E**, **Supplementary Figure 1**). In a P30 neuron (**Figure 2B**), membrane potential rapidly dropped to −20 mV, then showed brief and little recovery during TR phase, followed by TD to 0 mV, during which $R_m$ displayed an apparent increase to ∼1 GOhm (**Figure 2D**) presumably reflecting a passage from whole-cell to outside-out due to tissue displacement caused by aSD-triggered edema (Juzekaeva et al., 2018, 2020). In the P30 neuron, APs were completely suppressed, without any recovery starting from aSD (**Figure 2F**, **Supplementary Figure 1**). Thus, while the P30 neuron displayed an "adult-like" phenotype of rapid and irreversible $E_m$ loss during aSD together with an irreversible depression of APs, P4 neuron showed persistence of APs during aSD and TR, pointing to a qualitative difference of aSD in the immature neuron. All aSDs of different amplitudes were associated with a characteristic negative local field potential shift (**Figure 3B**), and a concomitant wave of increase in the brain tissue light transparency propagating across the entire slice of the cortex during OIS recordings (**Figures 3C,D**). Peak depolarization during aSD in L4 neurons was attained simultaneously with the peak negativity of the local field potential and the peak of light transparency during aSD wave in the vicinity of the recorded neuron (**Figure 3E**).

We next analyzed in detail the age-dependence in the depolarization level attained during aSD and associated changes in the neuronal firing (**Figure 4**). In the newborn animals (P3–8), neurons depolarized, on average, to ∼−40 mV, and APs persisted in their vast majority (73%; $n$ = 16 of 22 cells) at the aSD peak (**Figure 4A**, see also AP raster plots on **Figure 4B**). In the juvenile rats, peak depolarization during aSD attained on average −18 mV at P16–24, and −7 mV at P25–31. Along with a developmental increase in the aSD $E_m$ levels, the proportion of neurons maintaining the ability to fire APs during aSD decreased to 27% at P16–24 ($n$ = 4 of 15 cells), and to 10% at P25–31 ($n$ = 1 of 10 cells; **Figures 4A,B**). Loss of neuronal firing depended on the depolarization level attained during aSD within all age groups, as illustrated by responses to depolarizing steps in different cells on insets in **Figure 4A**. To estimate the AP inactivation threshold, we analyzed neuronal firing during the rising aSD phase. We found that failure in evoking APs by depolarizing current

10.3389/fncel.2023.1106268

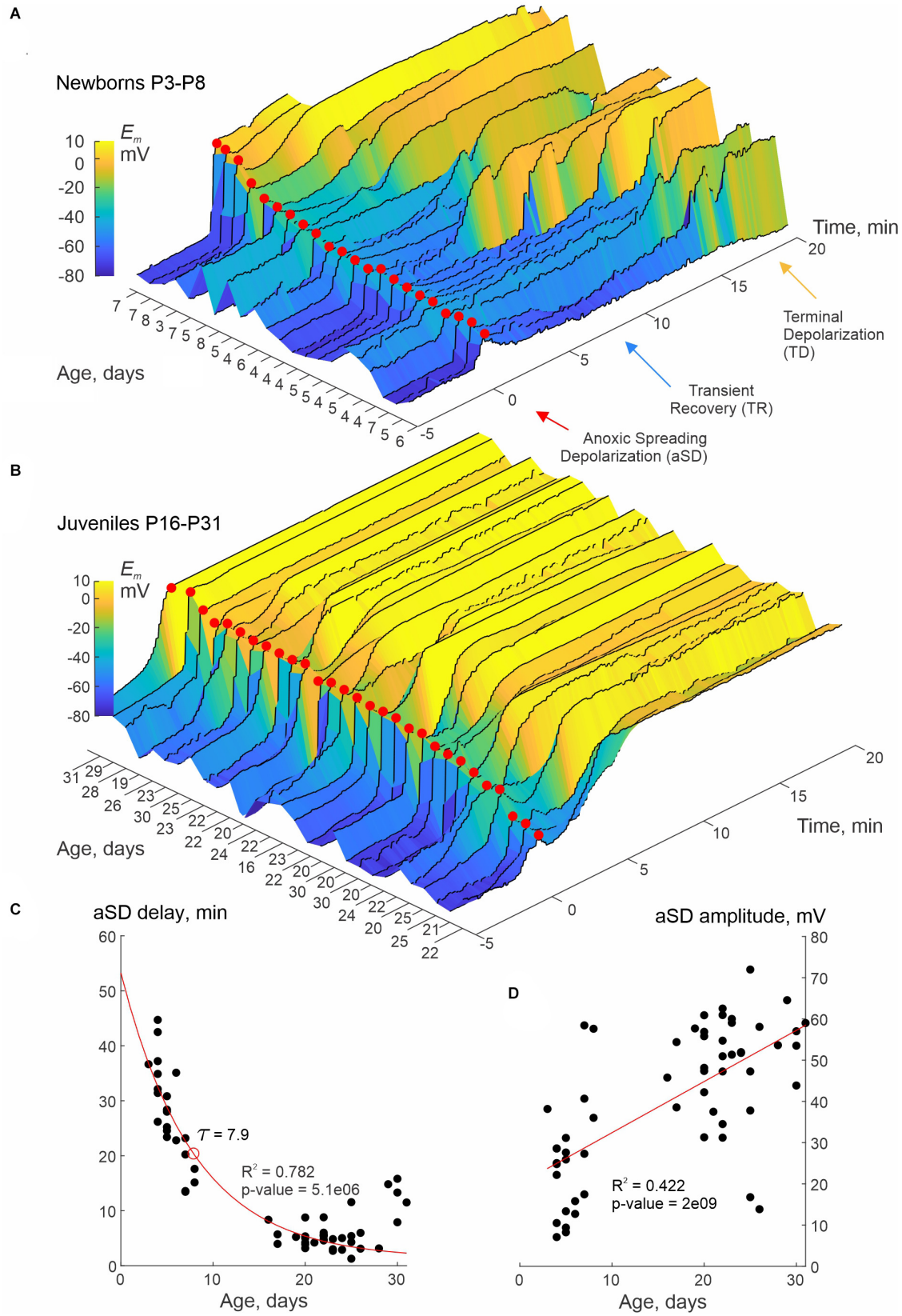


FIGURE 1
Smaller aSD amplitude and transient recovery of membrane potential in neurons of newborn rat cerebral cortex. **(A,B)** Dynamics of membrane potential ($E_m$) in L4 neurons recorded in whole-cell current-clamp mode during oxygen-glucose deprivation (OGD) in slices of somatosensory cortex prepared from neonatal (P3–8) **(A)** and juvenile (P16–31) **(B)** rats. The $E_m$ signal was low-pass filtered with a median filter using a sliding

(*Continued*)

FIGURE 1 (Continued)
window of 30 s and increment of 1 s to eliminate spikes and the responses to depolarizing current steps. Color-coded $E_m$ values are plotted with reference to aSD ($T$ = 0, red dots). Each trace corresponds to an individual neuron, the age of the animal is indicated on the left horizontal axis. Note the smaller aSD amplitude and the phase of transient $E_m$ recovery (TR) before the transition to terminal depolarization (TD) in the neonatal group. Pooled data from $n$ = 22 **(A)** and $n$ = 29 **(B)** neurons. In some cases, the recordings stopped when the TD reached a plateau. **(C,D)** Delay of aSD peak from the OGD onset **(A)** and aSD amplitude **(B)** as a function of age. Each dot corresponds to an individual neuron. The aSD amplitude was calculated from the baseline $E_m$ values between −3 and −1 min time interval before the aSD peak. The red lines show exponential **(A)** and linear **(B)** regression. Pooled data from $n$ = 58 neurons from P3 to P31 rats.

steps occurred when $E_m$ attained ∼−30 mV (**Figure 4C**). Thus, loss of neuronal firing during aSD critically depends on whether neuronal depolarization attains AP inactivation threshold, which barely occurs in the newborn neurons showing mainly moderate depolarization during aSD.

The phase of transient recovery in $E_m$ and neuronal firing also showed age-dependence. Neurons from newborn rats displayed more negative TR $E_m$ values and longer duration TR phase, and more frequently maintained AP firing than neurons from the juvenile group (**Figures 5A,B**; see also **Figures 2** and **4B**). Group data on the amplitude and time of TR at its peak negativity (the latter taken as a time reference point) and corresponding values of aSD and TD at their onset, neuronal firing during the TR phase, and age-dependence of TR amplitude and duration are summarized in **Figure 5C**. Noteworthy, the level and duration of TR negatively correlated with aSD amplitude and were more prominent in the newborn animals (**Figure 5C**, left and bottom violin plots). Also, TR lasted longer in cells with more negative levels of $E_m$ recovery, and this was associated with longer duration of neuronal firing during the TR phase (**Figures 5D,E**). Similar to aSD, the ability of cells to fire APs during the TR phase depended on whether the cell repolarized below the AP inactivation threshold at around -30 mV, which typically occurred in the newborn group (**Figures 5C,D**). The final TD $E_m$ values also showed an age dependence, reaching more negative values at P3–P8: −7.6 (−14.7 − +0.4) mV ($n$ = 17) than at P16–P24: +4.82 (−2.40 − +7.6) mV ($n$ = 22; $p$ = 0.00055) and at P25–P31: +10.5 (+0.0 − +14.6) mV ($n$ = 11; $p$ = 0.00038).

## Discussion

The main finding of the present study is that aSD has several developmentally unique features, including graded levels of depolarization and long-lasting post-aSD phase of transient repolarization preceding TD in the newborn cortical neurons. Furthermore, neuronal functions such as the ability to generate APs are barely depressed during neonatal aSD and TR phase. These results highlight a critical developmental difference in the response of the immature brain to metabolic deprivation and significantly broaden the SD spectrum from a developmental perspective.

Based on studies in the adult brain, aSD has been classically viewed as a binary process, during which neurons rapidly and completely lose their membrane potential (Rader and Lanthorn, 1989; Tanaka et al., 1997; Somjen, 2001; Dreier and Reiffurth, 2015; Toyoda et al., 2021; Andrew et al., 2022). Generative mechanisms of aSD are fundamentally similar to SD in other models and conditions, and involve an increase in extracellular potassium, glutamate, and activation of voltage and ligand—gated conductances (Leao, 1944, 1947; Somjen, 2001; Dreier, 2011; Pietrobon and Moskowitz, 2014; Ayata and Lauritzen, 2015; Dreier and Reiffurth, 2015; Hartings et al., 2017; Andrew et al., 2022). While $E_m$ repolarizes after SD in the metabolically preserved tissue with a pivotal contribution of Na, K—ATPase, under conditions of metabolic deprivation aSD is associated with permanent depolarization as energy sources to fuel Na, K—ATPase are limited. We found that in the immature neurons, aSD was associated with only mild levels of depolarization and was followed by transient repolarization during TR-phase. The stationary state of complete $E_m$ loss, which characterizes full-size aSD in adult neurons, was achieved only during the subsequent TD-phase. Small amplitude aSD likely produces smaller disturbance in the ionic gradients and thus less aggravates the metabolic status of the immature neurons than full-size aSD, leaving energy sources fueling Na, K—ATPase to restore $E_m$ after aSD during the TR phase. This is consistent with the inverse relationships between aSD amplitude and TR: indeed, TR was more prominent in neurons with small amplitude aSDs. Several developmental factors may contribute to unique aSD features in neonates. First, immature neurons have lower metabolic rate and thus are more tolerant to metabolic deprivation consistent with much longer aSD delays than in adults (Cherubini et al., 1989; Luhmann and Kral, 1997; Dzhala et al., 2000, 2001; Tyzio et al., 2006). Second, cortex in the newborns is less prone to SD in general, that could be due to large extracellular space, low levels of synaptic connectivity, the small density of ionic channels, and their different developmental properties (Bures, 1957; Schade, 1959; Richter et al., 1998; Hertelendy et al., 2019; Andrew et al., 2022). We propose that a combination of these developmental factors endows immature neurons with on one hand, higher tolerance to metabolic deprivation, and on the other hand—a lower ability to support mutual depolarization *via* synaptic and ephaptic mechanisms in the SD genesis, explaining small aSD amplitude and TR in the immature neurons. Importantly, these unique developmental aSD features could be only revealed in the present study using whole-cell $E_m$ recordings. aSD *per se* was also reliably detected as a characteristic negative shift of the extracellular field potential and increase in tissue transparency during OIS recordings [**Figure 3** and References Luhmann and Kral, 1997; Dzhala et al., 2000, 2001; Tyzio et al., 2006)], but the magnitude of these signals weakly correlated with the level of neuronal depolarization during aSD (**Supplementary Figure 1**). Also, TR and TD did not have clear manifestations during extracellular field potential and OIS recordings. Because we performed whole-cell recordings from only one neuron in the preparation, we cannot conclude whether the level of depolarization during aSD, level and duration of TR, and transition to TD were uniform in the entire neuronal population. Moreover, the lack of extracellular LFP and OIS manifestations suggests that TR duration and transition to TD are likely desynchronized between neurons. The desynchronized transition to TD in the immature cortex may result from metabolic

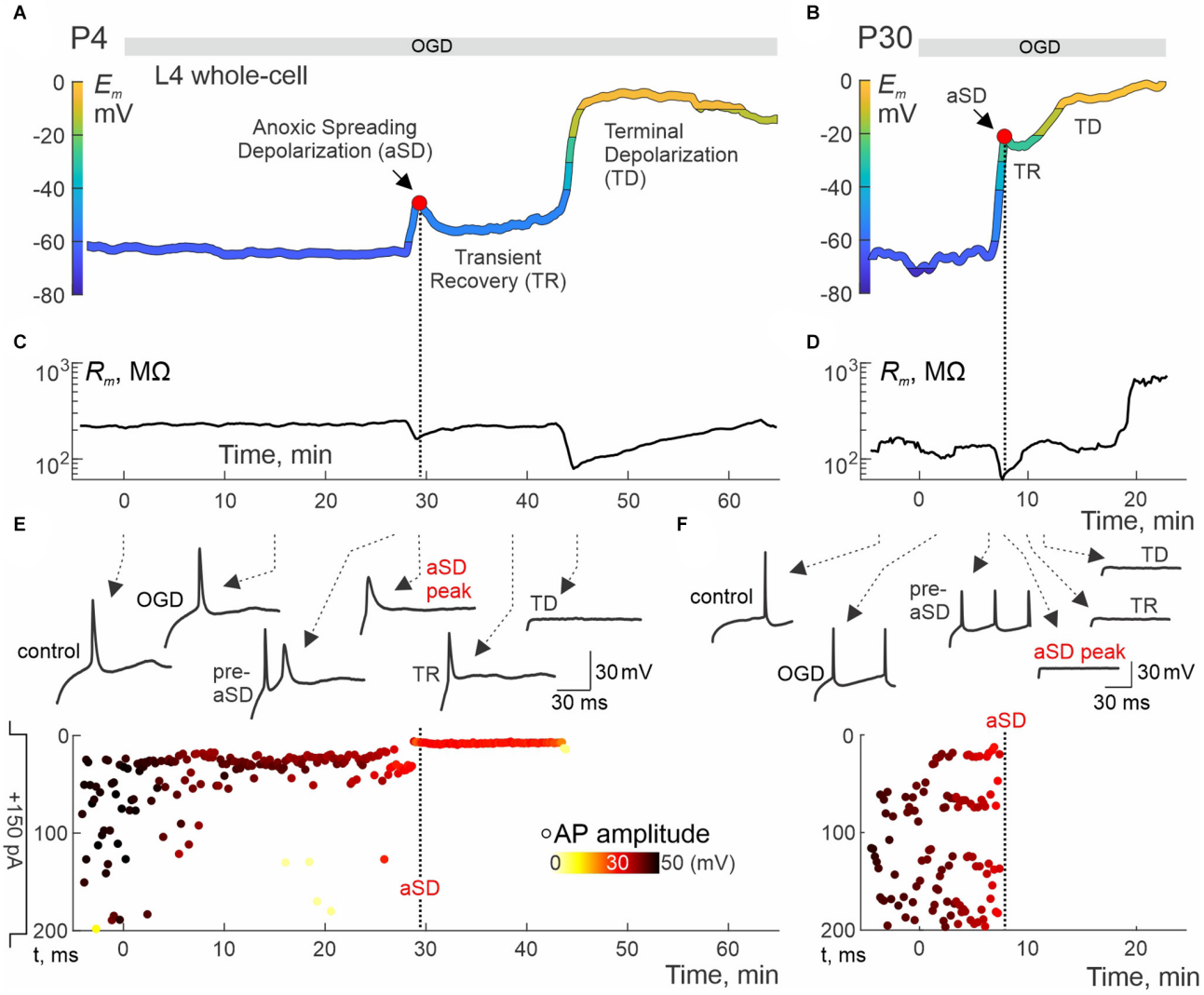


FIGURE 2
Immature neurons remain excitable during aSD and transient recovery phase. **(A,B)** Examples of $E_m$ recordings from L4 neurons in slices from P4 **(A)** and P30 **(B)** rats. $E_m$ traces are low-pass filtered and color-coded as in **Figure 1**. The exposure to OGD is indicated by the horizontal gray bar at the top. **(C,D)** Corresponding changes in input resistance ($R_m$). **(E,F)** Corresponding example responses to suprathreshold current steps at different time points indicated by arrows (top traces) and raster plots of APs evoked by suprathreshold (+150 pA, 200 ms) current steps (y-axis shows depolarizing step time (top: step start; bottom: step end); APs amplitude is color-coded) (bottom plots). Full trace examples are shown in **Supplementary Figure 1**. Note that the AP firing is maintained through the aSD and TR, and disappears only during the transition to TD in the P4 neuron, whereas in the P30 neuron APs irreversibly disappear as soon as aSD occurs. $T$ = 0 on the x-scale corresponds to the onset of OGD.

heterogeneity between neurons (e.g., due to their different age) and hence the different abilities to maintain $E_m$ during TR, greater extracellular space, low levels of synaptic connectivity, and low density of ion channels and hence smoother increases in extracellular glutamate and potassium. In future studies, it would be of interest to test this hypothesis using multiple whole-cell recordings, or calcium/voltage sensitive dye imaging. The latter approach could be advantageous in overcoming a problem of tissue swelling and displacement that starts after aSD and may cause loss of contact of the electrode with cell and apparent loss of $E_m$ during whole-cell recordings including a transition from whole-cell to outside-out configuration (**Figure 2B** and Juzekaeva et al., 2020). This artifact can lead to an underestimation of the TR duration, which may in fact be even longer than reported here, and can also affect the measurement of TD $E_m$ values. Interestingly, in the P25-P31 age group, we observed that TD $E_m$ reached positive values of ∼+10 mV, which may be due to a greater concentration of impermeable anions in the extracellular than in the intracellular space, a consequence of swelling and shrinkage of the extracellular space.

Our study also revealed that aSD in the neonates lacks the hallmark SD feature—depression of APs. In adults, at the aSD onset, when $E_m$ approaches values close to the AP threshold cortical neurons typically generate one or few APs, and then permanently lose neuronal firing upon further depolarization as a result of voltage-gated sodium channels inactivation and AP depolarization block (Grafstein, 1956; Dzhala et al., 2000, 2001; Canals et al., 2005). Synaptic activity may also display "paradoxical" recovery from

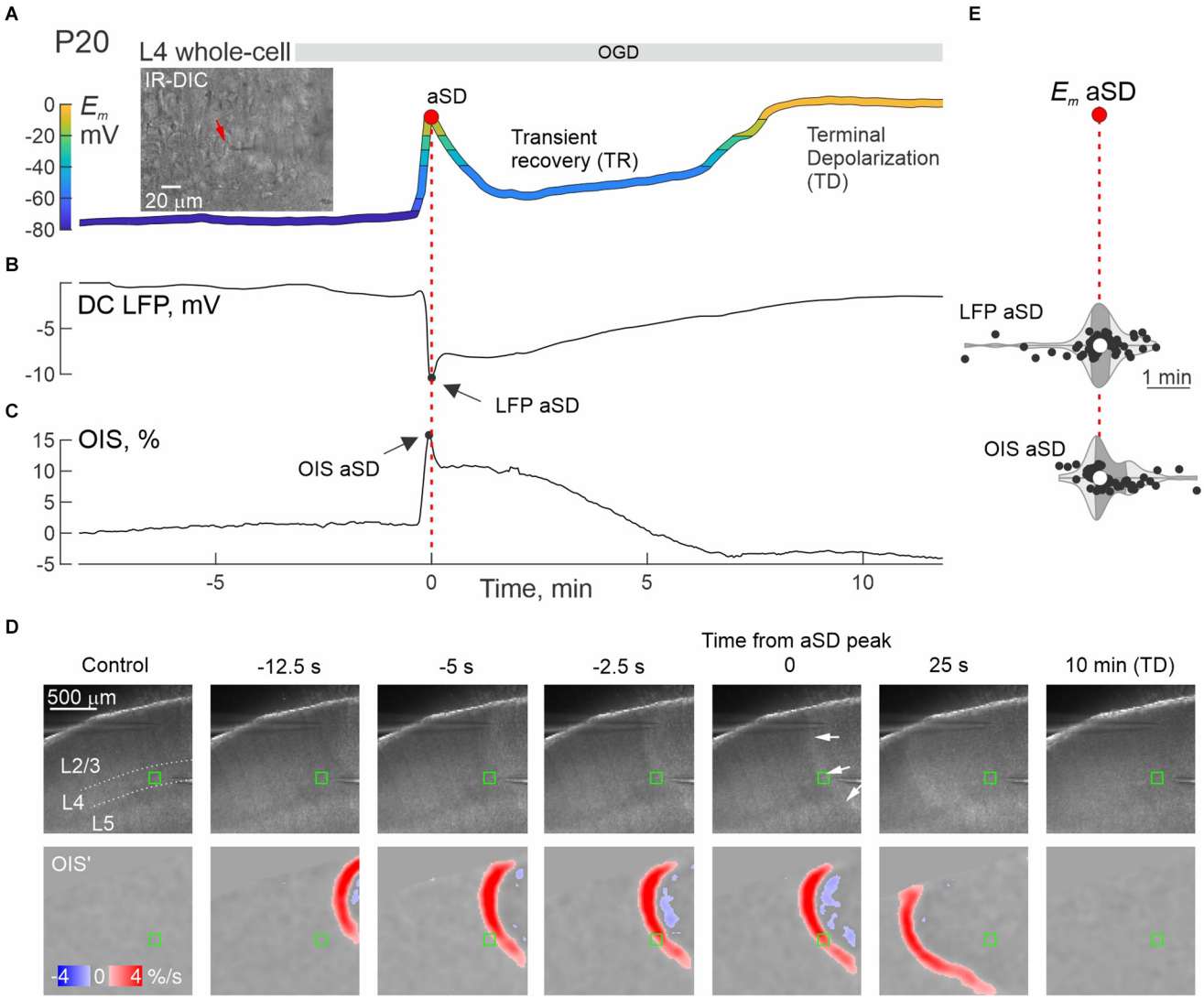


FIGURE 3
aSD correlates with negative LFP shifts and an increase in optical tissue transparency in the developing cortex. **(A–C)** Simultaneous whole-cell $E_m$ recordings from an L4 neuron **(A)**, extracellular DC-LFP recordings **(B)**, and OIS recordings **(C)** near the recorded neuron during OGD in a P20 rat somatosensory cortex slice. $T$ = 0 indicates aSD peak during whole-cell recordings ($E_m$—aSD). The inset on panel **(A)** shows an IR-DIC image of layer 4 (40x magnification), the neuron being recorded is marked with a red arrow. **(D)** Microphotograph of a slice (4x magnification, raw data, top panels) and the OIS first derivative (bottom panels) at different delays from aSD recorded from the L4 neuron shown on panel **(A)**. The region of interest (ROI) for OIS quantified in panel **(C)** is indicated by a green rectangle. **(E)** Distribution of aSD delays recorded by extracellular electrodes (LFP—aSD) and OIS (OIS—aSD) from aSD during whole-cell recordings ($E_m$—aSD, vertical dotted line). Hereafter, each dot corresponds to an individual cell/slice, the violin plots show the probability density of the data at different values smoothed by the kernel density estimator, the white circles are the median, and the dark shaded area is the interquartile range. Pooled data from $n$ = 58 cells/slices from P3 to P31 rats. There was no significant time lag between LFP—aSD ($p$ = 0.54), OIS—aSD ($p$ = 0.93, Wilcoxon rank sum test), and $E_m$—aSD.

non-spreading depression at the aSD onset followed by complete suppression of synaptic responses (Sick et al., 1987; Fowler, 1992; Khazipov et al., 1993; Zhu and Krnjevic, 1999; Dzhala et al., 2001). In contrast, we found that ability to fire APs persists during aSD, and that APs can be reliably triggered during post-aSD TR phase in the majority of neonatal neurons. Our results indicate that the persistence of neuronal firing is primarily due to mild levels of depolarization which barely reaches the threshold of AP inactivation in the immature neurons. Altogether, these findings point to significant developmental differences in aSD properties in immature neurons. We also propose that neonatal aSDs described in the present study broaden the existing SD spectrum (Somjen, 2001; Pietrobon and Moskowitz, 2014; Ayata and Lauritzen, 2015; Dreier and Reiffurth, 2015; Hartings et al., 2017) by adding to a family of full-sized SDs an immature phenotype with its notable mild depolarization levels, TR phase and lack of loss in neuronal functions. In future research, it would be interesting to determine the mechanisms underlying this peculiar phenotype of immature aSD, including the computational modeling approach (Zandt et al., 2013; Herreras and Makarova, 2020; Kalia et al., 2021).

How these unusual aSD features may impact hypoxic/ischemic injury in the neonatal brain? There is general agreement that aSD is a critical event during metabolic deprivation (Andrew et al., 2022).

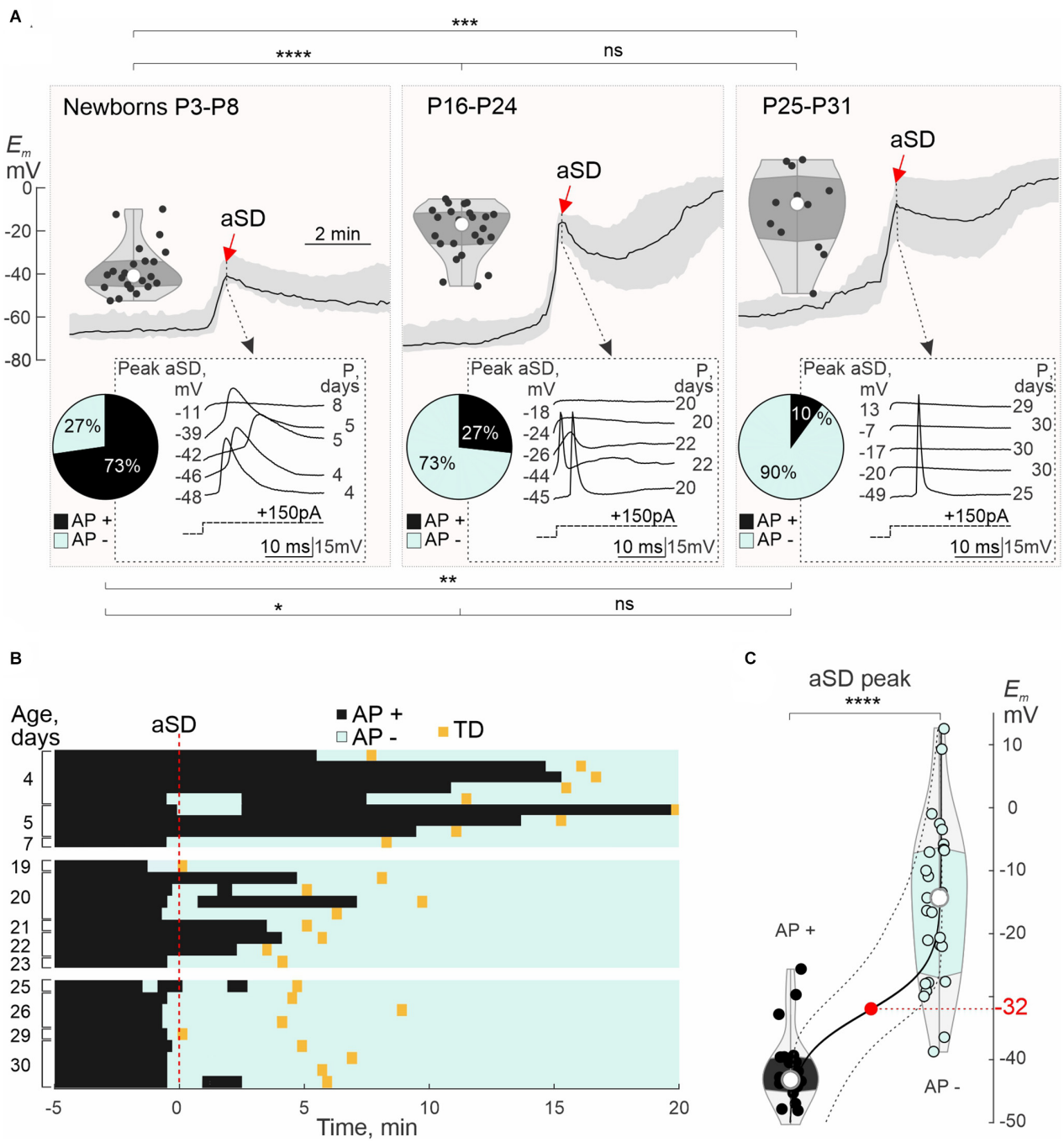


FIGURE 4
Postnatal changes in aSD peak value and neuronal firing during aSD: group data. **(A)** Top traces, grand average aSD (black trace—median *Em*; shaded area—interquartile range) and corresponding statistical plots of $E_m$ values at the aSD peak in L4 neurons from newborn (P3–P8, $n$ = 22 cells), and juvenile rats (P16–P24, $n$ = 24 cells; and P25–P31, $n$ = 12 cells). Gray insets below, examples of responses to depolarizing current steps at the aSD peak in five neurons from each age group, with the corresponding $E_m$ aSD peak value (left) and age (right). Circular histograms show neuronal firing at the aSD peak (black—AP+ neurons responding with APs to depolarizing steps, cyan—AP− neurons not showing APs in response to depolarizing steps). Note that in newborn animals, neuronal depolarization reaches only a weak level during aSD, that most newborn neurons retain neuronal firing during aSD, and that ability to fire APs during aSD diminishes with age. **(B)** Representative raster plots of APs evoked by depolarizing current steps (inter-step interval 10 s) in L4 neurons of different age groups during OGD-induced aSD ($T$ = 0, vertical red dashed line). The black and cyan bins denote responses with AP (AP+) and without AP (AP−), respectively. The transition to TD is indicated by a yellow rectangle. **(C)** Group data on neuronal firing during aSD as a function of peak $E_m$ depolarization during aSD. The black line is a binomial logistic regression fit, dashed lines are 95% confidence intervals for prediction. Half-probability of AP inactivation (or depolarization block) occurs during aSD attaining $E_m$ = −32 (−39/−24) mV [median (interquartile range)]. *, $P < 0.05$; **, $P < 0.01$; ***, $P < 0.0001$; ****, $P < 0.00001$; ns, not significant (Wilcoxon rank sum test).

In adult brain, aSDs are highly energy consuming events associated with a profound depletion of energy sources under conditions of a limited metabolic supply (Somjen, 2001; Strong et al., 2002; Hartings et al., 2003, 2017; Dreier et al., 2013, 2022;

10.3389/fncel.2023.1106268

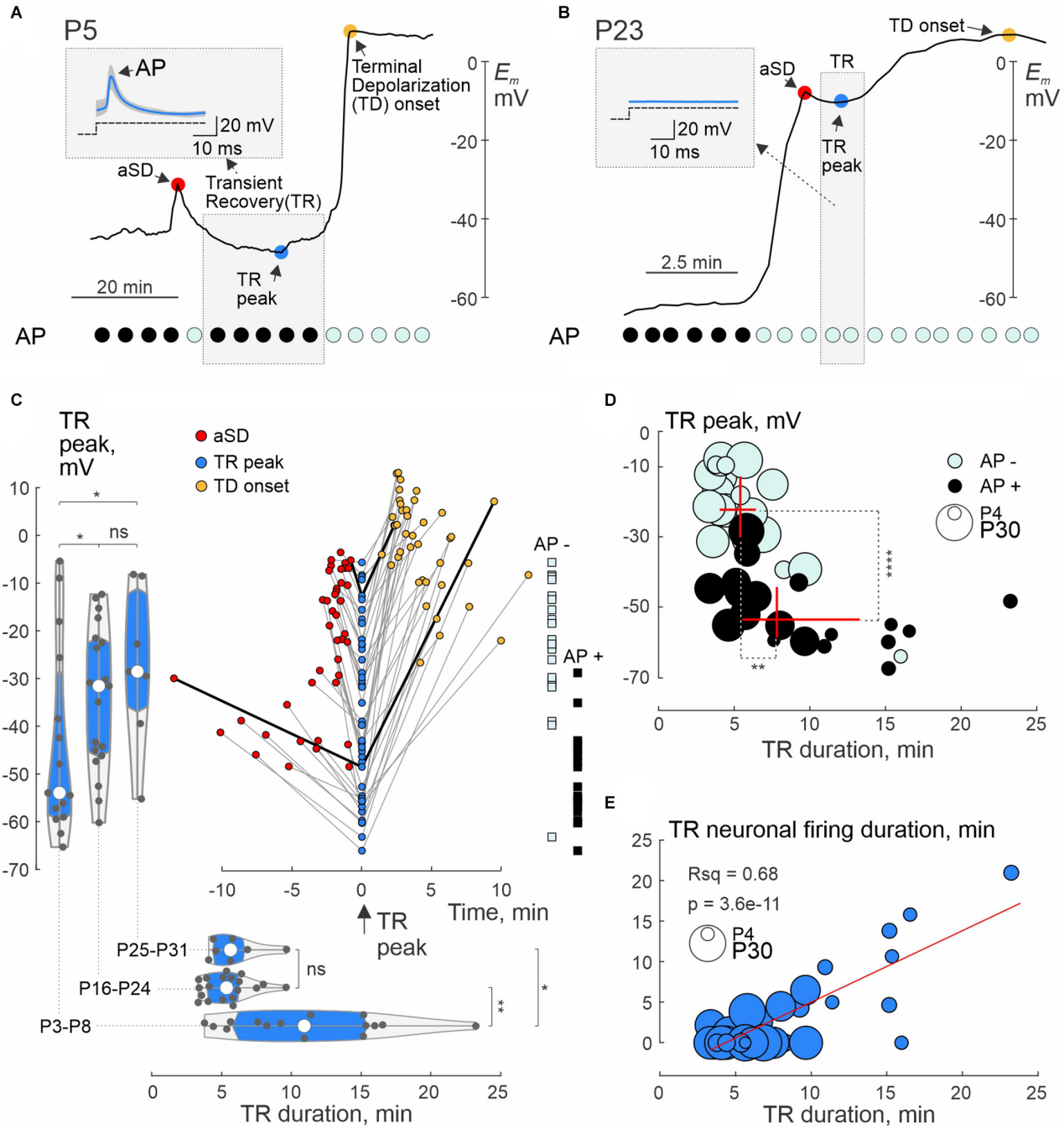


FIGURE 5
Postnatal changes in transient membrane potential recovery following aSD. **(A,B)** Examples of whole-cell recordings from L4 neurons in P5 **(A)** and P23 **(B)** rats. Red circle—peak aSD; blue circle—peak negativity during TR; TD—terminal depolarization. Top left insets—mean responses to depolarizing current steps during TR (median blue traces are superimposed on all gray traces). At the bottom are corresponding graphs indicating responses with APs (black circles) and without APs (cyan circles). Note the long TR with preservation of APs after a small aSD at P5, and weak short TR without APs at P23. **(C)** Summary plot of $E_m$ values achieved during TR, aSD, and TD in individual cells. The peak of negativity during TR is taken as a time reference point. TR, aSD, and TD from individual neurons are connected by gray lines, and values connected by black lines correspond to the examples shown in panels **(A)** and **(B)**. The left and bottom histograms show the distribution of maximum $E_m$ negativity achieved during TR and TR duration, respectively, in the three age groups. On the right, the distribution of TR—$E_m$ values according to the absence (AP–, cyan squares) and presence (AP+, black squares) of APs during TR. **(D)** Relationship between the TR—$E_m$ level and duration of TR as well as neuronal firing during the TR phase. Black (AP+) and cyan (AP–) circles indicate cells that showed or did not show APs in response to depolarizing steps during the TR phase, respectively. The age of the animal is coded by the size of the circle. The red crosses show the median ± interquartile range of TR—$E_m$ levels and duration of TR in the AP+ and AP– cell groups. Note the presence and longer persistence of neuronal firing in cells with more negative $E_m$ values reached during the TR phase. **(E)** The duration of the period within the TR phase, during which neurons retain the ability to fire APs in response to depolarizing steps, correlates with the duration of TR. The red line shows a linear regression fit. **(C–E)**: Pooled data from P3 to P8 ($n$ = 15), P16–P23 ($n$ = 19) and P25–P31 ($n$ = 7). Seventeen cells without TR were excluded from the analysis. *, $P < 0.05$; **, $P < 0.01$; ****, $P < 0.0001$; ns, not significant (Wilcoxon rank sum test).

Dreier and Reiffurth, 2015). Mild level aSDs in the neonatal neurons likely less disturb ionic gradients and thus consume less energy for their restoration. Therefore, it is conceivable that the inability to generate full-size aSDs is beneficial to the neonatal brain and may be a factor contributing to higher tolerance of the neonatal brain to hypoxia/ischemia. Indeed, a similar correlation between weak depolarization and higher tolerance to OGD was also observed in the adult hypothalamus (Brisson and Andrew, 2012). Yet, factors increasing energy consumption such as adenosine A1 receptor antagonists and drugs provoking epileptiform activity are known to accelerate the occurrence of aSD and neuronal death whereas energy-savers such as NKCC1 antagonists and oxytocin exert beneficial actions in the neonatal brain during metabolic deprivation (Dzhala et al., 2000; Tyzio et al., 2006; Khazipov et al., 2008). Even less energy consuming, immature aSD still should jeopardize metabolic status, and inevitably leads to delayed terminal depolarization if metabolic supply is not restored. Indeed, the transition to TD occurred faster in neurons with larger-size aSD. This suggests that aSD occurring simultaneously in the entire population of neurons recruited by aSD wave opens a time window during which neurons attain their cell-specific "commitment point" of irreversible $E_m$ loss and neuronal death at variable delays determined by the aSD size that is consistent with variable survival of neurons following aSD in the juvenile cortex (Juzekaeva et al., 2020). In future studies, it would also be interesting to determine how developmental changes in the composition of the intracellular milieu (notably chloride concentration) and extracellular metabolites (ketone bodies) influence the developmental changes in the aSD described in this study.

In conclusion, our study provides descriptions of aSD in the neonatal cortex at the cellular level. We have shown that aSD in the newborn cortical neurons displays several unique features, including mild levels of depolarization and transient depolarization. We also found that neuronal functions, including the ability to generate APs persist during aSD and TR in neurons with mild aSD. These results highlight a critical developmental difference in the response of the immature brain to metabolic deprivation and are important for understanding the development of cortical damage during hypoxia/ischemia in the neonatal brain.

## Data availability statement

The raw data supporting the conclusions of this article will be made available by the authors, without undue reservation.

## Ethics statement

The animal study was reviewed and approved by Local Ethical Committee of Kazan Federal University (#24/22.09.2020) and French National Institute of Health and Medical Research (APAFIS #16992-2020070612319346 v2). The animal experiments were carried out in compliance with the ARRIVE guidelines. Animal care and procedures were in accordance with EU Directive 2010/63/EU for animal experiments.

## Author contributions

RK conceptualized and drafted the manuscript. EJ, AG, and MM performed the experiments. AG analyzed data. AG, EJ, MM, and RK revised the manuscript and interpreted the data. All authors contributed to the article and approved the submitted version.

## Funding

This work was supported by RSF grant #22-15-00236.

## Conflict of interest

The authors declare that the research was conducted in the absence of any commercial or financial relationships that could be construed as a potential conflict of interest.

## Publisher's note

All claims expressed in this article are solely those of the authors and do not necessarily represent those of their affiliated organizations, or those of the publisher, the editors and the reviewers. Any product that may be evaluated in this article, or claim that may be made by its manufacturer, is not guaranteed or endorsed by the publisher.

## Supplementary material

The Supplementary Material for this article can be found online at: https://www.frontiersin.org/articles/10.3389/fncel.2023.1106268/full#supplementary-material.

## References

Aitken, P. G., Tombaugh, G. C., Turner, D. A., and Somjen, G. G. (1998). Similar propagation of SD and hypoxic SD-like depolarization in rat hippocampus recorded optically and electrically. *J. Neurophysiol.* 80, 1514–1521. doi: 10.1152/jn.1998.80.3.1514

Andrew, R. D., Hartings, J. A., Ayata, C., Brennan, K. C., wson-Scully, K. D., Farkas, E., et al. (2022). The critical role of spreading depolarizations in early brain injury: consensus and contention. *Neurocrit. Care* 37, 83–101. doi: 10.1007/s12028-021-01431-w

Ayata, C., and Lauritzen, M. (2015). Spreading depression, spreading depolarizations and the cerebral vasculature. *Physiol. Rev.* 95, 953–993. doi: 10.1152/physrev.00027.2014

Bogdanov, V. B., Middleton, N. A., Theriot, J. J., Parker, P. D., Abdullah, O. M., Ju, Y. S., et al. (2016). Susceptibility of primary sensory cortex to spreading depolarizations. *J. Neurosci.* 36, 4733–4743. doi: 10.1523/JNEUROSCI.3694-15.2016

Brisson, D. C., and Andrew, D. R. (2012). A neuronal population in hypothalamus that dramatically resists acute ischemic injury compared to neocortex. *J. Neurophysiol.* 108, 419–430. doi: 10.1152/jn.00090.2012

Bures, J. (1957). The ontogenetic development of steady potential differences in the cerebral cortex in animals. *Electroencephalogr. Clin. Neurophysiol.* 9, 121–130. doi: 10.1016/0013-4694(57)90116-5

Canals, S., Makarova, I., Lopez-Aguado, L., Largo, C., Ibarz, J. M., and Herreras, O. (2005). Longitudinal depolarization gradients along the somatodendritic axis of CA1 pyramidal cells: a novel feature of spreading depression. *J. Neurophysiol.* 94, 943–951. doi: 10.1152/jn.01145.2004

Cherubini, E., Ben-Ari, Y., and Krnjevic, K. (1989). Anoxia produces smaller changes in synaptic transmission, membrane potential and input resistance in immature rat hippocampus. *J. Neurophysiol.* 62, 882–895. doi: 10.1152/jn.1989.62.4.882

Clancy, B., Kersh, B., Hyde, J., Darlington, R. B., Anand, K. J., and Finlay, B. L. (2007). Web-based method for translating neurodevelopment from laboratory species to humans. *Neuroinformatics* 5, 79–94. doi: 10.1385/ni:5:1:79

Colonnese, M. T., Kaminska, A., Minlebaev, M., Milh, M., Bloem, B., Lescure, S., et al. (2010). A conserved switch in sensory processing prepares developing neocortex for vision. *Neuron* 67, 480–498. doi: 10.1016/j.neuron.2010.07.015

Colonnese, M., and Khazipov, R. (2012). Spontaneous activity in developing sensory circuits: Implications for resting state fMRI. *Neuroimage* 62, 2212–2221. doi: 10.1016/j.neuroimage.2012.02.046

Douglas-Escobar, M., and Weiss, M. D. (2015). Hypoxic-ischemic encephalopathy: a review for the clinician. *JAMA Pediatr.* 169, 397–403. doi: 10.1001/jamapediatrics.2014.3269

Dreier, J. P. (2011). The role of spreading depression, spreading depolarization and spreading ischemia in neurological disease. *Nat. Med.* 17, 439–447. doi: 10.1038/nm.2333

Dreier, J. P., Isele, T., Reiffurth, C., Offenhauser, N., Kirov, S. A., Dahlem, M. A., et al. (2013). Is spreading depolarization characterized by an abrupt, massive release of gibbs free energy from the human brain cortex? *Neuroscientist* 19, 25–42. doi: 10.1177/1073858412453340

Dreier, J. P., and Reiffurth, C. (2015). The stroke-migraine depolarization continuum. *Neuron* 86, 902–922. doi: 10.1016/j.neuron.2015.04.004

Dreier, J. P., Winkler, M. K. L., Major, S., Horst, V., Lublinsky, S., Kola, V., et al. (2022). Spreading depolarizations in ischaemia after subarachnoid haemorrhage, a diagnostic phase III study. *Brain* 145, 1264–1284. doi: 10.1093/brain/awab457

Dzhala, V., Ben-Ari, Y., and Khazipov, R. (2000). Seizures accelerate anoxia-induced neuronal death in the neonatal rat hippocampus. *Ann. Neurol.* 48, 632–640. doi: 10.1002/1531-8249(200010)48:4%3C632::AID-ANA10%3E3.3.CO;2-V

Dzhala, V., Khalilov, I., Ben Ari, Y., and Khazipov, R. (2001). Neuronal mechanisms of the anoxia-induced network oscillations in the rat hippocampus *in vitro*. *J. Physiol.* 536, 521–531. doi: 10.1111/j.1469-7793.2001.0521c.xd

Fowler, J. C. (1992). Escape from inhibition of synaptic transmission during in vitro hypoxia and hypoglycemia in the hippocampus. *Brain Res.* 573, 169–173. doi: 10.1016/0006-8993(92)90128-v

Grafstein, B. (1956). Mechanism of spreading cortical depression. *J. Neurophysiol.* 19, 154–171. doi: 10.1152/jn.1956.19.2.154

Hartings, J. A., Rolli, M. L., Lu, X. C., and Tortella, F. C. (2003). Delayed secondary phase of peri-infarct depolarizations after focal cerebral ischemia: relation to infarct growth and neuroprotection. *J. Neurosci.* 23, 11602–11610. doi: 10.1523/JNEUROSCI.23-37-11602.2003

Hartings, J. A., Shuttleworth, C. W., Kirov, S. A., Ayata, C., Hinzman, J. M., Foreman, B., et al. (2017). The continuum of spreading depolarizations in acute cortical lesion development: examining Leao's legacy. *J. Cereb. Blood Flow Metab.* 37, 1571–1594. doi: 10.1177/0271678X16654495

Herreras, O., and Makarova, J. (2020). Mechanisms of the negative potential associated with Leao's spreading depolarization: a history of brain electrogenesis. *J. Cereb. Blood Flow Metab.* 40, 1934–1952. doi: 10.1177/0271678X20935998

Hertelendy, P., Varga, D. P., Menyhart, A., Bari, F., and Farkas, E. (2019). Susceptibility of the cerebral cortex to spreading depolarization in neurological disease states: the impact of aging. *Neurochem. Int.* 127, 125–136. doi: 10.1016/j.neuint.2018.10.010

Joshi, I., and Andrew, R. D. (2001). Imaging anoxic depolarization during ischemia-like conditions in the mouse hemi-brain slice. *J. Neurophysiol.* 85, 414–424. doi: 10.1152/jn.2001.85.1.414

Juzekaeva, E., Gainutdinov, A., Mukhtarov, M., and Khazipov, R. (2018). Dynamics of the hypoxia-induced tissue edema in the rat barrel cortex *in vitro*. *Front. Cell Neurosci.* 12:502. doi: 10.3389/fncel.2018.00502

Juzekaeva, E., Gainutdinov, A., Mukhtarov, M., and Khazipov, R. (2020). Reappraisal of anoxic spreading depolarization as a terminal event during oxygen-glucose deprivation in brain slices *in vitro*. *Sci. Rep.* 10:18970. doi: 10.1038/s41598-020-75975-w

Juzekaeva, E., Nasretdinov, A., Gainutdinov, A., Sintsov, M., Mukhtarov, M., and Khazipov, R. (2017). Preferential initiation and spread of anoxic depolarization in layer 4 of rat barrel cortex. *Front. Cell Neurosci.* 11:390. doi: 10.3389/fncel.2017.00390

Kalia, M., Meijer, H. G. E., van Gils, S. A., van Putten, M. J. A. M., and Rose, C. R. (2021). Ion dynamics at the energy-deprived tripartite synapse. *PLoS Comput. Biol.* 17:e1009019. doi: 10.1371/journal.pcbi.1009019

Kaufmann, D., Theriot, J. J., Zyuzin, J., Service, C. A., Chang, J. C., Tang, Y. T., et al. (2017). Heterogeneous incidence and propagation of spreading depolarizations. *J. Cereb. Blood Flow Metab.* 37, 1748–1762. doi: 10.1177/0271678X16659496

Khazipov, R., Bregestovski, P., and Ben-Ari, Y. (1993). Hippocampal inhibitory interneurons are functionally disconnected from excitatory inputs by anoxia. *J. Neurophysiol.* 70, 2251–2259. doi: 10.1152/jn.1993.70.6.2251

Khazipov, R., and Luhmann, H. J. (2006). Early patterns of electrical activity in the developing cerebral cortex of humans and rodents. *Trends Neurosci.* 29, 414–418. doi: 10.1016/j.tins.2006.05.007

Khazipov, R., and Milh, M. (2018). Early patterns of activity in the developing cortex: focus on the sensorimotor system. *Semin. Cell Dev. Biol.* 76, 120–129. doi: 10.1016/j.semcdb.2017.09.014

Khazipov, R., Tyzio, R., and Ben-Ari, Y. (2008). Effects of oxytocin on GABA signalling in the foetal brain during delivery. *Prog. Brain Res.* 170, 243–257., 243–257. doi: 10.1016/S0079-6123(08)00421-4

Khazipov, R., Zaynutdinova, D., Ogievetsky, E., Valeeva, G., Mitrukhina, O., Manent, J. B., et al. (2015). Atlas of the postnatal rat brain in stereotaxic coordinates. *Front. Neuroanat.* 9:161. doi: 10.3389/fnana.2015.00161

Leao, A. A. P. (1944). Spreading depression of activity in the cerebral cortex. *J. Neurophysiol.* 7, 359–390. doi: 10.1152/jn.1944.7.6.359

Leao, A. A. P. (1947). Further observations on the spreading depression of activity in the cerebral cortex. *J. Neurophysiol.* 10, 409–414. doi: 10.1152/jn.1947.10.6.409

Lin, C. S., Polsky, K., Nadler, J. V., and Crain, B. J. (1990). Selective neocortical and thalamic cell death in the gerbil after transient ischemia. *Neuroscience* 35, 289–299. doi: 10.1016/0306-4522(90)90083-g

Luhmann, H. J., and Khazipov, R. (2018). Neuronal activity patterns in the developing barrel cortex. *Neuroscience* 368, 256–267. doi: 10.1016/j.neuroscience.2017.05.025

Luhmann, H. J., and Kral, T. (1997). Hypoxia-induced dysfunction in developing rat neocortex. *J. Neurophysiol.* 78, 1212–1221. doi: 10.1152/jn.1997.78.3.1212

Pietrobon, D., and Moskowitz, M. A. (2014). Chaos and commotion in the wake of cortical spreading depression and spreading depolarizations. *Nat. Rev. Neurosci.* 15, 379–393. doi: 10.1038/nrn3770

Rader, R. K., and Lanthorn, T. H. (1989). Experimental ischemia induces a persistent depolarization blocked by decreased calcium and NMDA antagonists. *Neurosci. Lett.* 99, 125–130. doi: 10.1016/0304-3940(89)90276-0

Richter, F., Lehmenkühler, A., Fechner, R., Manveljan, L., and Haschke, W. (1998). Postnatal conditioning for spreading cortical depression in the rat brain. *Brain Res. Dev. Brain Res.* 106, 217–221. doi: 10.1016/s0165-3806(98)00018-2

Saugstad, O. D. (2011). Reducing global neonatal mortality is possible. *Neonatology* 99, 250–257. doi: 10.1159/000320332

Schade, J. P. (1959). Maturational aspects of EEG and of spreading depression in rabbit. *J. Neurophysiol.* 22, 245–257. doi: 10.1152/jn.1959.22.3.245

Sick, T. J., Solow, E. L., and Roberts, E. L. J. (1987). Extracellular potassium ion activity and electrophysiology in the hippocampal slice: paradoxical recovery of synaptic transmission during anoxia. *Brain Res.* 418, 227–234. doi: 10.1016/0006-8993(87)90090-4

Somjen, G. G. (2001). Mechanisms of spreading depression and hypoxic spreading depression-like depolarization. *Physiol. Rev.* 81, 1065–1096. doi: 10.1152/physrev.2001.81.3.1065

Strong, A. J., Fabricius, M., Boutelle, M. G., Hibbins, S. J., Hopwood, S. E., Jones, R., et al. (2002). Spreading and synchronous depressions of cortical activity in acutely injured human brain. *Stroke* 33, 2738–2743. doi: 10.1161/01.str.0000043073.69602.09

Tanaka, E., Yamamoto, S., Kudo, Y., Mihara, S., and Higashi, H. (1997). Mechanisms underlying the rapid depolarization produced by deprivation of oxygen and glucose in rat hippocampal CA1 neurons *in vitro*. *J. Neurophysiol.* 78, 891–902. doi: 10.1152/jn.1997.78.2.891

Toyoda, H., Kawano, T., Sato, H., and Kato, T. (2021). Cellular mechanisms underlying the rapid depolarization caused by oxygen and glucose deprivation in layer III pyramidal cells of the somatosensory cortex. *Neurosci. Res.* 164, 1–9. doi: 10.1016/j.neures.2020.03.003

Tyzio, R., Cossart, R., Khalilov, I., Minlebaev, M., Hubner, C. A., Represa, A., et al. (2006). Maternal oxytocin triggers a transient inhibitory switch in GABA signaling in the fetal brain during delivery. *Science* 314, 1788–1792. doi: 10.1126/science.1133212

Vinokurova, D., Zakharov, A., Chernova, K., Burkhanova-Zakirova, G., Horst, V., Lemale, C. L., et al. (2022). Depth-profile

of impairments in endothelin-1 - induced focal cortical ischemia. *J. Cereb. Blood Flow Metab.* 42, 1944–1960. doi: 10.1177/0271678X22110 7422

Zandt, B.-J., Haken, B. t., and van Putten, M. J. A. M. (2013). Diffusing substances during spreading depolarization: analytical expressions for propagation speed, triggering and concentration time courses. *J. Neurosci.* 33, 5915–5923. doi: 10.1523/JNEUROSCI.5115-12.2013

Zhu, P. J., and Krnjevic, K. (1999). Persistent block of CA1 synaptic function by prolonged hypoxia. *Neuroscience* 90, 759–770. doi: 10.1016/s0306-4522(98) 00495-3

# Frontiers in
# Cellular Neuroscience

**Leading research in cellular mechanisms underlying brain function and development**

Part of the world's most cited neuroscience journal series that advances our understanding of the cellular mechanisms underlying cell function in the nervous system across all species.

---

## Discover the latest Research Topics

See more →

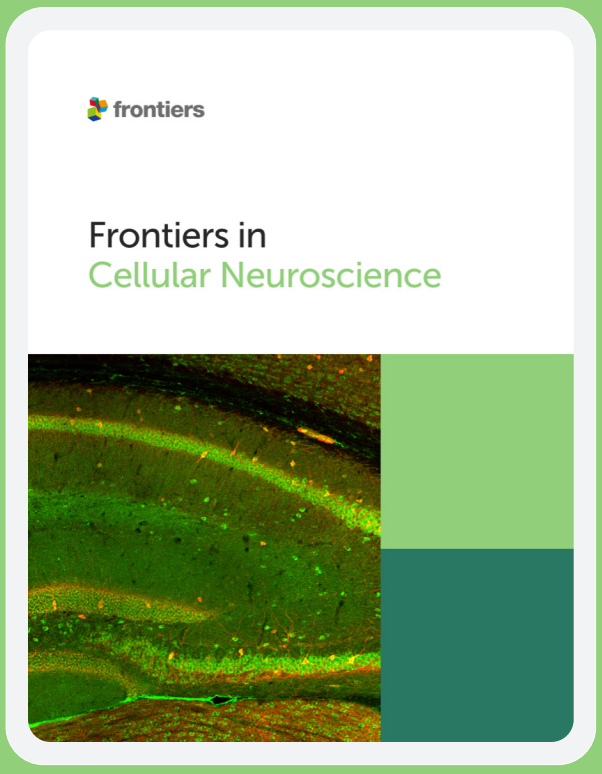


**Frontiers**

Avenue du Tribunal-Fédéral 34
1005 Lausanne, Switzerland
frontiersin.org

**Contact us**

+41 (0)21 510 17 00
frontiersin.org/about/contact